POWER CONVERTER CONTROL FOR OFFSHORE WIND ENERGY GENERATION AND TRANSMISSION

Eduardo Prieto Araujo

Doctoral Thesis

Barcelona, April 2016

Universitat Politècnica de Catalunya

Departament d'Enginyeria Elèctrica

Doctoral Thesis

Power converter control for offshore wind energy generation and transmission

Eduardo Prieto-Araujo

Thesis advisors:
Dr. O. Gomis-Bellmunt (UPC, Spain)
Dr. A. Junyent-Ferré (Imperial College London, UK)

Examination Commitee:
Dr. J. Doval-Gandoy (Universidade de Vigo, Spain)
Dr. D. Montesinos-Miracle (UPC, Spain)
Dr. L. Xu (University of Strathclyde, UK)

Thesis reviewers:
Prof. D. Jovcic (University of Aberdeen, UK)
Dr. S. Norrga (KTH, Sweden)

Barcelona, April 2016

Universitat Politècnica de Catalunya
Departament d'Enginyeria Elèctrica
Centre d'Innovació Tecnològica en Convertidors Estàtics i Accionaments
Av. Diagonal, 647. Pl. 2
08028, Barcelona

Primera impressió, Abril 2016

UNIVERSITAT POLITÈCNICA DE CATALUNYA
BARCELONATECH
Escola de Doctorat

Acta de qualificació de tesi doctoral

Curs acadèmic: 2015-2016

Nom i cognoms
Eduardo Prieto-Araujo

Programa de doctorat
Enginyeria Elèctrica

Unitat estructural responsable del programa
Departament d'Enginyeria Elèctrica

Resolució del Tribunal

Reunit el Tribunal designat a l'efecte, el doctorand / la doctoranda exposa el tema de la seva tesi doctoral titulada **Power converter control for offshore wind energy generation and transmission**

Acabada la lectura i després de donar resposta a les qüestions formulades pels membres titulars del tribunal, aquest atorga la qualificació:

☐ NO APTE ☐ APROVAT ☐ NOTABLE ☐ EXCEL·LENT

Jesús Doval-Gandoy President/a		Daniel Montesinos-Miracle Secretari/ària
Lie Xu Vocal	(Nom, cognoms i signatura) Vocal	(Nom, cognoms i signatura) Vocal

_____, _____ d'/de _____ de _____

El resultat de l'escrutini dels vots emesos pels membres titulars del tribunal, efectuat per l'Escola de Doctorat, a instància de la Comissió de Doctorat de la UPC, atorga la MENCIÓ CUM LAUDE:

☐ SÍ ☐ NO

(Nom, cognoms i signatura) President de la Comissió Permanent de l'Escola de Doctorat	(Nom, cognoms i signatura) Secretari de la Comissió Permanent de l'Escola de Doctorat

Barcelona, _____ d'/de _____ de _____

Diligència "Internacional del títol de doctor o doctora"

- Com a secretari/ària del tribunal faig constar que la tesi s'ha defensat en part, i com a mínim pel que fa al resum i les conclusions, en una de les llengües habituals per a la comunicació científica en el seu camp de coneixement i diferent de les que són oficials a Espanya. Aquesta norma no s'aplica si l'estada, els informes i els experts provenen d'un país de parla hispana.

Daniel Montesinos-Miracle Secretari/ària del Tribunal

To Eduardo, Esperanza,
Vidal, Maruja
and Anna

Acknowledgements

En primer lloc, voldria donar les gràcies als meus directors, per ajudar-me a desenvolupar tota aquesta feina. Fa uns anys, no m'hauria imaginat que pogués arribar on sóc avui i en gran part és per vosaltres. L'Oriol, sempre al costat, donant una resposta adequada a les mil i una preguntes plantejades, fossin o no relacionades amb la tesi, i l'Adrià, ajudant-me a resoldre els infinits dubtes sorgits al llarg d'aquests anys amb una paciència també infinita. Mil gràcies per la vostra confiança.

M'agradaria també agrair a tots els companys del CITCEA la seva col·laboració, sense excepció, ja que tots han contribuït al desenvolupament d'aquest treball: Energia, Urgell, Mecatrònica +2/-1/-1 bis i Gestió. De forma especial, als meus amics/companys de batalles des de l'inici: Agustí, Mònica i Paola i als actuals Joan, Enric, Ricard, Pol, Andreu P. i Mike. També als companys amb els que compartim, hem compartit i compartirem estones de discussions, alegries, frustracions i èxits: Andreu V., Gerard, Cheah, Joan Marc, Collados, Quim, Paco, Ignacio, Bullich, Francesc, Lloret, Guillem, Afsaneh, Abel, Reza, Kevin, Ana, Tomàs, Gabri, Àlex, Carlos, Llonch, Cristian, Macià, Marc, Dani, Javi, Maria i Jordi. Sense oblidar-me, per suposat, dels professors Toni, Sam, Andreas, Dani i Roberto, els quals sempre m'han donat un cop de mà i dels que he après moltíssim.

I would also like to thank Dr. Fainan Hassan and Dr. Sajjad Fekriasl for giving me the opportunity to collaborate with Alstom Grid UK, with special thanks to Jose, Jonathan, John and Nathan for their hospitality, their help and valuable advice. Thank you for making me part of the team. I also would like to thank Romain and Tricia for making my stay in Stafford enjoyable.

Als companys de l'IREC, en Fernando i en especial al David, amb qui hem compartit moltes estones al laboratori disfrutant de la màquina.

A Alstom Wind, que ens ha permès treballar en l'apassionant món dels aerogeneradors. En especial a l'Oriol Caubet, en Javier Luque i en Sergi Ratés, gràcies per les vostres recomanacions i consells.

També voldria donar les gràcies a la meva família, per estar sempre al meu costat, a tots els de Correchouso, als tiets i cosins de León i als Premianencs, als grans i als petits!

Especialment, a la meva mare, per transmetre'm la seva actitud davant la vida, optimista y alegre, per ser com és, constant, forta, un pilar bàsic de la meva vida, ets increïble. Als meus avis, per ser els meus segons pares, i

estar sempre estar disposats a cuidar-me i a ajudar-me en tot, sou els millors. Sense vosaltres això hagués estat impossible, mil gràcies per aguantar-me!

A l'Anna per estar sempre al meu costat, ser el meu suport incondicional i la meva il·lusió. Per animar-me sempre a continuar, entendre'm, respectar-me i compartir totes les decepcions i alegries al llarg d'aquesta aventura. I per ser una experta en eòlica i HVDC!

Per últim, i de forma més especial, no voldria acabar els agraïments sense escriure unes línies sobre el meu pare. L'única pega que li puc posar a la tesi és no tenir l'oportunitat d'explicar-li totes les idees, conceptes, problemes... tot el que he après, però estic completament segur que n'estaria molt orgullós. Si avui estic fent el que estic fent i com ho estic fent és gràcies a tu.

De nou, a tots, moltes gràcies!

This thesis has been supported by the Universitat Politècnica de Catalunya and CITCEA through a FPI grant. Also, the author has received support from other entities:

- Spanish Ministry of Economy and Competitiveness under the projects
  - ENE2009-08555
  - IPT-120000-2010-017
  - IPT-2011-1892-920000
  - ENE2012-33043
  - ENE2013-47296
- Alstom Grid UK, Stafford.
- Institut de Recerca en Energia de Catalunya.
- KIC InnoEnergy PhD School.
- Agència de Gestió d'Ajuts Universitaris i de Recerca.

Abstract

This thesis discusses the control of different power converters that will have a key role in future offshore wind power systems, enabling the integration of the power generated by the wind turbines into the mainland grid.

First, an overview of the evolution of wind turbines is presented, from the first prototypes to the latest topologies in use. Then, a new decentralized control strategy of a triple three-phase permanent magnet synchronous generator, a machine topology specifically designed for offshore wind, is presented. The proposed controller is tested on a wind turbine emulator with a scaled down 30 kW nine-phase generator.

It has been suggested that future wind power plants could use medium voltage DC collection networks. These would require DC/DC converters to adapt the voltages between the turbine output and the DC collection grid. Based on this idea, the control design of a DC/DC Dual Bridge Series Resonant Converter (DBSRC) unit is developed and tested in a scaled 50 kW converter prototype.

The availability of significant energy resources far from the coast favors the idea of creating offshore wind farms. This poses important technical and economical challenges. To this end, Voltage Source Converter-based High Voltage Direct Current (VSC-HVDC) technology enables high power transmission across distances where High Voltage Alternating Current (HVAC) is impractical. The Modular Multilevel Converter (MMC) is the preferred topology to reach high AC and DC voltages. In this work, the control design of a half-bridge based MMC to enable the converter operation under both normal and unbalanced AC voltage conditions, is addressed.

Finally, considering that many offshore wind power plants will be installed in the North Sea in the coming years, a multi-terminal HVDC grid interconnecting several production plants and different points of the mainland grid is envisaged. To deal with DC multi-terminal grid voltage stability, a methodology to address the grid primary voltage control design is proposed based on multivariable frequency methods which are able to evaluate the dynamic behavior of the system.

Resum

La present tesi tracta sobre el control dels diferents convertidors que tindran un paper essencial en els futurs sistemes eòlics marins, permetent la integració de la potència generada pels aerogeneradors a la xarxa terrestre.

En primer lloc, es presenta un estudi sobre l'evolució dels aerogeneradors, des dels primers conceptes a les opcions en ús més modernes. A continuació, es detalla una estratègia de control descentralitzada d'una màquina síncrona d'imants permanents de triple estator trifàsic, una topologia específicament dissenyada per eòlica marina. La proposta de control es valida per mitjà d'un emulador de turbina eòlica juntament amb una màquina de nou fases a escala de 30 kW.

En els darrers anys s'ha contemplat la possibilitat de que els futurs parcs eòlics emprin corrent continu dins la seva xarxa interna. Per tal de construir aquesta xarxa resulten necessaris convertidors d'adaptació DC/DC entre la sortida de la turbina i la xarxa interna del parc en corrent continu. En base a aquesta proposta, es realitza el disseny del control d'un convertidor DC/DC *Dual Bridge Series Resonant Converter* (DBSRC). Per validar els resultats obtinguts, es desenvolupa un prototip del convertidor a escala de 50 kW.

L'alta disponibilitat de recursos eòlics en indrets allunyats de la costa, afavoreix la creació de nous parcs eòlics marins, fet que presenta reptes econòmics i tècnics importants. Amb aquesta finalitat, la tecnologia *Voltage Source Converter High Voltage Direct Current* (VSC-HVDC) permet realitzar la transmissió de potència salvant llargues distàncies, on la transmissió *High Voltage Alternating Current* (HVAC) no és adient. El *Modular Multilevel Converter* (MMC) és la topologia preferida per assolir altes tensions en AC i DC. En aquest treball, es desenvolupa el disseny del control d'un convertidor MMC amb cel·les de mig pont per tal d'operar en presència de sots de tensió desequilibrats a la xarxa.

Finalment, degut a que en un futur proper s'instal·laran al mar del Nord un gran nombre de parcs eòlics marins, es preveu la creació d'una gran xarxa multiterminal HVDC interconnectant diferents plantes de producció eòlica amb diferents punts de la xarxa terrestre. Per tal d'assegurar l'estabilitat de la xarxa, es proposa una metodologia de disseny del control primari de tensió de la xarxa basada en l'anàlisi freqüencial multivariable, capaç d'avaluar el comportament dinàmic del sistema.

Contents

List of Figures

List of Tables

Nomenclature

AC	Alternating Current
CIGRÉ	Conseil International des Grands Réseaux Électriques
CITCEA	Centre d'Innovació en Convertidors Estàtics i Accionaments
CL	Current Loop
DAB	Dual Active Bridge
DBSRC	Dual Bridge Series Resonant Converter
DC	Direct Current
DFIG	Doubly Fed Induction Generator
DSP	Digital Signal Processor
dSPACE	Digital Signal Processing and Control Engineering
EMS	Energy Management System
EWEA	European Wind Energy Association
FEM	Finite Element Model
FRT	Fault Ride-Through
FPC	Full Power Converter
GSC	Grid Side Converter
HF	High Frequency
HV	High Voltage
HVDC	High Voltage Direct Current
HVAC	High Voltage Alternating Current
IGBT	Insulated-Gate Bipolar Transistor
IMC	Internal Model Control
IREC	Institut de Recerca en Energia de Catalunya
IRENA	International Renewable Energy Agency
LCC	Line-Commutated Converter
LV	Low Voltage
MMC	Modular Multilevel Converter
MOSFET	Metal-Oxide-Semiconductor Field-Effect Transistor
OWPP	Offshore Wind Power Plant
PCC	Point of Common Coupling

PI	Proportional-Integral controller
PIC	Peripheral Interface Controllers
PMSG	Permanent Magnet Synchronous Generator
PMSM	Permanent Magnet Synchronous Machine
PLL	Phase Locked Loop
PS	Power Supply
PV	Photovoltaic
PWM	Pulse Width Modulation
RMS	Root Mean Square
SCIG	Squirrel Cage Induction Generator
SCR	Short Circuit Ratio
TSO	Transmission System Operator
UPC	Universitat Politècnica de Catalunya
VSC	Voltage Source Converter
WEC	World Energy Council
WFC	Wind Farm Converter
WPP	Wind Power Plant

Chapter 1

Introduction

1.1 General context

Renewable power has been used by humans for a long time. In fact, until the Industrial Revolution, renewable power sources (including hydro, wind, biofuels and solar) were the only energy sources available. After the Industrial Revolution in the 18^{th} century, a new generation of energy sources came about, bringing with them a significant development. However, a few years later, this evolution caused an important increase in the global level of the planet's pollution. Apart from that, renewable energy sources were almost abandoned as the new machinery powered by coal engines were more practical and powerful. An important part of this evolution was the development of electrical engineering in the 19^{th} century, which allowed for the generation, transmission and distribution of electrical energy to supply loads. At first, generation was carried out in coal and hydro power plants. Then, fuel and nuclear power plants were installed more frequently to generate electricity.

During recent decades, society has realized that the generation and use of electricity has to be carried out in a sustainable manner to reduce CO_2 emissions, reduce pollution, stop global warming and mitigate the risks of accidents in nuclear power plants. The scientific evidence of such problems has created alarm in society which has pushed decision makers to take meaningful action. This action has facilitated the development of renewable energies (mainly hydro, wind and photovoltaic (PV) solar power) which are currently increasing their presence in the energy production market.

Nowadays, renewable energies are an important part of the energy industry, playing a key role in the energy mix of most countries. Such an increased presence presents a number of technical and economical challenges related to the grid integration of these renewable energy sources. The uncontrollability of these resources has motivated the development of advanced operation strategies for ensuring the safe and secure operation of power systems, launching a profound change at all levels in the development of

modern power systems, which need to include power electronic converters, flexible and manageable demand, energy storage, intelligent communication networks and advanced controllers.

Some numbers according to the International Renewable Energy Agency (IRENA) [1] (Fig. 1.1 and 1.2) show that in 2013 the cumulative worldwide renewable generation installed capacity was above 1600 GW, whereby 1138 GW corresponded to hydro power plants, 311 GW onshore wind, 7.5 GW offshore wind, 136 GW PV plants, 3.4 GW solar thermal, 73 GW solid biomass, 12 GW biogas, 11.7 GW geothermal and 0.5 GW tide, wave and ocean. Fig. 1.3 shows that China is leading worldwide in terms of installed capacity, followed by the US, Brazil and Germany. It is clear that the development of renewables is taking place worldwide, and not only in some specific countries. According to the World Energy Council (WEC) [2], future trends (Fig. 1.4) show an increasingly important role for solar thermal power plants, with strong development of both onshore and offshore wind.

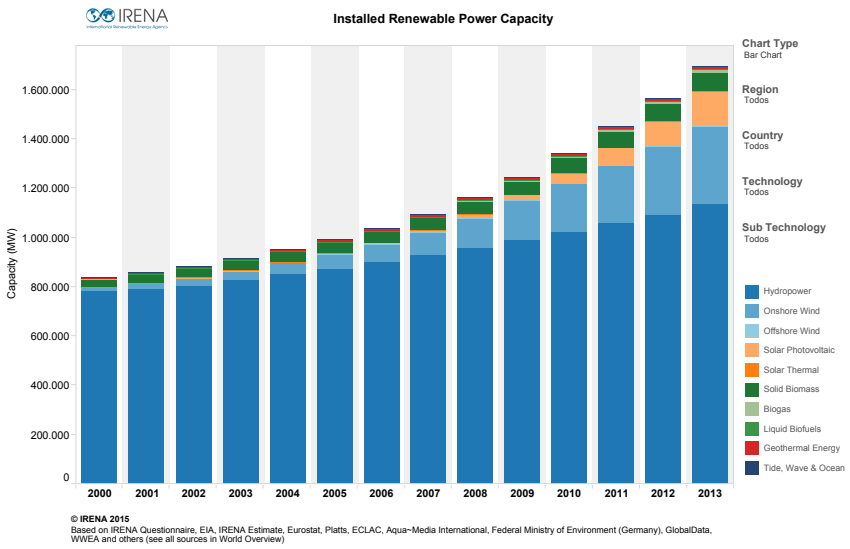

Figure 1.1: Installed renewable power capacity between 2000 and 2013 (see all sources in World Overview) [1]. Courtesy of IRENA.

Among these numbers, an important fact that must be considered is that the capacity factor (which can be defined as the ratio of the net MWh of electricity generated in a given year compared to the electricity that could have been generated at continuous full-power operation) of renewables tends

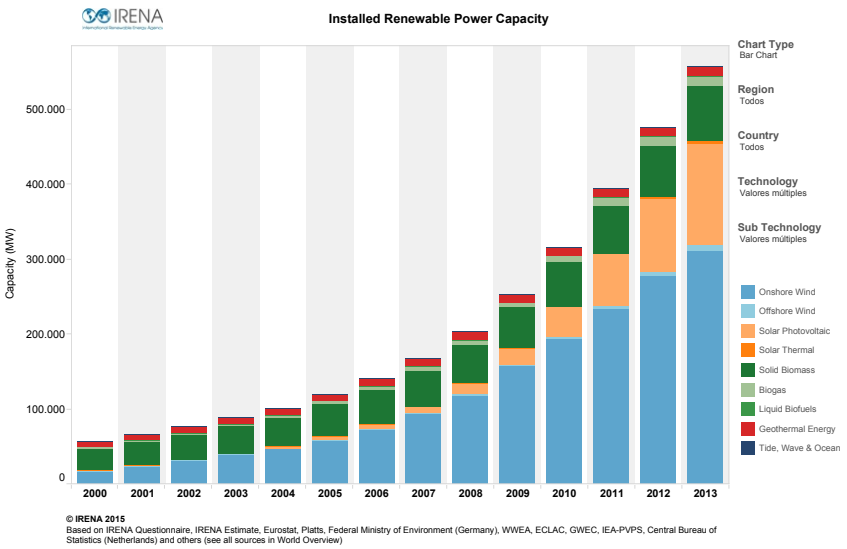

Figure 1.2: Installed renewable power capacity between 2000 and 2013 without hydro power plants (see all sources in World Overview) [1]. Courtesy of IRENA.

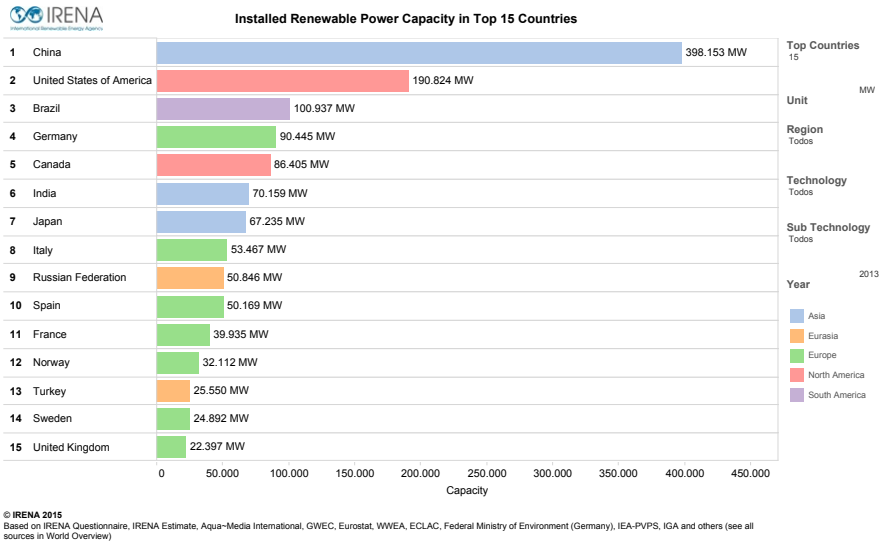

Figure 1.3: Renewable power capacity of different countries [1]. Courtesy of the IRENA.

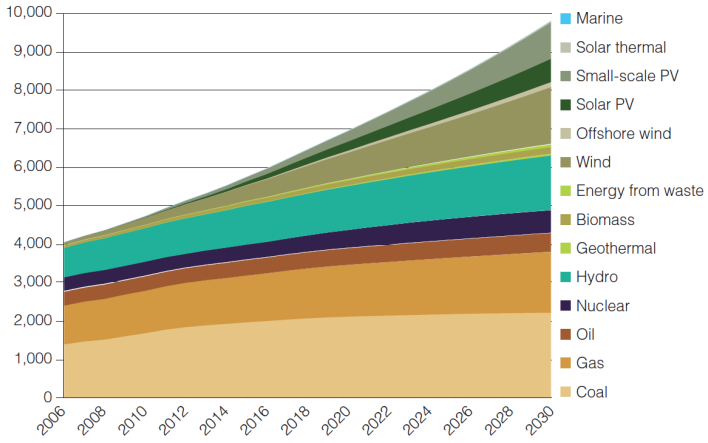

Figure 1.4: Cumulative installed power generation capacity (GW) [2]. Courtesy of WEC.

to be much lower than the capacity factor of conventional generation sources. This is due to the fact that the resource is not always available (clear for wind and solar energy). Fig. 1.5 shows that for wind or solar power a given power capacity leads to a more reduced energy production.

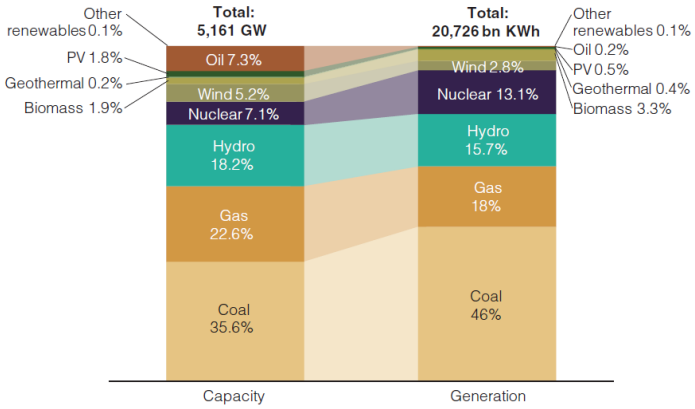

Figure 1.5: Installed electricity capacity versus net generation, 2011. Courtesy of WEC.

1.2 Offshore wind technology context

Offshore wind power is one of the most promising renewable generation technologies [3]. Over the next few years, a number of wind power plants will be commissioned in the North Sea. Offshore wind has various advantages compared to onshore wind, such as abundant wind resources [4], no turbine size limitation and reduced visual impact. On the other hand, offshore installations have some financial and technical challenges [5] such as the need for long-distance transmission systems and the complex and costly installation, operation and maintenance tasks.

In terms of offshore wind turbines, currently there is no dominant generator topology as the manufacturers are still proposing different concepts. Offshore turbines must be designed to be highly efficient, light and reliable [6, 7], with reduced maintenance requirements in order to increase the cost-effectiveness of the system to compensate the high initial investment cost. In the main, two different topologies are being installed offshore: Doubly Fed Induction Generators (DFIG) and Permanent Magnet Synchronous Generators (PMSG) with Full Power Converer (FPC) structure. However, although the DFIG topology is a mature and reliable concept, the market trend seems to drive the industry in favor of the PMSG technology. Different structures have been proposed within the PMSG technology. The key differences between these concepts are the number of generator poles, the gearbox and the generator number of phases. Focusing both on the gearbox and on the number of poles, three different topologies can be distinguished: a PMSG with a reduced number of poles and a gearbox with multiple stages, a medium speed PMSG with a reduced gearbox or a PMSG with a large number of poles without any gearbox (also known as direct-driven technology). Regarding the number of phases, conventionally three-phase generators have been installed on wind turbines. Nevertheless, there are different proposals that suggest increasing the number of phases, as the number is no longer limited to three due to the FPC. Among these various concepts, one of the most interesting topologies proposed for offshore wind that combines several of the previous introduced concepts is the direct-driven multi-pole triple three-phase PMSG with FPC [8–10], a machine that expands the operational possibilities of conventional three-phase generators. Multiphase machines have interesting advantages [11] compared to conventional ones, such as reduction of the grid converter power electronics ratings and improved fault tolerance capabilities due to the redundant structure. Specifically, this machine configuration allows the operation of each three-phase system independently from the other two, considering that each stator is connected to the grid by means of an

FPC. The active and reactive current flowing through each stator can be regulated to operate at different power levels, even allowing for operation with two or even one stators [9]. This structure presents different advantages that are highly interesting in terms of offshore wind.

Moving on to wind farms, the collection grid is another key element in the offshore system. Classic wind farm collection is typically carried out by employing a Medium Voltage (MV) Alternating Current (AC) grid. For offshore wind, collection is also done in AC, based on the already installed power plants and those commissioned. However, different Direct Current (DC) collection concepts, based on DC/DC converter structures, are currently being proposed for offshore wind power plants [12–16], especially for those located far away from the shore, which use High Voltage DC (HVDC) to transfer power from the wind power plant to the main grid. For this application DC/DC converter units are required and different topologies are being proposed [13]. Bidirectional DC/DC converters with isolation [17, 18] are interesting candidates for completing the voltage adaptation between the wind turbine machine side converter DC output and the DC wind farm grid, as they permit black-starting the wind turbine as well as conducting some maintenance, such as blade positioning.

In terms of the transmission grid, offshore facilities can be located tens or hundreds of kilometers away from the coast, connected to the main power grid by submarine cables. In these situations, studies have proved that the most convenient power transmission systems are the HVDC networks [19], consisting of two or more converters connected to a common DC grid [20]. Over the last years, the most common technology for HVDC power transmission has been Line-Commutated Converters (LCC) [21]. Nevertheless, for offshore wind applications, the use of Voltage Source Converters (VSC) is preferred [19, 22, 23] as this type of converters offer relevant operational possibilities for both the offshore wind farms and the transmission grid. VSC-HVDC technology permits independent control of active and reactive power and a continuous AC voltage regulation. They present no commutation failure, black-start capability, and there is no need for voltage polarity reversal to reverse power. As additional advantages, the filters are more compact and the cables lighter [24, 25]. On the other hand, the costs and the commutation losses are higher and they are able to handle only limited levels of voltage and power.

Focusing on the VSC converter topology, it is well-known that conventional VSC converters are based on a two-level structure, built employing two switches per phase. However, this structure is only suitable for HVDC applications if several switches are connected in series, as the blocking volt-

age of a single switch is not enough to withstand complete DC bus voltage [26]. An alternative solution proposed for HVDC is the Modular Multilevel Converter (MMC), first introduced in [27]. The converter is mainly built cascading a large number of submodules per arm. Then, different executions of the concept [28–30] have been adapted by several manufacturers. This converter topology allows not only the handling of the high DC bus voltage, but also provides a high quality voltage output due to the large number of applicable voltage levels. It also shows a reduced switching speed due the reduced number of switchings of each module. Only a few MMC converters have been installed worldwide, thus there is still much research to be done in this topic, especially in terms of its operation and control.

Assuming that in the near future there will be a large number of offshore wind farms connected via VSC-HVDC, it seems reasonable to devise offshore VSC-HVDC grids interfacing a number of such different terminals with different AC grids, resulting in the so-called multi-terminal VSC-HVDC system. Multi-terminal VSC-HVDC stands as an interesting solution to efficiently connect a number of offshore wind farms, but it also implies several technical challenges that will have to be addressed, including control [31], operation [25] and protection issues [24].

1.3 Objectives and scope

Fig. 1.6 shows a picture of an offshore wind system, compounded by two different offshore wind power plants, connected to the main AC grid by means of a multi-terminal HVDC grid. This picture summarizes the different power conversion systems whose control has been analyzed throughout this thesis.

First, a decentralized control strategy is proposed for a nine-phase permanent magnet synchronous generator-based wind turbine (1). In order to validate the control strategy, a scaled platform is developed including a wind turbine emulator and a scaled 30 kW nine-phase generator. In-depth research of the emulation possibilities for wind power is also carried out (2). On the wind farm side, the control design of a bidirectional DC/DC converter unit for DC collection is also addressed. A 50 kW prototype is built to test the converter operation (3). Focusing on the HVDC grid transmission, the study of the control of the MMC is carried out, mainly during unbalanced voltage sags (4). Finally, the primary voltage droop control design of the HVDC grid is developed (5), initially focusing only on the DC grid dynamics and then considering the possible interactions between the AC and

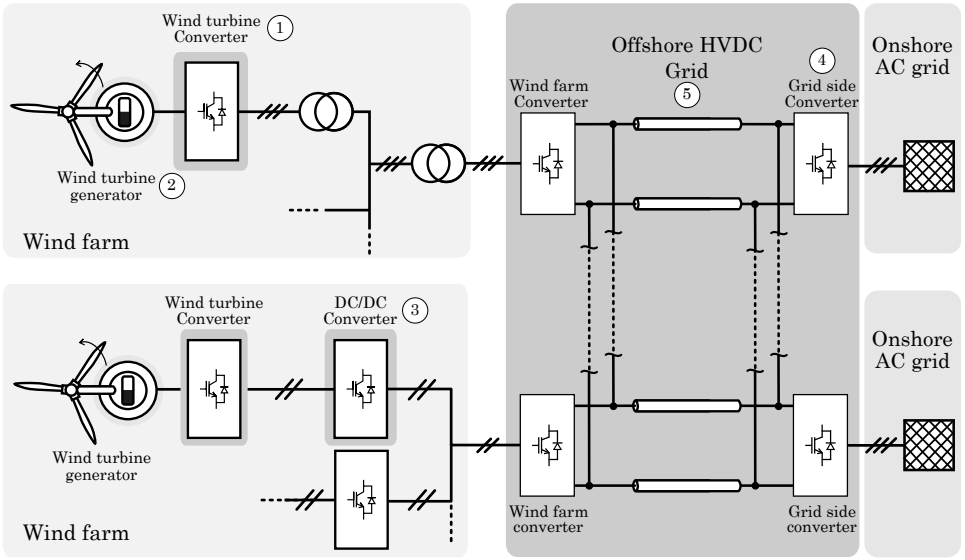

Figure 1.6: Global overview of an offshore multi-terminal grid

DC grid and converter dynamics. Once the different parts of the thesis have been introduced, the objectives and scope of the thesis are described:

- **Analyze the different wind turbine topologies proposed by manufacturers over recent years, focusing on current trend concepts for offshore wind**. A detailed description of the evolution of the wind turbines topologies is given. Starting from the classic Squirrel Cage Induction Generator (SCIG) connected directly to the grid to the DFIG, the current industry workhorse. This study is also extended to include the current proposals for future onshore and especially offshore wind turbines, showing the trend towards installing PMSG-based wind generation systems.

- **Design a decentralized control strategy for a nine-phase permanent magnet synchronous generator-based wind turbine, considering the magnetic coupling existing between the three different stators embedded in the same yoke.** Each stator is controlled by an independent back-to-back converter to inject the generated power to the wind farm grid. Having three different stators within the same machine causes magnetic interaction between them. Typically, centralized controllers can be employed to compensate for transient effects between stators. However, the proposed approach is

able to control the nine-phase machine, avoiding large interaction between the three different stators, by designing a proper stator current controller based on frequency techniques. The decentralized approach is validated using a real test bench based on a wind emulator and a 30 kW nine-phase scaled wind turbine generator.

- **Design the control of a Dual Bridge Series Resonant Converter (DBSRC) to interconnect the turbine converter output and the DC collection grid.** Different DC collection structures for offshore wind are being proposed. The DBSRC could be a candidate for this application due to its bidirectional nature and its isolation provided by the High Frequency (HF) transformer. For offshore wind, the HF stage also allows reduction of the dimensions of the equipment. Typically, this type of converters are controlled through a phase-shift control between the square waves created by the primary and the secondary bridge. This operation could cause large currents flowing through the HF AC side if the voltage at both sides varies from the nominal value. Thus, a modification of the classic phase-shift control is proposed, including the three-level modulation strategy. This modulation allows the reduction of the Root Mean Square (RMS) current flowing through the AC HF tank, thus reducing the converter losses. An optimization algorithm is proposed to obtain the converter minimum current operation points. A 50 kW test bench is built to test the converter operation.

- **Control design and simulation of a Modular Multilevel Converter.** A control design strategy to balance the energy of the MMC converter is proposed. The design of the different system controllers is detailed considering the energy regulators, the grid and inner current regulators and the corresponding reference calculation techniques. Specifically, the reference calculation for inner and AC currents is adapted to consider positive and negative sequence AC voltages so as to be able to operate properly under unbalanced conditions.

- **Design a control strategy for Modular Multilevel Converters to operate under unbalanced AC conditions with equal positive and negative sequence voltage components.** Under the mentioned voltage condition, the MMC control strategy proposed requires modification to be able to operate the converter safely. Specifically, the inner current reference calculation technique is not able to provide any valid current value to accomplish the power set-points ex-

tracted from the energy regulators. To overcome this problem, three different methodologies are proposed, one based on the disconnection of the energy regulators during this voltage condition and two others based on solving the current reference calculation issue using linear algebra tools for incompatible systems.

- **Analyze and design the current-based droop control to perform the primary voltage regulation of multi-terminal VSC-HVDC grids**. The design of the voltage controller is carried out based on a frequency analysis of the linear model of the DC grid. The DC grid state-space representation is obtained and based on this model, multivariable control tools are employed to design the controller considering restrictions both in steady state and in the frequency domain. The imposed design criteria are based on the maximum permitted voltage at the different grid nodes and the maximum current rating of the converters, restrictions that can be transferred as boundaries in the frequency domain.

- **Design the droop voltage control of a multi-terminal VSC-HVDC grid considering the DC grid, the AC grid and the converter dynamics.** In order to expand the scope of the previous work done, this analysis is performed to include in the droop design methodology, other dynamics that could affect its response. Thus, the AC grid, the converter filters, the Phase-Locked Loop (PLL), the current loop and the power and voltage loop dynamics are included in the model of the multi-terminal system that is analyzed to design the droop controller. The droop controller considered is a power-based droop, including a power oscillation damping loop to compensate fast dynamic voltage transients. Considering the different elements, a multivariable frequency response analysis is carried out to decide which are the most suitable droop controllers for the system.

- **Analyze the different emulation topologies that can be used to represent renewable energy sources.** An emulator is a device that is able to mimic the behavior of a renewable energy source at different levels. A detailed description and classification of the different emulators and laboratories that can be found in the literature is carried out. Different emulation levels can be identified based on the level of detail that the device is able to represent. A detailed review for each technology is performed and different emulation levels are identified.

1.4 Thesis related work and activities

In this section, an overview of the chronological activities developed during the PhD thesis are summarized. Predoctoral activities started in April 2011. During this period, the project ENE2009-08555 ("Multi-terminal HVDC systems for the integration of renewable energies to the electrical grid") funded by the Spanish Ministry of Economy and Competitiveness was already ongoing. The work developed by the author within this project was related to the dynamic modeling and control of multi-terminal HVDC grids. Derived from this project, the journal paper [J1][1], two conference papers [C1, C4] and two book chapters [B1, B3] were published.

At the time, there was a collaborative project with Alstom Wind and IREC named Windlider 2 ("Modeling and control of wind turbines and wind power plants") already ongoing. The tasks developed by the author during this project were related to the control of a permanent magnet-based wind turbine generator, specially analyzing grid integration issues as the fault ride-through capability and the possibility of injecting positive and negative sequence to the grid. Results from this research were published in the conference paper [C9]. The outcomes of this project are not included in the PhD thesis.

Deriving from the previous project, the collaborative project IPT-120000-2010-017 with Alstom Wind and IREC ("Research and development of an offshore wind generation system for deep waters") started. The author developed the control of a nine-phase permanent magnet synchronous generator-based wind turbine, validating it in a real setup. From this work, one journal article [J2], a book chapter [B2] and three conference papers [C3, C5, C7] have been published. Also, a patent was filed [P1].

In parallel to the wind turbine-related activities, two different projects focused on emulation techniques were developed, the Llavors project ("Zero Energy Building Lab") funded by the UPC, and the project IPT-2011-1892-920000, from the INNPACTO program funded by the Spanish Ministry of Economy and Competitiveness ("Design and development of a software for the smart organization and regulation of the energy management of council buildings"). The work developed within these projects aimed to perform a detailed analysis of the emulation possibilities of the different renewable resources as wind power or PV by designing an emulation platform where different resources could be emulated. From this work, two journal papers [J3, J5] and conference papers were published [C2, C10-C13, C16, C17].

[1] The description of the publications can be found in Appendix B.

The PhD European mobility lasted from June 2013 to October 2013, at Alstom Grid, Stafford, UK. The author participated in an ongoing project developing the control, building and testing a bidirectional isolated DC/DC converter. From this stage, a conference paper was written [C6].

During the first half of 2014, a second project with Alstom Grid started. The work completed consisted of developing a current flow controller for HVDC grids. From the results of this project, two different patents were filed [P2, P3], and an article has been published [J6]. The results of this project are not included in this thesis.

Besides, the project ENE2012-33043 ("Electrical transport systems for large offshore wind power plants") funded by the Spanish Ministry of Economy and Competitiveness, started in 2013. The author developed work related to the control and operation of offshore wind power plants. From this work, one journal paper has been published [J4], one journal manuscript has been submitted [S-J9] and a conference paper [C14] has been published.

Then, in 2014 the project ENE2013-47296 ("Offshore wind power plants integration in the Spanish electrical system by multi-terminal HVDC links") started in collaboration with the University Carlos III, funded by the Spanish Ministry of Economy and Competitiveness. The work developed by the author in this project is focused on the control of Modular Multilevel Converters for grid voltage condition. From this work, two different manuscripts have been submitted to two different journals [S-J7, S-J8] and a conference paper has been accepted for publication [C8].

Apart from that, another project in collaboration with RTE (Réseau de Transport d'Électricité), the University of Lille and the University of Aberdeen, to develop a scaled DC/DC converter prototype for HVDC grids, has started in 2015. Besides, a project related with the state of the art of FACTS technology in collaboration with REE (Red Eléctrica de España) also started in September 2015. The results of both projects are not part of this PhD thesis.

Also, as a result of collaborations with other researchers not linked with other projects, a conference paper has been accepted for publication [C15].

In addition, the author is participating in the CIGRÉ working group B4-70 ("Guide for Electromagnetic Transient Studies involving VSC converters") and has been a member of the local PES-IEEE Barcelona's chapter.

1.5 Thesis outline

Next, the content of each of the thesis chapters is detailed:

- **Chapter 2** describes the evolution of wind turbine concepts over the years. Each concept is analyzed chronologically explaining its main advantages and drawbacks. Also, the wind industry current trends for offshore applications are addressed.

- **Chapter 3** deals with the decentralized control design of a nine-phase permanent magnet synchronous generator-based wind turbine, one of the proposed topologies to be installed offshore. The suggested control strategy is able to regulate the machine stator currents individually while avoiding large dynamic interaction between stators. The design of the controller is developed using frequency techniques.

- **Chapter 4** describes the control design of a DC/DC Dual Bridge Series Resonant Converter. A modification of the classic phase-shift control is proposed, based on a three-level modulation strategy. This modulation technique allows reduction of the RMS current flowing through the AC HF tank, thus reducing the converter losses. An optimization algorithm is proposed to obtain the converter minimum current operation points. A 50 kW prototype has also been built to test the developments.

- **Chapter 5** presents a control strategy for MMCs during normal and unbalanced grid voltage conditions. A detailed control design procedure for the current and arm energy loops is included, to achieve the desired power exchange between the AC and DC grids while maintaining the converter energy balanced. The controllers and the reference calculation strategies are adapted to operate under any voltage condition.

- **Chapter 6** describes a modification of the MMC control proposal described in Chapter 5 to allow MMC operation during unbalanced AC grid conditions with equal positive and negative sequence voltage. This singular voltage condition could drive the converter to an unstable behavior. To overcome this problem, three different methodologies are proposed.

- **Chapter 7** presents the droop control design of a multi-terminal HVDC grid. A generic state-space model of the multi-terminal net-

work based on the linear equivalent model of the HVDC grid is obtained. Then, the transfer function matrices of the system are calculated to perform a multivariable frequency analysis of the system. This methodology permits designing the droop constant for the converters performing voltage control, based on maximum voltage error criteria while considering converter current constraints.

- **Chapter 8** expands on the work developed in the Chapter 7 on multi-terminal HVDC grid droop control. The DC grid model is extended including the AC grid and the control dynamics of the converters. A complete linearized model of the HVDC multi-terminal grid is derived to include the different dynamics that can affect the droop voltage control performance. Then, a multivariable frequency response analysis is carried out to decide which is the most suitable droop controller. The droop control design is developed, including an oscillation damping loop which is able to compensate fast transients of the DC grid voltage.

- **Chapter 9** draws the conclusions of the thesis and also gathers the future work research lines on the different topics addressed.

In addition, in Appendix A different emulation possibilities for wind power and also for different renewable energy resources are described. A detailed review of each technology is performed and different emulation levels are clearly identified.

Chapter 2

Wind turbine technologies

2.1 Introduction to wind energy

In the early stages of the electric power generation, resources such as coal and oil fuels presented a more consistent production of electricity than the fluctuating generation of wind power. This consistency was the key factor that positioned fossil fuels as the basic resource for electricity production for many decades. Although the first developments of electric power generation via wind turbines started during the 19^{th} century, it was not until the 1970s, and specially during the 1990s, that wind power became a more important energy source. Today, it is one of the most-used renewable energies to obtain electric power [32].

Focusing on wind turbines technology, in 1881 Poul LaCour built one of the first wind turbine generators to produce electric power [33]. Since then, many different topologies have been developed, ranging from a few to thousands of kilowatts, showing different types of rotor blades, including different generator topologies, among other variations. Despite of the different proposals and manufacturers, wind turbine power has always been increasing. For instance, in 1989 a common wind turbine could produce up to 300 kW and it had 30-meter rotor blades. However, a decade later, in 1998, the state of the art was a 1500 kW turbine with 70-meter rotor diameter [34] and today, the largest wind turbines can produce more than 8 MW of electric power. Analogously, there is also an increasing trend of the wind power installed worldwide, growing each year, with an installed capacity of 370 GW at the end of 2014 [35].

In recent years, wind turbines have been installed on the mainland in locations where wind speeds are more favorable. Nevertheless, there is a current trend towards installing wind turbines in the middle of the sea. Offshore wind shows several advantages in comparison with onshore locations, such as better wind climate, higher average wind speeds, reduced visual impact and unlimited turbine dimensions due to logistics [4]. On the other hand,

these installations present some drawbacks, such as complex wind turbine marine support structures and logistics for installation, operation and maintenance. These new conditions are leading wind power manufacturers to develop and design new turbine topologies for installation in future offshore wind power plants.

2.2 Parts of the wind turbine

Different wind turbine types have been proposed during the recent decades. A first division can be made between machines including a vertical-axis, such as Savonius, Darrieus or Giromill, or horizontal-axis turbines. Specifically, the most common structure installed worldwide is the well-known three-bladed rotor horizontal-axis turbine.

In this section, the main parts of this concept are described in detail, considering different possible layout variations. Fig. 2.1 shows a conceptual scheme of a generic horizontal-axis turbine. The rotor is mainly compounded by the hub, the blades and the mechanical shaft. The blades, which capture energy from the wind, are attached to the hub by mechanical joints and this energy is transferred to the generator by means of the shaft. Also, placed in the rotor, the pitch system allows the limitation of the incoming power from the wind by changing the blade angle so as to maintain the machine under its power limits. In addition, mechanical brakes are installed to restrict the speed of the machine during the operation. Usually, wind turbines include a gearbox to adapt the slow angular speed of the rotor blades to the high speed of the generator. This gearbox could also be removed in some topologies if the generator is modified to adapt the rotor speed to the generator electrical speed by itself, for instance through multipolar structures.

The high-speed gearbox output shaft is directly connected to the generator, where power conversion from mechanical to electrical is performed. Different generators types are typically included, mainly induction or synchronous machines. Depending on the generator installed and the turbine structure considered, power electronics converters could be connected at the machine rotor or stator terminals. The generator can be controlled by means of this converter, achieving better wind power extraction with proper grid integration of the produced energy. Conventionally, the generator output is connected to a transformer in order to adapt the voltage level and its corresponding switchgear is located before the connection to the wind farm grid. Regarding the distribution of the described elements inside the wind turbine, commonly the gearbox and the generator are embedded inside the

nacelle, and other parts as the converter or the transformer can be located either inside the nacelle or the tower. Fig. 2.2 shows a nacelle scheme of a current wind turbine including several of the elements presented above.

The previous component description applies to both onshore and offshore wind turbines. The main difference between them is the support structure employed. Onshore wind turbines are installed on a conventional concrete basement, whereas offshore wind turbines have different possibilities. Two main offshore structures can be differentiated: foundation and floating types. Foundation structures are based on supporting the wind turbines through a structure attached to the sea bed, whereas floating structures provide support systems without a physical joint with the sea bed, employing buoyancy or ballast techniques.

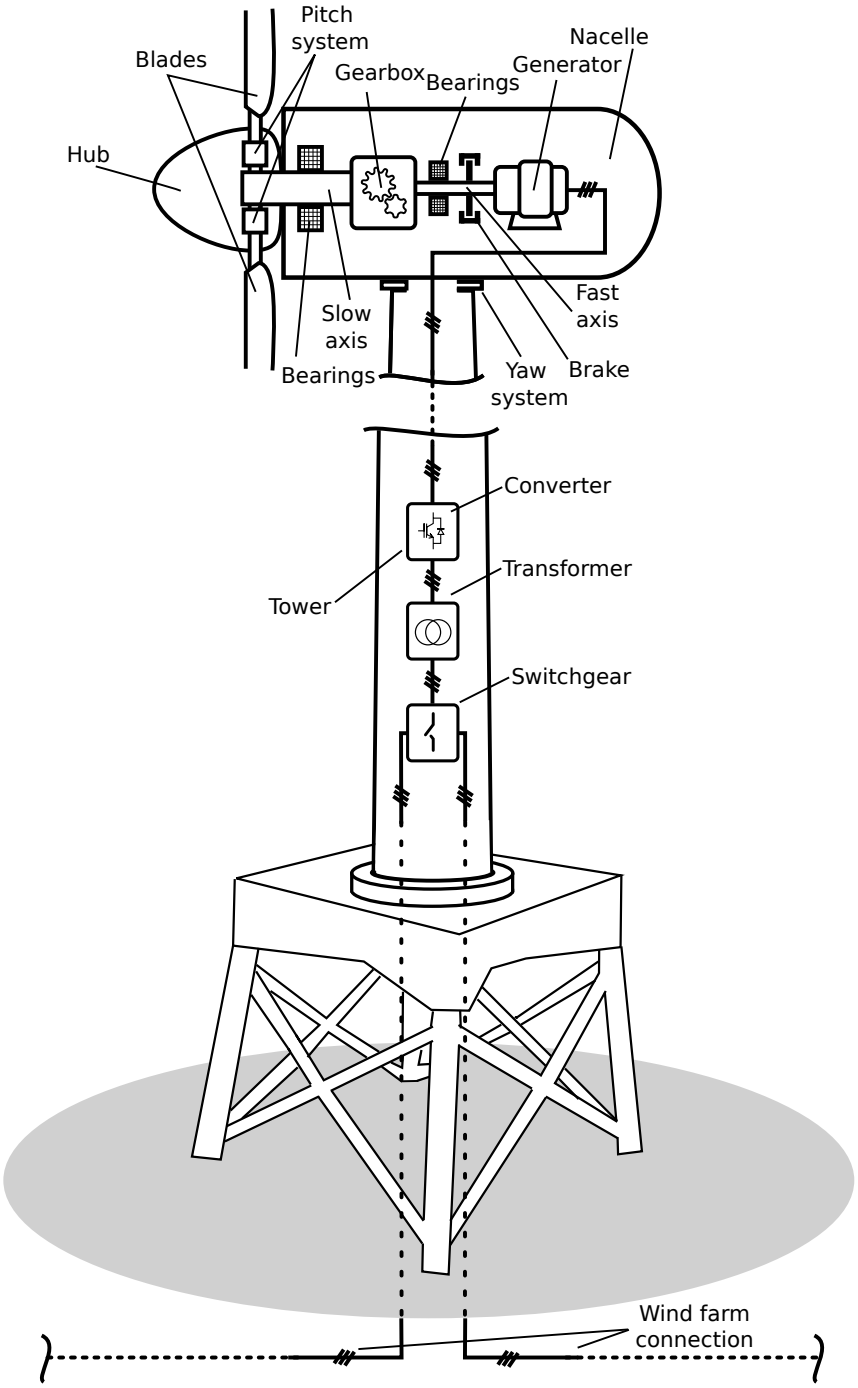

Figure 2.1: Horizontal-axis wind turbine conceptual scheme

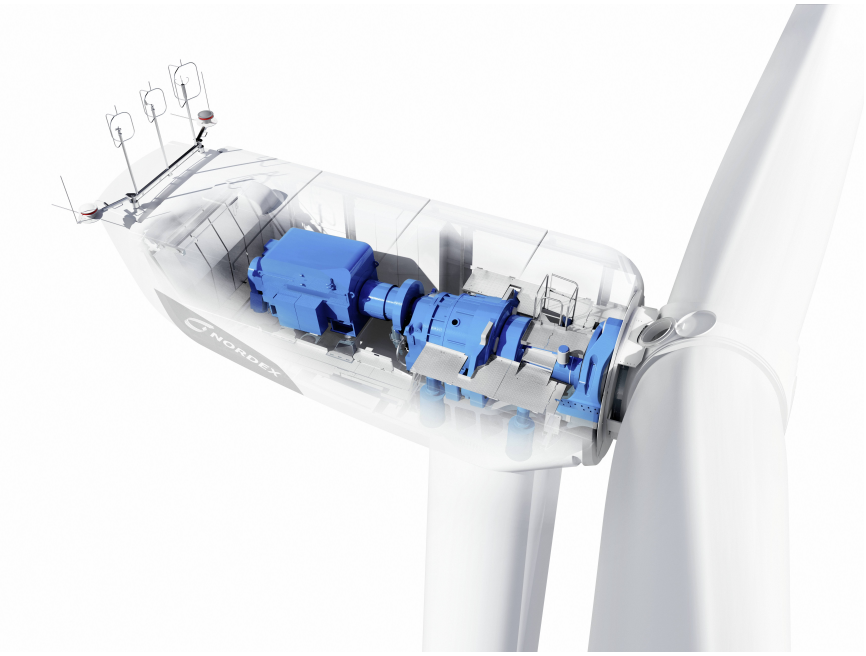

Figure 2.2: Horizontal-axis wind turbine view. Courtesy of Nordex.

2.3 Wind turbine types

This chapter deals with the most important types of wind turbines that have been proposed since 1970. They can be classified as [34]:

- Fixed-speed wind turbine
- Limited-speed wind turbine
- Variable-speed with partial-scale converter
- Variable-speed with full-scale converter

Each of these types is described, showing its possibilities, advantages and drawbacks.

2.3.1 Fixed-speed wind turbines

During 1980s and 1990s, the most relevant machine topology was the fixed-speed wind turbine. This solution, also known as 'the Danish concept' is usually composed of a three-bladed rotor, a multiple-stage gearbox and a Squirrel Cage Induction Generator (SCIG) connected directly to the grid by means of a transformer [36]. This machine topology is operated over and near the synchronous speed where the induction machine works as a generator, fixed due to its direct connection to the grid.

During operation, the SCIG needs to absorb reactive power to magnetize the machine, usually provided by a capacitor bank. In terms of power control, these turbines usually include a thyristor-based soft-starter used to start up the machine when it is connected to the grid in order to avoid large currents. Also, in order to increase the power extraction possibilities some generators incorporate two winding sets with a different number of pole pairs, so as to be able to change the synchronous speed. These machines can be divided in three different types depending on the power limiting system implemented, which can be passive or active stall and pitch [34].

The fixed-speed's main advantages are the robustness of the system, the relatively low production costs and its straightforward control [37]. These advantages were the main reasons that prompted the manufacturers to install this technology in the first wind farms. However, it also presented several early disadvantages that caused the shift to other topologies. The first drawback is related to the generator constant speed operation, which does not allow the machine to extract the maximum available power from the wind. Also, a fixed-speed implies high mechanical stress considering that

any wind speed fluctuations are transmitted in terms of torque, causing potential drive train failures. Other drawbacks were the requisites imposed by the grid operator as voltage/frequency support and fault ride-through requirements. The SCIG can not only not provide voltage support injecting reactive power, but also needs to absorb it during its normal operation. In terms of the fault ride-through capability, SCIG wind turbines are directly connected to the grid and it is difficult to avoid a disconnection due to high current flowing through the generator during a voltage sag [37].

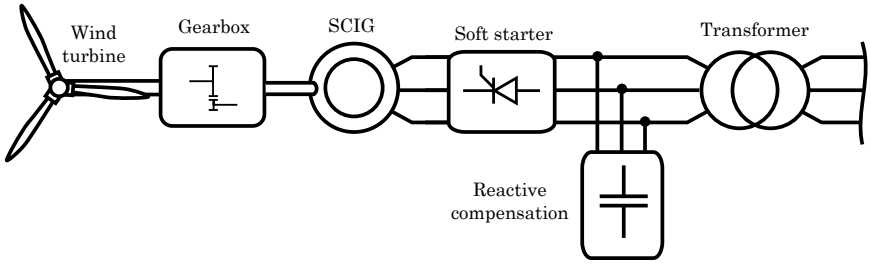

Figure 2.3: Fixed-speed wind turbine - SCIG - Multiple-stage gearbox

2.3.2 Limited variable-speed wind turbine

During the 1990s, limited variable-speed was proposed, changing the generator type from the conventional SCIG to a Wound Rotor Induction Generator (WRIG) [38]. This technology (Fig. 2.4), also known under the commercial name *Optislip* (Vestas manufacturing), introduced a variable rotor resistance to increase the speed operation range (typically from 0 to 10%). By changing the rotor resistances value via a power electronic converter, the slip of the machine (and therefore the speed) can be modified. Nevertheless, in order to achieve this level of control, some power has to be lost in the wound rotor resistances. In summary, these machines partially solved the requirement of needing a variable speed to increase the aerodynamic efficiency, but by large they still had the same problems than the fixed-speed concept. This was one of the first steps towards the variable-speed concept, which is leading the wind turbine market today.

2.3.3 Variable-speed with partial-scale converter wind turbines

The variable-speed concept appeared in order to increase the operation performance of the wind turbines. Specifically, this concept (Fig. 2.5) consists of a WRIG generator connected to the grid directly by the stator and through

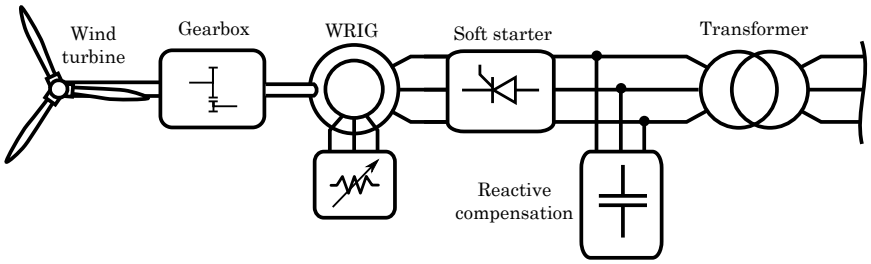

Figure 2.4: Limited variable-speed - SCIG - Multiple-stage gearbox

the rotor by a partial-scale power converter, resulting in the so called Doubly Fed Induction Generator (DFIG) [39]. This power converter allows the machine control over a wider speed range (typically from -40% to +30%) than the more limited-speed topologies. Using the converter, a proper active and reactive power control can be carried out on the machine to optimize wind power extraction. In terms of the grid integration, the partial-scale converter increases the possibilities of the system. The grid side part, operated independently from the machine side, can be controlled to achieve a better ride-through capability of the wind turbine [40] and for voltage support.

However, this concept has different drawbacks [34]. Slip rings are needed in order to extract the power from the rotor and are one of the components causing machine operation failures. Moreover, the stator is still directly connected to the grid and so during grid faults managing a proper ride-through operation is complicated.

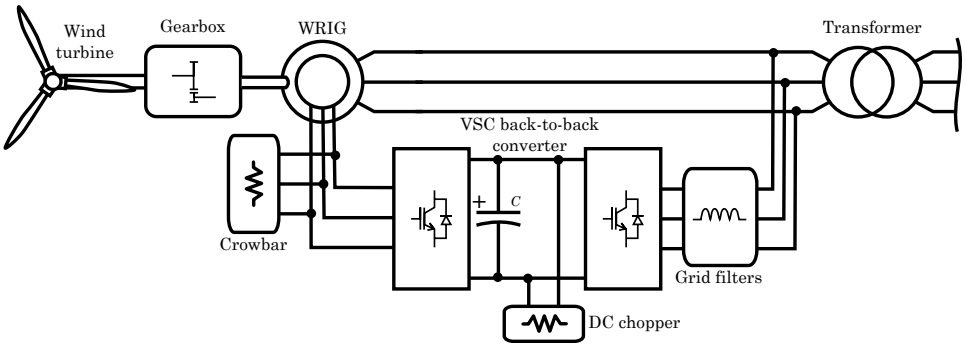

Figure 2.5: Variable-speed - DFIG - Multiple-stage gearbox

2.3.4 Variable-speed with full-scale converter wind turbines

The variable-speed topology with full-scale converter maximizes the speed operation range of the machine. Therefore, the maximum available power from the wind can be extracted within the rated limits. In addition, the grid operators requirements can be satisfied by considering a proper grid side converter control. These systems can provide support to the grid voltage/frequency and they can incorporate ride-through strategies. Usually, a Direct Current (DC) chopper is included in the DC bus link to bypass the voltage sags during the operation. This concept can be implemented for different types of generator, SCIG, Permanent Magnet Synchronous Generator (PMSG), Wound Rotor Synchronous Generator (WRSG) [41]. Next, the most common proposals are described.

SCIG Generator

In terms of the induction generators, the common variable-speed proposal is based on a SCIG generator and a full power converter [42]. Through the converter, the generator is totally isolated from the grid, so the speed is completely controllable. Also, the reactive power needed for the machine operation can be supplied by the machine side converter. This concept is not available without gearbox due to the construction inconveniences of having multi-polar SCIG generators [43]. One of the main drawbacks could be the relatively low efficiency of the overall system considering the generator, gearbox and full power converter losses [36].

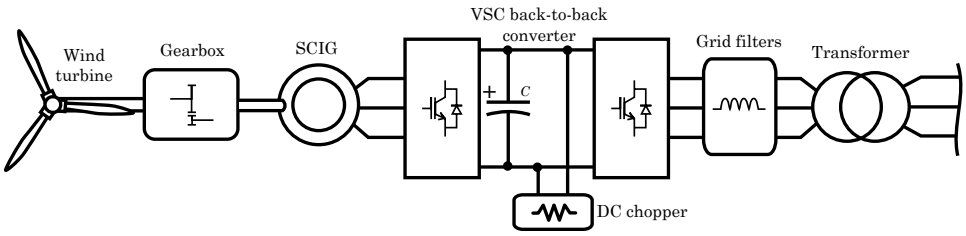

Figure 2.6: Variable-speed - SCIG - Multiple-stage gearbox

Direct-driven WRSG

This concept consists of a WRSG with DC rotor excitation connected to the grid by means of a back-to-back converter. This type is usually implemented without gearbox through incrementing the number of poles of the rotor, thus

obtaining a direct-driven system. The increase in the number of poles implies a large generator diameter, thus giving a machine of bigger dimensions [44]. On the one hand, the associated costs of the gearbox are eliminated. On the other hand, the generator costs are increased. Another interesting feature of this machine is the controllable DC excitation. Through the DC converter, the rotor flux can be controlled for different purposes: field-weakening strategies for high-speed operation, loss minimization techniques, among others [45]. Nevertheless, it must be considered that the excitation control is performed by a converter located outside the rotor and commonly connected to the machine windings through slip rings. This system implies losses during operation due to the current flowing through the DC winding. In addition, regular maintenance must be considered if slip rings are used.

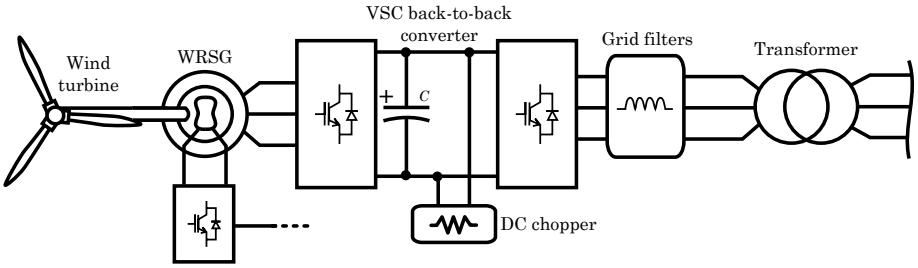

Figure 2.7: Variable-speed - WRSG - Direct-driven

Direct-driven PMSG

Related to the previous WRSG concept, the PMSG direct-driven generator connected to the grid by means of a full power converter is proposed. This type of generator comes from the idea of substituting the wound rotor DC excitation by magnets, thus eliminating excitation losses [45].

The possibilities of the PMSG being isolated from the grid through the converter are equivalent to the WRSG. PMSG rotors can also be constructed with a large number of poles. However, PMSGs are smaller and lighter when including a large number of poles than the equivalent WRSG [44], therefore this topology achieves a higher power density.

On the other hand, working with permanent magnets can be difficult during the manufacturing and operation stages. Furthermore, the permanent magnet materials are quite expensive. Nevertheless, in recent years its cost has been considerably reduced [36].

During the operation, the fact of having a constant flux in the rotor produced by the magnets may cause large voltage values at the machine ter-

minals for high speeds, forcing the converter to apply larger voltages which might not be available. In the WRSG, excitation could be weakened in order to reduce rotor flux, through reducing DC excitation voltage. In a PMSG, the flux cannot be reduced because the excitation is permanent. Given this, a flux-weakening technique must be employed to reduce the terminal voltages at high speed [46]. This technique must be done without too much effort in order not to demagnetize the magnets. This demagnetization can also be caused by certain possible faults in the machine. In addition, these magnets are sensitive to the temperature, therefore this factor should be controlled during the operation.

There are many different types of PMSG which can be classified by their flux direction, type of rotor, type of magnets and the winding layout.

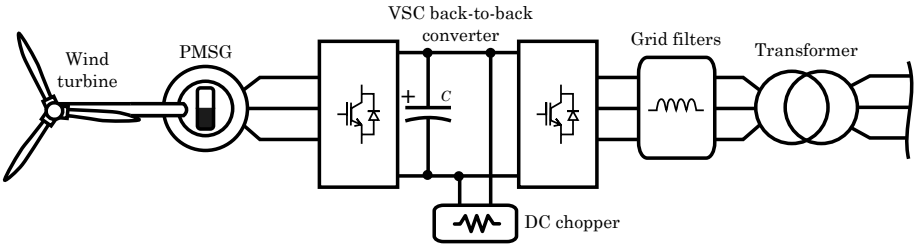

Figure 2.8: Variable-speed - PMSG - Direct-driven

PMSG with a single/multiple-stage gearbox

This topology combines a PMSG with a single-stage or a multiple-stage gearbox system in order not to construct a bigger generator with a large number of poles [44]. The single-stage topology does not achieve a high transmission ratio. This is of interest because it combines a small gearbox with a relatively small generator with a reduced number of poles. Therefore, the generator does not need to be overly large and expensive and gearbox complexity can also be reduced. The generator is operated with medium speed and torque characteristics.

On the other hand, the PMSG with a multiple-stage gearbox can operate a conventional low-torque, high-speed generator [36]. The PMSG used for this design is lighter than the other topologies, with a normal number of poles. The main drawbacks are the cost, weight, maintenance and complexity of the gearbox needed for this solution.

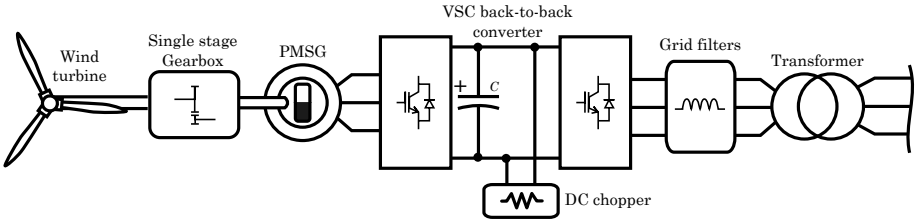

Figure 2.9: Variable-speed - PMSG - Single-stage gearbox

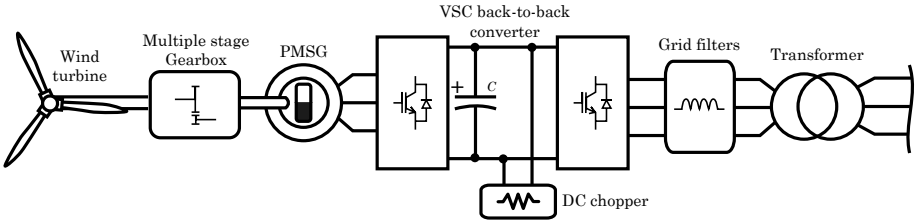

Figure 2.10: Variable-speed - PMSG - Multiple-stage gearbox

Direct-driven multiple three-phase PMSG

Recently with the growing interest on the offshore wind power plants, factors such as reliability and efficiency have gained importance. Three-phase PMSGs are one of the topologies which could be installed in these offshore plants. However, the back-to-back converter offers other possibilities which could be profitable for offshore operation. Since the generator is isolated from the grid, the number of the generator phases is not limited to three, therefore redundant structures based on multi-phase machines can be constructed in order to increase system reliability [41].

One of the proposed technologies is the direct-driven multipolar PMSG with multiple stators, which may include two or more three-phase winding sets with isolated neutral points [47]. Each stator is connected to a three-phase back-to-back converter in order to control the power flowing through each of them. This structure increases the reliability by means of redundancy, allowing for different fault tolerance strategies. Moreover, these redundant structures reduce the amount of power flowing through each converter, compared to a single three-phase one, thus decreasing the stress suffered by the power electronics.

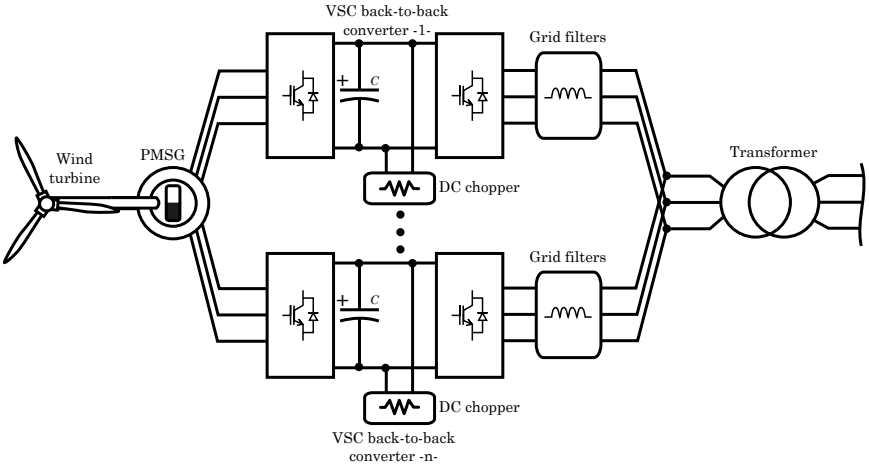

Figure 2.11: Variable-speed - Multiphase PMSG - Direct-driven

Other proposals

In the literature, other new wind turbine topologies can be found. One of these topologies is the brushless DFIG (BLDFIG) [41] which consists of eliminating the the DFIG concept slip rings which are one of the main drawbacks of the topology. This is achieved by constructing a machine with a double stator, connecting the partial-scale converter to the second one so avoiding the slip rings of the rotor connection. This machine is operated similarly to a conventional DFIG machine.

2.4 Conclusions

Since the first steps of wind power generation, manufacturers have proposed a number of turbine concepts. Two of these types, fixed-speed and variable-speed with partial-scale converter wind turbines, have been the workhorses of the wind industry the past decades. However, the current trend is leading wind technology towards full-scale converter wind turbines due to the possibilities offered by this concept together with the price reduction of the power electronics and the increasing restrictions imposed by the transmission operator grid codes. To conclude, the evolution of the wind turbine topologies can be explained as a combination of the technology improvements and other factors related to the wind industry.

Figure 2.12: Alstom Haliade-150 Offshore Wind turbine.
Courtesy of Alstom.

Chapter 3

Decentralized control of a nine-phase permanent magnet synchronous generator for offshore wind turbines

3.1 Introduction

The workhorse machine of the offshore wind industry is still being defined and manufacturers are proposing different topologies. However, it seems clear that there is a trend towards the use of a Full Power Converter (FPC) structure together with a Permanent Magnet Synchronous Generator (PMSG). This concept itself has different variants, such as considering (or not) the incorporation of the gearbox or the number of phases of the PMSG. In terms of reliability and maintenance, direct-driven multi-polar generator topologies avoid the installation of the gearbox [7], thus avoiding its associated costs. Also, the number of generator phases is not limited to three anymore, due to the FPC. Then, generators with a large number of phases can be installed to increase the redundancy of the system as well as reducing converter semiconductor stress [11]. Specifically, the multi-polar triple three-phase PMSG is an interesting topology for offshore wind due to its redundancy and its direct-driven configuration.

Nevertheless, including a multi-phase generator (with more than three phases) in the system complicates the control task due to the internal magnetic coupling present between the phases. Different approaches for controlling the multi-star machine currents have been proposed in the literature [11]. Classic vector control can be extended for multi-phase machines [11] considering that each FPC converter can regulate its corresponding three-phase stator current, even including a centralized controller able to decouple the effects between stators [48–50]. In order to apply this decoupling, fast communications between the converter controllers or a centralized control are required. However, in this work the nine-phase machine control is de-

signed to be performed by local stator controllers [51] without communications between them, posing the challenge of handling the stator coupling interaction.

The proposed strategy could be of interest for applications that do not include communications among the different converters connected to each Permanent Magnet Synchronous Machine (PMSM) stator. If fast communications between converters or a centralized controller are available, control approaches capable of decoupling the interaction between stators may be implemented [48–50] due to their notable performance. Nevertheless, if these communications fail or the bandwidth is not high enough to compensate the stator couplings, the system could still be controlled with the proposed decentralized strategy, thus ensuring proper behavior.

For wind power multi-star generators, the decentralized control methodology could be interesting as the machine can still be operated, even in case of a communication failure between the stator controllers. This problem becomes especially important for offshore wind power plants where maintenance tasks are more complicated compared to onshore sites, due to limited accessibility [6]. In addition, failures could last for a longer period of time. Thus, this control strategy could avoid disconnection of an offshore machine that otherwise might remain non-operative for a long period of time, with the corresponding negative economic impact.

To the best of the author's knowledge, there is no methodology for designing a decentralized vector control of a triple three-phase PMSM without communications among the different converter local current controllers which ensures a proper machine performance by limiting the interaction between the different stator currents. This work describes the procedure to design a decentralized current control for a direct-driven triple three-phase PMSM. The active and reactive power flowing through each of the machine stators are regulated through six different controllers, implementing two of them at each of the three-phase converters. The main issue during the design of the controllers is the existing coupling between machine phases. A detailed machine model is obtained assuming non-zero mutual coupling between the three stators in order to analyze the existing interactions. Once the model is derived, the machine current regulators are designed based on the machine open and closed loop frequency response of the multivariable system. The control objectives defined are: the current set-points tracking with a proper dynamic performance and a reduced interaction between stators during transients. The proposed decentralized controller is validated through dynamic simulations and implemented in a real test rig including a scaled 30 kW nine-phase PMSM.

The chapter is organized as follows: the equations of a generic triple three-phase machine model are obtained in Section 3.2. These equations are used in Section 3.3 to define the methodology to design the decentralized current controllers. In Section 3.4, this methodology is applied to design the control of a triple three-phase wind turbine generator and in Section 3.5 the simulation results of the proposed controller are shown. Finally, in Section 3.6 experimental results of the operation of a scaled nine-phase wind turbine generator based on the proposed decentralized control are presented.

3.2 Machine modeling

This section details the nine-phase PMSM model derivation in the reference frame fixed in the rotor. Multi-phase machine modeling in the conventional *qd* reference frame has been previously addressed in [52] for an induction machine with multiple winding sets. Among the different multi-phase machine topologies, the dual-stator induction machine has been widely analyzed in the literature [11, 48, 53, 54]. In terms of dual-stator PMSMs, different modeling approaches can be found in [55, 56], even for wind generation systems in [47]. Also, specific modeling techniques for nine-phase PMSMs have been proposed [8, 9]. For the present study, the following assumptions are made to obtain the model:

- Nine-phase, triple three-phase stator configuration.
- Generic winding configuration.
- Round rotor machine. The inductances are considered to be independent from the rotor position [52].
- Saturation effects are not considered.

Next, the voltage equations of the nine-phase machine are presented. The electrical phase layout of the machine stators (s1, s2, s3) is shown in Fig. 3.1.

Each stator has its own isolated neutral point and each one is shifted 40 electrical degrees ($2\pi/9$ radians) from the other two. Phases a_{s1}, b_{s1}, c_{s1}, a_{s2}, b_{s2}, c_{s2} and a_{s3}, b_{s3}, c_{s3} form stators 1, 2 and 3 respectively. The machine voltage equations can be defined as [52]

$$v_s^{\overline{abc}} = \mathbf{R_s} i_s^{\overline{abc}} + \frac{d}{dt} \lambda_s^{\overline{abc}} \tag{3.1}$$

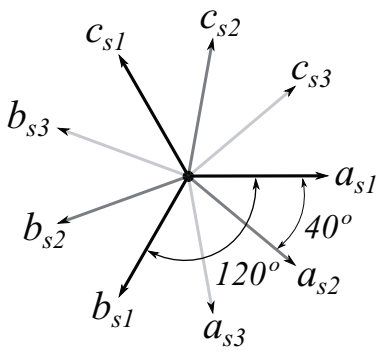

Figure 3.1: Machine electrical phase distribution

where $v_s^{\overline{abc}}$ is the vector of voltages applied to the machine by the converters, $i_s^{\overline{abc}}$ is the vector of currents flowing through the machine, $\lambda_s^{\overline{abc}}$ is the flux linkage vector of the stator windings and $\mathbf{R_s}$ is the diagonal matrix that represents the resistance R of the machine windings. The dimension of these vectors is 9x1 and internally, the variables are sorted as

$$x = \left[x_{s1}^a, x_{s2}^a, x_{s3}^a, x_{s1}^b, x_{s2}^b, x_{s3}^b, x_{s1}^c, x_{s2}^c, x_{s3}^c\right]^T \tag{3.2}$$

where x is either a current, voltage or flux magnitude, a, b and c are the phases and s_i the corresponding stator. The flux linkage term λ_s^{abc} can be expanded as

$$\lambda_s^{\overline{abc}} = \mathbf{L_s} i_s^{\overline{abc}} + \lambda_m \begin{bmatrix} \sin(\theta) \\ \sin(\theta - \varphi) \\ \vdots \\ \sin(\theta - 8\varphi) \end{bmatrix} \tag{3.3}$$

where $\mathbf{L_s}$ is the inductance matrix of the machine, λ_m is the flux linkage of the magnets, φ is the electrical angle between two phases (in this case 40 degrees) and θ is the electrical angle of the machine. It is assumed that the flux created by the magnets is sinusoidally distributed along the air-gap. Specifically, the inductance matrix $\mathbf{L_s}$ of a nine-phase machine, considering

a generic winding distribution, can be expressed as [8, 9]

$$\mathbf{L_s} = \begin{bmatrix} L & M_1 & M_2 & M_3 & M_4 & M_4 & M_3 & M_2 & M_1 \\ M_1 & L & M_1 & M_2 & M_3 & M_4 & M_4 & M_3 & M_2 \\ M_2 & M_1 & L & M_1 & M_2 & M_3 & M_4 & M_4 & M_3 \\ M_3 & M_2 & M_1 & L & M_1 & M_2 & M_3 & M_4 & M_4 \\ M_4 & M_3 & M_2 & M_1 & L & M_1 & M_2 & M_3 & M_4 \\ M_4 & M_4 & M_3 & M_2 & M_1 & L & M_1 & M_2 & M_3 \\ M_3 & M_4 & M_4 & M_3 & M_2 & M_1 & L & M_1 & M_2 \\ M_2 & M_3 & M_4 & M_4 & M_3 & M_2 & M_1 & L & M_1 \\ M_1 & M_2 & M_3 & M_4 & M_4 & M_3 & M_2 & M_1 & L \end{bmatrix} \tag{3.4}$$

The inductance terms of the matrix can be analytically calculated [56–58] for a specific winding. Alternatively, if detailed information about the geometry is available, Finite Element Models (FEM) can be used to calculate the numerical value of the inductances. The correlation of the machine inductance values is depicted in Fig. 3.2.

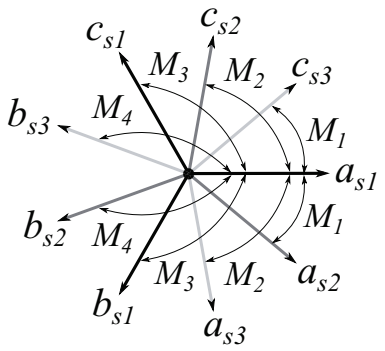

Figure 3.2: Inductance values phase relations

Finally, in order to obtain the complete voltage equations of the machine, the flux term (3.3) is substituted into (3.1)

$$v_s^{\overline{abc}} = \mathbf{R_s} i_s^{\overline{abc}} + \mathbf{L_s} \frac{d}{dt} i_s^{\overline{abc}} + \lambda_m \omega \begin{bmatrix} \cos(\theta) \\ \cos(\theta - \varphi) \\ \vdots \\ \cos(\theta - 8\varphi) \end{bmatrix} \tag{3.5}$$

where ω is the electrical rotational speed of the machine.

3.3 Decentralized control of the machine

In this section, the decentralized current controller is designed analyzing the obtained machine voltage differential equations. The main control objectives are:

- Stator independent active and reactive power regulation.
- Ensure a time response performance for an active or reactive current reference change.
- Minimize the interactions between stators.

3.3.1 Machine equations in the rotating reference frame

In order to simplify the control problem, the well-known Park variable transformation [59] is applied to each of machine stator equations, referenced to the electrical rotation angle θ

$$\mathbf{T}(\theta) = \frac{2}{3}\begin{bmatrix} \cos(\theta) & \cos(\theta - \frac{2\pi}{3}) & \cos(\theta + \frac{2\pi}{3}) \\ \sin(\theta) & \sin(\theta - \frac{2\pi}{3}) & \sin(\theta + \frac{2\pi}{3}) \\ \frac{1}{2} & \frac{1}{2} & \frac{1}{2} \end{bmatrix} \tag{3.6}$$

This transformation is extended for three stators, considering the electrical angle displacement between them [49, 60]

$$\mathbf{T}^{\overline{qd}}(\theta) = \frac{2}{3}\begin{bmatrix} \mathbf{T}(\theta) & \mathbf{0_{3x3}} & \mathbf{0_{3x3}} \\ \mathbf{0_{3x3}} & \mathbf{T}(\theta - \varphi) & \mathbf{0_{3x3}} \\ \mathbf{0_{3x3}} & \mathbf{0_{3x3}} & \mathbf{T}(\theta - 2\varphi) \end{bmatrix} \tag{3.7}$$

being each component of (3.7) a 3x3 matrix dimension. Note that this transformation is applied for vectors sorted as

$$x = \left[x_{s1}^a, x_{s1}^b, x_{s1}^c, x_{s2}^a, x_{s2}^b, x_{s2}^c, x_{s3}^a, x_{s3}^b, x_{s3}^c\right]^T \tag{3.8}$$

Then, in order to properly apply the transformation to the variables sorted as shown in (3.2), the elements of (3.7) should be rearranged. By ordering and applying (3.7) to the machine equations (3.5), the following system is obtained

$$v_s^{\overline{qd}} = \left[\mathbf{R_s} + \mathbf{A_1}\right] i_s^{\overline{qd}} + \mathbf{A_2}\frac{d}{dt} i_s^{\overline{qd}} + v_m^{\overline{qd}} \tag{3.9}$$

where $v_s^{\overline{qd}}$, $v_m^{\overline{qd}}$ and $i_s^{\overline{qd}}$ are the converter voltages applied to the machine, the machine voltages due to the magnet flux linkages and the current flowing

through the machine respectively, in the new reference frame. The generic variable arrangement is

$$x_s^{\overline{qd}} = \left[x_{s1}^q, x_{s2}^q, x_{s3}^q, x_{s1}^d, x_{s2}^d, x_{s3}^d\right]^T \tag{3.10}$$

Note that the number of equations has been reduced from nine to six because the machine windings have an isolated neutral point for each stator; thus, zero sequence currents flowing through the machine are null. Specifically, matrices $\mathbf{A_1}$ and $\mathbf{A_2}$ in (3.9) show the relations between the variables of the machine in the new reference frame

$$\mathbf{A_1} = \omega \begin{bmatrix} 0 & -C & C & A & B & B \\ C & 0 & -C & B & A & B \\ -C & C & 0 & B & B & A \\ -A & -B & -B & 0 & -C & C \\ -B & -A & -B & C & 0 & -C \\ -B & -B & -A & -C & C & 0 \end{bmatrix}$$

$$\mathbf{A_2} = \begin{bmatrix} A & B & B & 0 & C & -C \\ B & A & B & -C & 0 & C \\ B & B & A & C & -C & 0 \\ 0 & -C & C & A & B & B \\ C & 0 & -C & B & A & B \\ -C & C & 0 & B & B & A \end{bmatrix} \tag{3.11}$$

$$\begin{aligned} A &= L - M_3 \\ B &= -\cos\tfrac{\pi}{9} M_4 - \cos\tfrac{5\pi}{9} M_2 + \cos\tfrac{2\pi}{9} M_1 \\ C &= -\cos\tfrac{7\pi}{18} M_4 + \cos\tfrac{\pi}{18} M_2 - \sin\tfrac{2\pi}{9} M_1 \end{aligned}$$

Finally, the machine voltages vector, due to the magnet flux linkages, can be expanded as

$$v_m^{\overline{qd}} = \lambda_m \omega \begin{bmatrix} 1 & 1 & 1 & 0 & 0 & 0 \end{bmatrix}^T \tag{3.12}$$

Besides, the torque equation of the machine can also be obtained in the new reference frame

$$T_m = \frac{3}{2} \lambda_m P (i_{s1}^q + i_{s2}^q + i_{s3}^q) \tag{3.13}$$

where P is the number of machine pole pairs. Hence, (3.13) shows that the machine torque only depends on the current q variables, considered from

now on as the active current components. On the other hand, the current d variables are considered reactive components, as they do not contribute to the machine torque. There is no reluctance torque component due to the round rotor machine configuration.

3.3.2 Decentralized vector control

The decentralized control design is based on the classic vector control. It is designed considering that no communications are available between stators, so three different vector controllers are designed, one for each stator. To do so, the equations for one stator are extracted from the total machine model (3.9) considering only the variables of the same stator, painted in gray in (3.11)

$$\begin{bmatrix} v_{si}^q \\ v_{si}^d \end{bmatrix} = \begin{bmatrix} R & \omega(L-M_3) \\ -\omega(L-M_3) & R \end{bmatrix} \begin{bmatrix} i_{si}^q \\ i_{si}^d \end{bmatrix} + \begin{bmatrix} L-M_3 & 0 \\ 0 & L-M_3 \end{bmatrix} \frac{d}{dt} \begin{bmatrix} i_{si}^q \\ i_{si}^d \end{bmatrix} + \lambda_m \omega \begin{bmatrix} 1 \\ 0 \end{bmatrix} + \begin{bmatrix} d_q \\ d_d \end{bmatrix} \quad (3.14)$$

where d_q and d_d gather the interaction elements between stators. The controller approach considers d_q and d_d to be exogenous signals or disturbances for the controller and they are not considered within this design stage. Then, the corresponding equations of one of the machine stators (3.14) are equivalent to a conventional three-phase machine. Thus, the classic design vector control can be employed [61], including the decoupling loop between the q and d variables. Hence, the first design step consists of applying the following variable change to the equations (3.14)

$$\begin{bmatrix} v_{si}^q \\ v_{si}^d \end{bmatrix} = \begin{bmatrix} \hat{v}_{si}^q + \omega(L-M_3) i_{si}^d + \lambda_m \omega \\ \hat{v}_{si}^d - \omega(L-M_3) i_{si}^q \end{bmatrix} \quad (3.15)$$

Substituting (3.15) in (3.14), decouples the machine q and d variables

$$\begin{bmatrix} \hat{v}_{si}^q \\ \hat{v}_{si}^d \end{bmatrix} = \begin{bmatrix} R & 0 \\ 0 & R \end{bmatrix} \begin{bmatrix} i_{si}^q \\ i_{si}^d \end{bmatrix} + \begin{bmatrix} L-M_3 & 0 \\ 0 & L-M_3 \end{bmatrix} \frac{d}{dt} \begin{bmatrix} i_{si}^q \\ i_{si}^d \end{bmatrix} \quad (3.16)$$

Once q and d variables are decoupled, two Single Input Single Output (SISO) transfer functions in the Laplace domain can be found

$$\frac{I_{si}^q(s)}{\hat{V}_{si}^q(s)} = \frac{1}{(L-M_3)s+R}; \quad \frac{I_{si}^d(s)}{\hat{V}_{si}^d(s)} = \frac{1}{(L-M_3)s+R} \quad (3.17)$$

where I_{si}^q, I_{si}^d, $\hat{V}_{si}^q$ and $\hat{V}_{si}^d$ are the Laplace variables for the q and d voltages and currents of the stator s_i. Based on the plants obtained, two different controllers are designed, one for each corresponding current, based on the Internal Model Control (IMC) design methodology [61, 62]. This technique allows for a controller that cancels the plant internal dynamics, while imposing a desired one. Applying this technique to the two system transfer functions (3.17) aiming to obtain a first order time response for the closed loop system, the controller to be implemented results in a conventional PI

$$K_c(s) = \frac{K_p s + K_i}{s} \tag{3.18}$$

with the following parameters

$$K_p = \frac{L - M_3}{\tau}; \quad K_i = \frac{R}{\tau} \tag{3.19}$$

where τ is the first order time constant of the closed loop system. In order to control the complete machine, two different PI controllers per stator are required with their corresponding decoupling loops between q and d variables (3.15), as shown in Fig. 3.3. To complete the control design, the closed loop response time constant τ should be selected.

3.3.3 Dynamic analysis and interaction between stators

The controllers bandwidth is strictly related to the effect that a current change in one of the stators has over the currents in other stators. Then, a multivariable frequency analysis is performed on the machine control system (Fig. 3.4) to properly select the controller closed loop time response to achieve good control performance, all the while maintaining the effects between stators under certain boundaries. The control design steps are detailed next.

Open loop analysis

First, the open loop transfer function matrix of the machine is obtained (Matrix **G** in Fig. 3.4) in order to analyze machine dynamics before including a controller. This transfer function matrix can be calculated as

$$\mathbf{G} = \mathbf{C_s} \left[s\mathbf{I_{6x6}} - \mathbf{A_s} \right]^{-1} \mathbf{B_s} \tag{3.20}$$

where $\mathbf{I_{6x6}}$ is a 6x6 identity matrix and $\mathbf{A_s}$, $\mathbf{B_s}$ and $\mathbf{C_s}$ are the state-space matrices of the machine model, that can be obtained by isolating the deriva-

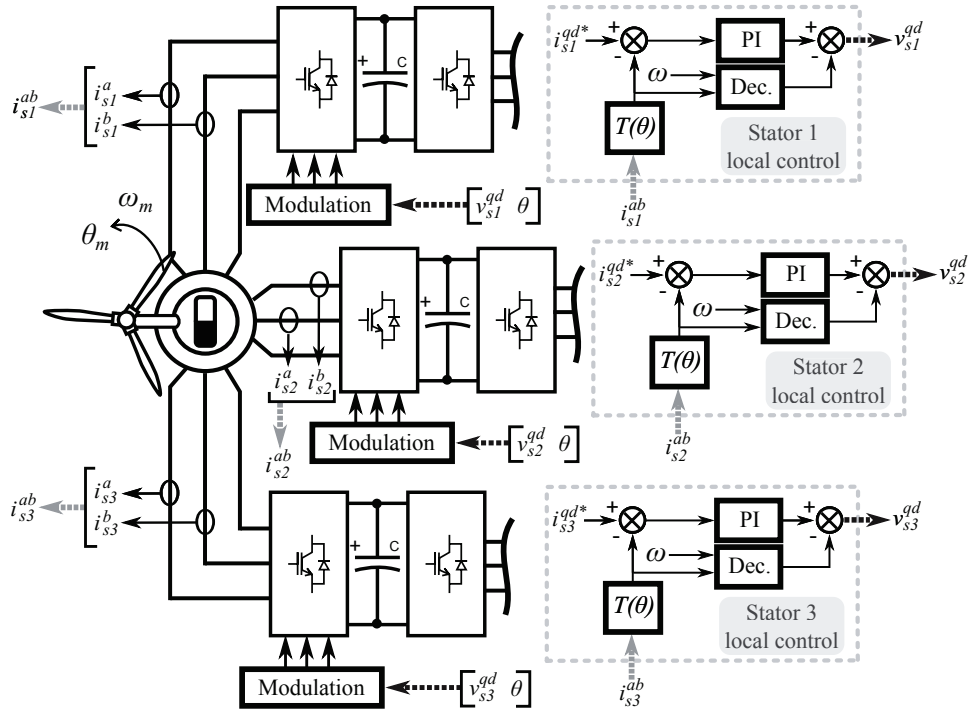

Figure 3.3: Wind turbine nine-phase generator control

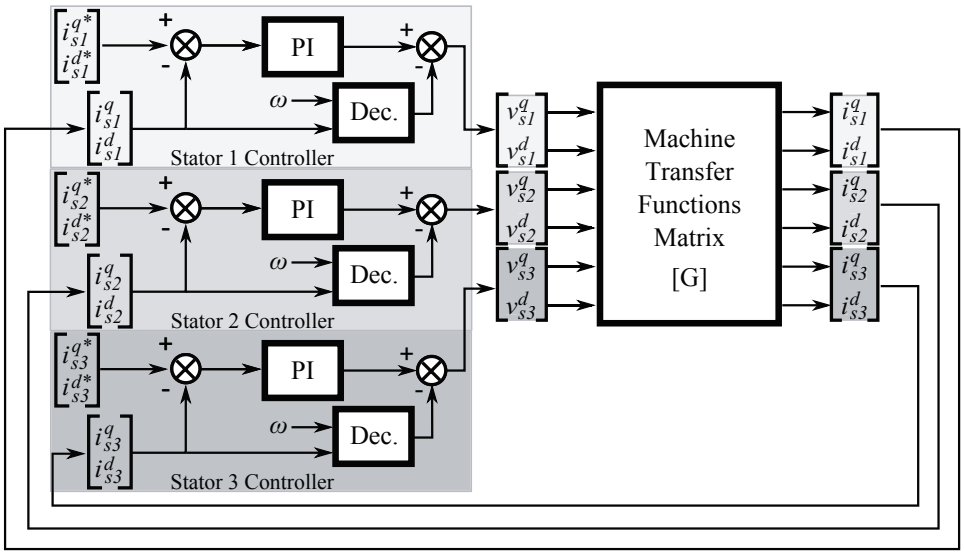

Figure 3.4: Closed loop control of the multivariable control system. Inputs: Current set-points in *qd* reference. Outputs: machine currents in *qd* reference.

tives of the current from the machine equations (3.9). Note that open loop equations (3.9)-(3.11) show that the machine model is dependent on the rotational speed. Therefore, open loop frequency analysis of the machine must be performed for different rotational speeds. Once the frequency response is obtained, large frequency gains that could cause interaction between stators should be identified. The open loop transfer function matrix $\mathbf{G}$ has six voltage inputs and six current outputs (Fig. 3.4) giving thirty-six different transfer functions. Due to the symmetry of the machine model, only one voltage input (considering all current outputs) should be analyzed, because the frequency response is analogous for all the other inputs.

Closed loop analysis

Once the open loop analysis is completed, the frequency response of the closed loop multivariable system is carried out, based on the closed loop transfer function matrix $\mathbf{T}$. This matrix can be obtained as

$$\mathbf{T} = \mathbf{GK}\left[\mathbf{I_{6x6}} + \mathbf{GK}\right]^{-1} \tag{3.21}$$

where $\mathbf{K}$ is a diagonal matrix with the designed PI controllers (3.18) in each

component. The frequency response of the $\mathbf{T}$ matrix shows the dynamics between the current set-points i_{si}^{q*} and i_{si}^{d*} and the actual machine currents i_{si}^{q} and i_{si}^{d} in closed loop. Through frequency analysis of the $\mathbf{T}$ matrix, the dynamics of the decentralized controller can be evaluated in closed loop, considering the following objectives:

- The current set-points i_{si}^{q*} and i_{si}^{d*} should be tracked without steady state errors, ensuring an approximate first order system response.
- Limit the error of the local current controllers caused by current changes in the other stators. The closed loop matrix $\mathbf{T}$ relates the set-points i_{si}^{qd*} with the machine actual currents i_{si}^{qd}. Then, setting a maximum allowed gain on the frequency representation of $\mathbf{T}$, the dynamic interaction between the different closed loop controllers is limited. In other words, the gain limitation can be understood as the maximum current deviation allowed in one stator current controller caused by a reference change Δi_{si}^{qd*} introduced in the current controller of another stator.

It is also interesting to plot the matrix $\mathbf{T}$ frequency response graph for different rotational speeds, due to the effect that speed has on the machine behavior. Also note that, as in the open loop study, the frequency analysis of the $\mathbf{T}$ matrix is performed for a single set-point input (considering all the current outputs) due to the model symmetry.

3.3.4 Grid side converter control

In order to perform the machine control, the machine side converter requires a controlled Direct Current (DC) bus voltage to be able apply voltages to the corresponding stator. The mentioned DC voltage regulation is carried out by each of the Grid Side Converters (GSCs), as shown in Fig. 3.5. The output of the DC regulator corresponds to the input for the active current set-point of a classic vector control [61] carried out in the synchronous reference frame, defined by the grid angle obtained through a Phase Locked Loop (PLL) system [63]. Note that the control of the different GSCs does not interfere in the decentralized control approach as long as it is operated properly.

3.4 Case study

In this section, the methodology to design the decentralized control of the machine is applied to a specific triple three-phase wind generator. The characteristics are summarized in Table 3.1.

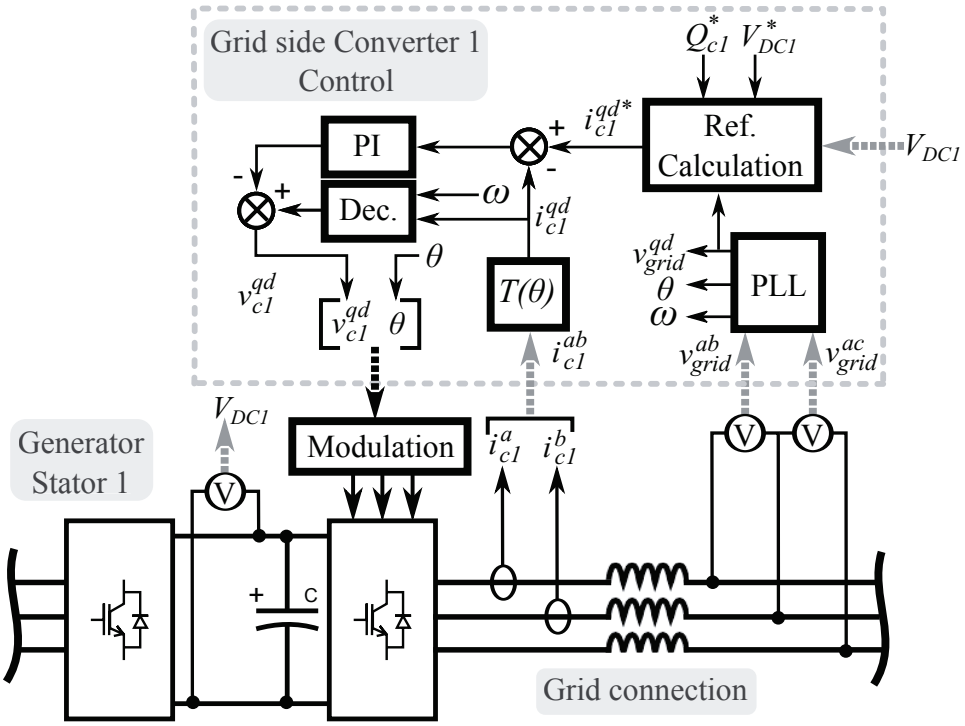

Figure 3.5: Wind turbine grid side converters control

Table 3.1: Nine phase generator parameters

Parameter	**Value**	**Units**
Inductance L	1.73	mH
Inductance M_1	-0.121	mH
Inductance M_2	-0.036	mH
Inductance M_3	-0.052	mH
Inductance M_4	-0.346	mH
Phase resistance R	10	mΩ
Rated Phase voltage V_{an}	550	V
Pole pairs P	60	-
Rated mechanical speed ω_n	11	min^{-1}

First, substituting values from Table 3.1 into the machine model equations the open loop **G** transfer function matrix is obtained. The input selected for plotting the Bode diagram is the stator 1 q axis voltage v_{s1}^{q} and as outputs all the machine currents i_{si}^{q} and i_{si}^{d}, obtaining six different curves. This diagram is obtained for four machine speeds: rated speed ω_n, 2/3 and 1/3 of the rated speed and zero speed (Fig. 3.6).

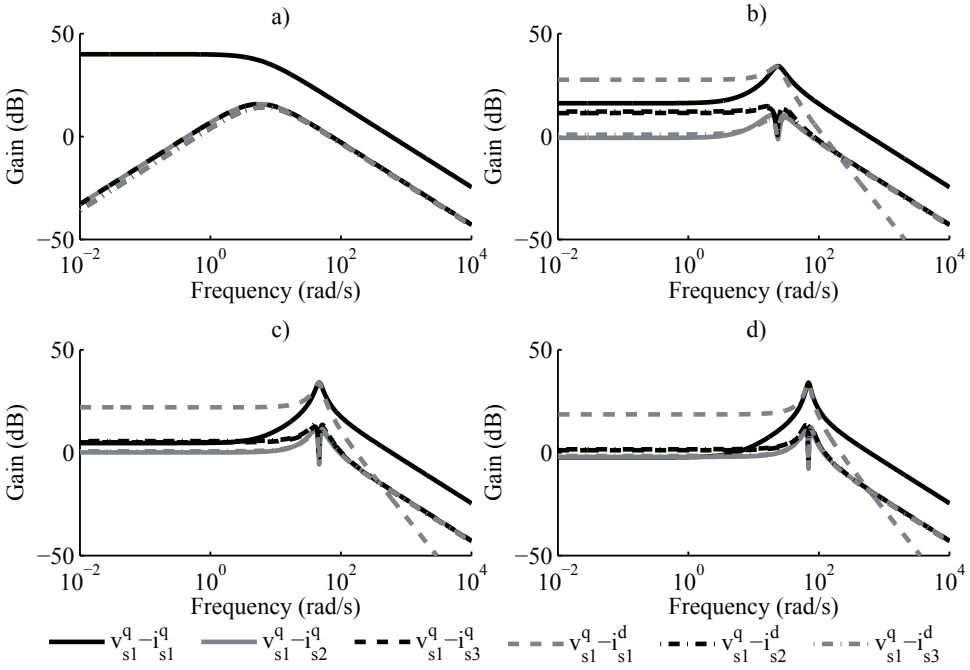

Speed: a) 0 rpm, b) 1/3 ω_n min^{-1}, c) 2/3 ω_n min^{-1}, d) ω_n min^{-1}.

Figure 3.6: Open loop transfer function matrix Bode diagram representation at different rotational speeds. Input: stator 1 q axis voltage. Outputs: machine currents in qd reference.

The open loop Bode diagram shows that the influence that the input voltage v_{s1}^{q} has over the current i_{s1}^{d} is strong at all rotational speeds due to the existing coupling between q and d variables (3.14), except at very low speeds. This fact reinforces the requirement of the decoupling loop within each of the three-phase vector controllers. Moreover, cases b, c and d show large gains close to the rotational speed at which the Bode diagram is calculated.

Following the discussion of the open loop system, the closed loop transfer function matrix **T** is computed based on the decentralized control approach

employing six different PI controllers (3.18)-(3.19), leaving the closed loop time constant undefined. In order to properly select this constant, the frequency dynamic analysis of the closed loop transfer function **T** is performed. The Bode diagram representation, considering as input the stator 1 q axis current set-point i_{s1}^{q*} and as outputs all the machine currents i_{si}^{q} and i_{si}^{d}, is plotted for different closed loop time responses of the controller: 100, 50, 20 and 10 ms. This procedure is repeated for different machine rotational speed values as it is shown in Figs. 3.7, 3.8, 3.9 and 3.10. In order to limit the coupling effect between stators, it is considered that a set-point i_{s1}^{q*} amplitude change Δi_{s1}^{q*} should deviate the current from the other stators (i_{si}^{q} and i_{si}^{d}, for i=2, 3), less than a 10% of the amplitude Δi_{s1}^{q*}. Then, the corresponding gain limitation is

$$G_{lim} = 20\log_{10}(0.1) = -20 \text{ dB} \tag{3.22}$$

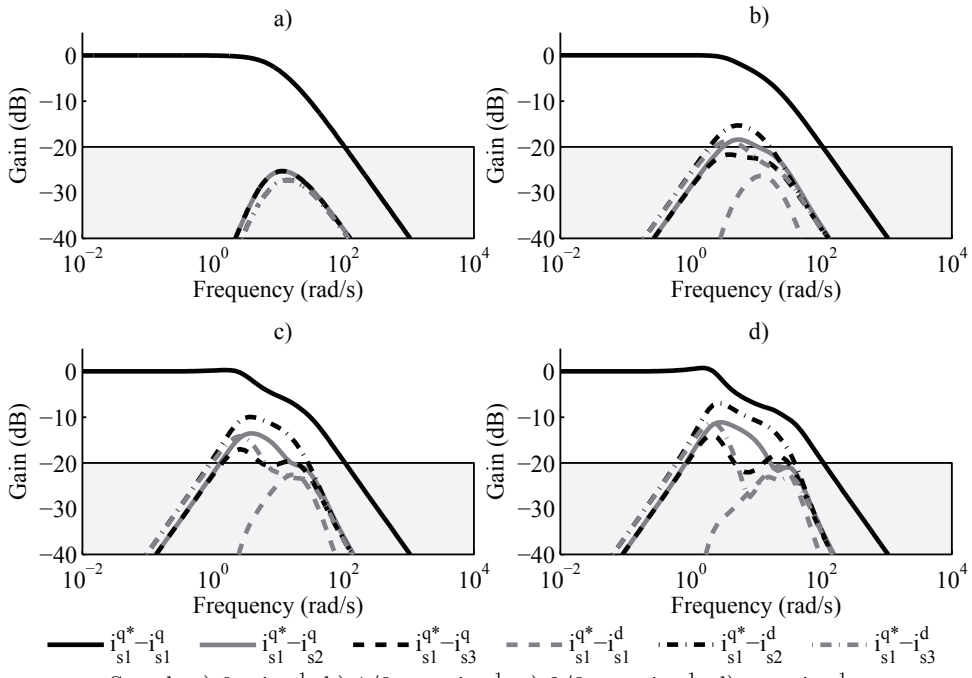

Speed: a) 0 min^{-1}, b) 1/3 ω_n min^{-1}, c) 2/3 ω_n min^{-1}, d) ω_n min^{-1}.

Figure 3.7: Closed loop transfer function matrix Bode diagram representation at different rotational speeds. Input: stator 1 q axis current set-point. Outputs: machine currents in qd reference. Closed loop time response design: 100 ms.

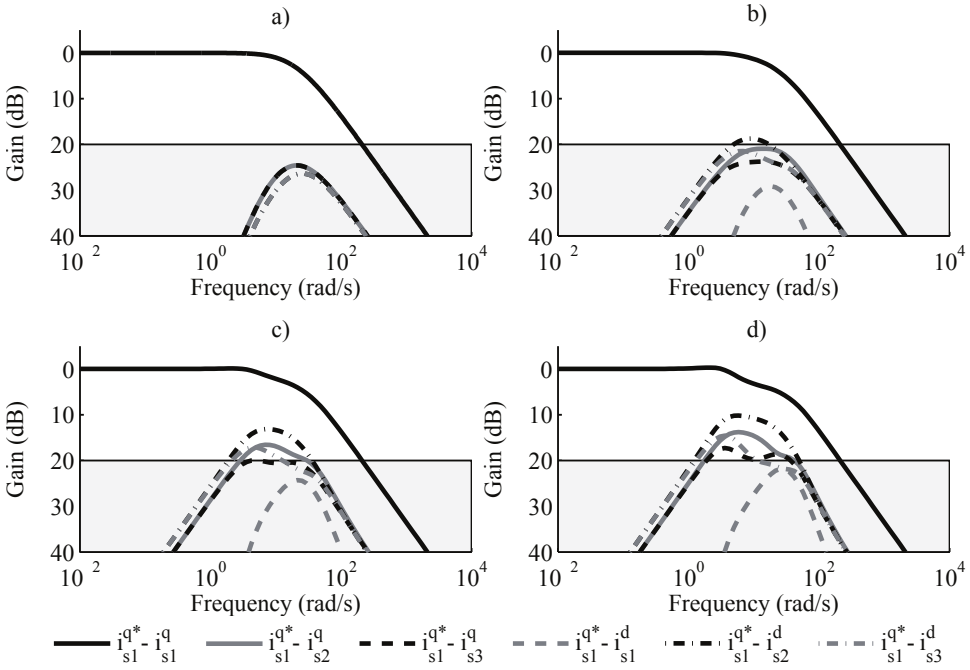

Speed: a) 0 min^{-1}, b) 1/3 ω_n min^{-1}, c) 2/3 ω_n min^{-1}, d) ω_n min^{-1}.

Figure 3.8: Closed loop transfer function matrix Bode diagram representation at different rotational speeds. Input: stator 1 q axis current set-point. Outputs: machine currents in qd reference. Closed loop time response design: 50 ms.

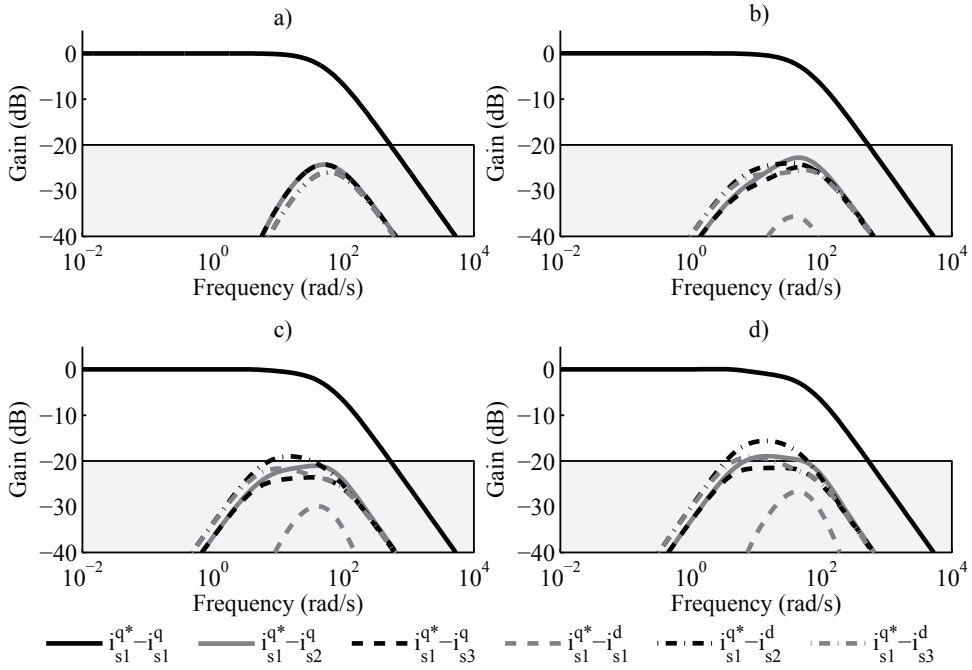

Speed: a) 0 min^{-1}, b) 1/3 ω_n min^{-1}, c) 2/3 ω_n min^{-1}, d) ω_n min^{-1}.

Figure 3.9: Closed loop transfer function matrix Bode diagram representation at different rotational speeds. Input: stator 1 q axis current set-point. Outputs: machine currents in qd reference. Closed loop time response design: 20 ms.

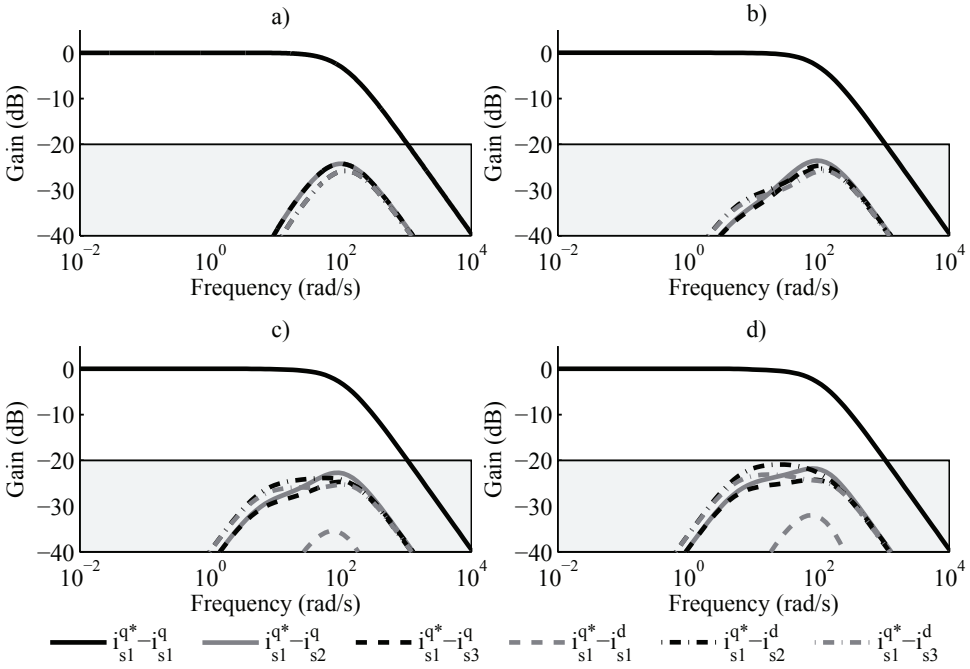

Speed: a) 0 min^{-1}, b) 1/3 ω_n min^{-1}, c) 2/3 ω_n min^{-1}, d) ω_n min^{-1}.

Figure 3.10: Closed loop transfer function matrix Bode diagram representation at different rotational speeds. Input: stator 1 q axis current set-point. Outputs: machine currents in qd reference. Closed loop time response design: 10 ms.

Fig. 3.7 shows the closed loop Bode diagram for different rotational speeds between i_{s1}^{q*} and all the machine currents for a closed loop time constant of 100 ms. The curve relating i_{s1}^{q*} and i_{s1}^{q} presents 0 dB at zero frequency, which implies that the local controller is able to track current references. Besides, the curve relating the set-point i_{s1}^{q*} and the current i_{s1}^{d} presents reduced gains at all rotational speeds, fact that validates the decoupling loop action. However, it is observed that at non-zero rotational speeds, the curve relating stator 1 q axis set-point i_{s1}^{q*} and the q and d currents of the other stators show large gains, even exceeding the gain limitation imposed of -20 dB, fact that discards this PI settings for the machine current control.

Analogous Bode diagrams are depicted in Figs. 3.8 and 3.9 for closed loop time response constants of 50 and 20 ms respectively. Both figures show that the coupling gains between stator one and the others have been reduced, but they are still exceeding the gain limitation. From these graphs it can be concluded that faster controllers present better control performance, reducing level of coupling between stators. This fact is reasonable because faster local controllers allow rapid compensation of the current deviations caused by current changes in other stators.

Finally, Fig. 3.10 shows the $\mathbf{T}$ matrix frequency response setting the closed loop time response to 10 ms. It can be seen that the gain curve relating the q set-point and current flowing through the q axis of the stator one (i_{s1}^{q*} and i_{s1}^{q}), presents 0 dB gain for constant reference inputs. Then, the controller involving these two variables is able to perfectly track constant current references. Besides, the gain curves related with the interactions between controllers do not exceed the established limitation. Then, it can be concluded that this controller is suitable for the machine because it accomplishes the defined control objectives.

It should also be considered that there is a maximum allowed bandwidth for the current loop. Typically, for classic converters, the fastest allowed time response should be at least 10 times slower than the switching period of the converter. Wind turbine converters, usually present operational switching frequencies in the low kilohertz range (1 to 5 kHz). Therefore, assuming a 2 kHz switching frequency, the fastest allowed closed loop time response should be larger than 5 ms.

3.5 Control validation

In this section, the previously designed controller is validated through time domain simulations of the machine carried out in Matlab Simulink®. To evaluate the current controller performance, two different case studies are

prepared. In both cases, the simulation consists of introducing a step change to the stator 1 q axis current set-point i_{s1}^{q*} while maintaining the other current references set to zero in order to validate the performance of the decentralized controller. This simulation is repeated at two different machine speeds to observe the influence of the speed on controller performance.

The frequency design analysis performed in the previous section has concluded that 10 ms was a suitable closed loop time response for the system. However, these simulations include also the other analyzed controllers (controller time response: 100, 50 and 20 ms) with the aim of validating the conclusions obtained during the design stage.

3.5.1 Current set-point step change at rated speed

This experiment is performed at the machine rated speed. A step change of 500 A is applied to the stator 1 q axis current set-point i_{s1}^{q*}. Simulation results are shown in Fig. 3.11a.

The designed controller (τ = 10 ms) shows a good performance during the current step change. The current i_{s1}^{q} tracks the reference with a first order system behavior, reaching 63% of the final value in approximately 10 ms, validating the IMC controller design. In addition, the current d of the stator 1 is maintained near zero during the step change due to the decoupling loop. It can also be seen that although the effects between the different stators are present, the current deviations are compensated in a few milliseconds by their respective local controllers, never exceeding 10% of the set-point step amplitude (50 A).

Analyzing the temporal response of the slower controllers, it can be seen that all of them are able to track the current reference. However, after the reference step change, current deviations larger than the maximum established deviation appear (10% of the set-point change Δi_{s1}^{q*}). These results are consistent with the analysis performed in the control design stage.

3.5.2 Current set-point step change at reduced speed

The same experiment is performed at one third of the rated speed. Again, a step change of 500 A is applied to the stator 1 q axis current set-point i_{s1}^{q*}. Simulation results are shown in Fig. 3.11b.

This simulation shows a satisfactory performance of the designed controller (τ = 10 ms), even better than the previous one. It is also observed that the step change in the stator 1 q axis current set-point i_{s1}^{q*} affects the other stators less than at higher speeds. These results confirm that as the

machine speed increases, the coupling effects between the variables are more difficult to compensate.

It should be considered that in the previously presented simulations the current set-points are changed in a stepwise manner. In real applications, reference changes should be ramp-limited because fast variations of these variables (q axis currents in this case) could imply fast fluctuations of the machine torque that may cause mechanical problems on the wind turbine.

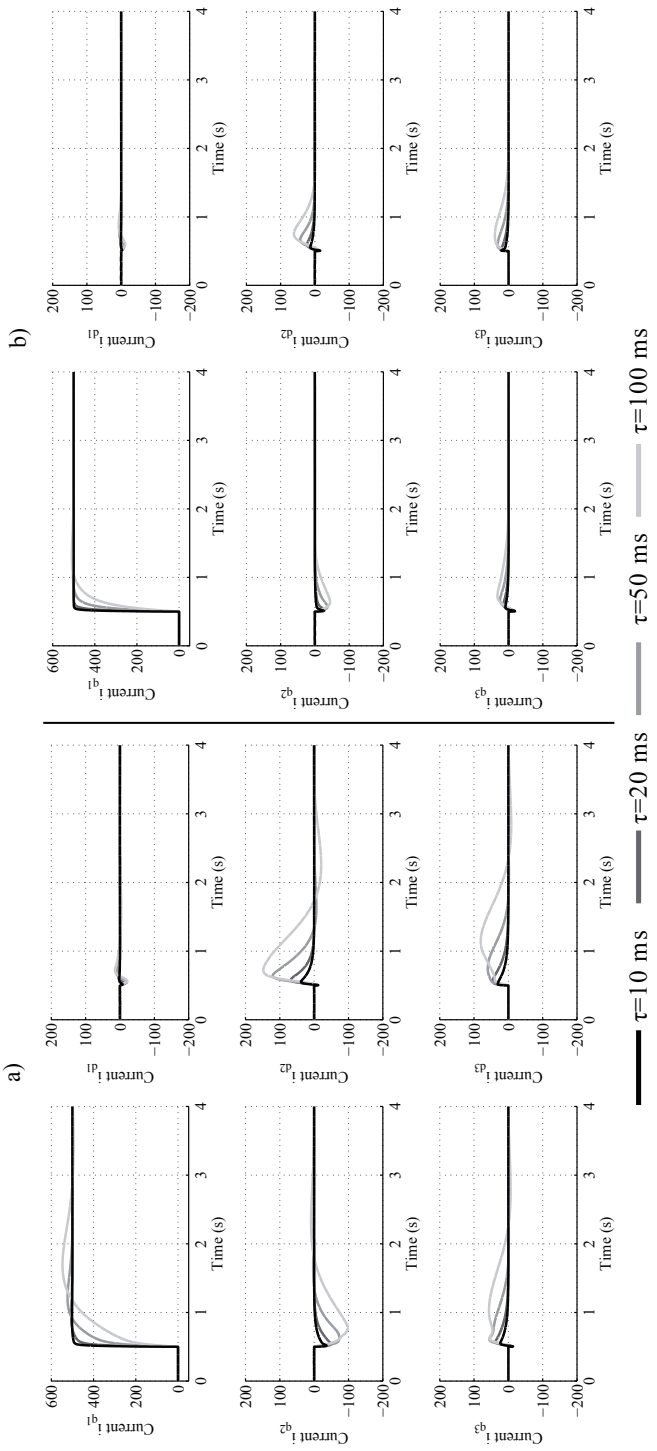

Figure 3.11: Simulation of a set-point q of the stator 1 i_{s1}^{q*} step change, for different controller designs. Rotational speed: a) Rated speed, b) 1/3 of rated speed.

3.6 Scaled wind turbine test rig

Once the methodology for designing the decentralized control is tested in simulation, the control algorithms are validated in a scaled wind turbine test rig. This rig is composed of two 30 kW PMSMs, one acting as a motor and the other as a generator, mechanically connected through their shafts. The motor is a conventional three-phase machine connected to a standard frequency converter. The generator is a nine-phase machine with three independent star-connected stators, connected to the grid by means of three independent back-to-back converters. Fig. 3.12 shows the aforementioned machines, the cabinet where the frequency converter and the back-to-back converters for controlling the multi-phase machine are enclosed and a complete conceptual diagram of the setup.

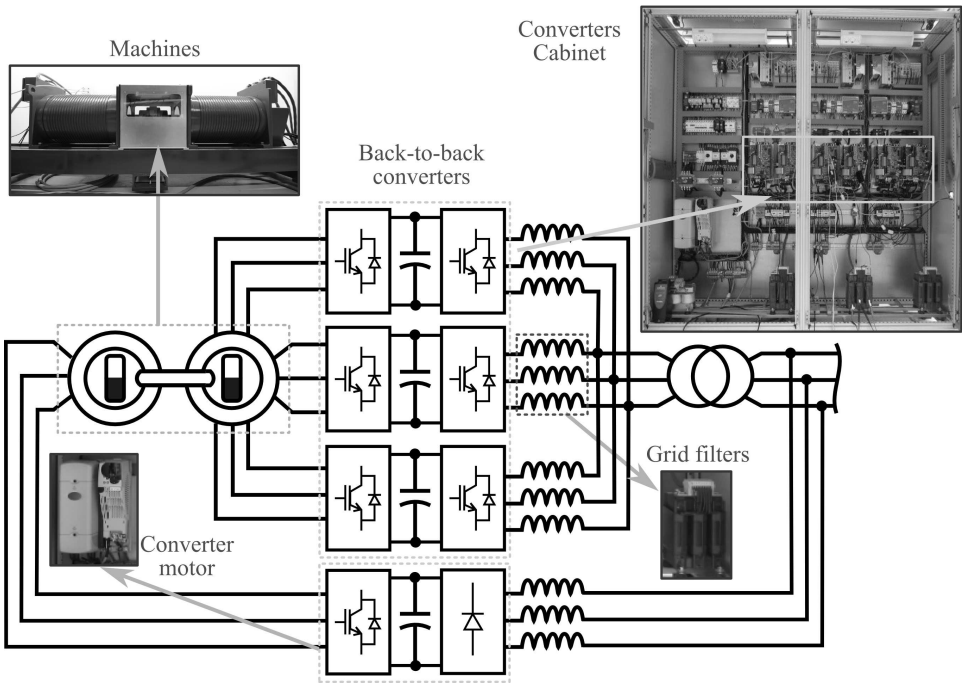

Figure 3.12: Scaled wind turbine test rig photographs and conceptual drawing

The system is operated as follows: the motor acts as a wind emulator, using the frequency converter to regulate the speed of its shaft. The generator regulates the machine currents by means of the designed decentralized controller. The grid side converters carry out a voltage control of the DC

bus to inject the active power coming from the generator to the grid.

In terms of generator control, the decentralized control strategy has been implemented following the steps presented above. First, the machine model has been obtained based on the parameters from a FEM simulation, together with experimental tests developed with the machine. Then, applying the presented control design methodology, six PI current controllers (two for each stator) have been obtained and implemented on each of the Digital Signal Processor (DSP) control boards of the back-to-back converters. The closed loop time response obtained from the study is 60 ms for each stator controller. Fig. 3.13 shows the transient response of the decentralized controller for an active step change of the stator one current i_{s1}^{q*} while maintaining the other current set-points at zero, for three different speeds. It can be seen that the interaction between stators is reduced, even at high speeds. In addition, the current a of stator one shows a first order response with a time constant of approximately 60 ms, as chosen in the design stage. This test ensures that the decentralized controller implemented is able to regulate the machine currents without large interactions among stators during current transients.

Fig. 3.14a shows the experimental results of the decentralized control operation while extracting the same amount of active power from each of the stators. The oscilloscope capture shows that the currents flowing through the phase a of each stator are identical according to the power extraction scenario. In addition, a phase shift between the currents is observed caused by the electrical phase displacement (40°) existing between the stator winding sets. Fig. 3.14b shows the grid side converter variables during the same experiment. It can be seen that the DC bus voltage is maintained at a constant value by means of the DC voltage regulator injecting the incoming power from the generator to the grid. This capture (Fig. 3.14b) also shows that the three phase a currents are in phase, because these converters are all connected to the same AC grid.

Fig. 3.15 shows the results of a second experiment, in which the decentralized control is used to extract a different amount of active power from each of the stators. It can be observed that the controller is able to regulate different active current set-points for each stator. Again, the phase shift between the machine phase a currents is present.

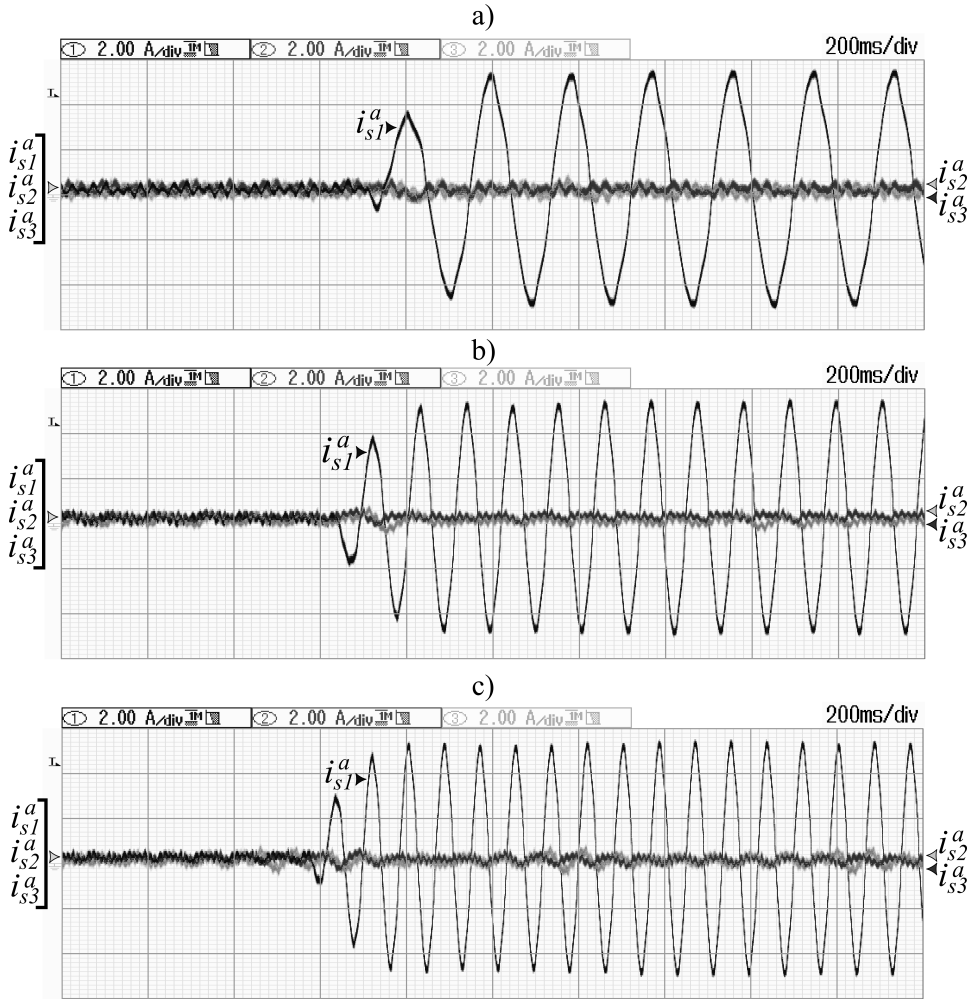

Figure 3.13: Step change of the current q set-point of the stator 1 i^{q*}_{s1} for the decentralized controller designed, at different mechanical rotational speeds: a) 40 min^{-1}, b) 70 min^{-1}, c) 90 min^{-1} (rated mechanical speed). Machine side converter phase a stator currents.

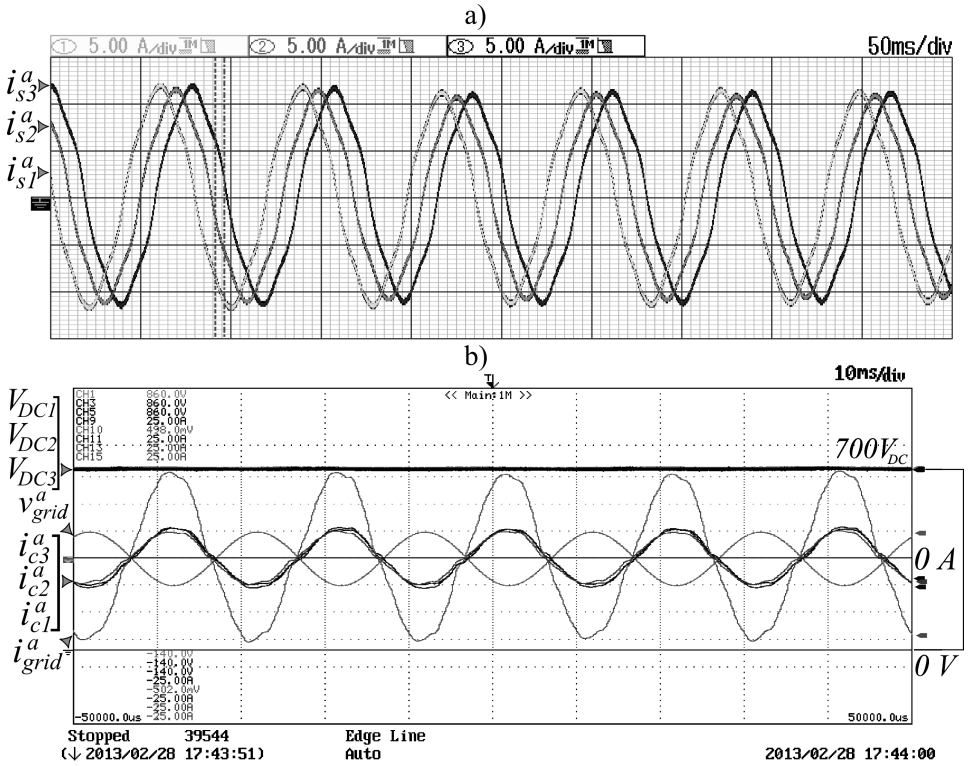

Figure 3.14: Three converters extracting the same amount of power. a) Machine side converter phase a stator currents. b) Grid side converter variables.
AC currents scale: 5 A/div.

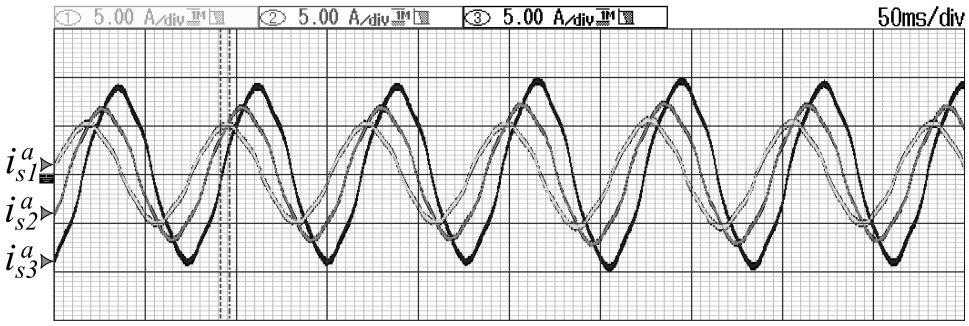

Figure 3.15: Three converters extracting a different amount of power. Machine side converter phase a stator currents.

3.7 Conclusions

The decentralized control design of a triple three-phase wind turbine generator is presented. The control is performed by three independent back-to-back converters connected to each of the generator stators. Each converter carries out its own vector control without sharing information with the rest of the converters. A complete control design methodology based on the classic vector control, combined with frequency analysis of the closed loop controller is carried out. The control design methodology is applied to a nine-phase generator, tested in simulation and validated in a scaled wind turbine generator test rig. The performed tests have shown satisfactory results proving the concept viability. These results confirm that this generator configuration combined with the designed controllers could be an interesting alternative for offshore applications, showing additional capabilities in terms of redundancy and control possibilities.

Chapter 4

Control and experimental validation of a dual active bridge series resonant converter

4.1 Introduction

Remote located offshore wind power plants use High Voltage Direct Current (HVDC) technology to transmit the energy produced to the mainland Alternating Current (AC) grid. Focusing on the offshore wind farm grid, there are two different options for collecting the power produced by the wind turbines: a classic Alternating Current (AC) grid or an innovative Direct Current (DC) collection grid. For the DC option, several collection structures have been proposed, employing bidirectional DC/DC converter units to step up the voltage between the machines' output and the DC medium/high voltage grid [12–16]. Bidirectional operation is preferred as it allows for black-starting the wind turbine and also to conduct some maintenance actions such as blade positioning.

Regarding the DC/DC converter unit itself, the Dual Active Bridge (DAB) [17] or the Dual Bridge Series Resonant Converter (DBSRC) [18] are interesting topologies to be used within the mentioned DC/DC structures [13], due to their bidirectional nature, the isolation and turns ratio provided by the High Frequency (HF) transformer, and their soft-switching operational capability, which allows reduction of the operational losses. The main difference between both structures is the HF resonant tank. The DAB converter has a HF tank compounded only by a HF transformer or a HF transformer and an inductor in series, whereas the DBSRC has the same structure as the DAB plus a capacitor connected in series with the HF tank. Then, comparing the HF AC currents of both converters, the effect of the capacitor included in the DBSRC provides a nearly sinusoidal current in the HF AC side of the converter, while the DAB AC current shows a triangular

waveform with evident high order current harmonics.

The DBSRC can be operated at variable or fixed frequency. In [64] the design and operation of the converter for fixed frequency mode is detailed. The converter power transfer is achieved similarly to the power exchanged between two AC voltage sources [65], consisting of generating two voltage square waves with both bridges controlling the power flow with a variation of its relative angle. The converter switching operational frequency is set above the resonant frequency of the HF AC tank, to allow the converter to operate in continuous mode [64]. This operation mode has an important drawback, which is the large current flowing through the HF AC side under certain conditions, even if the system is transferring a reduced amount of power. In order to solve this problem, the three-level modulation strategy [66] can be employed in both bridges, permitting reduction of the current stress. This fact is analyzed in [67], where a steady state analysis of the converter to find the minimum current trajectories is described for a DBSRC built using Metal-Oxide-Semiconductor Field-Effect Transistor (MOSFET) devices.

This chapter is focused on the operation and control of a 50 kW DBSRC based on Insulated-Gate Bipolar Transistors (IGBT). Based on the converter mathematical model, an optimization problem is posed to operate at a reduced HF AC current level using a three-level modulation strategy. The solution to this problem gives the operational point at which the current flowing through the AC circuit is minimum for the defined working conditions, accomplishing the demanded power transfer. This strategy is compared to simulations with the classic two-level modulation phase-shifted control. Then, the experimental results with the developed prototype are shown operating with the classic two-level modulation.

The chapter is structured in several sections. Section 4.2 describes the DBSRC converter. Then, in Section 4.3 the converter model is obtained. Based on this model, two different controllers for the converter are described in Section 4.4, including the proposed optimization algorithm, as well as simulations comparing both control performances. Finally, results showing the converter operation using the conventional controller are presented in Section 4.5.

4.2 System description

The DBSRC (Fig. 4.1) is a DC/DC converter compounded by two H-Bridge converters connected by a HF transformer along with an inductor and a capacitor in series. The transformer is usually included to provide isola-

tion between both DC systems, as well as applying a voltage turns ratio relation between the primary and the secondary voltages. The converter is able to transmit power in both directions without changing the operation mode. The resonant tank compounded by the capacitor and the inductor is usually tuned to a frequency slightly lower than the switching frequency to operate the system in continuous mode [64]. Specifically, the presence of the capacitor in the resonant circuit leads to sinusoidal currents, reducing the harmonic content of the HF currents. Also, this capacitor blocks possible DC currents flowing through this circuit that could saturate the transformer [68].

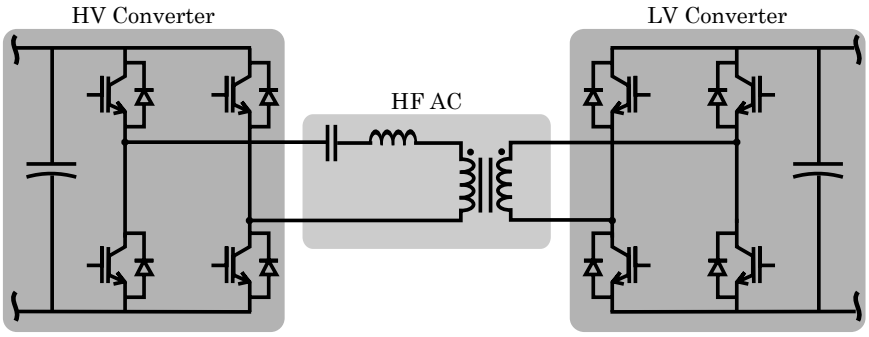

Figure 4.1: Simplified structure of the DBSRC

Apart from the configuration shown in Fig. 4.1, other DBSRC structures could be implemented. For instance, splitting the series capacitor and inductor between the primary and the secondary side of the transformer is an interesting possibility. This scheme is suggested in the literature to achieve a better performance for bidirectional power applications [69]. Besides, the components of the primary could be divided between the phase cables, to increase the symmetry of the system. This technique is used in single-phase converters to suppress the common mode flowing through the converter.

4.3 Converter model

The DBSRC power flow control is inspired by the operation of a power system line. Both H-bridges apply high frequency voltage square waves that can be analyzed as sinusoidal waves at the switching frequency with an infinite added number of harmonics [70]. For this analysis, only the sinusoidal component of the square wave is considered. Note that for the DBSRC case, this simplification is reasonable due to the fact that the AC currents flowing

through the HF circuit are nearly sinusoidal. Fig. 4.2 shows the equivalent scheme of the HF circuit used for the mathematical description.

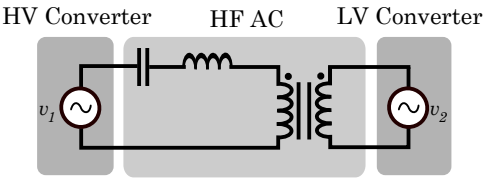

Figure 4.2: Equivalent average model of the DBSRC

Fig. 4.3 shows the fundamental component of a square wave, with a peak voltage amplitude of $\frac{4}{\pi}V_{DC}$. This voltage waveform can be obtained by applying a two-level modulation. Then, the voltages applied by both H-bridges are expressed as

$$v_1(t) = \frac{4}{\pi}V_1 \cos(\omega t) \tag{4.1}$$

$$v_2(t) = \frac{4}{\pi}V_2 \cos(\omega t + \delta) \tag{4.2}$$

where V_1 and V_2 are the DC voltages, ω is the frequency of the square wave and δ is the phase shift between the voltages applied by the two bridges. These expressions could be modified if the modulation is able to apply zero voltage for a certain period (Fig. 4.4). This is the particular case of the three-level modulation which is able to apply three voltage levels at the output of the converter $+V_{DC}$, $-V_{DC}$ and 0 V.

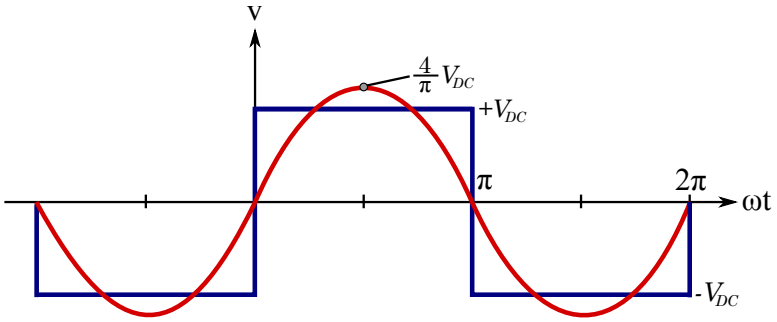

Figure 4.3: Sinusoidal approximation of the AC voltage (two voltage levels)

Considering that the voltage v_1 is synthesized using three-level modula-

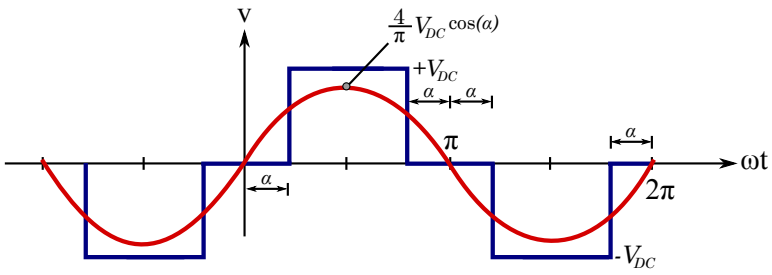

Figure 4.4: Sinusoidal approximation of the AC voltage (three voltage levels)

tion, the system equations become

$$v_1(t) = \frac{4}{\pi} V_1 \cos\alpha \cos(\omega t) \tag{4.3}$$

$$v_2(t) = \frac{4}{\pi} V_2 \cos(\omega t + \delta) \tag{4.4}$$

Note that if α is zero, equations (4.1)-(4.2) and (4.3)-(4.4) are equivalent. Therefore, the two-level modulation can be considered a particular case of the three-level modulation. Next, the system equations for the active P and reactive power Q are deduced considering that the HV bridge is operated using three-level modulation[1]. This assumption is made because three-level modulation can be employed to reduce the Root Mean Square (RMS) voltage applied by the HV bridge to minimize the currents flowing through the AC circuit, as further explained in Section 4.4. Also, it is possible to apply three-level modulation to both bridges, or only to the secondary bridge if required, for instance, during the converter start-up. Then, the voltage equations (4.3) and (4.4) can be expressed as

$$v_1(t) = \frac{4}{\pi} V_1 \cos\alpha \cos(\omega t) \tag{4.5}$$

$$v_2'(t) = \frac{4}{\pi} G_v V_1 \cos(\omega t + \delta) \tag{4.6}$$

where $G_v = \dfrac{V_2'}{V_1} = \dfrac{V_2\, n_t}{V_1}$ is defined to link the secondary voltage to the primary (Fig. 4.5) and n_t is the HF transformer ratio. In addition, the

[1]For the equations derivation, it is assumed that the power is flowing from the HV side to the Low Voltage (LV) side.

reactance of the resonant tank can be expressed as

$$X = L\omega - \frac{1}{C\omega} \tag{4.7}$$

where L is the equivalent HF inductor and C is the HF capacitor. Then the AC current flowing through the tank can be calculated in the phasor domain as

$$\underline{I}_{ac} = \frac{\underline{V}_1 - \underline{V}_2'}{jX} \tag{4.8}$$

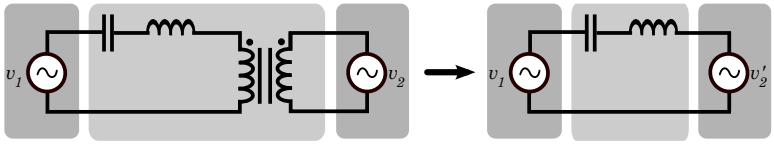

Figure 4.5: Reduction of the AC circuit to the primary

Once the equations are defined, it is possible to obtain the active P and reactive Q power expressions along with the AC and DC current equations at the output, considering power flowing from the HV bridge to the Low Voltage (LV) bridge. For the equations deduction, if the parasitic resistance of the AC circuit is not considered, then

$$P = -\frac{8}{X\pi^2} V_1^2 G_v \cos\alpha \sin\delta \tag{4.9}$$

$$Q = \frac{8}{X\pi^2} V_1^2 \cos\alpha(\cos\alpha - G_v \cos\delta) \tag{4.10}$$

Note that active power sign is negative because the power is calculated at the voltage source v_1, which is delivering power for positive angles δ. Also, the I_{DC} output current expression is obtained dividing the power transmitted by the voltage V_2

$$I_{DC} = \frac{8}{V_2 X\pi^2} V_1^2 G_v \cos\alpha \sin\delta \tag{4.11}$$

Then, defining the values of the capacitor, the inductor, the transformer ratio and the voltage ranges for the DC input and output, a detailed study of the system can be performed. Specifically, these equations are used to analyze the steady state operation of the converter and also to pose the optimization problem that allows reduction of the current flowing through the AC circuit by using the three-level modulation.

Once the mathematical model is introduced, the converter analysis is car-

ried out based on the parameters and nominal values shown in Table 4.1.

Table 4.1: System parameters and nominal values

Magnitude	**Value**	**Units**
Power	50	kW
DC Voltage input V_1	650	V
DC Voltage output V_2	400	V
DC current input (HV)	77	A
DC current output I_{DC} (LV)	125	A
Maximum AC current	150	A_{rms}
AC HF inductor	145	μH
AC HF Capacitor	0.55	μF
AC Frequency	20	kHz
Transformer ratio	1.3	-

4.4 Converter control

In this section, two different control strategies for the DBSRC (see Fig. 4.6) are detailed. First, the different modulation techniques used to operate the converter are described. Once the converter modulation is introduced, the classic phase shift control and the optimized current control are explained. Simulations of both controllers are included in order to illustrate and compare their operation.

4.4.1 Converter modulation

The voltage modulation is the basis of the converter operation. The proposed modulation is known as three-level modulation, as it is able to apply three different voltage levels. As mentioned above, the two-level modulation is a particular case of the three-level modulation, when the shift between the two legs of the same H-bridge is 180°.

Applying two-level modulation, the duty cycle is fixed at 50% and a certain dead time is included to avoid a leg short-circuit. Fig. 4.7 shows the square waves obtained using a triangular wave and a comparator. Applying the previous modulation, the voltages obtained are those depicted in Fig. 4.8.

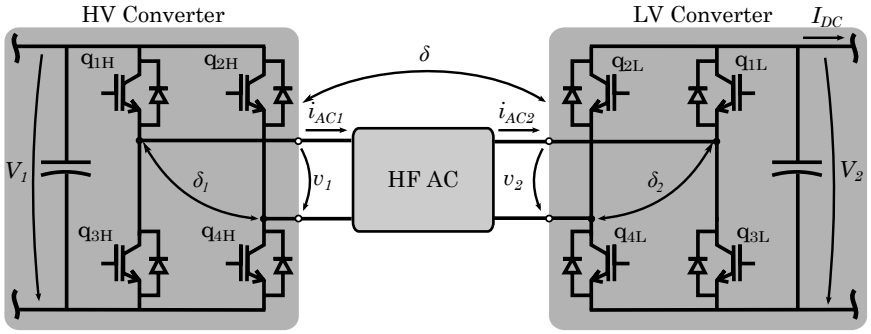

Figure 4.6: DBSRC control scheme

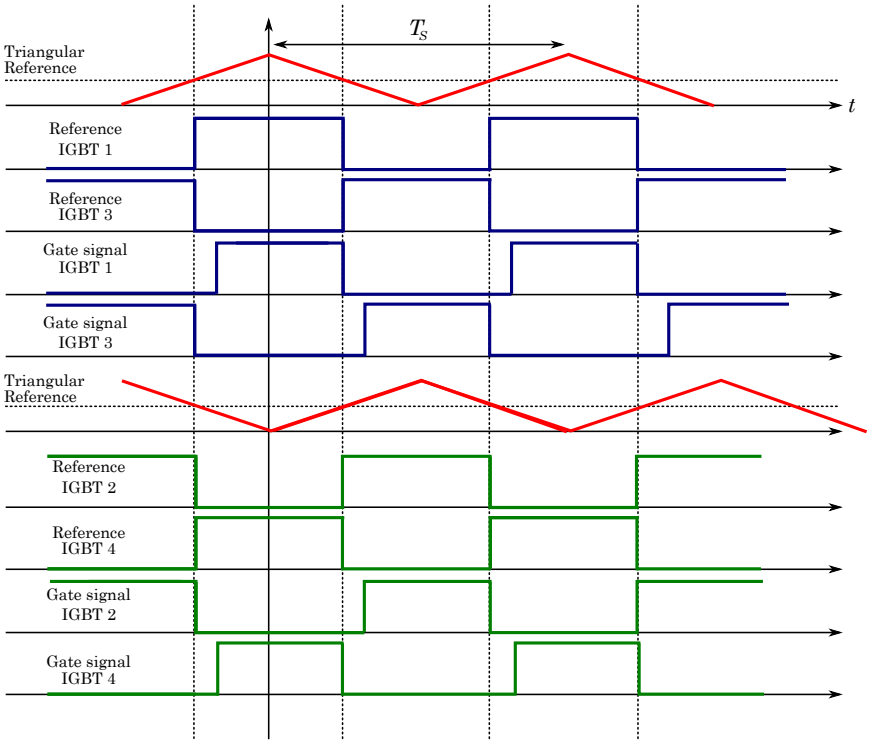

Figure 4.7: Gate control signals created for the two-level modulation

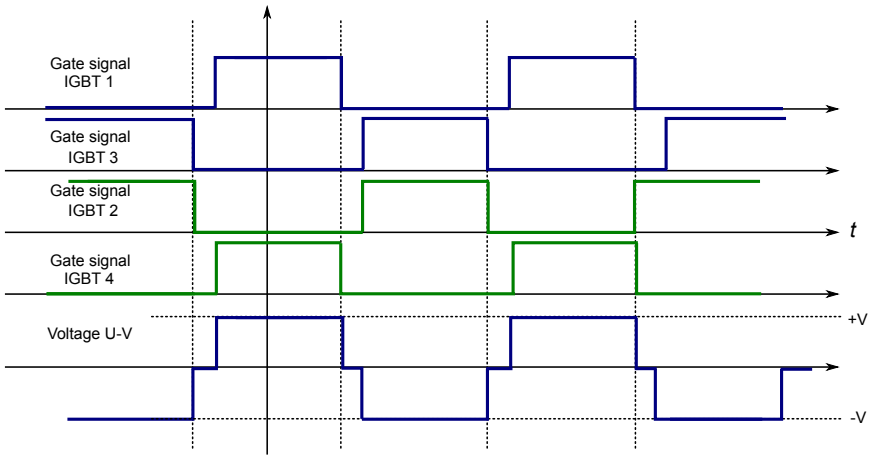

Figure 4.8: Gate signals and voltages applied by the converter for the two-level modulation

The phase shift between the first and second leg can be modified by changing the initial value of one of the triangular square waves, in order to apply the three-level modulation. Fig. 4.9 shows the diagram for a 90° phase shift between both legs. Applying the previous modulation, the voltages obtained are those depicted in Fig. 4.10.

If the triangular wave of the first leg of the HV converter is used as a reference, then it is possible to define three different angles to control the converter:

- Phase shift between HV H-bridge converter legs (δ_1)
- Phase shift between LV H-bridge converter legs (δ_2)
- Phase shift between both H-bridges (δ)

Note that there is an equivalence between the angle α defined previously (Fig. 4.4) and the phase shift between the legs of the converter δ_1 or δ_2, as changing the angle between the H-bridge legs, the three-level voltage output changes accordingly. Specifically, for δ_1, the mentioned equation is (in degrees)

$$\delta_1 = 180^\circ - 2 \cdot \alpha \tag{4.12}$$

Once the implemented modulation has been defined, the conventional phase shift and the optimized converter control strategies are described.

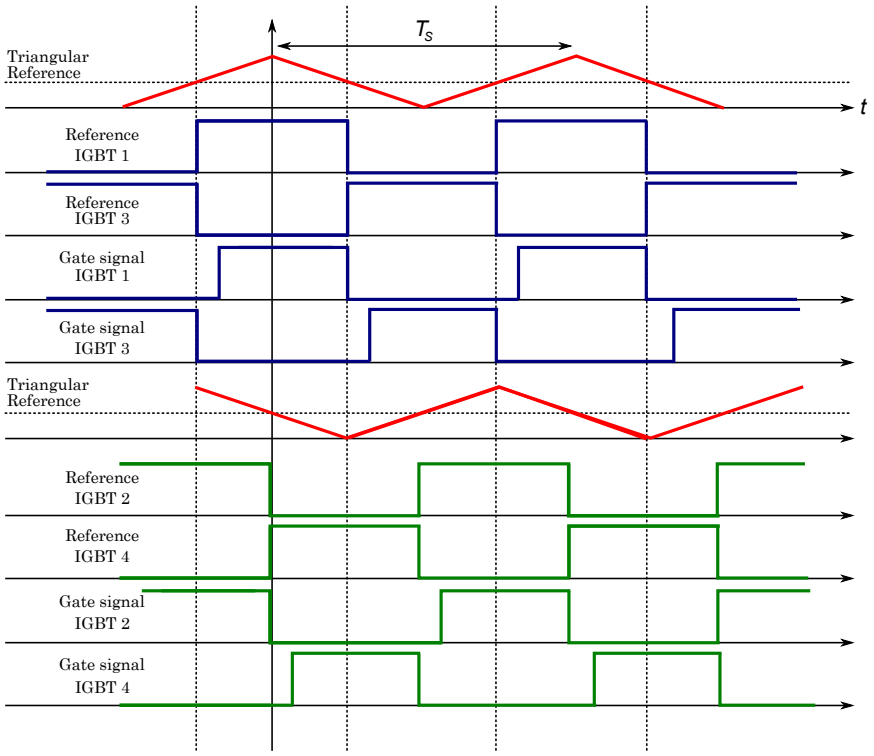

Figure 4.9: Gate control signals created for the three-level modulation

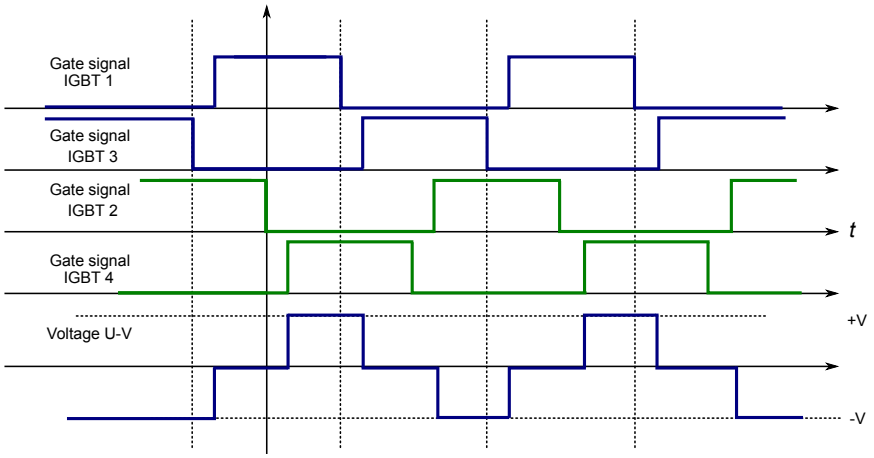

Figure 4.10: Gate signals and voltages applied by the converter for the three-level modulation

4.4.2 Classic DC current control

The classic current control of the DBSRC is based on the two-level modulation strategy (Fig. 4.11). Setting the duty cycle of both converter legs at 50% and shifting the corresponding generated voltage square waves 180° ($\delta_1 = \delta_2 = 180°$), results in a voltage square wave that is applied between the two middle-point connections of each H-bridge. Then, to establish the power transfer between the HV and the LV H-bridges, the angle between the two voltage square waves generated must be shifted an angle δ.

In order to perform a closed loop control, the DC current I_{DC} at the LV side is selected as the controlled variable. The controller can be a simple PI regulator or a more sophisticated one if an improved performance is required. The PI controller is able to regulate the output current, shifting the secondary bridge an angle δ from the primary bridge, which is acting as the AC slack. While operating the converter using this control strategy, the effect of the modulation switching dead time should be taken into account. It is continuously adding a constant deviation to the desired phase shift δ imposed by the control. This is not a major inconvenience because the controller is able to compensate this deviation thus achieving zero steady state current error. However, if so desired, in order to simplify the controller operation a constant phase shift δ_{DB} to compensate the effect of the dead time can be added to the control loop [71], as shown in Fig. 4.12.

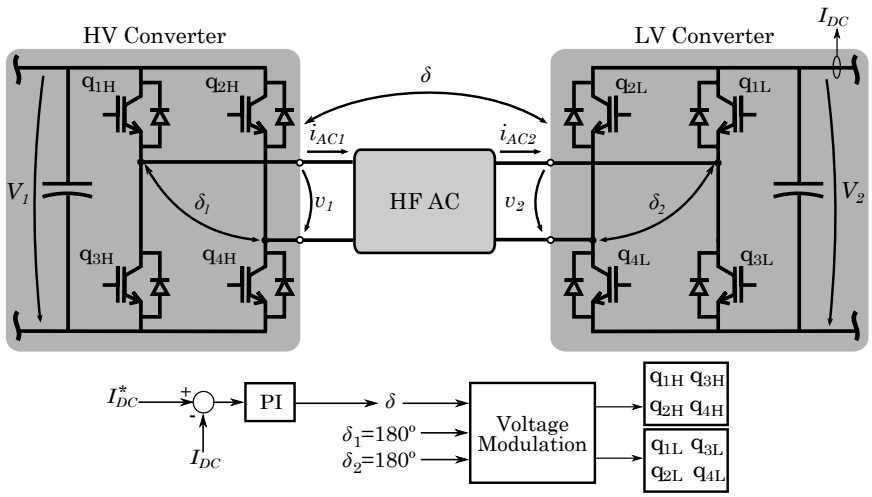

Figure 4.11: Classic DC current control strategy

Based on the parameters shown in Table 4.1 two different scenarios are

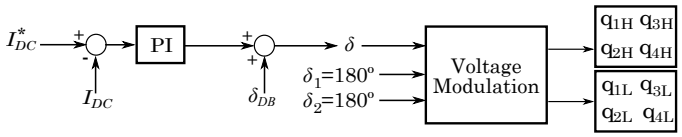

Figure 4.12: Classic DC current control strategy with dead time phase shift compensation

simulated using Matlab Simulink® to illustrate the operation of the classic control. Fig. 4.13 shows the simulation results imposing a nominal DC voltage input of 650 V and a DC voltage output of 348 V, while regulating the DC current to 25 A. It can be observed that the system is able to track the current reference without steady state error. Note also that the voltages v_1 and v_2 are purely square waves, as the two-level modulation is employed. Regarding AC currents, both the primary and the secondary side currents are larger than the output DC current, as much as four times, which is undesirable as an important part of the AC current is not used to transfer active power. Fig. 4.14 shows the same system operating between the same primary DC voltage input and a DC voltage output of 400 V, while regulating the DC current to 100 A. Again, the system is able to track the current reference. Note that in both scenarios the AC current magnitudes are similar, thus revealing that the current flowing through the AC circuit during the first simulation is excessive, as the power transfer in the second case is around 4.5 times higher.

The main advantage of this type of control is the straightforward implementation of the modulation and the controller. With a simple two-level modulation and a conventional PI, the output of the converter can be regulated. On the other hand, large currents can be seen in the AC tank even for low DC current outputs, due to the voltage difference between the AC applied voltages, which increases the losses of the converter.

4.4.3 Optimized current control

Based on a simple steady state analysis, it can be stated that applying a reduced RMS voltage with the HV H-Bridge, the HF AC current can be reduced, maintaining the active power transfer. This voltage reduction can be achieved by applying a three-level modulation, properly selecting the angle δ_1 between the two voltage square waves created by the HV converter legs.

Then, the control strategy proposed consists of regulating the DC output

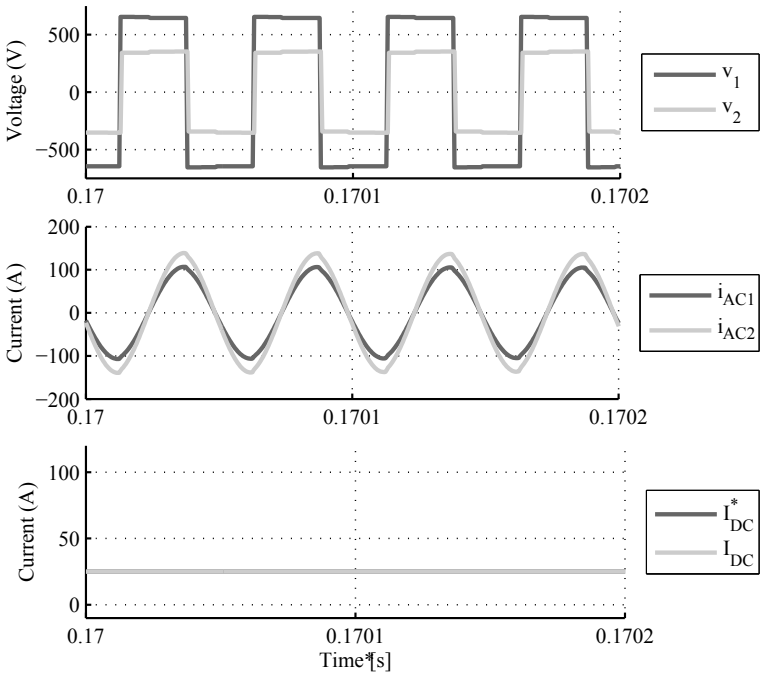

Figure 4.13: Classic DC current control strategy. DC current reference $I^*_{DC} = 25$ A. DC input voltage $V_1 = 650$ V. DC output voltage $V_2 = 348$ V.

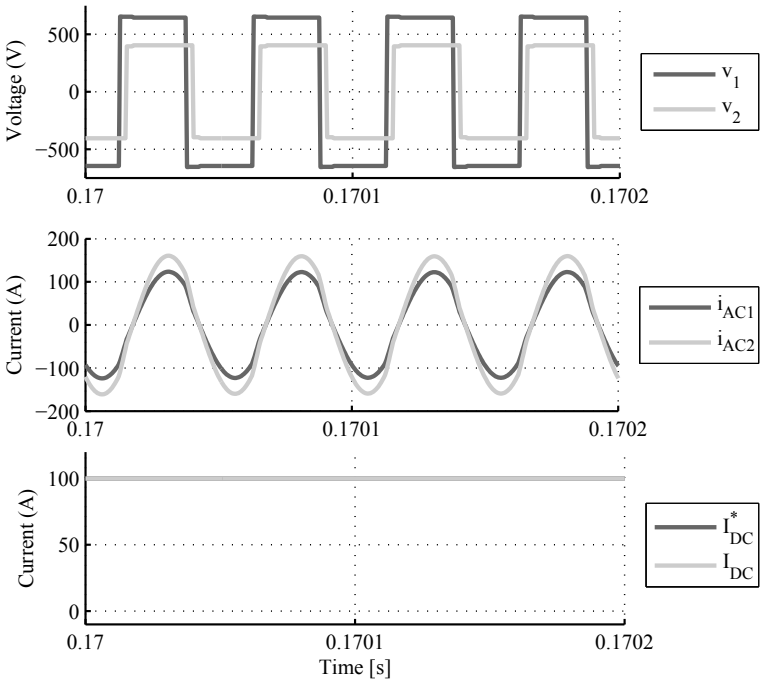

Figure 4.14: Classic DC current control strategy. DC current reference $I^*_{DC} = 100$ A. DC input voltage $V_1 = 650$ V. DC output voltage $V_2 = 400$ V.

current using the phase-shift angle δ between the two H-Bridges, while minimizing the AC current flowing through the resonant tank, reducing the HV RMS applied voltage. The LV bridge, is maintained applying a two-level modulation (δ_2 at 180°). Therefore, for given conditions, an optimization problem can be defined in order to find a pair of δ and δ_1 angles that minimize the current flowing through the AC circuit.

Next, the optimization problem is described. For the sake of simplicity, the angle α is used instead of δ_1 (see (4.12)), as the system equations are simpler to analyze. The objective function F to minimize is the modulus of the AC current

$$F[MIN] = \frac{4}{\pi X}\sqrt{V_1^2(\cos^2\alpha + G_v^2 - G_v\cos\alpha\cos\delta)} \tag{4.13}$$

This function is minimized under different restrictions. The most important condition is that the DC current reference I_{DC}^* must be tracked

$$\frac{8}{V_2\,X\,\pi^2}V_1^2 G_v\cos\alpha\sin\delta - I_{DC}^* = 0 \tag{4.14}$$

Also, restrictions to the operational angles applied by the converter can be imposed. For instance

$$\alpha \leq 60^\circ \tag{4.15}$$

$$\delta \leq 60^\circ \tag{4.16}$$

Note that no losses are considered within the converter, neglecting the parasitic resistances of the circuit elements. As the optimization restrictions and the objective function are not linear equations, a nonlinear solver must be employed. In this case, the problem is solved using the Matlab® tool *fmincon* [72], selecting the solver algorithm *interior point*.

The results of the optimization are a pair of α (or δ_1) and δ values for given conditions of DC primary voltage V_1, DC secondary voltage V_2 and current reference I_{DC}^*. Applying these angles to the system through the converter modulation (Fig. 4.9), the DC current required I_{DC}^* by the application should be delivered while minimizing the AC current flowing through the HF AC circuit.

If the optimization problem is solved for different voltages V_2 and current references I_{DC}^*, given an input DC voltage V_1, a predefined calculation of the angles δ and δ_1 that minimize the AC current for all the operational points of the converter can be calculated. Based on this offline calculation,

two different lookup tables can be defined to calculate the angles δ_1 and δ, introducing the operational conditions (V_2, I^*_{DC}), which in theory could lead the converter to deliver the demanded current I^*_{DC} while minimizing the HF AC current. However, as the optimization does not consider effects such as parasitic resistances or the dead time of the IGBTs, a closed loop control system is still required to properly track the current reference.

The complete control structure is shown in Fig. 4.15. The converter is able to regulate the LV DC current I_{DC}, setting the phase shift δ between the two bridges through a PI controller, while the angle δ_1 is imposed through the lookup table obtained from the offline optimization, based on the operational inputs I^*_{DC} and V_2. Also, another lookup table could be included to calculate the δ angle included in the control scheme as a feed-forward term in order to simplify the controller operation. The application of the angles δ and δ_1 is filtered to avoid fast transients.

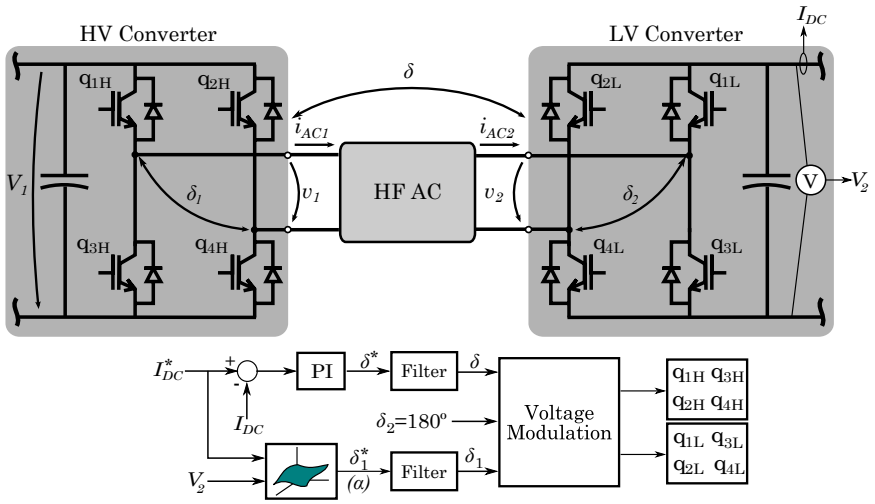

Figure 4.15: Optimized DC current control strategy

In order to validate the optimization, Fig. 4.16 and Fig. 4.17 are depicted. These graphs show the system DC and AC currents for different α and δ operation points, given the DC input and output voltage conditions V_1 and V_2.

Specifically, Fig. 4.16a shows, labeled with a red square, the optimal operation point calculated considering that the converter should deliver a DC current I^*_{DC} of 25 A, while operating between DC voltages $V_1 = 650$ V and $V_2 = 348$ V. It also shows, labeled with black squares, other α and δ operation points that are able to deliver the same DC current output. Ad-

ditionally, Fig. 4.16b shows the AC current magnitude of the highlighted points in Fig. 4.16a. It confirms that the red square represents the optimal operation point because it is able to deliver 25 A at the output, while minimizing the HF AC current. This procedure is repeated in Fig. 4.17a and Fig. 4.17b considering that the converter should deliver a DC current I^*_{DC} of 100 A while operating between DC voltages $V_1 = 650$ V and $V_2 = 400$ V. Again, it can be seen that the red square point minimizes the AC current flowing through the tank.

In order to validate the operation of the converter including the AC current minimization, the same scenarios presented for the conventional control (Fig. 4.13 and Fig. 4.14) are again simulated including the proposed control strategy (Fig. 4.18 and Fig. 4.19). Specifically, Fig. 4.18 ($V_1 = 650$ V, $V_2 = 348$ V and $I^*_{DC} = 25$ A) shows that the three-level modulation is able to significantly reduce the current flowing through the AC resonant tank, compared with the classic control under the same conditions (Fig. 4.13). On the other hand, the optimized control results, shown in Fig. 4.19 ($V_1 = 650$ V, $V_2 = 400$ V and $I^*_{DC} = 100$ A), are similar in terms of AC current to the classic control results (Fig. 4.14). Thus, it can be stated that the optimized control can achieve a larger AC current reduction when the difference between both DC voltages (even considering the transformer ratio) is large. When both DC voltages are similar, the optimized control does not achieve an important AC current reduction.

On comparing the results from the offline optimization and the simulations, a small difference is detected when comparing the angles and the AC current. The deviation between both can be explained because the optimization does not consider either the parasitic resistances of the circuit, or the IGBTs switching dead time. Even so, the closed loop DC current control is able to compensate the small differences to achieve a perfect DC current I_{DC} regulation.

Optimized control dynamic design

In terms of system dynamics, the plant to represent the converter is obtained using the Matlab® tool *System Identification Toolbox*. A step input is applied to the phase shift δ angle, while observing the DC current output I_{DC} evolution. Based on the result, an approximate simple first order transfer function can be obtained. Then, based on the simplified plant obtained (relating δ and I_{DC}) a conventional PI controller can be employed to regulate the DC current. The parameters of the PI control are designed using the Internal Model Control (IMC) technique [62], which is able to impose the

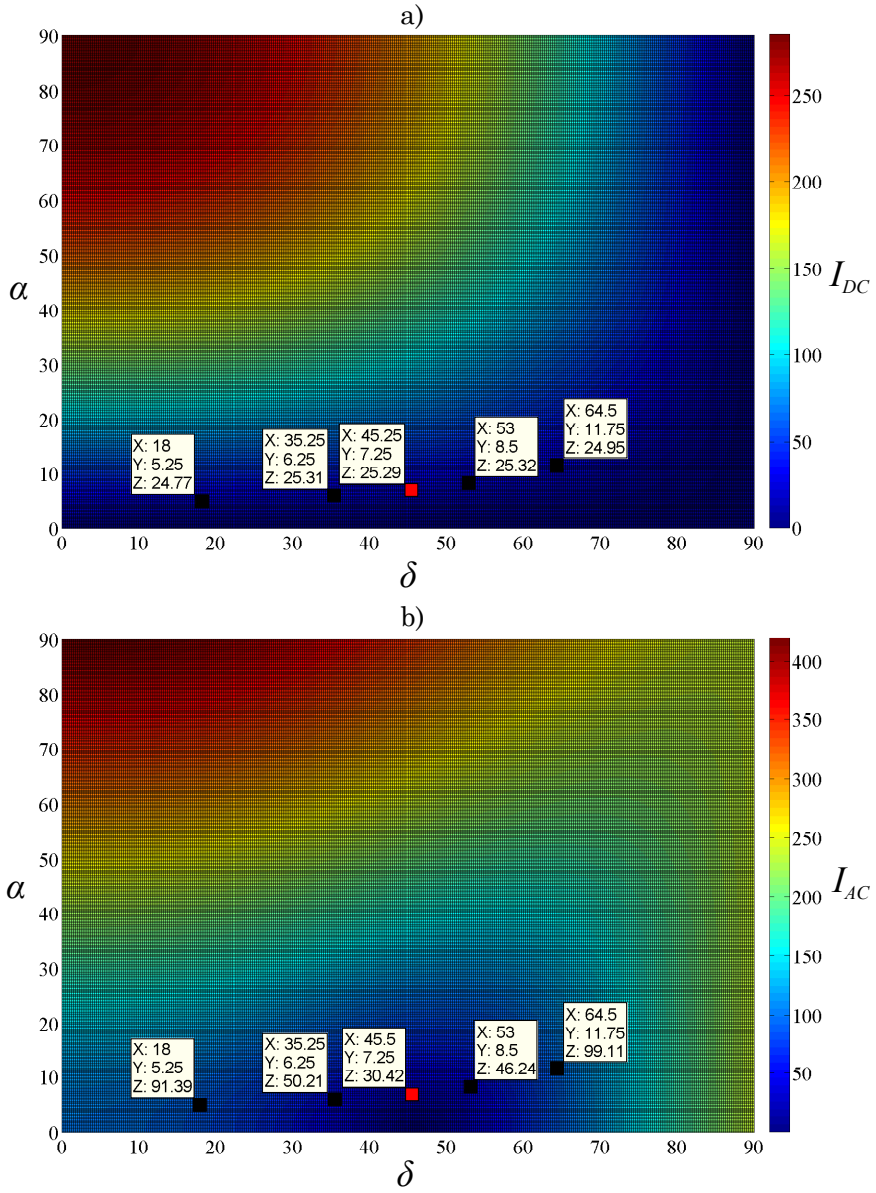

Figure 4.16: AC and DC currents for different α and δ angles. Conditions: $V_1 = 650$ V $V_2 = 348$ V. a) DC current I_{DC} for different operation points α and δ. b) AC current I_{AC} for different operation points α and δ.

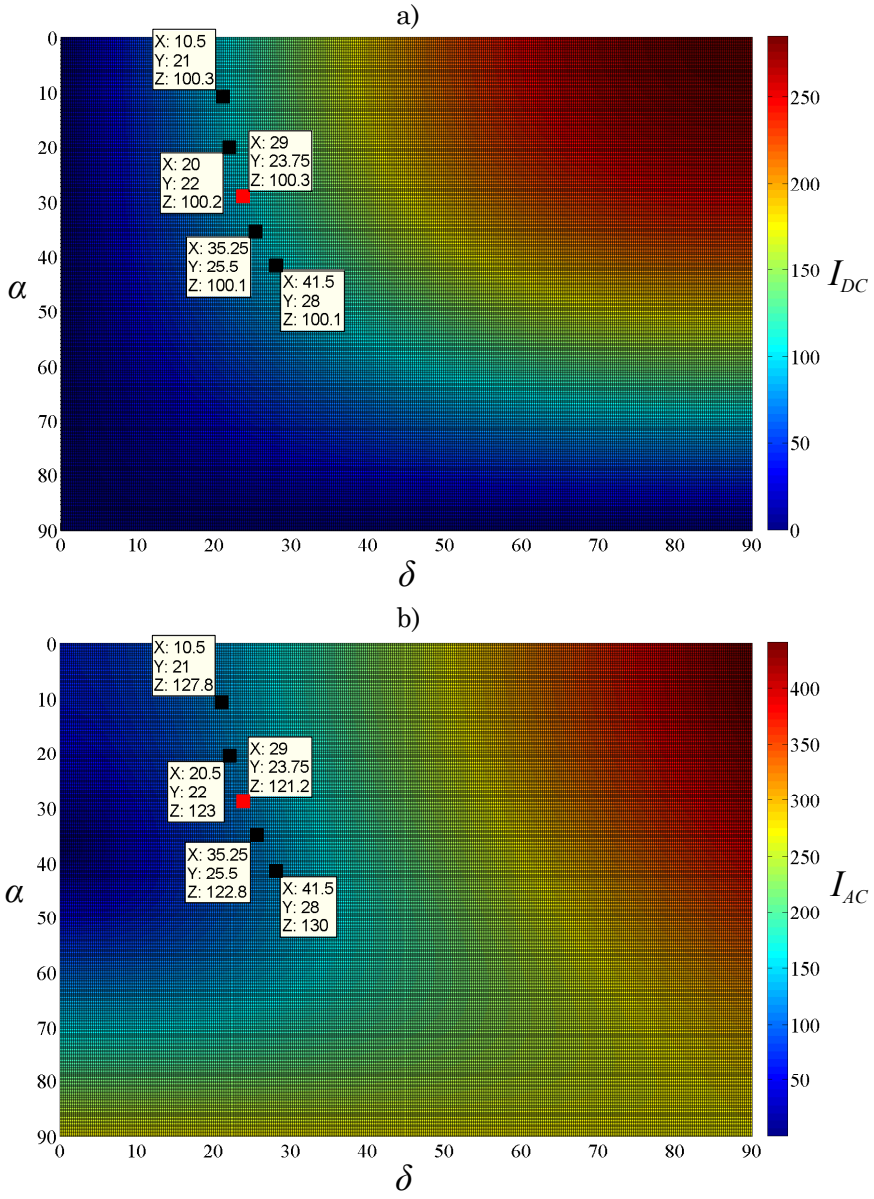

Figure 4.17: AC and DC currents for different α and δ angles. Conditions: $V_1 = 650$ V $V_2 = 400$ V. a) DC current I_{DC} for different operation points α and δ. b) AC current I_{AC} for different operation points α and δ.

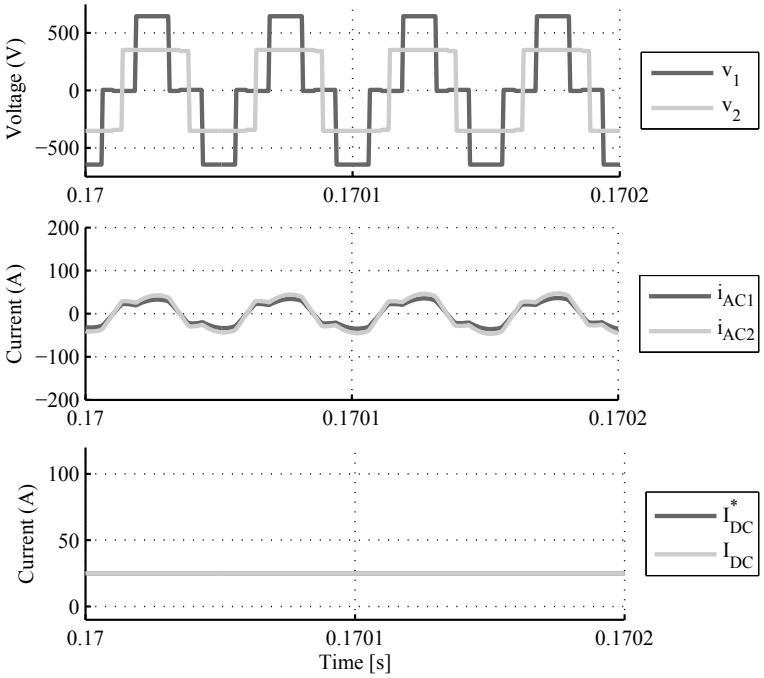

Figure 4.18: Optimized DC current control strategy. DC current reference $I^*_{DC} = 25$ A. DC input voltage $V_1 = 650$ V. DC output voltage $V_2 = 348$ V.

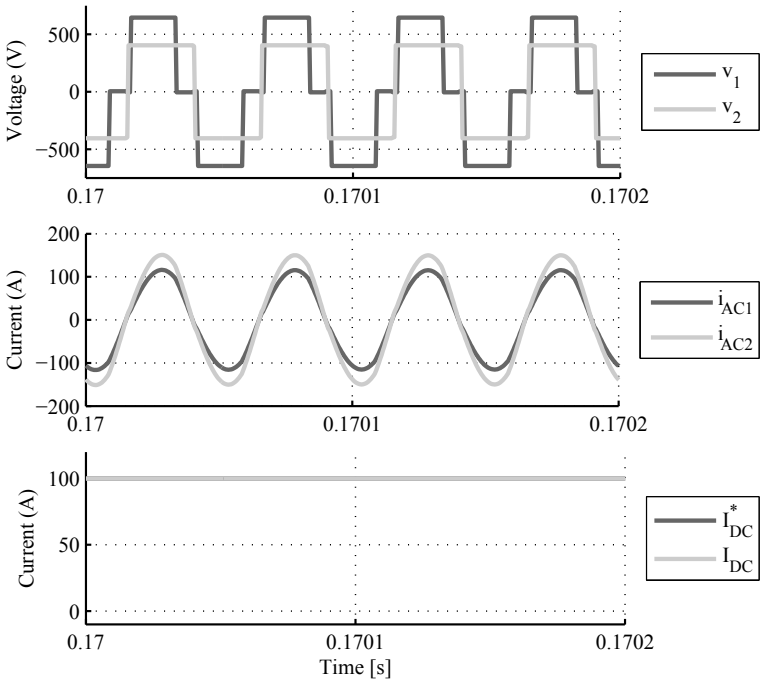

Figure 4.19: Optimized DC current control strategy. DC current reference $I^*_{DC} = 100$ A. DC input voltage $V_1 = 650$ V. DC output voltage $V_2 = 400$ V.

closed loop dynamics. The settling time for the closed loop controller is set to 100 ms. Fig. 4.20 shows the simulation results of a current reference step change I^*_{DC} from 0 to 100 A at 0.1 s. It can be observed that the DC current I_{DC} reaches the steady state value approximately in 100 ms, accomplishing the design specification. Also, if required, the DC current references can be filtered to obtain a smoother current evolution.

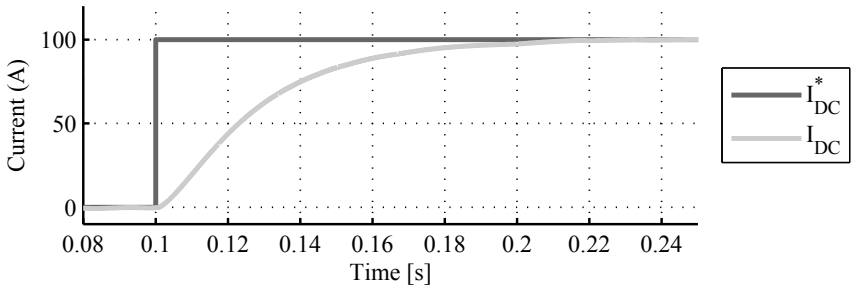

Figure 4.20: Dynamic response of the controller to a DC current step reference input from 0 to 100 A at 0.1 s

The optimized controller does not require a complex implementation in comparison with the classic controller. Using a three-level modulation, a lookup table for the angle optimization results and a conventional PI, the output of the converter can be regulated while reducing the current flowing through it. Control system simplicity is an important factor when implementing the regulator in a real microprocessor.

4.5 Experimental results

Fig. 4.21 shows a photograph of the implementation of a 50 kW DBSRC. The prototype is built based on the system parameters and the rated values shown in Table 4.1. Both H-Bridges are Semikron Semikube (Model IGD-1-424-P1N4-DL-FA) converters. The inductor and the transformer (designed by Himag) are both planar. The HF capacitor is compounded connecting several HF capacitors (designed by NWL) in parallel in order to handle the rated converter AC current. So as to perform the experimental tests, the output of the converter is connected to the input, as shown in Fig. 4.22. Note that as the transformer has a turns ratio of 1.3 and the converter output is connected back to the input, the system will not be operating under its nominal values (V_1 and V_2), as the output should have a reduced voltage compared to the input. The control system is implemented in a Texas

Instruments Digital Signal Processor (DSP) TMS320F2809. The modulation is programmed using the ePWM Peripheral, which is able to apply an angle shifting to the different triangular waves required for the operation (Fig. 4.9). The following results show the converter operation controlled using the classic phase shift control with the dead time angle δ_{DB} compensation. The three-level modulation has been implemented and tested during the start-up, in order to smoothly ramp up the voltages applied by both converters, but it has not been tested under normal operation.

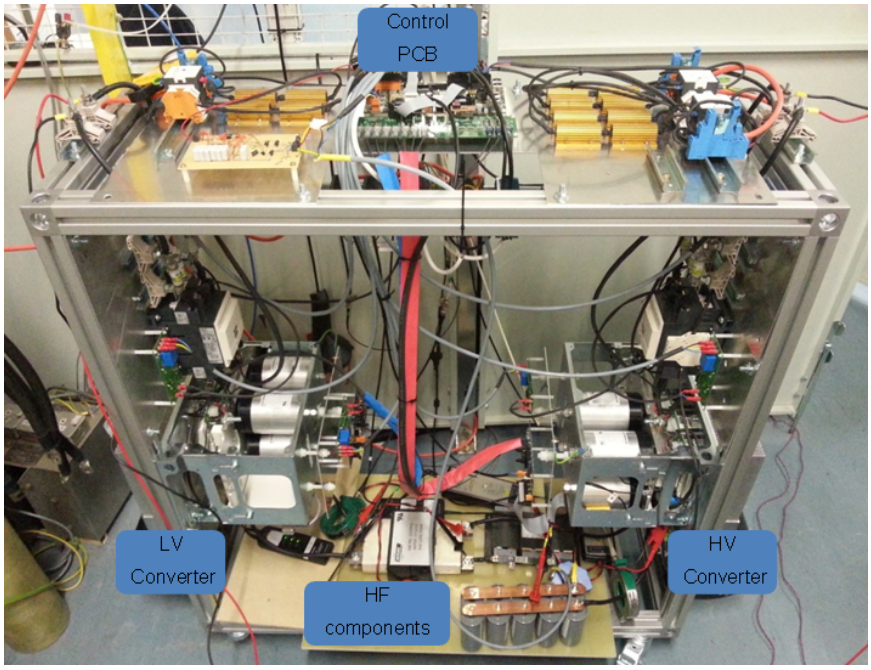

Figure 4.21: Experimental prototype of the DBSRC

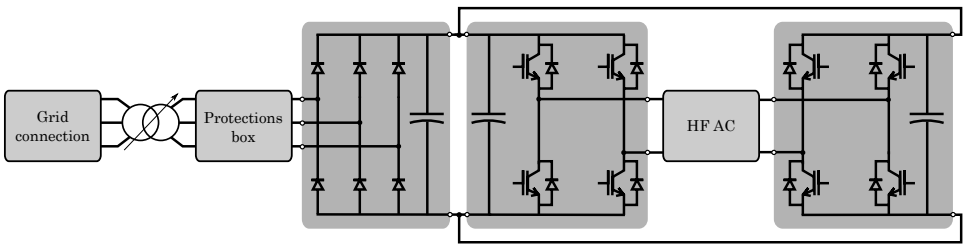

Figure 4.22: Experimental testing implementation

Fig. 4.23 shows the oscilloscope captures of the converter operation while transferring power from the primary side to the secondary side. Both DC voltages are 400 V, imposed by the diode rectifier. It can be observed that the peak current in the AC primary side is 75 A and in the secondary is 97.5 A. The DC current output measured during the test is approximately 21 A. The system shows a good behavior, both during start-up and normal operation. Note that the current flowing through the AC circuit is higher compared with the DC current output, mainly caused by two different reasons. On the one hand, the converter is not operating within its expected voltage ratio between the primary and secondary DC voltage. On the other hand the operation is based on the classic two-level modulation. An optimized operation of the converter could help to reduce the amount of AC current, even far of the nominal DC voltage values.

4.6 Conclusions

The DBSRC control design is addressed. First, the mathematical model of the system is derived. Then, the classic control is explained and its behavior is detailed through simulations. This analysis reveals that this control strategy may present large current values flowing through the HF AC side, even for a reduced active power flow transmission, particularly if the voltage ratio of the DC interconnected systems is far from the nominal value. In order to solve this problem, an optimized controller based on three-level modulation is developed, which is able to minimize the HF AC currents during the converter operation. Simulations of the proposed control are carried out to compare both control strategies, showing that it is able to reduce the AC current importantly, especially for large differences between the input and output DC voltages. Also, a 50 kW DBSRC converter prototype is developed. Several tests are performed employing the classic control showing a proper behavior. As expected, this operation mode shows large currents flowing through the AC circuit, even transferring a reduced amount of active power. This fact confirms that the optimized control proposed, can be an interesting option to operate this type of converters, as it can increase the efficiency of the system.

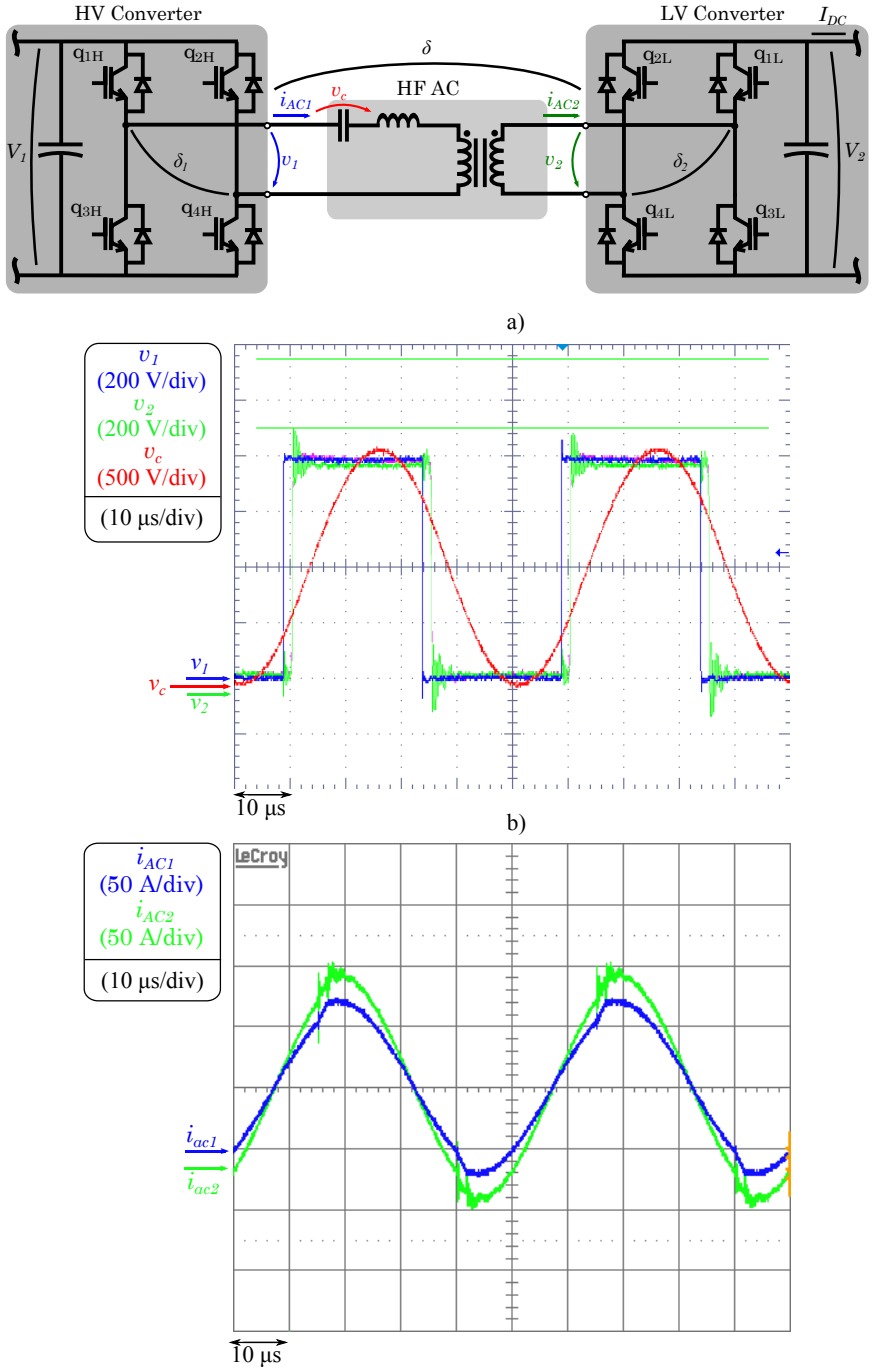

Figure 4.23: Experimental results of the performed tests. a) System voltages. b) System currents.

Chapter 5

Control design of modular multilevel converters in normal and AC fault conditions for HVDC grids

5.1 Introduction

Voltage Source Converters (VSCs) are common in low and medium power motor drives and renewable generation systems. Typically, a VSC uses Insulated-Gate Bipolar Transistors (IGBTs), enabling a controlled two or three-level voltage output driven by Pulse Width Modulation (PWM) [73]. This is not well suited for high voltage applications as the rated voltage of IGBTs is limited to a few kilovolts. Some manufacturers, notably ABB, chain multiple IGBTs to create high voltage switches; however, this requires a sophisticated drive circuit that is not easy to scale for very high voltages. To overcome this problem, Modular Multilevel Converters (MMCs) were first proposed in [27] and different topologies have been adopted by different manufacturers since then [28–30]. MMC is foreseen as the technology of choice for VSC High Voltage Direct Current (HVDC) transmission. Besides enabling higher voltages, they have several additional benefits such as reduced harmonic content, reduced transformer dv/dt stress and a great potential for standardization.

Unlike two-level VSCs, MMCs combine a large number of individually-controlled sub-modules (see Fig. 5.1) rather than chained IGBTs, requiring a sophisticated control structure. When compared to former well-known converter topologies, the MMC is more challenging to control due to its use of combined Alternating Current (AC) and DC current and voltage waveforms which have different roles in regulating the energy of the converter. These roles are not obvious but must be fully utilized in order to ensure that the converter can operate in all possible scenarios, including those with asymmetrical network voltages. A number of publications have

addressed the basics of the control of MMCs [74–80]. In terms of unbalanced grid voltage operation, MMC control has also been analyzed in the literature [81–93]. Some of the proposed MMC control structures are based on extensions of the methods employed in conventional VSC inverters with feed-forward additions that mitigate some of the issues that only happen in MMCs (for example, the so-called inner or circulating currents of the converter). Other control structures do not cover all the converter degrees of freedom, thus leaving certain internal variables uncontrolled. Also, a dynamic design methodology for the regulators used to control the converter variables is not always provided.

In this chapter a complete control structure for a VSC-HVDC providing a comprehensive and in-depth analysis of the controller design process is presented. First, a steady-state analysis of the system is conducted, which enables an intuitive understanding of the role of the different current and voltage components. Based on this analysis, particular current components are selected to regulate specific degrees of freedom of the converter. Next, a discussion of the current reference calculation for both the grid and inner currents is provided, considering unbalanced grid voltage operation. Then, the current and energy controllers design is addressed. Finally, the complete control design proposal is validated through simulation studies under both normal and unbalanced grid conditions.

This chapter is organized as follows: Section 5.2 describes the converter and the basic equations of the system. Then, in Section 5.3 a steady state analysis of the converter is developed, identifying the uses of the current components within the converter control. In Section 5.4 the different parts of the converter control are described and the current and energy regulators are designed. Finally, in 5.5 simulation results to validate the proposed control design in normal operation and during a voltage sag are shown.

5.2 System description

The MMC has N_{arm} sub-modules (SM) in each arm[1]. These can be controlled individually to either insert their capacitor in series with the arm or to bypass it, which allows the arm to behave as a controllable voltage source fed from an aggregated capacitor-based energy storage device [75]. The voltage of the arms can be used to control the current flowing through the converter. The target current is chosen to achieve the desired exchange

[1]Each phase of the converter is commonly called a *leg*; whereas the upper and the lower halves of a leg are commonly called *arms* (see Fig. 5.1).

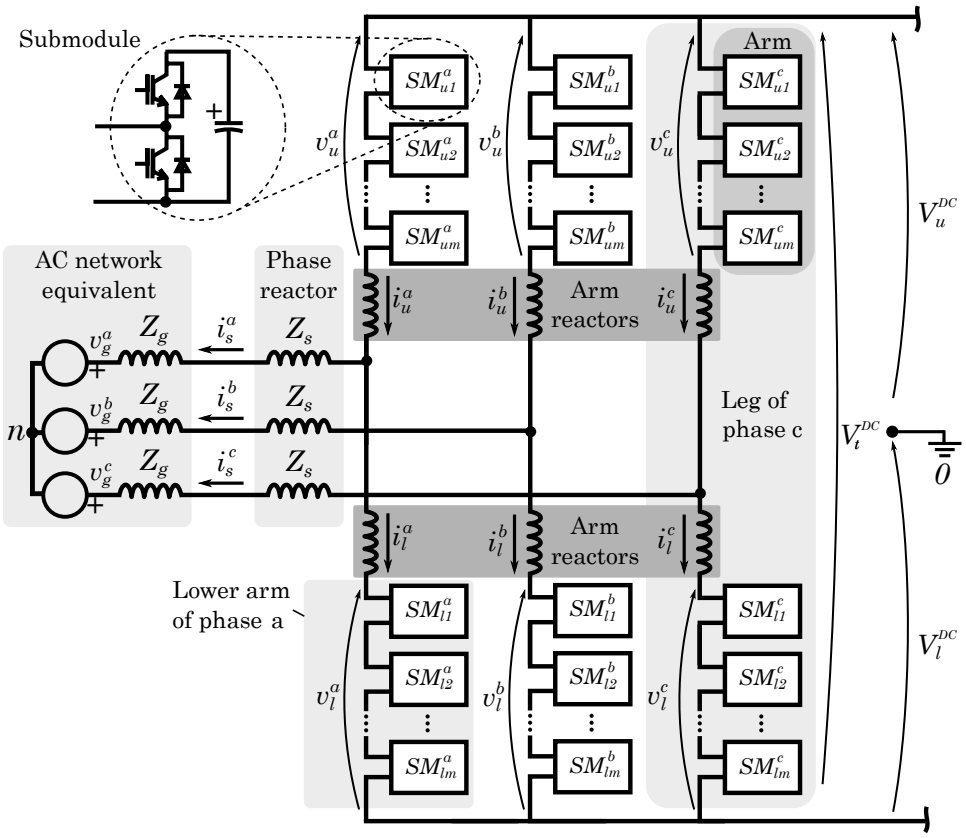

Figure 5.1: Complete scheme of an MMC converter

of power between the AC grid and the DC grid as well as maintaining the internal energy balance of the converter. To represent the converter [94], the circuit equations can be obtained per each phase j $(j = a, b, c)$

$$V_u^{DC} - v_u^j - v_g^j - v_n = R_a i_u^j + L_a \frac{di_u^j}{dt} + (R_s + R_g) i_s^j + (L_s + L_g) \frac{di_s^j}{dt} \quad (5.1)$$

$$- V_l^{DC} + v_l^j - v_g^j - v_n = -R_a i_l^j - L_a \frac{di_l^j}{dt} + (R_s + R_g) i_s^j + (L_s + L_g) \frac{di_s^j}{dt} \quad (5.2)$$

where R_a and L_a are the resistance and inductance of the arm inductor respectively, R_s and L_s correspond to the phase inductor, R_g and L_g correspond to the equivalent impedance of the AC grid, V_u^{DC} and V_l^{DC} are the voltages of the upper and the lower halves of the HVDC link, v_g^j is the AC grid voltage, v_u^j and v_l^j are the voltages applied by the upper and the lower arms respectively, i_u^j and i_l^j are the currents flowing through the upper and lower arms respectively and i_s^j is the AC grid current. Further, the following variables and parameters are defined

$$\begin{cases} v_{diff}^j \triangleq \dfrac{1}{2}(-v_u^j + v_l^j) \\ v_{sum}^j \triangleq v_u^j + v_l^j \\ i_{sum}^j \triangleq \dfrac{1}{2}(i_u^j + i_l^j) \\ R \triangleq R_s + R_g + \dfrac{R_a}{2} \\ L \triangleq L_s + L_g + \dfrac{L_a}{2} \end{cases} \quad \text{and} \quad \begin{cases} v_u^j = -v_{diff}^j + \dfrac{1}{2} v_{sum}^j \\ v_l^j = v_{diff}^j + \dfrac{1}{2} v_{sum}^j \\ i_u^j = \dfrac{1}{2} i_s^j + i_{sum}^j \\ i_l^j = -\dfrac{1}{2} i_s^j + i_{sum}^j \end{cases} \quad (5.3)$$

where v_{diff}^j and v_{sum}^j are the differential and the additive voltages applied by the converter respectively and i_{sum}^j is the additive (inner) current, which is common to the upper and lower arms. Adding and subtracting equations (5.1) and (5.2) while applying the aforementioned variable change leads to

$$\underbrace{\frac{1}{2}(V_u^{DC} - V_l^{DC})}_{\triangleq V_{off}^{DC}} + v_{diff}^j - v_g^j - v_n = R\, i_s^j + L\, \frac{di_s^j}{dt} \quad (5.4)$$

$$v_{sum}^j - \underbrace{(V_u^{DC} + V_l^{DC})}_{\triangleq V_t^{DC}} = -2R_a i_{sum}^j - 2L_a \frac{di_{sum}^j}{dt} \quad (5.5)$$

where V_{off}^{DC} is half the imbalance between the voltage of positive and the negative HVDC poles. This will normally be close to zero but can be large under pole-to-ground faults in the HVDC grid. Also, note that (5.4) is related to AC side current i_s^j, whereas (5.5) is related to additive currents i_{sum}^j.

Then, assuming that no neutral connection is available

$$i_s^a + i_s^b + i_s^c = 0 \tag{5.6}$$

This can be combined with the summation of (5.4) over $j = a, b, c$ to obtain the voltage of the neutral point v_n

$$v_n = \underbrace{\frac{1}{3}(v_{diff}^a + v_{diff}^b + v_{diff}^c)}_{\triangleq v_{diff}^0} - \underbrace{\frac{1}{3}(v_g^a + v_g^b + v_g^c)}_{\triangleq v_g^0} + V_{off}^{DC} \tag{5.7}$$

Note that v_{diff}^0 is controlled by the converter but does not produce any current. This is normally exploited by VSCs to extend the AC output voltage range using third harmonic voltage injection [95]. Due to symmetry, (5.4) and (5.5) can be written in vector form by combining a, b and c as

$$v_{diff}^{abc} - v_g^{abc} + (V_{off}^{DC} - v_n)\begin{bmatrix}1 & 1 & 1\end{bmatrix}^T = \mathbf{R}\, i_s^{abc} + \mathbf{L}\,\frac{di_s^{abc}}{dt} \tag{5.8}$$

$$v_{sum}^{abc} - V_t^{DC}\begin{bmatrix}1 & 1 & 1\end{bmatrix}^T = -2\mathbf{R_a} i_{sum}^{abc} - 2\mathbf{L_a}\frac{di_{sum}^{abc}}{dt} \tag{5.9}$$

where $\mathbf{R}$, $\mathbf{R_a}$, $\mathbf{L}$ and $\mathbf{L_a}$ are 3x3 diagonal matrices with R, R_a, L and L_a terms at the diagonal, respectively.

5.3 Steady state analysis

The voltage applied by the converter arms and the current flowing through them contain both AC and DC components. These play different roles in the power exchange between the AC and DC networks and the energy stored in the converter itself. In order to better understand these roles, it is useful to perform a decoupled AC and DC steady state analysis of the circuit. A summary detailing the uses of each converter current component can be seen in Table 5.1.

5.3.1 AC analysis

For the AC analysis, assuming V_{off}^{DC} is purely DC, equation (5.8) can be expressed in the phasor domain as

$$\underline{V}_{diff}^{abc} - \underline{V}_{g}^{abc} - \underline{V}_{n}\begin{bmatrix}1 & 1 & 1\end{bmatrix}^{T} = \underline{\mathbf{Z}}\,\underline{I}_{s}^{abc} \tag{5.10}$$

where $\underline{\mathbf{Z}}$ is a 3x3 diagonal matrix with the term $R + j\omega L$ at the diagonal[2]. It is convenient to apply the Fortescue transformation to the previous equation [96]. The Fortescue transformation $\underline{\Theta}^{+-0}$ of a phasor vector $\underline{\Theta}^{abc}$ is defined as

$$\underline{\Theta}^{+-0} \triangleq \mathbf{F}\underline{\Theta}^{abc} = \frac{1}{3}\begin{bmatrix}1 & \underline{p}^2 & \underline{p}\\ 1 & \underline{p} & \underline{p}^2\\ 1 & 1 & 1\end{bmatrix}\underline{\Theta}^{abc}$$

with $\underline{p} = e^{j\frac{-2\pi}{3}}$. Multiplying equation (5.10) by $\mathbf{F}$ leads to

$$\underline{I}_{s}^{+-} = \underline{Z}^{-1}\left[\underline{V}_{diff}^{+-} - \underline{V}_{g}^{+-}\right] \tag{5.11}$$

As noted earlier, the zero sequence component of the current flowing towards the AC grid is zero and therefore can be removed from the result. The current flowing towards the AC network $\underline{I}_{s}^{+-}$ is used to exchange power with the AC network and can be controlled using the differential voltage $\underline{V}_{diff}^{+-}$. In addition, multiplying the phasor domain expression of (5.9) by $\mathbf{F}$ yields

$$\underline{I}_{sum}^{+-0} = -\frac{1}{2\underline{Z}_{a}}\underline{V}_{sum}^{+-0} \tag{5.12}$$

The positive and negative sequence components of the additive current $\underline{I}_{sum}^{+-}$ can be used to exchange energy between the upper and the lower halves of the converter to achieve internal balance while the zero component $\underline{I}_{sum}^{0}$ should be kept close to zero to avoid AC voltage distortion in the DC network.

5.3.2 DC analysis

The DC analysis is performed by making the derivatives of the currents in (5.8) and (5.9) equal to zero. As with the AC analysis, it is convenient to distinguish between the zero sequence component and the rest of the current. In the DC case, this can be done by using the Clarke transformation [97],

[2] ω is the grid frequency

which is defined as

$$\Theta^{\alpha\beta 0} \triangleq \mathbf{C}\Theta^{abc} = \frac{1}{3}\begin{bmatrix} 2 & -1 & -1 \\ 0 & -\sqrt{3} & \sqrt{3} \\ 1 & 1 & 1 \end{bmatrix} \Theta^{abc} \tag{5.13}$$

Transforming the steady state DC form of (5.8) leads to

$$V_{diff}^{\alpha\beta DC} = R\, I_s^{\alpha\beta DC} \tag{5.14}$$

As in the AC case, the zero sequence component of I_s is strictly zero; however, the remaining DC current $I_s^{\alpha\beta DC}$ can flow through the transformer windings and must be kept equal to zero in order to avoid undesired core saturation. This can be controlled using $v_{diff}^{\alpha\beta DC}$. In addition, applying (5.13) to the steady state DC form of (5.9) leads to

$$I_{sum}^{\alpha\beta DC} = -\frac{1}{2R_a} V_{sum}^{\alpha\beta DC} \tag{5.15}$$

and

$$I_{sum}^{0DC} = \frac{1}{2R_a}(V_t^{DC} - V_{sum}^{0DC}) \tag{5.16}$$

The zero sequence component of the additive DC current is used to exchange power between the converter and the DC network and can be controlled using V_{sum}^{0DC}. On the other hand, $I_{sum}^{\alpha\beta DC}$ is controlled through $V_{sum}^{\alpha\beta DC}$ and can be used to exchange energy between the different legs of the converter to achieve internal energy balance. This will be important under severe voltage unbalances in the AC network, where the power exchanged by the different legs will be significantly different.

Table 5.1: Converter current components and their uses

Current	**Freq.**	**Component**	**Use**
I_s	AC	+,-	Active and reactive current to the AC grid (continuous).
		0	Equal to 0 due to three-wire connection.
	DC	α,β	Controlled to zero to prevent DC current flowing through the AC grid.
		0	Equal to 0 due to three-wire connection.
I_{sum}	AC	+,-	Internal power exchange between upper and lower arms (transient).
		0	Controlled to zero to avoid AC distortion in the DC grid.
	DC	α,β	Internal power exchange between the legs of the converter (continuous/transient).
		0	Power flowing to the DC grid (continuous).

5.4 Converter control

In this section, a design methodology for the converter controllers is proposed based on the parameters shown in Table 5.2. An overview of the control structure proposed for the converter is shown in Fig. 5.2, detailing the different stages and possible operational modes.

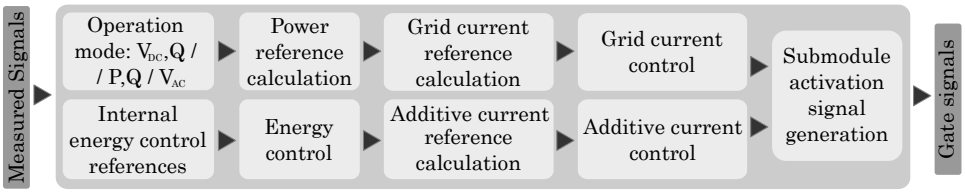

Figure 5.2: Overall MMC control structure

The control strategy must be designed to meet several objectives:

- Control the different degrees of freedom of the MMC by means of specific current components.
- Control the grid and additive currents flowing through the converter.
- Establish a power exchange between the AC and the DC grid.
- Continuous balancing of the energy stored in the converter arms, avoiding large deviations.
- Enable the converter operation under any grid condition.

To meet these objectives, the following parts of the control structure are addressed:

- Grid and additive current reference calculation considering unbalanced AC grid voltage conditions.
- Design of the grid and additive current regulators to track AC and DC current references.
- Design of the energy regulators to balance the energy stored in the converter arms.

Based on this structure a complete control scheme can be implemented as shown in Fig. 5.3 and Fig. 5.4. Next, the design of each part of the structure is addressed in detail.

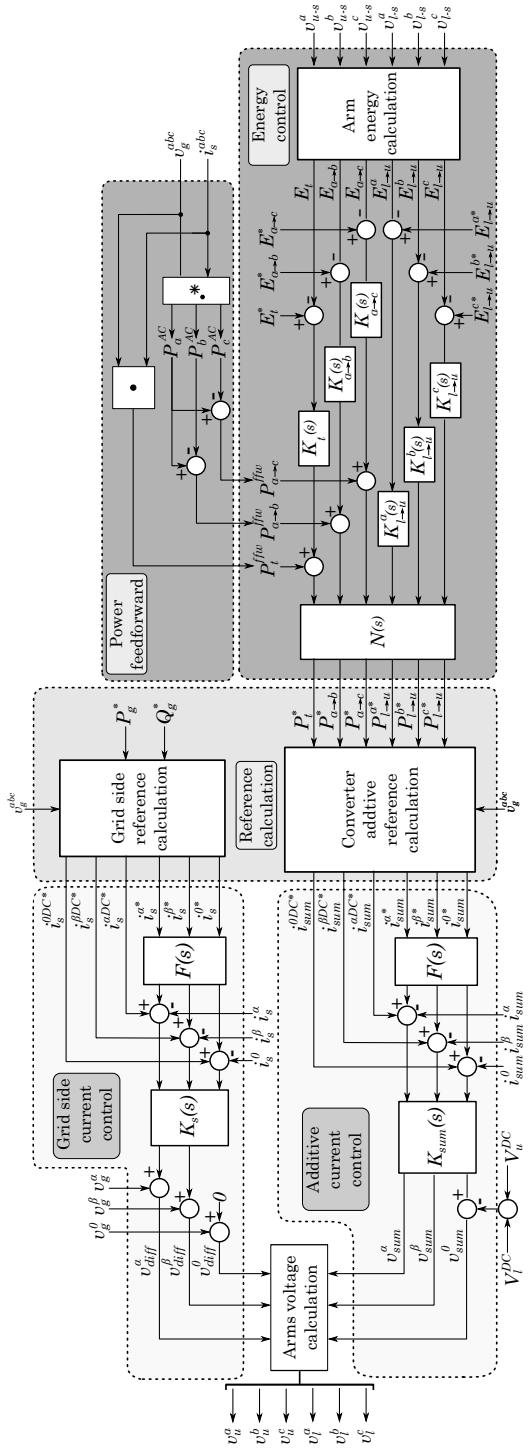

Figure 5.3: MMC control structure - Part I

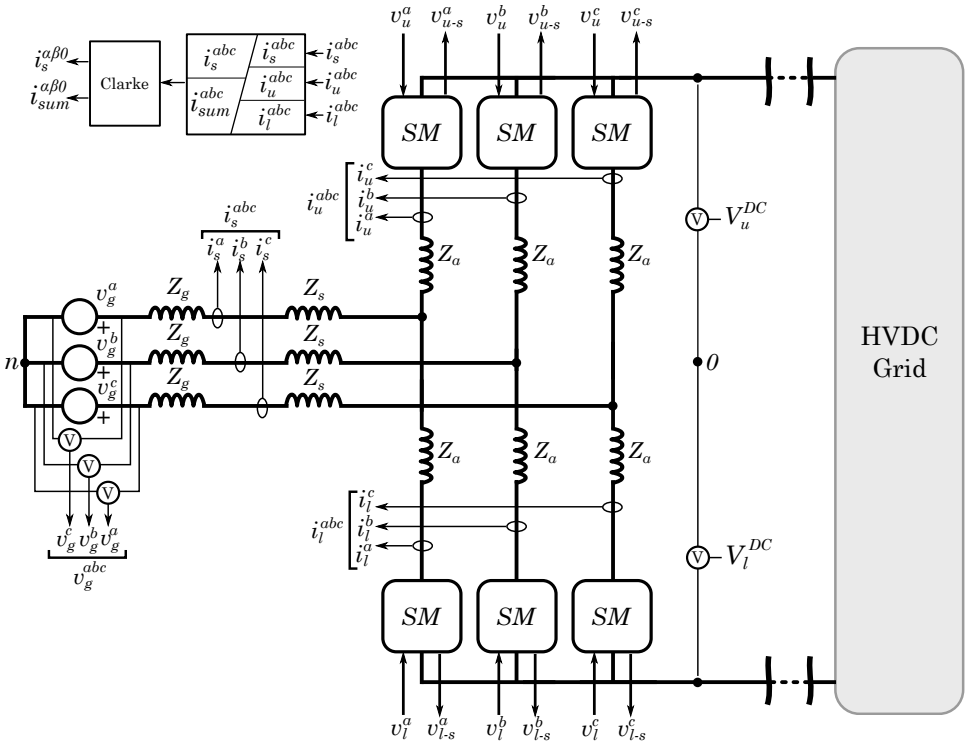

Figure 5.4: MMC control structure - Part II

5.4.1 Current reference calculation

As in most VSC topologies, the control structure for an MMC consists of a high-level power and energy controller which produces current reference values for a nested current controller, which in turn gives output voltage commands to a switching signal generator (see Fig. 5.2). Although the calculation of current reference values has elements in common with that of a two-level converter, the greater number of degrees of freedom of the MMC makes it of greater complexity.

AC network current reference calculation

DC component of the AC network current
As discussed earlier, the zero sequence component of the AC network current is strictly zero due to the three-wire connection, and the reference of $I_s^{\alpha\beta DC}$ is set to zero and must be controlled to avoid transformer saturation.

Table 5.2: System parameters for an example MMC

Parameter	Symbol	Value	Units
Rated power	S	526	MVA
Rated power factor	$\cos\varphi$	0.95 (c)	-
AC-side voltage	U	320	kV RMS ph-ph
HVDC link voltage	V_{DC}	±320	kV
Grid equivalent impedance	Z_g	0.01+j 0.1	pu
Phase reactor impedance	Z_s	j 0.05	pu
Arm reactor impedance	Z_a	0.01+j 0.2	pu
Converter sub-modules per arm	N_{arm}	400	sub-modules
Average sub-module voltage	V_{module}	1.6	kV
Sub-module capacitance	C_{module}	8	mF

AC component of the AC network current

The AC network current references can be calculated using the same methods as in classic two-level converters. Under balanced conditions, the two degrees of freedom of the current can be adjusted to obtain the desired active and reactive power exchange with the AC network [97]. However, when considering unbalanced AC network voltages several options exist [98], and the preferred solution has not been selected yet. The most common choice is to set the negative sequence current to zero and export only positive sequence current chosen to obtain the desired active and reactive power exchange. This causes an asymmetrical exchange of power between the AC network and the different legs of the converter even in steady state, which needs to be compensated by the converter to ensure internal energy balance. The calculation of the current reference is simplified by applying the so-called Park transformation matrix $\mathbf{T}(\theta)$ to voltage and current variables. The Park transformation is equivalent to the Clarke transformation combined with a rotation of angle θ and can be obtained as

$$\Theta^{qd0} = \underbrace{\mathbf{C}\,\mathbf{R}(\theta)}_{\mathbf{T}(\theta)}\,\Theta^{abc}; \quad \mathbf{R}(\theta) = \begin{bmatrix} \cos\theta & -\sin\theta & 0 \\ \sin\theta & \cos\theta & 0 \\ 0 & 0 & 1 \end{bmatrix} \tag{5.17}$$

Following the nomenclature introduced by Akagi [97,99], the non-oscillatory terms of the instantaneous active and reactive power of the power exported to the AC grid, P_g and Q_g respectively can be calculated from the positive

voltage and current qd components as

$$P_g = \frac{3}{2}\left(v_g^{q+} i_s^{q+} + v_g^{d+} i_s^{d+}\right); \quad Q_g = \frac{3}{2}\left(v_g^{q+} i_s^{d+} - v_g^{d+} i_s^{q+}\right) \tag{5.18}$$

Assuming v_g^{d+} to be zero, which can be granted if the angle of the Park transformation is chosen to match the angle of the positive sequence, the current references can be calculated as

$$i_s^{q^*} = \frac{2}{3}\frac{P_g^*}{v_g^{q+}}; \quad i_s^{d^*} = \frac{2}{3}\frac{Q_g^*}{v_g^{q+}} \tag{5.19}$$

This approach is sometimes known as the feed-forward method, as opposed to an alternative approach where the current reference is obtained from the output of a PI controller fed with the error between measured power and reference power. A discussion about their advantages and drawbacks can be found in [100]. If the converter is connected to a weak grid, the coupling between output current and grid voltage seen by the converter may require further consideration as shown in [101]. Finally, if the losses of the converter filter are not negligible, these can be included in the calculation of (5.19) for better accuracy [98].

Additive current reference calculation

DC component of the additive current

The zero sequence component of the DC additive current I_{sum}^{0DC} is used to export power from the converter to the DC grid P_t, whereas the rest of the DC additive current is used to exchange power between converter legs $P_{a\to b}$ and $P_{a\to c}$. It is convenient to define the following new power variables

$$P_{a\to b} \triangleq P_a - P_b, \quad P_{a\to c} \triangleq P_a - P_c, \quad P_t \triangleq \sum_{j=a,b,c} P_j \tag{5.20}$$

where $P_j \approx V_t^{DC} i_{sum}^{jDC}$.

Similarly to the case of the AC network current, the approximation above assumes the losses of the arm inductors to be negligible. This enables calculating the current references in the Clarke reference frame as

$$\begin{bmatrix} i_{sum}^{\alpha DC^*} \\ i_{sum}^{\beta DC^*} \\ i_{sum}^{0DC^*} \end{bmatrix} = \frac{1}{3\ V_t^{DC}} \begin{bmatrix} 0 & 1 & 1 \\ 0 & \sqrt{3} & -\sqrt{3} \\ 1 & 0 & 0 \end{bmatrix} \begin{bmatrix} P_t^* \\ P_{a\to b}^* \\ P_{a\to c}^* \end{bmatrix} \tag{5.21}$$

Under normal operation, most of the DC additive current will be zero sequence component and it will be in charge of ensuring that the power exchanged between the converter and the AC network is equal to the power exchanged with the HVDC link. However, under severe voltage imbalances in the AC network, the DC additive current of phases a, b and c can be significantly different in order to compensate the power imbalance between phases.

AC component of the additive current

The AC voltage applied by the converter arms will be close to the AC network voltage. This can be seen from (5.11) given that $\underline{Z}$ is small. When comparing the AC voltage of the upper and the lower arms, they will have opposite signs. Therefore, the additive AC current $\underline{I}_{sum}^{+-}$ can be used to exchange power between the upper and lower arms of the converter. On the other hand, the zero sequence component $\underline{I}_{sum}^{0}$ must be set to zero to prevent AC current flowing to the HVDC link. Unlike the AC network current, the additive current can contain positive and negative sequence components with no impact on the AC grid. The power exchanged between upper and lower arms can be obtained by multiplying the AC arm voltage by the AC additive current. The AC arm voltage can be approximated as

$$v_l^{abc} \approx -v_u^{abc} \approx \sqrt{2} \begin{bmatrix} V_g^+ \cos(\omega t) + V_g^- \cos(\omega t + \psi) \\ V_g^+ \cos(\omega t - \frac{2\pi}{3}) + V_g^- \cos(\omega t + \psi + \frac{2\pi}{3}) \\ V_g^+ \cos(\omega t + \frac{2\pi}{3}) + V_g^- \cos(\omega t + \psi - \frac{2\pi}{3}) \end{bmatrix} \tag{5.22}$$

where ψ is the angle between the positive and the negative grid voltages. The AC additive current can be expressed as

$$i_{sum}^{abc} = \sqrt{2} \begin{bmatrix} I_{sum}^+ \cos(\omega t + \gamma) + I_{sum}^- \cos(\omega t + \alpha) \\ I_{sum}^+ \cos(\omega t + \gamma - \frac{2\pi}{3}) + I_{sum}^- \cos(\omega t + \alpha + \frac{2\pi}{3}) \\ I_{sum}^+ \cos(\omega t + \gamma + \frac{2\pi}{3}) + I_{sum}^- \cos(\omega t + \alpha - \frac{2\pi}{3}) \end{bmatrix} \tag{5.23}$$

where γ and α are the angles of the positive and negative sequence additive current respectively, taking the positive sequence grid voltage as the reference of angles. Multiplying the arm voltages by the additive currents for phases a, b and c while eliminating the oscillatory terms at the double line

frequency yields

$$P^a_{l\to u}(t) = V_g^- I^+_{sum}\cos(\gamma-\psi) + V_g^+ I^+_{sum}\cos\gamma + V_g^- I^-_{sum}\cos(\psi-\alpha) + V_g^+ I^-_{sum}\cos\alpha \quad (5.24)$$

$$P^b_{l\to u}(t) = V_g^- I^+_{sum}\cos\left(\gamma-\psi-\frac{4\pi}{3}\right) + V_g^+ I^+_{sum}\cos(\gamma) + V_g^- I^-_{sum}\cos(\psi-\alpha) + V_g^+ I^-_{sum}\cos\left(\alpha+\frac{4\pi}{3}\right) \quad (5.25)$$

$$P^c_{l\to u}(t) = V_g^- I^+_{sum}\cos\left(\gamma-\psi+\frac{4\pi}{3}\right) + V_g^+ I^+_{sum}\cos(\gamma) + V_g^- I^-_{sum}\cos(\psi-\alpha) + V_g^+ I^-_{sum}\cos\left(\alpha-\frac{4\pi}{3}\right) \quad (5.26)$$

Note that there are four parameters that need to be chosen (I^+_{sum}, I^-_{sum}, α and γ) in order to adjust three power variables ($P^a_{l\to u}$, $P^b_{l\to u}$ and $P^c_{l\to u}$). The redundant degree of freedom can be used for secondary purposes such as minimizing losses. Here γ is chosen to be zero, thus the positive sequence current is chosen to be aligned with the positive sequence voltage. By introducing this condition, the former equations can be rewritten in a more compact form

$$\underbrace{\begin{bmatrix}P_1\\P_2\\P_3\end{bmatrix}}_{P} = \underbrace{\begin{bmatrix}V_g^+ & 0 & V_g^-\cos\psi\\ 0 & V_g^+ & -V_g^-\sin\psi\\ V_g^-\cos\psi & -V_g^-\sin\psi & V_g^+\end{bmatrix}}_{X}\underbrace{\begin{bmatrix}I^-_{sum}\cos\alpha\\ -I^-_{sum}\sin\alpha\\ I^+_{sum}\end{bmatrix}}_{I} \quad (5.27)$$

where the new power variables are defined as

$$\begin{aligned} P_1 &\triangleq \frac{1}{3}(-P^c_{l\to u} - P^b_{l\to u} + 2P^a_{l\to u})\\ P_2 &\triangleq \frac{1}{3}(\sqrt{3}P^c_{l\to u} - \sqrt{3}P^b_{l\to u})\\ P_3 &\triangleq \frac{1}{3}(P^a_{l\to u} + P^b_{l\to u} + P^c_{l\to u}) \end{aligned} \quad (5.28)$$

Based on the power references given by the energy controllers to maintain

the energy balance between upper and lower arms, the current references can be obtained from (5.27) as

$$\underbrace{\begin{bmatrix} I^-_{sum}\cos\alpha \\ -I^-_{sum}\sin\alpha \\ I^+_{sum} \end{bmatrix}}_{I} = \underbrace{\frac{1}{(V_g^+)^2-(V_g^-)^2}\cdot\begin{bmatrix} M_{11} & M_{12} & M_{13} \\ M_{21} & M_{22} & M_{23} \\ M_{31} & M_{32} & M_{33} \end{bmatrix}}_{M}\underbrace{\begin{bmatrix} P_1 \\ P_2 \\ P_3 \end{bmatrix}}_{P} \tag{5.29}$$

$$M_{11} = \frac{2(V_g^+)^2+(\cos(2\psi)-1)(V_g^-)^2}{2V_g^+}$$

$$M_{22} = \frac{2(V_g^+)^2+(-\cos(2\psi)-1)(V_g^-)^2}{2V_g^+}$$

$$M_{12} = M_{21} = -\frac{\sin(2\psi)(V_g^-)^2}{2V_g^+}; \quad M_{33} = V_g^+$$

$$M_{13} = M_{31} = -\cos(\psi)V_g^-; \quad M_{23} = M_{32} = \sin(\psi)V_g^-$$

This equation has a discontinuity when $V_g^+ = V_g^-$, resulting in very high current reference values when voltage sags with high imbalance occur. One way to overcome this problem is to disable the AC component of the additive current upon detecting such disturbance and enabling it once the fault is cleared. Even though this makes the converter unable to control the balance between upper and lower arms during the sag, it is worth noting that there are no sources of sustained drift between upper and lower arms unless faults occur within the converter itself. The converter control during this specific voltage condition is analyzed in detail in Chapter 6, providing three different possible solutions to the mentioned issue.

5.4.2 Current control

Although the equivalent circuit of the MMC is more complex than that of a two-level converter, by using the transformations introduced earlier it is possible to transform it into two separate circuits that can be controlled independently using well-known inverter control techniques. However, in the MMC, additive currents contain DC plus AC components and modulation techniques are prone to introduce disturbances in both domains. Therefore, the current controllers must be designed to track references and to reject AC and DC disturbances. Under such requirements, there is no advantage in transforming voltages and currents using the rotating Park matrix (5.17). Therefore, the Clarke transformation matrix (5.13) is applied in order to

separate the zero sequence component from the rest. Applying (5.13) to (5.8) and (5.9) yields

$$v_{diff}^{\alpha\beta} - v_g^{\alpha\beta} = \mathbf{R}\, i_s^{\alpha\beta} + \mathbf{L}\, \frac{di_s^{\alpha\beta}}{dt} \tag{5.30}$$

$$v_{sum}^{\alpha\beta 0} - V_t^{DC} \begin{pmatrix} 0 & 0 & 1 \end{pmatrix}^T = -2\mathbf{R_a} i_{sum}^{\alpha\beta 0} - 2\mathbf{L_a} \frac{di_{sum}^{\alpha\beta 0}}{dt} \tag{5.31}$$

Note that all these equations are decoupled, therefore individual single-input single-output (SISO) controllers can be used for each of them. Here, the current controller of choice is a two-degree of freedom structure with a conventional PI controller and an AC reference pre-filter $F(s)$ [62]. The control structure is shown in Fig. 5.3, in the grid and additive current control part. This strategy enables the controller to track both AC and DC references with the desired tracking error. The parameters of the PI controllers are chosen using an inverse-based design [61] where the PI is set to cancel out the current dynamics and to introduce an integrator that enables achieving the desired performance. In the case of the AC network current, the transfer function of the controller $K_s(s)$ is defined as

$$K_s(s) = \frac{k_{p-s}s + k_{i-s}}{s}, \quad k_{p-s} = \frac{L}{\tau_s}, \quad k_{i-s} = \frac{R}{\tau_s} \tag{5.32}$$

where τ_s is the resulting closed loop time constant which is normally chosen in the range of few milliseconds [102]. The same controller structure $K_{sum}(s)$ can be used for the additive currents, by choosing

$$K_{sum}(s) = \frac{k_{p-sum}s + k_{i-sum}}{s},\ k_{p-sum} = \frac{2\,L_a}{\tau_{sum}},\ k_{i-sum} = \frac{2\,R_a}{\tau_{sum}} \tag{5.33}$$

Once the current controller has been defined, the AC reference pre-filter is calculated to compensate the deviation applied by the closed loop controller. The pre-filter $F(s)$ is a lead compensator that corrects the gain M_t and phase M_p deviation at the grid frequency ω, as

$$F(s) = \alpha K_f \frac{s+\omega_1}{s+\omega_2}; \quad \alpha = \frac{1+M_p}{1-M_p}; \quad \begin{cases} \omega_1 = \omega/\sqrt{\alpha} \\ \omega_2 = \omega\sqrt{\alpha} \end{cases} \tag{5.34}$$

$$K_f = \frac{1}{M_t\, M_f}; \quad M_f = \sqrt{\frac{1+M_p}{1-M_p}} \tag{5.35}$$

As an example, the grid current controller is designed according to the parameters in Table 5.2 to track references in 10 ms (settling time). Fig. 5.5 presents the bode diagram relating the DC (Fig. 5.5a) and AC (Fig. 5.5b) component reference with the respective current components, showing that the controller is able to track AC and DC current references with 0 dB and 0 phase delay.

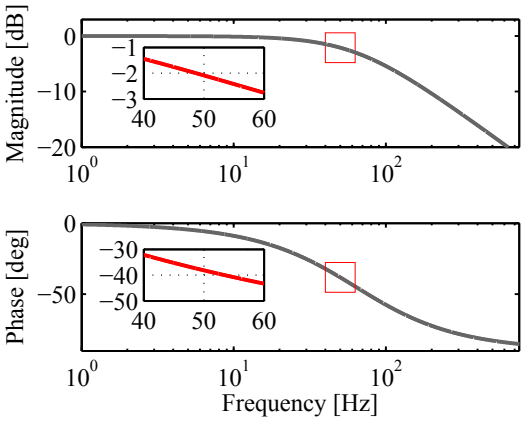

a)

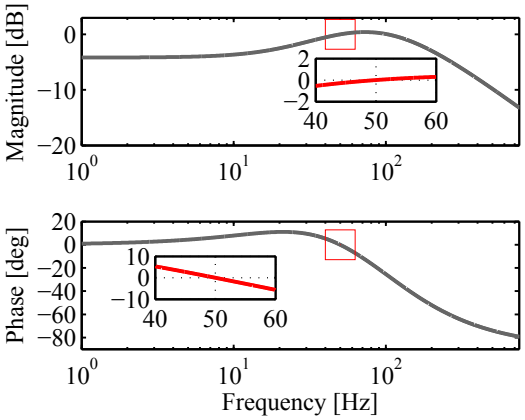

b)

Figure 5.5: Closed loop transfer function for the grid current controller. a) DC current regulation: without an AC reference pre-filter. b) AC current regulation: with an AC reference pre-filter.

5.4.3 Energy Control

The energy regulators of the MMC sit on top of the additive current controllers. There are six energy variables (as many as arms in the MMC) controlled by six different regulators. It is useful to define a new set of energy variables, which will be controlled using the converter additive currents

$$E_t = \sum_{j=a,b,c} E_u^j + \sum_{j=a,b,c} E_l^j \tag{5.36}$$

$$E_{a\to b} = (E_u^a + E_l^a) - (E_u^b + E_l^b) \tag{5.37}$$

$$E_{a\to c} = (E_u^a + E_l^a) - (E_u^c + E_l^c) \tag{5.38}$$

$$E_{l\to u}^j = E_l^j - E_u^j \tag{5.39}$$

where E_t is the total energy stored in the converter, $E_{a\to b}$ and $E_{a\to c}$ are the energy differences between legs a and b and a and c respectively, and $E_{l\to u}^j$ is the difference of energy between the upper and lower arms of leg j, with $j = a, b, c$. These are linear combinations of the total energy stored in the arms, which can be approximated as [77]

$$E_u^j \approx \frac{1}{2}\frac{C_{module}}{N_{arm}}\left(v_{u-s}^j\right)^2; \quad E_l^j \approx \frac{1}{2}\frac{C_{module}}{N_{arm}}\left(v_{l-s}^j\right)^2 \tag{5.40}$$

where v_{u-s}^j and v_{l-s}^j are the sums of the capacitor voltages of all sub-modules of the upper and lower converter arms, respectively.

In order to achieve sustained operation, energy differences between legs and between upper and lower arms must be regulated to zero while the total energy of the converter must be regulated to its rated value, given by

$$E_t^* = 6 \cdot \frac{1}{2}\frac{C_{module}}{N_{arm}}\left(V_t^{DC*}\right)^2 \tag{5.41}$$

Total energy and energy differences between legs

The total energy of the arms E_t is affected by the mismatch between the power exchanged with the AC network and the DC network. Then, although the total energy could be regulated using the AC or the DC power references, it is normally controlled using the DC power reference P_t^*. In addition, the energy differences between legs $E_{a\to b}$ and $E_{a\to c}$ are caused by the differences between the active power exchanged by each converter leg under AC network voltage imbalances. These differences can be controlled using the DC power exchanged between legs $P_{a\to b}^*$ and $P_{a\to c}^*$.

The energy controller structure can be seen in Fig. 5.3 within the energy control part. These controllers are composed of a feedback term, plus a feed-forward term corresponding to the power exchanged by each converter leg with the AC grid P_j^{AC}, expressed in terms of the total power exchanged P_t^{ffw} and the differences between legs $P_{a\to b}^{ffw}$ and $P_{a\to c}^{ffw}$, as

$$P_j^{AC} \approx v_g^j \, i_s^j \tag{5.42}$$

$$P_{a\to b}^{ffw} \triangleq P_a^{AC} - P_b^{AC}, \quad P_{a\to c}^{ffw} \triangleq P_a^{AC} - P_c^{AC} \tag{5.43}$$

$$P_t^{ffw} \triangleq \sum_{j=a,b,c} P_j^{AC} \tag{5.44}$$

To design the controllers, a simplified scheme of the system is depicted in Fig. 5.6. The transfer function between power and energy is an integrator, while the transfer function between power references and actual power $G_{i_{sum}}(s)$ can be modeled as a first-order system with unit gain and a time constant set according to the design specifications of the additive current controllers. The feed-forward loop includes a first-order low-pass filter $F_{fw}(s)$ to avoid exceeding the bandwidth of the additive current controller. Moreover, a notch filter $N(s)$ is also included to avoid that the controller attempts to compensate the energy oscillations due to the natural AC ripple.

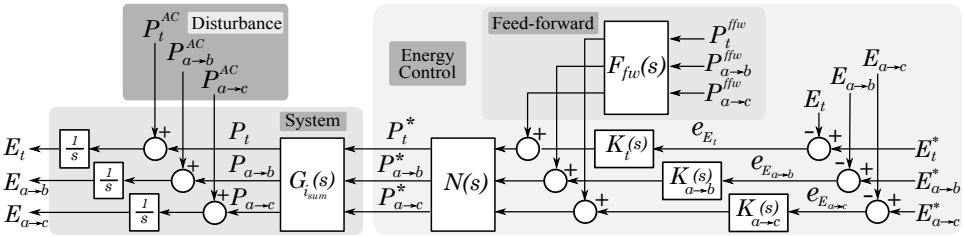

Figure 5.6: Simplified scheme to design the energy regulators to balance the total energy of the converter and the energy differences between the converter legs

The following 2^{nd} order notch filter structure can be used to cancel a specific frequency

$$N_{\omega_n}(s) \triangleq \frac{s^2 + \omega_n^2}{1 + 2\omega_n/Q + \omega_n^2} \tag{5.45}$$

where ω_n is the AC frequency to be avoided and Q is the quality factor of the filter. In this case, $N(s)$ is chosen as a series combination of $N_\omega(s)$

and $N_{2\omega}(s)$ in order to cancel line and double-line frequencies. The effect of choosing different values of Q is shown in Fig. 5.7. Here, a quality factor of 3 is chosen, which shows good performance filtering the AC components without a significant degradation of the time response.

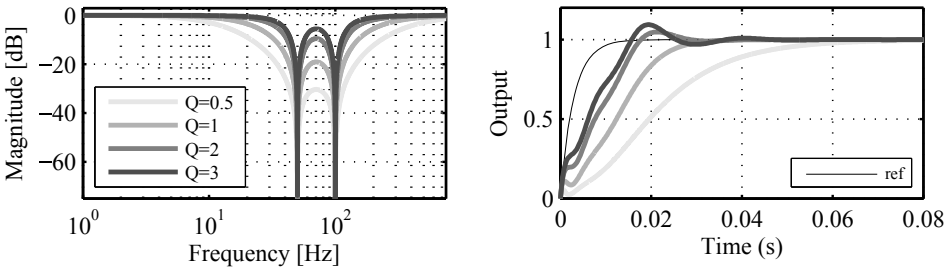

Figure 5.7: Bode plot (left) and step response (right) of the notch filter used for canceling line and double-line frequencies

The energy controllers are designed considering a disturbance rejection problem through a loop shaping strategy. The control specifications are:

- Maximum energy allowed error: 10% of the rated total energy.
- Settling time of 1 s to achieve a ±2% deviation from the set-point value, after a power disturbance.

Based on this requirements, a tentative frequency response of the system can be defined. For the three controllers, the worst-case scenario disturbance assumed is a step change of the nominal power. Hence, as the system plant to be controlled (Fig. 5.6) and the worst disturbance input are equivalent, the regulators employed to control E_t, $E_{a\to b}$ and $E_{a\to c}$ are also equivalent. To design them, the relevant transfer function to be analyzed is the one that relates the power disturbances (P_t^{AC}, $P_{a\to b}^{AC}$ and $P_{a\to c}^{AC}$) with its corresponding energy error (e_{E_t}, $e_{E_{a\to b}}$ and $e_{E_{a\to c}}$), typically named SG_d [62]. Then, a maximum gain imposed to this transfer function can be defined based on the maximum disturbance input (500 MW) and the maximum energy error (10% deviation)

$$|SG_{d_{max}}| = 20\log_{10}\frac{e_{max}}{d_{max}} = 20\log_{10}\frac{0.1\cdot E_t^*}{500\cdot 10^6} \approx -46 \text{ dB} \tag{5.46}$$

In addition, the low corner frequency of SG_d is chosen to be 1 rad/s, in order to achieve the desired settling time. Based on these boundaries, the shadowed area in Fig. 5.8a is defined. Then, the parameters of the controller can

be selected to fit within the defined area. To verify the design methodology in Fig. 5.8b, the response of the designed controller for a nominal power step response is included, showing that the disturbance is rejected in 1 second without exceeding the maximum defined error.

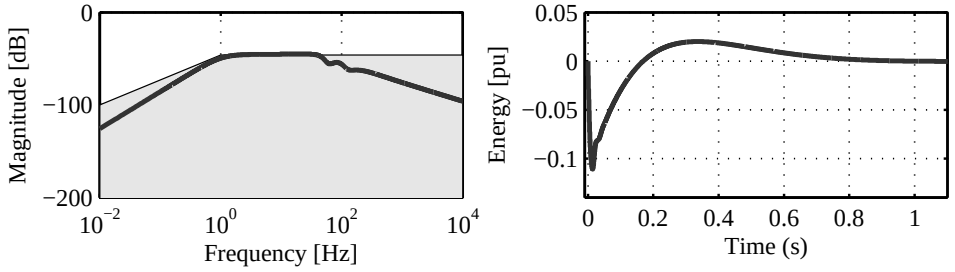

Figure 5.8: Bode diagram and step response of SG_d transfer function

Energy differences between upper and lower arms

Imbalanced AC grid voltages are not a source of sustained drift of the differences between the energy stored in the upper and lower arms. However, a small amount of error may still appear during transients, which favors the inclusion of a feedback controller. The plant to be controlled (shown in Fig. 5.9) has a similar structure to that of the total energy (see Fig. 5.6); therefore, the regulator design methodology employed is equivalent.

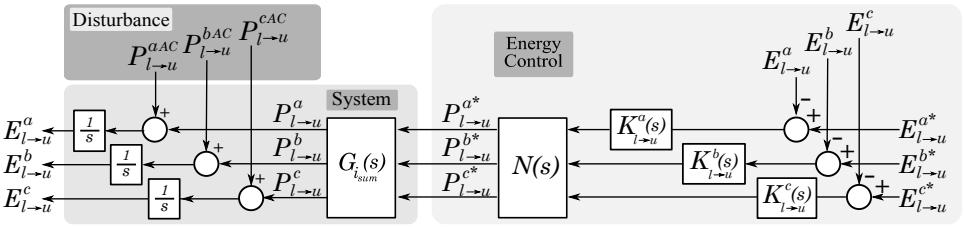

Figure 5.9: Simplified scheme to design the energy regulators to balance the upper and lower arms of the converter

5.5 Case study

Simulations are carried out under Matlab Simulink® with the parameters shown in Table 5.2 in order to validate the overall design. Two different transients are simulated showing:

- A power step change of the converter under normal conditions.
- Unbalanced voltage sag operation while injecting nominal power.

5.5.1 Simulation model description

The MMC model used for the simulations is built based on the accelerated model proposed in [103]. This model allows access to each individual sub-module voltage and provides enough accuracy compared to a complete model [104]. Each sub-module is represented by a capacitor that is charged or discharged depending on its switching state and the current that is flowing through its arm. The modulation technique implemented is the Nearest Level Control (NLC) technique [105], which calculates the number of active sub-modules in each arm and uses a reduced switching frequency strategy to increase the efficiency of the converter.

5.5.2 Normal operation mode

Fig. 5.10 shows the converter response to a power reference set-point change from 0 to nominal power (injecting to the AC grid) at time 1 s. The power reference is changed following a first order system evolution with a settling time constant of 100 ms [102]. It can be observed that the converter AC and DC power reach the steady state in the defined time. Fig. 5.10 confirms that the total sum of the energy of the arms is affected. However, the energy controller is able to compensate the effect.

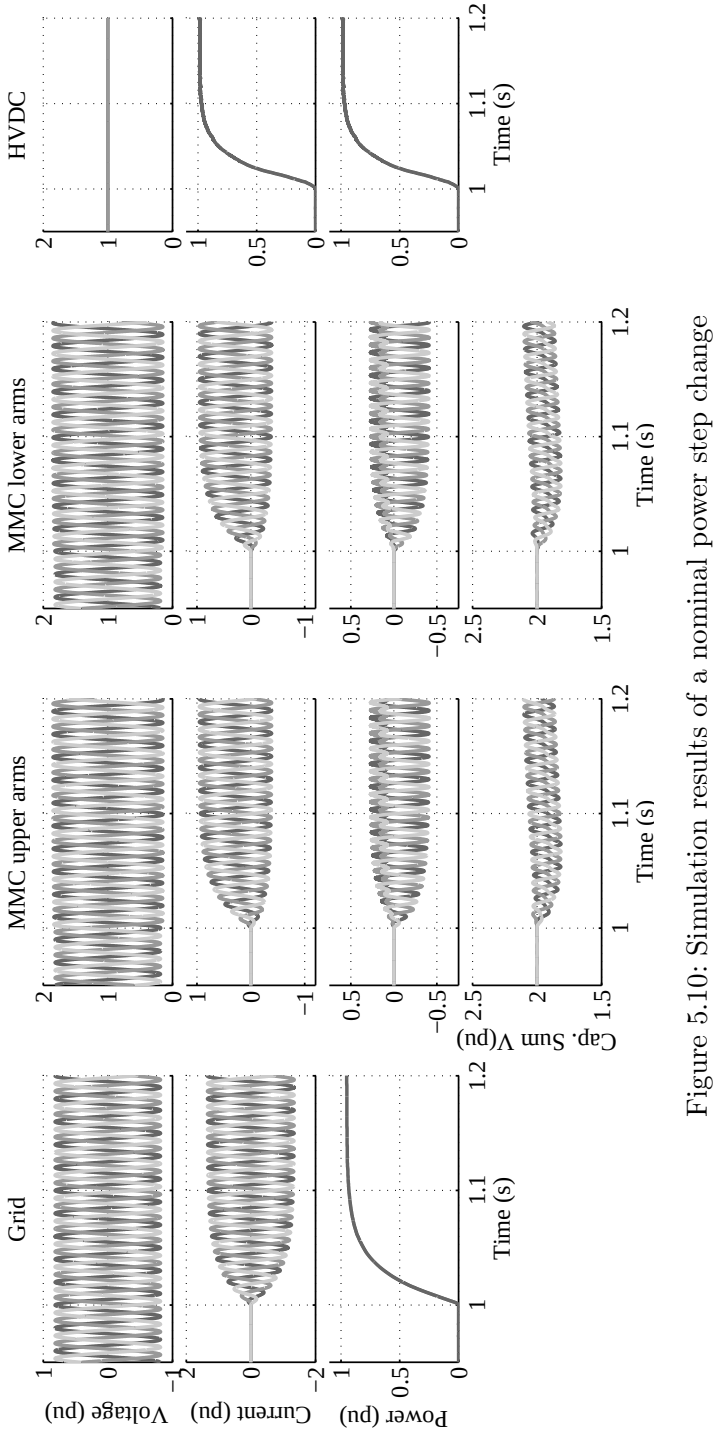

Figure 5.10: Simulation results of a nominal power step change

5.5.3 Unbalanced voltage sag

Fig. 5.11 and Fig. 5.12 show the converter response to an asymmetrical type G voltage sag [106], considering a remaining positive sequence voltage of 0.5 pu and a negative sequence voltage of 0.25 pu. The simulated voltage sag starts at time 3 s and the voltage is fully restored at time 5 s. Although in a real network, a deep and highly unbalanced voltage sag condition would be sustained for less than 250 ms [107], in this case, the sag has been extended for 2 s to validate the controller stability.

Note that the converter only injects positive sequence current. Due to the voltage imbalance, the power injected to the grid presents an oscillatory component at double line frequency. The power injection is reduced by the same ratio as the positive sequence voltage of the grid. Besides, the remaining converter current capacity is employed to inject reactive current to the grid, as required by grid codes [108]. It can be observed that the total sum of the capacitor voltages (converter energy) is affected by the voltage sag (see Fig. 5.11). However, the proposed controllers are able to regulate the converter energy back to their normal state. Finally, Fig. 5.12 shows how the converter goes back to its initial state upon clearing the fault without a significant deviation.

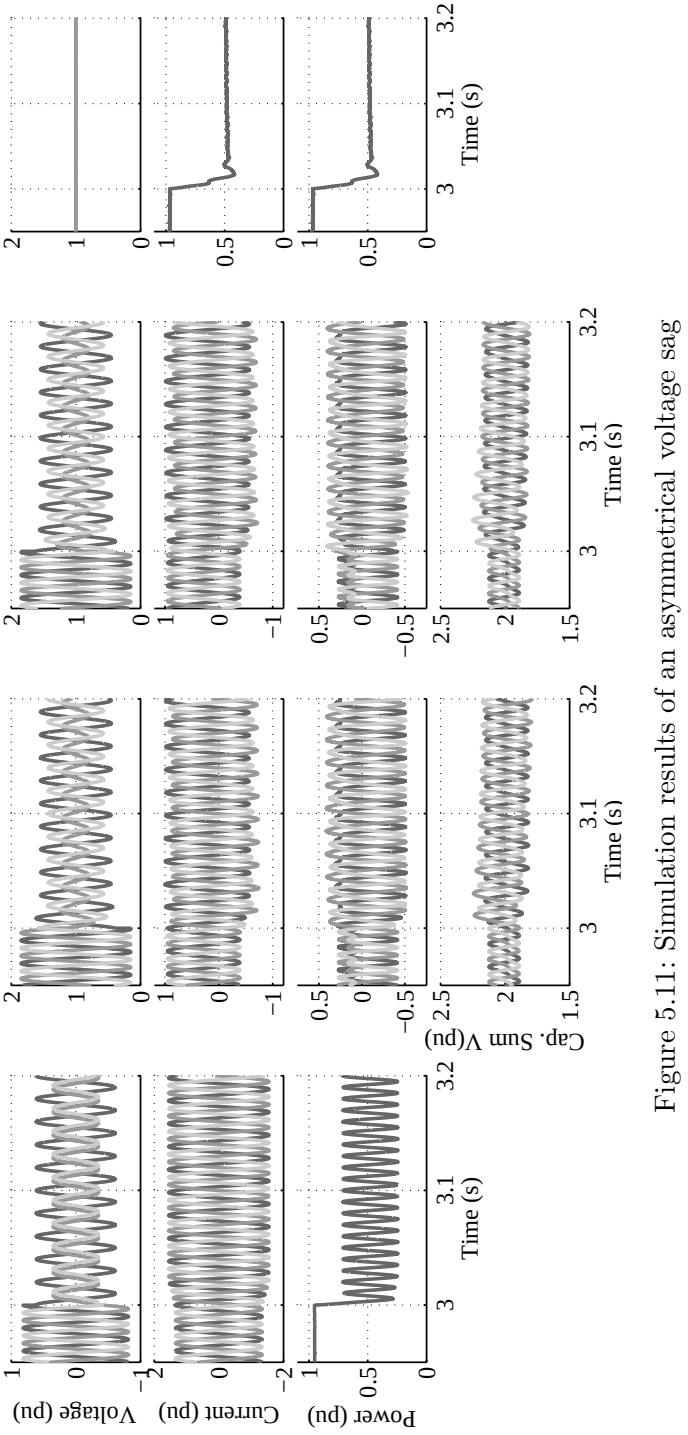

Figure 5.11: Simulation results of an asymmetrical voltage sag

Figure 5.12: Simulation results of an asymmetrical voltage sag

5.6 Conclusions

A control structure for the half-bridge-cell based MMC to operate in any grid condition has been presented. First, a steady state analysis of the converter is carried out to identify the current components to be used to regulate the converter degrees of freedom. Based on this analysis, a complete reference calculation strategy to obtain the grid and additive current references from the corresponding power references is described, also considering unbalanced grid conditions. To apply these current references, current regulators are designed to be able to track both AC and DC current components. Finally, regulators to balance the converter arms stored energy are designed using simplified models of the converter. With the proposed control structure, the converter is able to operate despite the grid conditions, maintaining the converter balanced. The control strategy proposed is validated through simulations under both normal and unbalanced grid conditions.

Chapter 6

Control of modular multilevel converters under singular unbalanced voltage conditions with equal positive and negative sequence components

6.1 Introduction

The operation of Modular Multilevel Converters (MMCs) during unbalanced Alternating Current (AC) grid conditions has been addressed in the literature [81–93]. Among the different control structures proposed, those including a current reference calculation stage could eventually fail during a specific voltage condition, particularly when the positive and negative sequence of the AC grid voltage become equal. This voltage state, referred to as singular voltage condition, may result in singularities in the calculation of current references, which could cause instability in the converter unless corrective actions are taken. This issue has been studied in the past for two-level Voltage Source Converters (VSCs) [98] where the resulting low-frequency power ripple going into the Direct Current (DC) bus was a concern. A similar problem arises in MMCs for both the AC grid and inner current reference calculation stages, as can be seen in the previous chapter and in [89,91]. The discussion introduced in [98] for the AC grid current reference calculation is also valid for MMCs. In terms of the inner current references, a solution based on applying offset voltage is presented in [91] for double line faults.

In this chapter, three alternative methodologies that enable the operation of the converter under all possible faults that cause the singular voltage condition are proposed. The first methodology is based on disabling the problematic elements of the arm energy-balancing controllers upon detection of the singular voltage condition. The two other methods are based on solving the current reference calculation problem using linear algebra tools

for incompatible systems. In order to validate these methods, a detailed analysis of the different types of voltage sags that result in the singular voltage condition is developed. Simulations are carried out to demonstrate the performance achieved using the different methods.

The chapter is organized as follows: the system converter variables and the controller employed are described in Section 6.2. Then, the reference calculation problem is explained in Section 6.3. In Section 6.4, three different methodologies are proposed to overcome the reference calculation problem. In Section 6.5, the different type of voltage sags that can cause the mentioned voltage condition are identified. Finally, in Section 6.6, the proposed modifications of the reference calculation techniques are validated through simulations of the cases found in the previous section.

6.2 Converter description and control

The present analysis is based on the MMC structure previously detailed in Section 5.2 (see Fig. 5.1). In this section, a brief description of the converter main variables and control is included again for the sake of clarity. The converter has three phase units with two arms in each. Each arm has N_{arm} sub-modules (SMs), presenting a half-bridge topology [27]. Each SM can be either inserted or by-passed, allowing the arm to behave as a positive controllable voltage source [75]. The voltage applied by the arms is used to control their current, which in turn is used to transfer power and achieve internal energy balance in the converter.

6.2.1 System variables

Next, the relevant system variables detailed in Fig. 5.1 are again introduced. The voltages involved are: v_g^j is the grid voltage, v_u^j and v_l^j are the upper and lower arm voltages respectively, and V_u^{DC} and V_l^{DC} are the voltages of the upper and the lower poles of the High Voltage DC (HVDC) link. In addition, another two variables that do not appear in Fig. 5.1, but play an important role in the energy balancing of the converter, are the sums of the SM capacitor voltages of the upper and the lower arms v_{u-s}^j and v_{l-s}^j, respectively. The relevant currents are the grid current i_s^j and the upper i_u^j and lower i_l^j converter arm currents. Regarding the converter circuit impedances, R_a and L_a are the parasitic resistance and the inductance of the arm reactors respectively, R_s and L_s are the resistance and inductance of the

phase inductors[1], and R_g and L_g correspond to the equivalent impedance of the AC grid. Besides, as described in Section 5.2 the additive and differential currents and voltages are defined based on the following expressions

$$\begin{cases} v^j_{diff} \triangleq \dfrac{1}{2}(-v^j_u + v^j_l) \\ v^j_{sum} \triangleq v^j_u + v^j_l \\ i^j_{sum} \triangleq \dfrac{1}{2}(i^j_u + i^j_l) \end{cases} \quad \text{and} \quad \begin{cases} v^j_u = -v^j_{diff} + \dfrac{1}{2}v^j_{sum} \\ v^j_l = v^j_{diff} + \dfrac{1}{2}v^j_{sum} \\ i^j_u = \dfrac{1}{2}i^j_s + i^j_{sum} \\ i^j_l = -\dfrac{1}{2}i^j_s + i^j_{sum} \end{cases} \tag{6.1}$$

where v^j_{diff} and v^j_{sum} are the differential and the additive voltages applied by the converter, and i^j_{sum} is the additive (inner) current flowing through the converter.

6.2.2 Control system

The control scheme employed in this chapter has been previously described in detail in Section 5.4, specifically in Fig. 5.2, Fig. 5.3 and Fig. 5.4. In this part, the generic scheme has been simplified as shown in Fig. 6.1, where the main control stages can be straightforwardly identified.

Next, the relevant control variables and features for the analysis developed in this chapter are detailed. P^*_g and Q^*_g are the AC grid active and reactive power references. The corresponding AC output current reference $i^{\alpha\beta 0*}_s$ is obtained through a reference calculation structure which takes into account unbalanced voltage situations [98], while its DC component $i^{\alpha\beta 0DC*}_s$ is set to zero to prevent DC current flowing through the AC grid, for instance to avoid transformer saturation.

In order to balance the internal energy of the converter, six separated energy control loops are required. Specifically, the controlled energy variables are: the total energy of the converter E_t, the energy differences between the converter legs $E_{a\to b}$ and $E_{a\to c}$, and the energy difference between the upper and lower arms of leg j $E^j_{l\to u}$, with $j = a, b, c$. The output of the energy regulators are power references P^*_t, $P^*_{a\to b}$, $P^*_{a\to c}$ and $P^{j*}_{l\to u}$. These are fed to a reference calculation stage (see Section 5.4.1) in order to obtain the additive AC and DC current references, $i^{\alpha\beta 0*}_{sum}$ and $i^{\alpha\beta 0DC*}_{sum}$.

[1] In some cases the leakage inductance of a grid-interface transformer may be used as the phase inductor.

The current references $i_s^{\alpha\beta 0*}$, $i_s^{\alpha\beta 0DC*}$, $i_{sum}^{\alpha\beta 0*}$ and $i_{sum}^{\alpha\beta 0DC*}$ are regulated using current controllers in the stationary reference frame ($\alpha\beta 0$), which are able to track AC and DC components through applying voltages with the converter arms (see Section 5.4.2).

6.3 Reference calculation problem

Table 5.1 in the previous chapter summarizes the different current components flowing through the converter [78] and their uses within the control structure. The reference values of all components of the current are calculated from the power references given the instantaneous measured AC and DC grid voltages. A variation of the AC grid voltage affects the AC components, whereas a variation of the DC grid voltage causes the DC components to change.

The choice of the AC grid current reference during an unbalanced voltage sag has been discussed in the past [98] and the most common approach to date is to set its negative sequence to zero and to export active and reactive power using positive sequence current only. In such a scenario, the active power exchanged between each leg of the converter and the AC grid is different, resulting in a sustained drift of their energy that must be compensated using additive DC current.

On the other hand, the additive AC current is normally used to control the differences between the energy of the upper arms and the energy of the lower arms which may suffer from deviations during transients. The output voltage of the converter is close to the grid voltage, therefore the power exchanged between upper and lower arms per phase $P^j_{l\rightarrow u}$, eliminating the oscillatory terms, is expressed in (5.27). For the sake of clarity, the system of equations is here detailed again

$$\underbrace{\begin{bmatrix} P_1 \\ P_2 \\ P_3 \end{bmatrix}}_{P} = \underbrace{\begin{bmatrix} V_g^+ & 0 & V_g^- \cos\psi \\ 0 & V_g^+ & -V_g^- \sin\psi \\ V_g^- \cos\psi & -V_g^- \sin\psi & V_g^+ \end{bmatrix}}_{\mathbf{X}} \underbrace{\begin{bmatrix} I_{sum}^- \cos\alpha \\ -I_{sum}^- \sin\alpha \\ I_{sum}^+ \end{bmatrix}}_{I} \tag{6.2}$$

where V_g^+ is the Root Mean Square (RMS) positive sequence voltage, V_g^- is the RMS negative sequence voltage, and ψ is the angle between the positive and the negative sequence voltage. Regarding the currents, I_{sum}^+ is the RMS positive sequence component of the additive AC current (which is chosen to be in phase with the positive sequence voltage), I_{sum}^- is the RMS

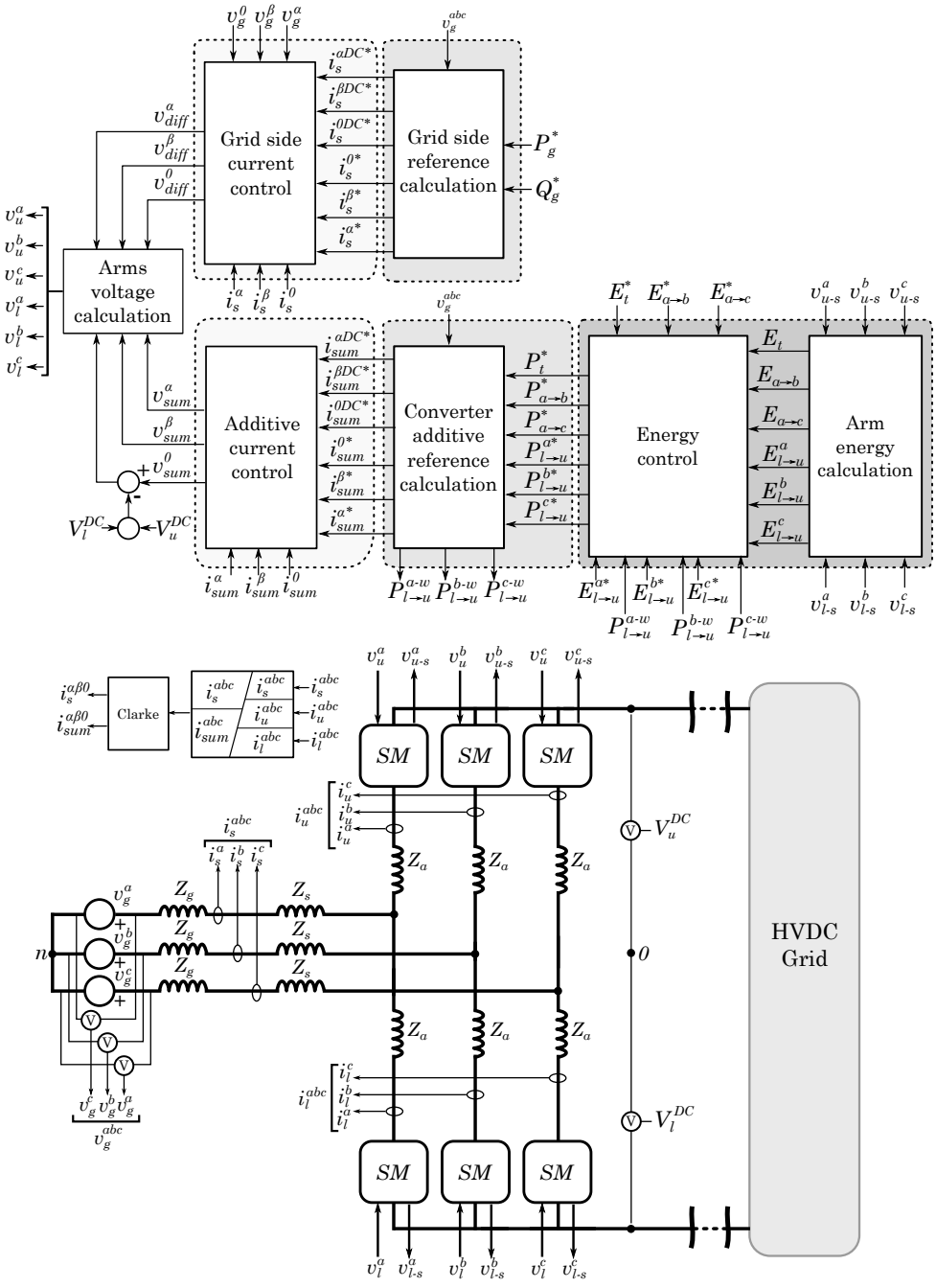

Figure 6.1: Control structure of the MMC converter

negative sequence component of the additive AC current, and α is the angle between the negative sequence current and the positive sequence voltage [78]. The power references P_1, P_2, P_3 are obtained as a combination of power exchanged between upper and lower arms of each leg (see (5.28)).

This system of equations in (6.2) can be inverted to obtain the additive AC current references as a function of the power references given by the energy controllers that maintain the energy balance between upper and lower arms (see Fig. 6.1)

$$\underbrace{\begin{bmatrix} I^-_{sum}\cos\alpha \\ -I^-_{sum}\sin\alpha \\ I^+_{sum} \end{bmatrix}}_{I} = \underbrace{\frac{1}{(V_g^+)^2-(V_g^-)^2}\cdot\begin{bmatrix} M_{11} & M_{12} & M_{13} \\ M_{21} & M_{22} & M_{23} \\ M_{31} & M_{32} & M_{33} \end{bmatrix}}_{\mathbf{M}}\underbrace{\begin{bmatrix} P_1 \\ P_2 \\ P_3 \end{bmatrix}}_{P} \tag{6.3}$$

$$M_{11} = \frac{2(V_g^+)^2 + (\cos(2\psi)-1)(V_g^-)^2}{2V_g^+} \tag{6.4}$$

$$M_{22} = \frac{2(V_g^+)^2 + (-\cos(2\psi)-1)(V_g^-)^2}{2V_g^+} \tag{6.5}$$

$$M_{12} = M_{21} = -\frac{\sin(2\psi)(V_g^-)^2}{2V_g^+}; \quad M_{33} = V_g^+ \tag{6.6}$$

$$M_{13} = M_{31} = -V_g^-\cos\psi; \quad M_{23} = M_{32} = V_g^-\sin\psi \tag{6.7}$$

As has been discussed above, the system of equations has a discontinuity when $V_g^+ = V_g^-$ (singular voltage condition), resulting in infinite current being requested when positive and negative sequence voltages are very close in magnitude. This singularity causes the additive current references to saturate, which compromises the performance of the energy-balancing controllers.

6.4 Modification of the additive current calculation technique

This section discusses three different methods that can be used to overcome the issue presented in the previous part.

Method 1 - Temporary disabling the upper to lower arms energy balance control

Unbalanced AC voltage sags do not cause sustained drift between the energy of the upper arms and the lower arms of the converter. However, stepwise deviations may be caused by transients. The normal approach to control these deviations (see (6.3)) would require a very large additive AC current under voltage imbalances close to the singular voltage condition. Thus, a possible solution is to disable the energy controller that balances the differences between the energy of the upper and the lower arms during the voltage sag. The main drawback of this method is that the energy deviation may build up during very long fault clearance times and will not be reduced until the fault is cleared, and the energy regulator is activated again.

Method 2 - Kernel-based approach

The second approach is based on the idea of avoiding the use of current that does not contribute to power exchange. Such a current can be found by studying the kernel of matrix $\mathbf{X}$ in (6.2), which loses rank under singular voltage conditions. A vector v, is said to belong to the kernel of $\mathbf{X}$ if $\mathbf{X} \cdot v = 0$. Such a vector can be easily found using classic linear algebra techniques and yields

$$v = \begin{bmatrix} \dfrac{V_g^- \cos\psi}{\sqrt{V_g^{+2} + V_g^{-2}}} & \dfrac{-V_g^- \sin\psi}{\sqrt{V_g^{+2} + V_g^{-2}}} & \dfrac{-V_g^+}{\sqrt{V_g^{+2} + V_g^{-2}}} \end{bmatrix}^T \tag{6.8}$$

The vector only belongs to the kernel $\mathbf{X}$, when $\mathbf{X}$ loses rank. This can be easily proven by multiplying v by $\mathbf{X}$

$$\mathbf{X} \cdot v = \begin{bmatrix} 0 & 0 & -\dfrac{V_g^{+2} - V_g^{-2}}{\sqrt{V_g^{+2} + V_g^{-2}}} \end{bmatrix}^T \tag{6.9}$$

where it can be observed that a vector of current v does not produce any sustained power exchange under the condition of $V_g^+ = V_g^-$. A linear transformation matrix $\mathbf{S}$ can be used to express the additive current in a new basis where the third component corresponds to the direction that does not produce power exchange under singular voltage conditions

$$\mathbf{S} = \begin{bmatrix} 1 & 0 & \frac{V_g^- \cos\psi}{\sqrt{V_g^{+2}+V_g^{-2}}} \\ 0 & 1 & \frac{-V_g^- \sin\psi}{\sqrt{V_g^{+2}+V_g^{-2}}} \\ 0 & 0 & \frac{-V_g^+}{\sqrt{V_g^{+2}+V_g^{-2}}} \end{bmatrix} \tag{6.10}$$

Applying this transformation to (6.2) leads to

$$P = \mathbf{X} \cdot I \rightarrow P = \underbrace{\mathbf{X} \cdot \mathbf{S}}_{\mathbf{X}'} \cdot \underbrace{\mathbf{S}^{-1} \cdot I}_{I'} \tag{6.11}$$

where I' is the new current vector in the new basis and $\mathbf{X}'$ is

$$\mathbf{X}' = \begin{bmatrix} V_g^+ & 0 & 0 \\ 0 & V_g^+ & 0 \\ V_g^- \cos\psi & -V_g^- \sin\psi & -\frac{V_g^{+2}-V_g^{-2}}{\sqrt{V_g^{+2}+V_g^{-2}}} \end{bmatrix} \tag{6.12}$$

When expressed in the new basis, it is clear that a singular voltage condition makes the last column of (6.12) be zero. Under such condition, it is not possible to independently control P_1, P_2 and P_3, thus a compromise solution is needed. One possible choice is to leave P_3 as a function of P_1 and P_2, under singular voltage conditions. This can be done by using the following modified inverse of matrix $\mathbf{X}'$

$$(\mathbf{X}')^{-1} = \begin{bmatrix} \frac{1}{V_g^+} & 0 & 0 \\ 0 & \frac{1}{V_g^+} & 0 \\ \beta C_1 \left(\frac{V_g^- \cos\psi}{V_g^+}\right) & -\beta C_1 \left(\frac{V_g^- \sin\psi}{V_g^+}\right) & -\beta\ C_1 \end{bmatrix} \tag{6.13}$$

where β is a controllable weighting factor and

$$C_1 \triangleq \frac{\sqrt{V_g^{+2} + V_n^{+2}}}{V_g^{+2} - V_g^{-2}} \tag{6.14}$$

The inverted matrix $(\mathbf{X}')^{-1}$ can be used under conditions where V_g^+ is significantly different than V_g^- to obtain the same solution that would be obtained from (6.3). For conditions where $V_g^+ \approx V_g^-$, β can be set to zero to avoid large current reference values caused by the singularity in C_1. Finally, the desired current vector can be obtained in the original basis by doing

$$I = \mathbf{S} \cdot (\mathbf{X}')^{-1}|_\beta \cdot P \tag{6.15}$$

The elimination of one degree of freedom of the additive current in Method 2 makes P_3 to be a function of P_1 and P_2 rather than tracking its reference value. P_3 is the sum of the power references $P^j_{l\to u}$ for the three phases in (6.2). Therefore, the controller will not be able to compensate the total deviation between upper and lower arms under singular voltage conditions until the AC network voltages are restored.

Method 3 - Pseudoinverse-based approach

The third method uses the Moore-Penrose pseudoinverse to find a different compromise solution to the incompatible system. Assuming that the third component of I' (see $\mathbf{X}'$ in (6.12)) is made to be zero when $V_g^+ = V_g^-$, the matrix $\mathbf{X}'$ can be reduced to the following 3 by 2 matrix

$$\mathbf{X}'' = \begin{bmatrix} V_g^+ & 0 \\ 0 & V_g^+ \\ V_g^- \cos\psi & -V_g^- \sin\psi \end{bmatrix} \tag{6.16}$$

The Moore-Penrose pseudoinverse can be used to find the current vector that leads to the feasible power exchange that is closest to the desired power. This idea has been extensively used in other fields such as in control of robot manipulators close to their singularities [109]. The pseudoinverse of $\mathbf{X}''$ (6.16) imposing the singular voltage condition is

$$(\mathbf{X}'')^{-1} = \begin{bmatrix} -\dfrac{\cos(2\psi) - 3}{4\,V_g^+} & \dfrac{\sin(2\psi)}{4\,V_g^+} & \dfrac{\cos\psi}{2\,V_g^+} \\ \dfrac{\sin(2\psi)}{4\,V_g^+} & \dfrac{\cos(2\psi) + 3}{4\,V_g^+} & -\dfrac{\sin\psi}{2\,V_g^+} \end{bmatrix} \tag{6.17}$$

As with Method 2, the desired current vector can be obtained by undoing the kernel transformation with

$$I = \mathbf{S} \cdot (\mathbf{X}'')^{-1} \cdot P \tag{6.18}$$

Anti-windup implementation for the reference current

The proposed methods are able to maintain the additive current references bounded during singular voltage conditions. However, when the fault is cleared and normal operating conditions are recovered, integral windup problems may appear in the energy regulators that control the difference between the energy of the upper and the lower arms $E^{j}_{l\to u}$. These problems are caused by the mismatch between the power set-points of the energy controllers $P^{j*}_{l\to u}$, and the actual power exchange.

To overcome this problem, an anti-windup structure controlling the integral terms of the energy regulators must be implemented. This structure calculates the difference between the power reference given by the energy regulators $P^{j*}_{l\to u}$, and the actual achievable power exchange recalculated from the chosen current references. The error $P^{j-w}_{l\to u}$ is then subtracted to the input of the integrators to keep them from increasing indefinitely.

6.5 Analysis of the different types of voltages sags

In this section, a detailed analysis of the specific voltage sags that can cause the singular voltage condition ($V_g^+ = V_g^-$) is performed. Table 6.1 shows a classification of the different types of voltage sags [106]. Note that while type A is a symmetrical voltage sag, the other types correspond to unbalanced cases. Two variables are used to describe the three-phase voltages during the sag: the pre-fault voltage E_1, and the voltage in the faulted phase (or between faulted phases) V.

The analysis procedure consists of applying the Fortescue transformation [96] to the voltage equations for each type of voltage sag. The Fortescue transformation $\underline{\Theta}^{+-0}$ of a phasor vector $\underline{\Theta}^{abc}$ is defined as

$$\underline{\Theta}^{+-0} \triangleq \mathbf{F}\cdot\underline{\Theta}^{abc} = \frac{1}{3}\begin{bmatrix}1 & \underline{p}^2 & \underline{p}\\ 1 & \underline{p} & \underline{p}^2\\ 1 & 1 & 1\end{bmatrix}\cdot\underline{\Theta}^{abc} \tag{6.19}$$

with $\underline{p} = e^{j\frac{-2\pi}{3}}$. Then, the positive $\underline{V}_g^+$ and negative $\underline{V}_g^-$ sequence phasors are made to be equal in magnitude in order to find the fault states V that cause this condition. An example of this procedure is shown next for a voltage sag of type C.

Table 6.1: General classification of voltage sags

Type	Voltages	Phasors *abc*
A	$\underline{V}_g^a = V$ $\underline{V}_g^b = -\frac{1}{2}V - \frac{1}{2}jV\sqrt{3}$ $\underline{V}_g^c = -\frac{1}{2}V + \frac{1}{2}jV\sqrt{3}$	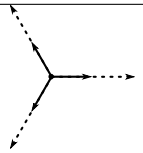
B	$\underline{V}_g^a = V$ $\underline{V}_g^b = -\frac{1}{2}E_1 - \frac{1}{2}jE_1\sqrt{3}$ $\underline{V}^c = -\frac{1}{2}E_1 + \frac{1}{2}jE_1\sqrt{3}$	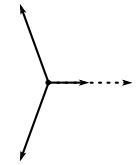
C	$\underline{V}_g^a = E_1$ $\underline{V}_g^b = -\frac{1}{2}E_1 - \frac{1}{2}jV\sqrt{3}$ $\underline{V}_g^c = -\frac{1}{2}E_1 + \frac{1}{2}jV\sqrt{3}$	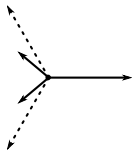
D	$\underline{V}_g^a = V$ $\underline{V}_g^b = -\frac{1}{2}V - \frac{1}{2}jE_1\sqrt{3}$ $\underline{V}_g^c = -\frac{1}{2}V + \frac{1}{2}jE_1\sqrt{3}$	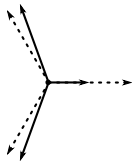
E	$\underline{V}_g^a = E_1$ $\underline{V}_g^b = -\frac{1}{2}V - \frac{1}{2}jV\sqrt{3}$ $\underline{V}_g^c = -\frac{1}{2}V + \frac{1}{2}jV\sqrt{3}$	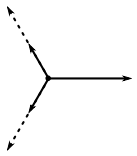
F	$\underline{V}_g^a = V$ $\underline{V}_g^b = -\frac{1}{2}V - \left(\frac{1}{3}E_1 + \frac{1}{6}V\right)j\sqrt{3}$ $\underline{V}_g^c = -\frac{1}{2}V + \left(\frac{1}{3}E_1 + \frac{1}{6}V\right)j\sqrt{3}$	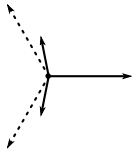
G	$\underline{V}_g^a = \frac{2}{3}E_1 + \frac{1}{3}V$ $\underline{V}_g^b = -\frac{1}{3}E_1 - \frac{1}{6}V - \frac{1}{2}jV\sqrt{3}$ $\underline{V}_g^c = -\frac{1}{3}E_1 - \frac{1}{6}V + \frac{1}{2}jV\sqrt{3}$	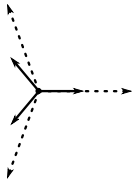

6.5.1 Analysis of voltage sag type C

The equations for the voltage sag type C are

$$\underline{V}_g^{abc} = \begin{bmatrix} E_1 \\ -\frac{1}{2}E_1 - \frac{1}{2}jV\sqrt{3} \\ -\frac{1}{2}E_1 + \frac{1}{2}jV\sqrt{3} \end{bmatrix} \tag{6.20}$$

Applying the Fortescue transformation to (6.20) gives

$$\underline{V}_g^{+-0} = \mathbf{F} \cdot \underline{V}_g^{abc} = \begin{bmatrix} \frac{1}{2}E_1 + \frac{1}{2}V \\ \frac{1}{2}E_1 - \frac{1}{2}V \\ 0 \end{bmatrix} \tag{6.21}$$

Solving for the case when $|\underline{V}^+| = |\underline{V}^-|$ yields

$$\left|\frac{1}{2}E_1 + \frac{1}{2}V\right| = \left|\frac{1}{2}E_1 - \frac{1}{2}V\right| \tag{6.22}$$

Assuming that E_1 and V are positive, this equation implies that $V = 0$. Therefore, the voltage in *abc* variables is of the form

$$\underline{V}_g^{abc} = \mathbf{F}^{-1} \cdot \underline{V}_g^{+-0}|_{V=0} = \begin{bmatrix} E_1 \\ -\frac{1}{2}E_1 \\ -\frac{1}{2}E_1 \end{bmatrix} \tag{6.23}$$

Following an analogous procedure for the other types of voltage sags, the results shown in Table 6.2 are obtained. Note that voltage sags type A[2] and B cannot produce a singular voltage condition while types C, D, E, F and G can.

[2]For type A, the singular voltage condition appears when a short-circuit at the output of the converter is produced. Under such condition it is not possible to exchange any power.

Table 6.2: Voltage sags with singular voltage condition

Type	Voltages *abc*	Voltages $+-0$	Phasors *abc*
A	$\underline{V}_g^a = 0$ $\underline{V}_g^b = 0$ $\underline{V}_g^c = 0$	$\underline{V}_g^+ = 0$ $\underline{V}_g^- = 0$ $\underline{V}_g^0 = 0$	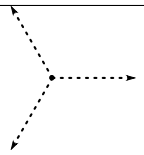
B	-	-	-
C	$\underline{V}_g^a = E_1$ $\underline{V}_g^b = -\frac{1}{2}E_1$ $\underline{V}_g^c = -\frac{1}{2}E_1$	$\underline{V}_g^+ = \frac{1}{2}E_1$ $\underline{V}_g^- = \frac{1}{2}E_1$ $\underline{V}_g^0 = 0$	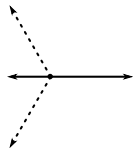
D	$\underline{V}_g^a = 0$ $\underline{V}_g^b = -\frac{1}{2}jE_1\sqrt{3}$ $\underline{V}_g^c = +\frac{1}{2}jE_1\sqrt{3}$	$\underline{V}_g^+ = \frac{1}{2}E_1$ $\underline{V}_g^- = -\frac{1}{2}E_1$ $\underline{V}_g^0 = 0$	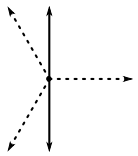
E	$\underline{V}_g^a = E_1$ $\underline{V}_g^b = 0$ $\underline{V}_g^c = 0$	$\underline{V}_g^+ = \frac{1}{3}E_1$ $\underline{V}_g^- = \frac{1}{3}E_1$ $\underline{V}_g^0 = \frac{1}{3}E_1$	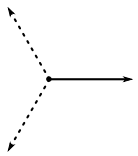
F	$\underline{V}_g^a = 0$ $\underline{V}_g^b = j\frac{\sqrt{3}}{3}E_1$ $\underline{V}_g^c = j\frac{\sqrt{3}}{3}E_1$	$\underline{V}_g^+ = \frac{1}{3}E_1$ $\underline{V}_g^- = -\frac{1}{3}E_1$ $\underline{V}_g^0 = 0$	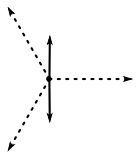
G	$\underline{V}_g^a = \frac{2}{3}E_1$ $\underline{V}_g^b = -\frac{1}{3}E_1$ $\underline{V}_g^c = -\frac{1}{3}E_1$	$\underline{V}_g^+ = \frac{1}{3}E_1$ $\underline{V}_g^- = \frac{1}{3}E_1$ $\underline{V}_g^0 = 0$	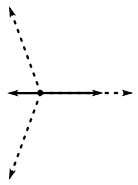

6.6 Case study

In this section, various simulations are carried out in Matlab Simulink® to study the behavior of the proposed methods under the voltage conditions described in Table 6.2. The model presented in Section 5.5 is also used in this chapter to validate the developed methodologies. First, the results for the methodologies proposed are analyzed in detail for the voltage sag type C. Then, simulations are carried out for the rest of the voltage sag types focusing on the impact of each methodology in the converter energy. The system parameters used for this study are detailed in Table 5.2.

6.6.1 Simulation model description

The simulation model is based on the accelerated model proposed in [103]. It allows access to each individual SM voltage providing enough accuracy compared to a fully-detailed model [104]. Each sub-module is represented by its equivalent capacitor that is charged and discharged depending on its insertion state. The modulation implemented is the Nearest Level Control (NLC) technique [105], which calculates the number of active sub-modules in each arm and uses a reduced switching strategy to increase the efficiency of the converter.

6.6.2 Simulation results - Case C

In this section, the behavior of the converter during a type C voltage sag with singular voltage condition is simulated. Four scenarios are considered: the first one is based on not taking any special precaution to handle the sag (Method 0) and is shown in Fig. 6.2. The second one, based on Method 1 (disconnecting the energy-balancing controller), is shown in Fig. 6.3. Method 2 (the Kernel-based approach) is shown in Fig. 6.4. Finally, Method 3 (the Pseudoinverse-based approach) can be seen in Fig. 6.5. A comparison between the four simulations is also shown in Fig. 6.6. The comparison is done in terms of the evolution of the average energy difference between the upper and the lower arms of the converter during the fault, which is where the main differences between the aforementioned methods become apparent.

The simulated voltage sag starts at time 3 s and the voltage is fully restored at time 5 s. Although in a real network a deep and highly unbalanced voltage sag condition would be sustained for less than 250 ms [107], in this case, the sag has been extended for 2 s, to highlight the differences between

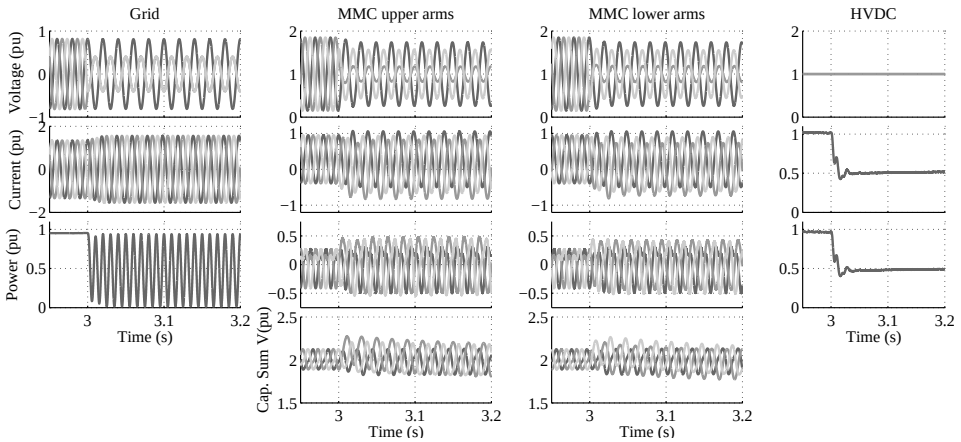

Figure 6.2: Simulation results of the MMC operation. Voltage sag type C. Method 0 - Conventional control.

the different methods compared.

Fig. 6.2 shows the converter behavior during the first milliseconds after the fault when Method 0 is used. Although most variables appear to be stable during the first few cycles, a drift of the arm energies occurs and leads to the need to disconnect the converter around 1 s after the inception of the fault as shown in Fig. 6.6a. In the simulation, the disconnection is triggered when there is a sustained deviation of the average arm energy of more than 5%. The drift is caused by the saturation of the current references due to the singularity in the calculation of the additive AC current, which compromises the effectiveness of the energy regulators.

Fig. 6.3 shows the behavior of the converter when Method 1 is used. During the fault, the converter remains stable even though the transient causes a deviation of the energy balance between upper and lower arms that is not corrected (see Fig. 6.6b). When the fault is cleared, the energy deviation will remain unless the balance controller is enabled again (see Fig. 6.3b and Fig. 6.6b.

The response can be improved by using Method 2, shown in Fig. 6.4. With this method, a singular voltage condition does not cause the current references to saturate. Therefore, even though the deviation between upper and lower arms of the converter caused by the transient is not corrected during the voltage imbalance, the remaining energy-balancing controls remain functional leading to a lower energy deviation (see Fig. 6.6c). It is worth noting that with this method the average energy imbalance between upper

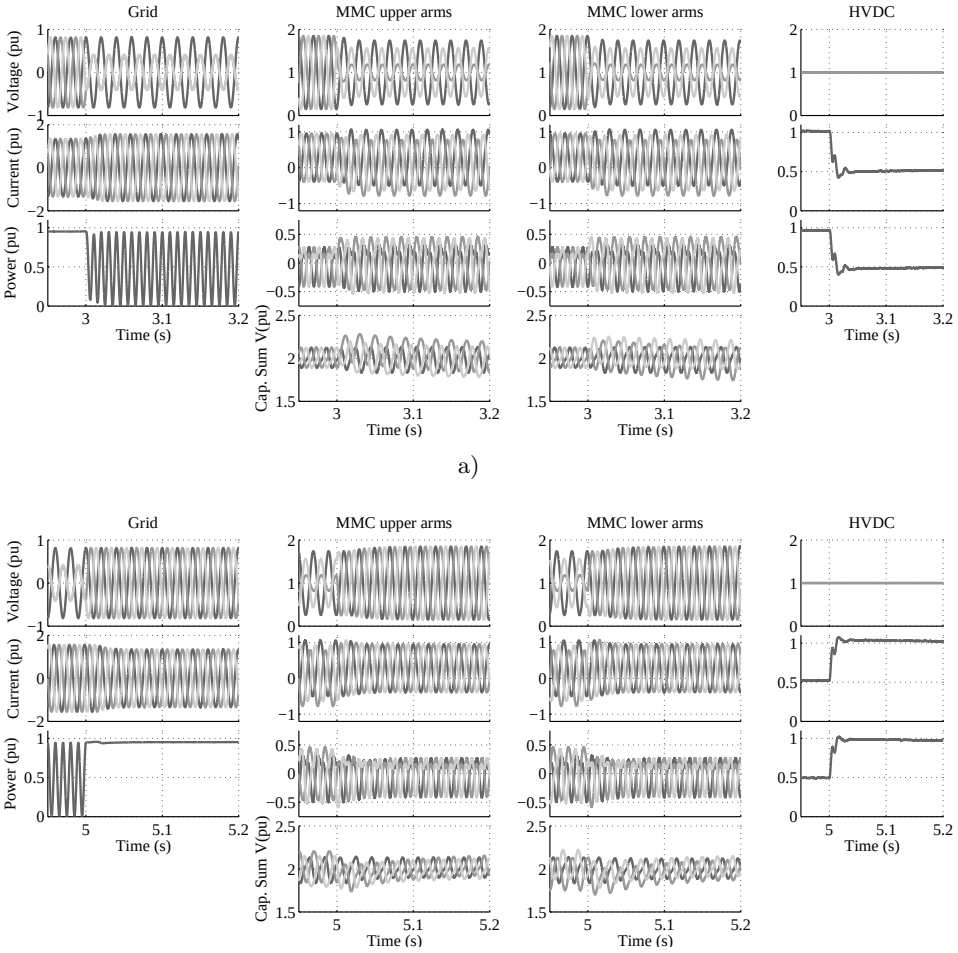

Figure 6.3: Simulation results of the MMC operation. Voltage sag type C. Method 1 - Energy balancing disconnection.

and lower arms during the fault is the same in each of the three legs of the converter. This is an inherent property of Method 2, which loses control over the total balance between upper and lower arms only. Also, unlike Method 1, the energy balance is fully recovered upon restoration of the network AC voltage (see Fig. 6.4b and Fig. 6.6c).

Finally, Fig. 6.5 shows the results for the last proposed solution, Method 3. The benefit of Method 3 when compared to Method 2 is that rather than dismissing P_3, it chooses the additive AC current reference that produces the closest feasible power to that requested by the energy-balancing controls, which results in the lowest deviation of the energy balance (even though this may not be symmetrical when comparing the three legs of the converter), as shown in Fig. 6.6d.

6.6.3 Simulation results - Other cases

Next, a series of simulations are performed for voltage sags type D, E, F and G with singular voltage condition. The purpose of these tests is to confirm that the conclusions obtained for a type C voltage sag can also be extended to all other sag types. The results are focused on the evolution of the average energy balance between the upper and the lower arms and are shown in Fig. 6.7 for type D, Fig. 6.8 for type E, Fig. 6.9 for type F and Fig. 6.10 for type G.

The simulations confirm that Method 0 results in a sustained energy drift that eventually leads to the disconnection of the converter. By contrast, Methods 1, 2 and 3 keep the energy balance stable. Method 1 results in a greater deviation of the energy and must be disabled upon recovery of normal voltage conditions, while Methods 2 and 3 present a natural transition between fault and normal operating conditions and result in lower energy deviation. Method 2 produces the same imbalance between the energy of the upper and the lower arms in all three legs of the converter while Method 3 results in an asymmetrical imbalance with lower total deviation.

6.7 Conclusions

Unbalanced voltage sags with singular voltage condition pose a challenge for the regulation of the energy balance between the upper and the lower arms of the converter. The analysis presented in this section has shown how this specific condition may cause a singularity in the conventional current reference calculation. This singularity causes the current references to saturate,

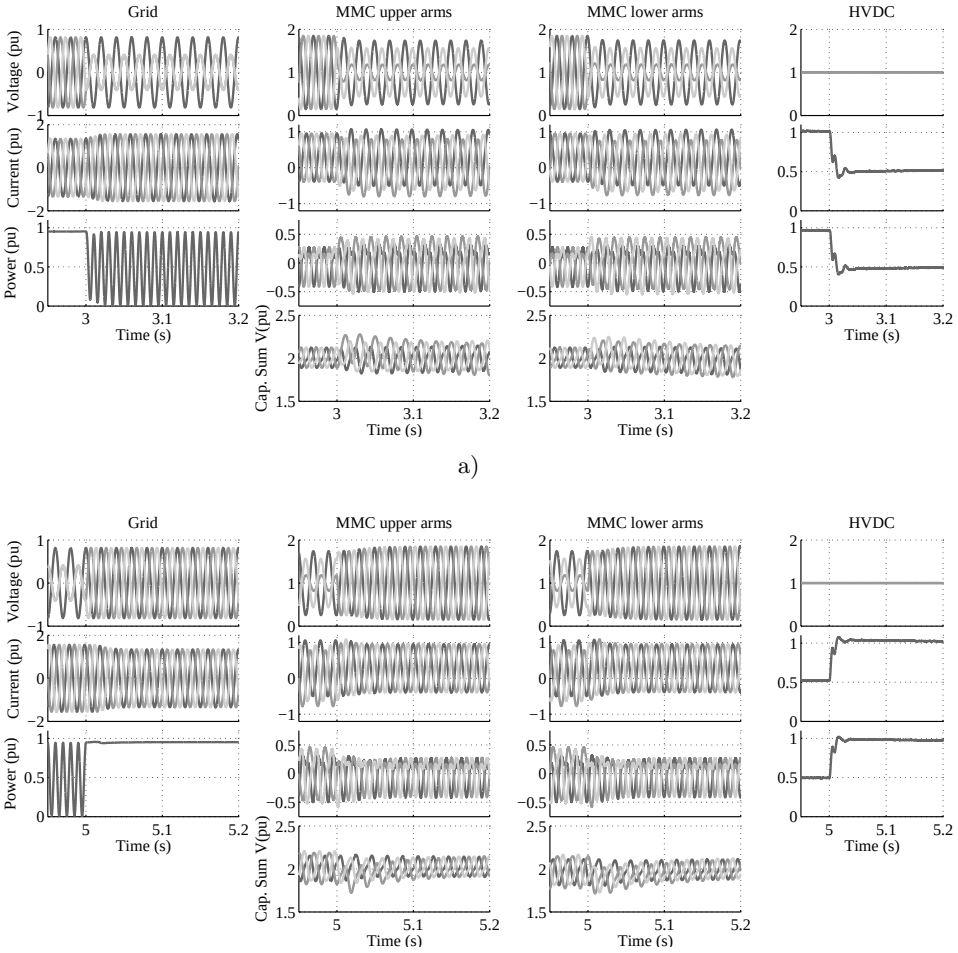

Figure 6.4: Simulation results of the MMC operation. Voltage sag type C. Method 2 - Kernel-based approach.

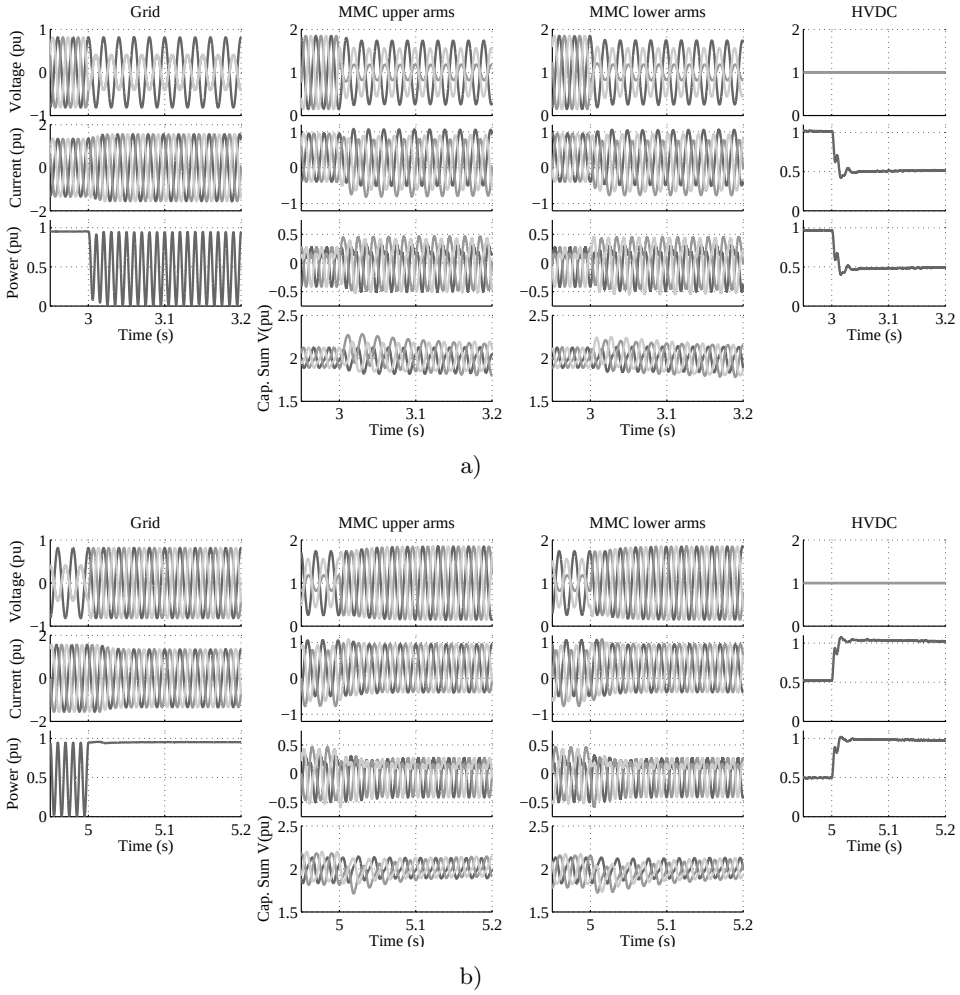

Figure 6.5: Simulation results of the MMC operation. Voltage sag type C. Method 3 - Pseudoinverse-based approach.

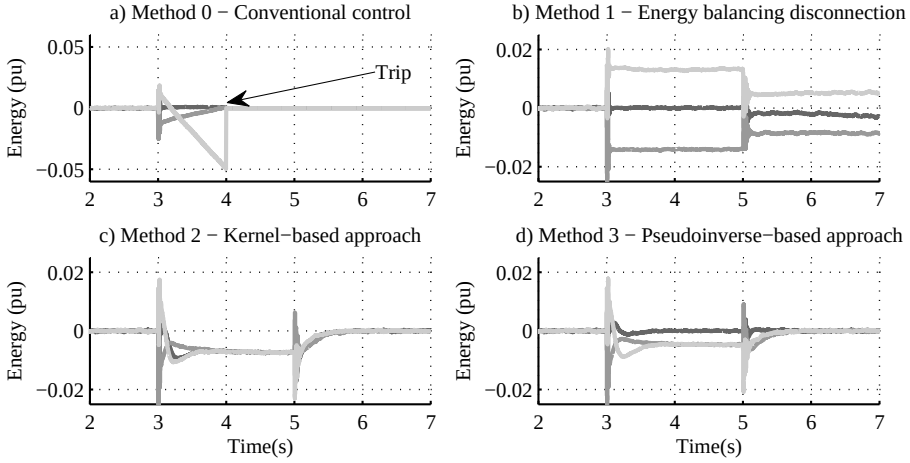

Figure 6.6: Average energy comparison between the proposed methods. Voltage sag type C.

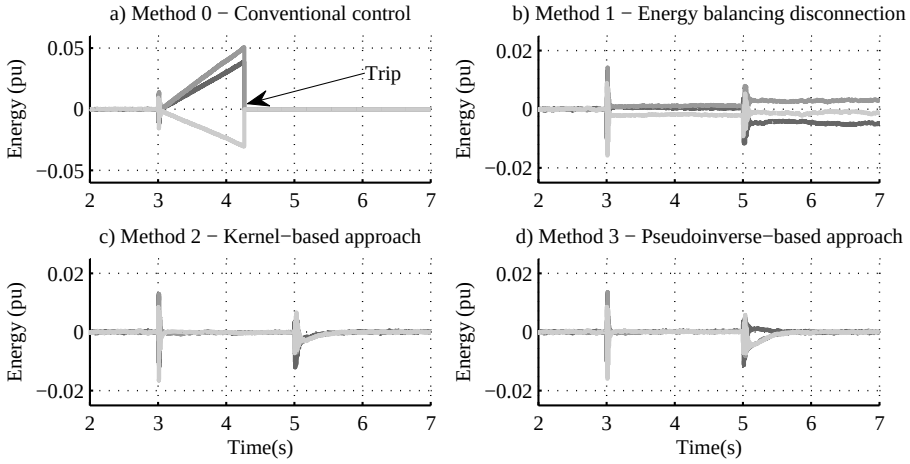

Figure 6.7: Average energy comparison between the proposed methods. Voltage sag type D.

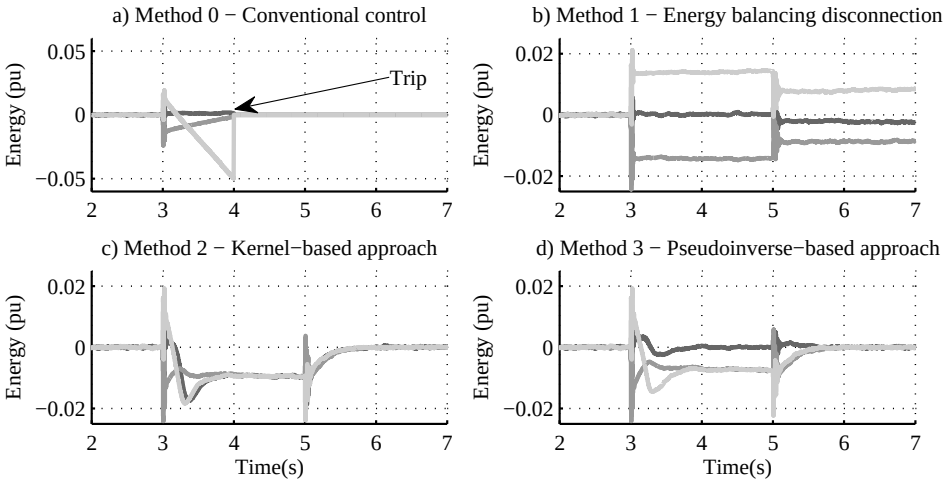

Figure 6.8: Average energy comparison between the proposed methods. Voltage sag type E.

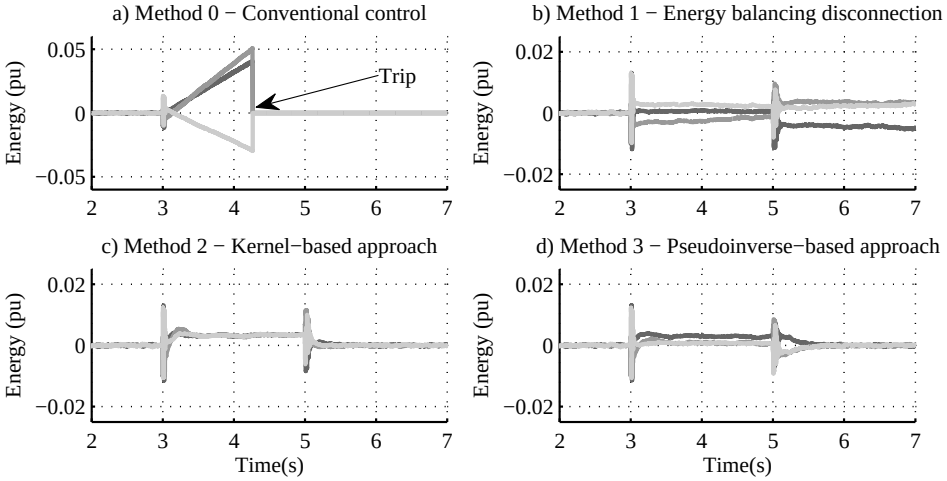

Figure 6.9: Average energy comparison between the proposed methods. Voltage sag type F.

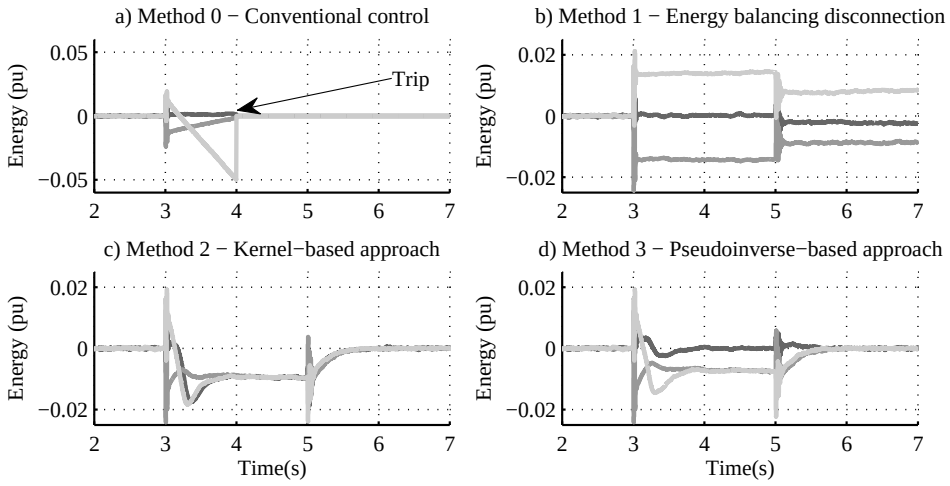

Figure 6.10: Average energy comparison between the proposed methods. Voltage sag type G.

which compromises the performance of the energy-balancing controllers.

In order to overcome this issue, one option is to disable the energy-balancing controller during the fault, which makes the system stable but results in greater energy deviation. Alternatively, two new calculation methods have been presented which improve the deviation of the energy during the fault and naturally regain normal operation once the fault is cleared. The basis of the aforementioned methods have been discussed in detail and their benefits have been validated in a simulation model under all possible AC fault scenarios that produce the singular voltage condition.

Chapter 7

Methodology for droop control dynamic analysis of multi-terminal VSC-HVDC grids for offshore wind

7.1 Introduction

In the near future, there will be a large amount of offshore wind farms connected to the mainland grid via Voltage Source Converter High Voltage Direct Current (VSC-HVDC) transmission links. Then, it seems reasonable to devise offshore VSC-HVDC grids interfacing a number of such different terminals with different AC grids, resulting in the so-called multi-terminal VSC-HVDC system. Multi-terminal VSC-HVDC stands as an interesting solution to efficiently connect a number of offshore wind farms, but also implies several technical challenges that will have to be addressed, including control [31], operation [25] and protection issues [24].

The stability of Alternating Current (AC) power systems has been widely discussed in the literature, see for example [110, 111]. These studies also include HVDC systems and their possible contribution to improve AC system stability. Some DC grid management strategies based on coordinated closed loop DC voltage control and DC droop characteristics were proposed and simulated in [112]. Also, the modeling and simulation of multi-terminal VSC-HVDC transmissions for offshore wind power were studied in [31]. This chapter analyzes the stability and the dynamic behavior of multi-terminal HVDC grids for offshore wind farm applications. A design methodology of a current-based DC voltage droop control for a generic multi-terminal VSC-HVDC grid based on a multivariable frequency response analysis is introduced, considering both the DC grid dynamics and the system operational limitations.

The chapter is organized as follows. The next section provides a brief discussion of the control of VSC-HVDC multi-terminal networks. Section 7.3

presents the main contribution, a modeling procedure for complex VSC-HVDC multi-terminal systems and a methodology for the selection of the droop constant. The application of the proposed procedure is illustrated in the case of a four-terminal grid in Section 7.4. Finally, in Section 7.5, some conclusion remarks are drawn.

7.2 Multi-terminal grid control

Fig. 7.1 illustrates a multi-terminal HVDC network. It consists of the DC grid, the main AC grid (or AC grids), the wind farm grids, the Wind Farm Converters (WFCs) and the AC Grid Side Converters (GSCs). The multi-terminal HVDC network permits the transfer of power among the different units, where the WFCs act as power sources and the GSCs as loads. In this power transmission scheme, the sources inject all the available power into the grid whereas the control of the GSCs seeks to maintain the DC voltage. This also includes the power sharing among the different GSCs. The normal operation may be altered when some of the converters reach the current limits, which usually occurs during severe voltage faults in the AC grid. Under these circumstances, in this study it is considered that the WFCs enter in voltage regulation mode and the GSCs extract the maximum possible power without regulating the DC voltage. In both operation modes, some converters seek to maintain the DC voltage and the others inject or extract power without controlling the voltage [25].

To regulate the DC voltage, the so-called droop control is employed, which is a technique that allows power distribution among different terminals without communications. The control of each converter is usually implemented in two levels, an inner loop controlling the currents and an outer loop regulating the DC voltage. The droop control acts on the outer loop imposing a current reference I^* to the inner loop. The current, and thus the power, in the converter is directly governed by the current control in accordance with the reference imposed by the voltage loop. This control scheme is shown in Fig. 7.2. The control law is given by the following expression

$$I^* = K(E - E^*) \tag{7.1}$$

where E is the DC voltage, E^* is DC voltage reference and K is the droop gain. For the present study, the dynamics of current loop can be considered much faster than the outer loop. Therefore, the DC current I flowing through the converter will be assumed to be equal to the reference I^*.

The selection of the gain K for each converter must be done taking into

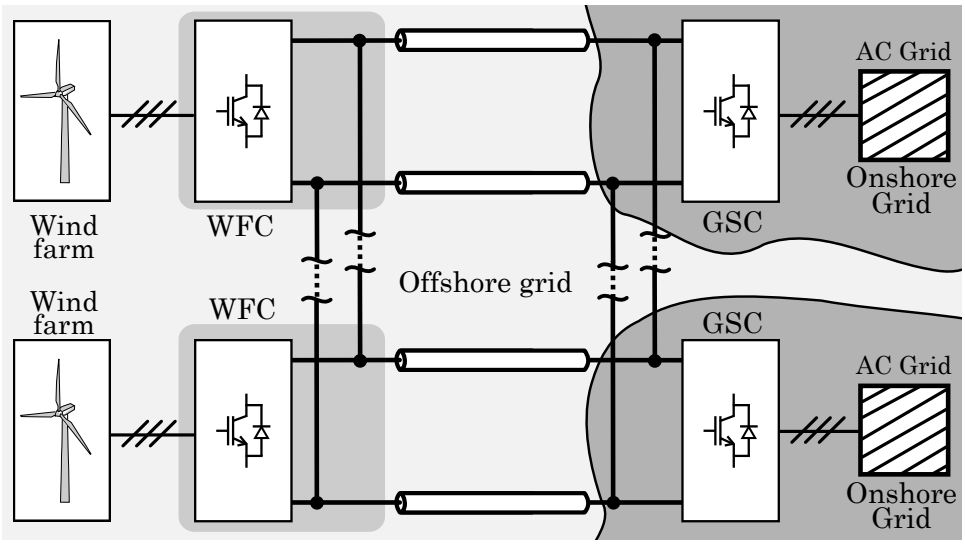

Figure 7.1: HVDC multi-terminal network

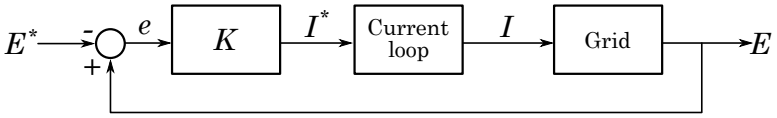

Figure 7.2: Droop control scheme of a VSC

account the entire multi-terminal behavior. In addition to the static consideration associated to the distribution of the power sources and sinks, each local controller can affect the global stability and the DC voltage in other terminals. For these reasons, the droop constant selection must be addressed in the context of the multivariable system theory.

7.3 Frequency response analysis for droop gain selection

In this section, a methodology for the droop constant selection based on multivariable frequency response analysis is presented. Before presenting this methodology, a systematic procedure to obtain a linear representation of complex multi-terminal HVDC networks is introduced.

7.3.1 Multi-terminal HVDC networks modelling

From the viewpoint of a DC grid analysis, the multi-terminal can be represented as the interconnection of nodes and branches. An example of this representation is shown in Fig. 7.3. The WFCs injecting power into the grid are the power input nodes and the GSCs extracting power from the grid are the power output nodes. The cables interconnecting the nodes are the branches. There are also nodes where only cables converge; those ones are called intermediate nodes. The general multi-terminal setup depicted in Fig. 7.3 consists of m power input nodes, n power output nodes, p intermediate connection nodes and r branches. This last number depends on the particular interconnection pattern. Next, the modeling of each type of nodes is explained briefly.

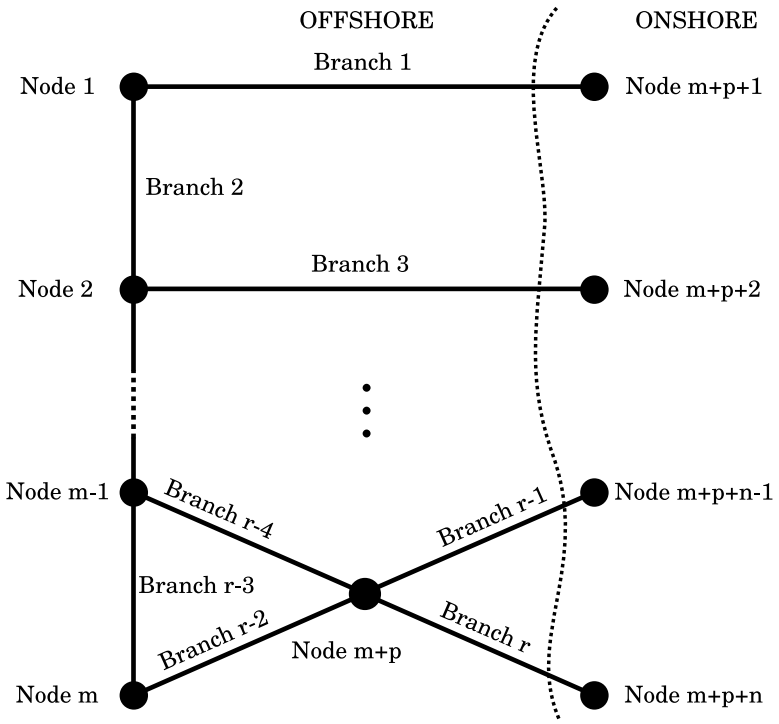

Figure 7.3: A node and branch scheme of a multi-terminal HVDC grid

Input and output power nodes

The wind farms and AC systems are connected to the HVDC grid through VSC-HVDC power converters. For the present analysis, it is sufficient to consider the average dynamic behavior. In this situation, the AC side of the converters is modeled as three voltage sources and the DC side as a current source and a capacitor [113]. Using this simplified representation, each wind farm and each AC system are modeled as DC current sources, as illustrated in Fig. 7.4. At the converter DC side, the power flow in the node k is represented by a current I_k

$$I_k = \frac{P_k}{E_k} \tag{7.2}$$

where P_k is the incoming power and E_k is the DC voltage at the node k. It will be assumed that the voltage E_k remains close to the nominal values E^*. Under this assumption, the current I_k can be assumed proportional to the power P_k.

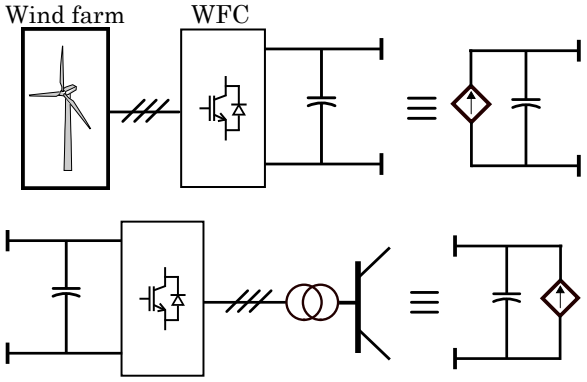

Figure 7.4: Equivalent representation of the wind farm and the AC grid converters for a DC grid analysis

Branches

The cables between nodes are modeled by π-equivalent circuits (see Fig. 7.5). When these circuits converge to input or output nodes and to other π-circuits, there are several capacitors in parallel. In these circumstances, and with the aim of keeping the number of variables as few as possible, the total

capacitances can be reduced to an equivalent one given by

$$C_k = \sum_{i=1}^{l} C_i \tag{7.3}$$

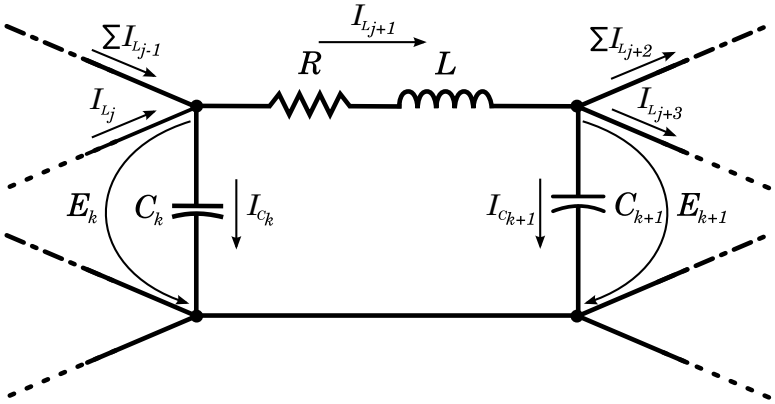

Figure 7.5: π-circuit modeling a branch element

Intermediate nodes

The cables in the DC grid may join two or more terminals at intermediate points. These nodes, an example of which is marked with $m + p$ in Fig. 7.3 will be denoted as intermediate nodes. Again, the number of capacitances can be reduced by replacing the capacitances of the π-equivalent circuits and the input and output nodes by total capacitances given by (7.3).

An equivalent circuit can be obtained from the interconnection of the nodes and branches after the simplifications above-mentioned. Then, using circuits laws and after some variable manipulations, it is possible to find a set of first order differential equations describing the dynamic behavior of the entire multi-terminal HVDC grid. These differential equations are known as the state-space representation and can be expressed in the following compact form

$$\frac{dx}{dt} = \mathbf{A}x + \mathbf{B_w}w + \mathbf{B_u}u \tag{7.4}$$

$$z = \mathbf{C_z}x \tag{7.5}$$

$$y = \mathbf{C_y}x \tag{7.6}$$

where x is the state vector, w and u are the inputs, z and y are the outputs, and $\mathbf{A}$, $\mathbf{B_w}$, $\mathbf{B_u}$, $\mathbf{C_z}$ and $\mathbf{C_y}$ are matrices of suitable dimensions. These matrices are obtained after arranging the variables and applying matrix computation laws.

The state vector x consists of internal variables that characterize the entire state of the system. In electrical systems, the currents in the inductors and the voltages in the capacitors are commonly selected as states. Therefore, in the case of the multi-terminal HVDC network in Fig. 7.3, the state vector is given by

$$x = [E_1, \cdots, E_{m+p+n}, I_{L_1}, \cdots, I_{L_r}]^T \tag{7.7}$$

Each node has one capacitor and each branch one inductor, therefore the total number of states is $n + p + m + r$.

The inputs are divided into two vectors, the vector u gathers the variables that can be used to control the system and w are disturbances, namely, external variables that are not possible to manipulate. In the case of the multi-terminal HVDC networks, the inputs of the system are the current injected or extracted by the converters, therefore

$$w = [I_1, \ldots, I_j, \ldots, I_{n_{\mathrm{nc}}}]^T \quad j \in \mathcal{J}_{\mathrm{nc}} \tag{7.8}$$

$$u = [I_1, \ldots, I_j, \ldots, I_{n_{\mathrm{c}}}]^T \quad j \in \mathcal{J}_{\mathrm{c}} \tag{7.9}$$

where $\mathcal{J}_{\mathrm{nc}}$ corresponds to the set of indexes of the nodes where the converters inject or extract power without voltage control and $\mathcal{J}_{\mathrm{c}}$ denotes the set of indexes of the nodes where the droop control is applied. Notice that the relation $n_{\mathrm{c}} + n_{\mathrm{nc}} = m + n$ must be held.

Similarly, the output is partitioned into two vectors. The vector y contains the variables that can be used in the control of the DC voltage. On the other hand, z stands for the vector of variables that are not available to be used by the controller. In the multi-terminal HVDC scheme, the controllers can only use the information provided by the voltage at the nodes where droop control is applied. The rest of the voltages must also be maintained close to the rated values but they cannot be fed back to the controllers. Hence,

$$z = [E_1, \ldots, E_j, \ldots, E_{n_{\mathrm{nc}}}]^T \quad j \in \mathcal{J}_{\mathrm{nc}} \tag{7.10}$$

$$y = [E_1, \ldots, E_j, \ldots, E_{n_{\mathrm{c}}}]^T \quad j \in \mathcal{J}_{\mathrm{c}} \tag{7.11}$$

The transfer function matrix of the system

$$\mathbf{G}(s) = \begin{bmatrix} \mathbf{G_{zw}}(s) & \mathbf{G_{zu}}(s) \\ \mathbf{G_{yw}}(s) & \mathbf{G_{yu}}(s) \end{bmatrix} \tag{7.12}$$

is obtained from the state-space equation (7.4), where

$$\mathbf{G_{zw}}(s) = \mathbf{C_z} \left[s\mathbf{I} - \mathbf{A} \right]^{-1} \mathbf{B_w} \tag{7.13}$$

$$\mathbf{G_{zu}}(s) = \mathbf{C_z} \left[s\mathbf{I} - \mathbf{A} \right]^{-1} \mathbf{B_u} \tag{7.14}$$

$$\mathbf{G_{yw}}(s) = \mathbf{C_y} \left[s\mathbf{I} - \mathbf{A} \right]^{-1} \mathbf{B_w} \tag{7.15}$$

$$\mathbf{G_{yu}}(s) = \mathbf{C_y} \left[s\mathbf{I} - \mathbf{A} \right]^{-1} \mathbf{B_u} \tag{7.16}$$

The transfer function matrices $\mathbf{G_{zu}}(s)$ and $\mathbf{G_{yu}}(s)$ relate the currents imposed by the controller with the controlled and non directly controlled voltages, respectively. On the other hand, the transfer function matrices $\mathbf{G_{zw}}(s)$ and $\mathbf{G_{yw}}(s)$ connect the current not used in the control with the controlled and non directly controlled voltages, respectively.

7.3.2 Droop gain selection

In a multi-terminal scheme, the distance between converters is usually large and the communications are not reliable enough to be used in the DC voltage control. As a consequence, each controller must compute the control variables from the information provided by the voltage at its own node. In matrix terms, the multivariable controller has an expression of the form

$$\mathbf{K} = \begin{bmatrix} K_g \cdot q_1 & & 0 \\ & \ddots & \\ 0 & & K_g \cdot q_{n_c} \end{bmatrix} = K_g \begin{bmatrix} q_1 & & 0 \\ & \ddots & \\ 0 & & q_{n_c} \end{bmatrix} \tag{7.17}$$

where K_g is a scalar parameter to be determined and q_j are the n_c constants obtained from a steady-state study [112]. These constants are associated with the resistance values of the line and the amount of power incoming or outgoing from each terminal. These constants are positive in the case of power output nodes and negative in the case of power input nodes.

The droop control scheme is depicted in Fig. 7.6. It can be observed that only the variable y is fed back into the controller $\mathbf{K}$. The objective of the droop control is to maintain the DC voltage within desired limits when the system is disturbed by the varying currents of the nodes without voltage control. The control input also must be kept under the limits imposed by

the maximum currents in the converters. Therefore, the selection of the gain K_g must take into account these performance specifications besides guaranteeing closed loop stability. From Fig. 7.6, it is easy to prove that the variables of interest are given by the following expressions

$$e(s) = y(s) - E^*(s) = \begin{bmatrix}\mathbf{S}(s)\mathbf{G_{yw}}(s) & -\mathbf{S}(s)\end{bmatrix} v(s) \tag{7.18}$$

$$z(s) = [(\mathbf{G_{zw}}(s) + \mathbf{G_{zu}}(s)\mathbf{K}\mathbf{S}(s)\mathbf{G_{yw}}(s)) \\ -\mathbf{G_{zu}}(s)\mathbf{K}\mathbf{S}(s)]\, v(s) \tag{7.19}$$

$$u(s) = \begin{bmatrix}\mathbf{K}\mathbf{S}(s)\mathbf{G}_{yw}(s) & -\mathbf{K}\mathbf{S}(s)\end{bmatrix} v(s) \tag{7.20}$$

where $v(s) = [w(s)\ E^*(s)]^T$, $\mathbf{S}(s) = [\mathbf{I_{n_c}} - \mathbf{G_{yu}}(s)\mathbf{K}]^{-1}$ is the sensitivity transfer function matrix with $\mathbf{I_{n_c}}$ the identity matrix of dimension $n_c \times n_c$.

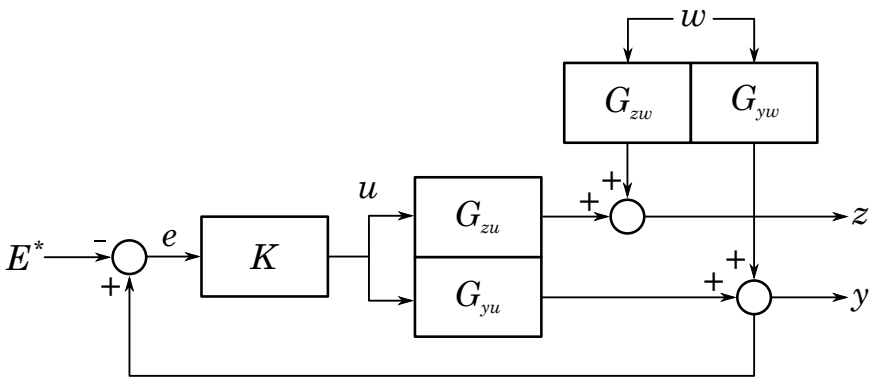

Figure 7.6: Droop control scheme in a multi-terminal grid

The effect of the gain K_g on stability can be analyzed by computing the eigenvalues of the closed loop matrix $\mathbf{A}_{\text{cl}}$. Replacing $u = \mathbf{K}(y - E^*)$ in the state-space equations (7.4), the closed loop matrix is given by $\mathbf{A}_{\text{cl}} = \mathbf{A} + K_g\mathbf{B_u}\mathbf{C_y}$. Then, for closed loop stability, the gain K_g must ensure that all eigenvalues of $\mathbf{A}_{\text{cl}}$ have negative real part. A simple power analysis reveals that the closed loop system is stable for any $K_g > 0$. In fact, since the control law makes the current I_k (with $k \in \mathcal{J}_c$) proportional to the voltage E_k at the same node, the gain $K_g q_k$ can be interpreted as a passive admittance. That is, the droop control is similar to add energy dissipation to the system and therefore the closed loop system will be always stable for $K_g > 0$.

The relation between the gain K_g and the performance objectives can be analyzed with the help of the frequency response of the system. This analysis consists in evaluating the transfer function in $s = j\omega$ and analyzing

the singular values of the resultant complex matrix functions of $j\omega$. The singular values of the frequency response of $\mathbf{G}(\mathbf{s})$ are denoted as

$$\sigma_i(\mathbf{G}(j\omega)) = \sqrt{\lambda_i(\mathbf{G}(j\omega)^T\mathbf{G}(j\omega))} \tag{7.21}$$

where $\lambda_i(\cdot)$ denotes the i-th eigenvalue of the matrix. The singular values provide information about how a vector of sinusoidal signals of frequency ω is altered by the system. In multi-input multi-output linear systems, a vector of sinusoidal signals suffers not only a change in its magnitude and phase, but also a change in its direction. The maximum amplification that the vector can experience is given by the maximum singular value $\bar{\sigma}(\mathbf{G}(j\omega))$ and the minimum amplification by the minimum singular value $\underline{\sigma}(\mathbf{G}(j\omega))$. This analysis can be interpreted as the extension of the popular single-input single-output frequency response analysis to multivariable systems. Here, the magnitude of the frequency response is replaced by the singular values (see [62] for a more detailed explanation).

The performance specifications are set to minimize the effect of the disturbances on the DC voltages and to maintain the control input under reasonable limits. These specifications can be expressed in terms of the singular values in order to determine the constraints on K_g. For example, the maximum energy of the error caused by any input v of bounded energy is given by

$$\max_{v\neq 0} \frac{\|e\|_2}{\|v\|_2} = \max_{\omega} \bar{\sigma}(\mathbf{T_{ev}}(j\omega)) \tag{7.22}$$

where $\|e\|_2 = \int e^T e\, dt$ denotes the 2-norm of e. Therefore, to minimize the effects of the disturbance v on the voltage error e and on z can be interpreted as minimizing

$$\bar{\sigma}\left(\begin{bmatrix}\mathbf{S}(j\omega)\mathbf{G_{yw}}(j\omega) & -\mathbf{S}(j\omega)\end{bmatrix}\right) \tag{7.23}$$

$$\bar{\sigma}\left([(\mathbf{G_{zw}}(j\omega) + \mathbf{G_{zu}}(j\omega)\mathbf{KS}(j\omega)\mathbf{G_{yw}}(j\omega)) \quad -\mathbf{G_{zu}}(j\omega)\mathbf{KS}(j\omega)]\right) \tag{7.24}$$

and to maintain the control input under reasonable limits can be expressed as ensuring that

$$\bar{\sigma}\left(\begin{bmatrix}\mathbf{KS}(j\omega)\mathbf{G_{yw}}(j\omega) & -\mathbf{KS}(j\omega)\end{bmatrix}\right) \tag{7.25}$$

is bounded in the frequencies of interest.

In general, large values of K_g achieve a smaller voltage error but may also demand large control inputs. The optimal K_g is a compromise among all these objectives.

Table 7.1: Parameters of the four-terminal example

Grid parameters	Value
Line resistance R_1	0.50 Ω
Line resistance R_2	0.25 Ω
Line resistance R_3	0.40 Ω
Line inductance L_1	5.0 mH
Line inductance L_2	2.5 mH
Line inductance L_3	4.0 mH
Capacitances C_k $(k = 1, \ldots, 4)$	150 μF
Rated line current I_L^{rtd}	667 A
Rated input current I_k^{rtd}	667 A
Converter rated power P_k	100 MW
Rated DC voltage E_k	150 kV
Reference voltage E^*	145 kV

7.4 Four-terminal grid example

A simple four-terminal HVDC grid is used to illustrate the droop selection methodology presented in previous sections. The four-terminal grid scheme is depicted in Fig. 7.7 and consists of two offshore wind power plants connected to the HVDC grid through two different converters WFC1 and WFC2, and two onshore grid side converters GSC1 and GSC2 connected to the AC grid. The values of the parameters are listed in Table 7.1 and the linear model is illustrated in Fig. 7.8. The four-terminal HVDC grid has two power input nodes, two power output nodes and three branches representing the cables linking the converters. The capacitors are the result of combining the capacitances of the nodes and the corresponding branch side, as explained in Section 7.3.1.

Two scenarios are analyzed. In the first case, droop control is applied in both grid side converters whereas the wind farm converters inject all the wind power available. In the second scenario, due to a fault in the AC grid, both wind farm converters regulate the DC voltages and the grid side converters extract power from the HVDC grid at their maximum capacity.

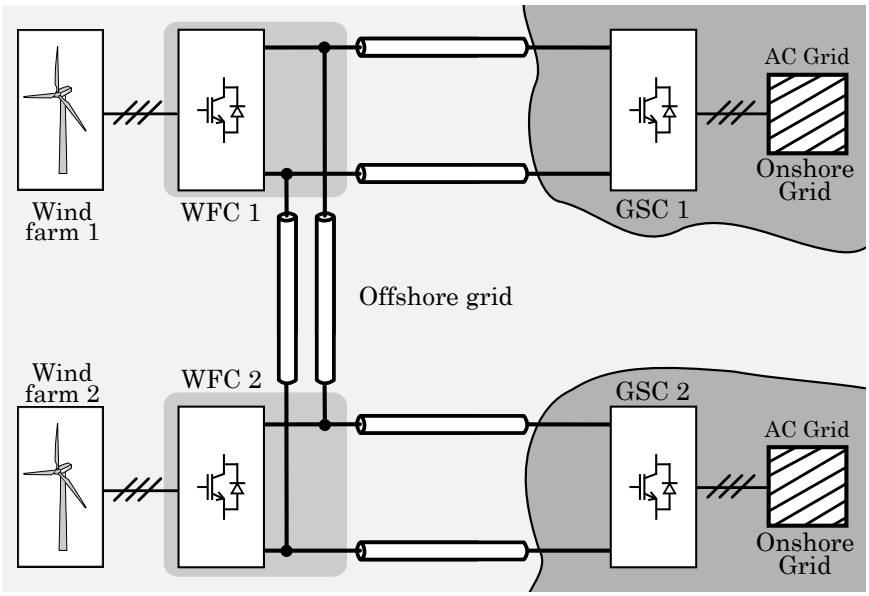

Figure 7.7: Four-terminal grid case study scheme

7.4.1 Case 1: Droop control in the AC grid side

Applying circuit laws to the four-terminal grid in Fig. 7.8, the following differential equations can be obtained

$$\frac{dE_1}{dt} = \frac{1}{C_1} I_{C_1}, \quad \frac{dE_2}{dt} = \frac{1}{C_2} I_{C_2} \tag{7.26}$$

$$\frac{dE_3}{dt} = \frac{1}{C_3} I_{C_3}, \quad \frac{dE_4}{dt} = \frac{1}{C_4} I_{C_4} \tag{7.27}$$

$$\frac{dI_{L_1}}{dt} = \frac{1}{L_1}(-R_1\, I_{L_1} + E_1 - E_3) \tag{7.28}$$

$$\frac{dI_{L_2}}{dt} = \frac{1}{L_2}(-R_2\, I_{L_2} + E_1 - E_2) \tag{7.29}$$

$$\frac{dI_{L_3}}{dt} = \frac{1}{L_3}(-R_3\, I_{L_3} + E_2 - E_4) \tag{7.30}$$

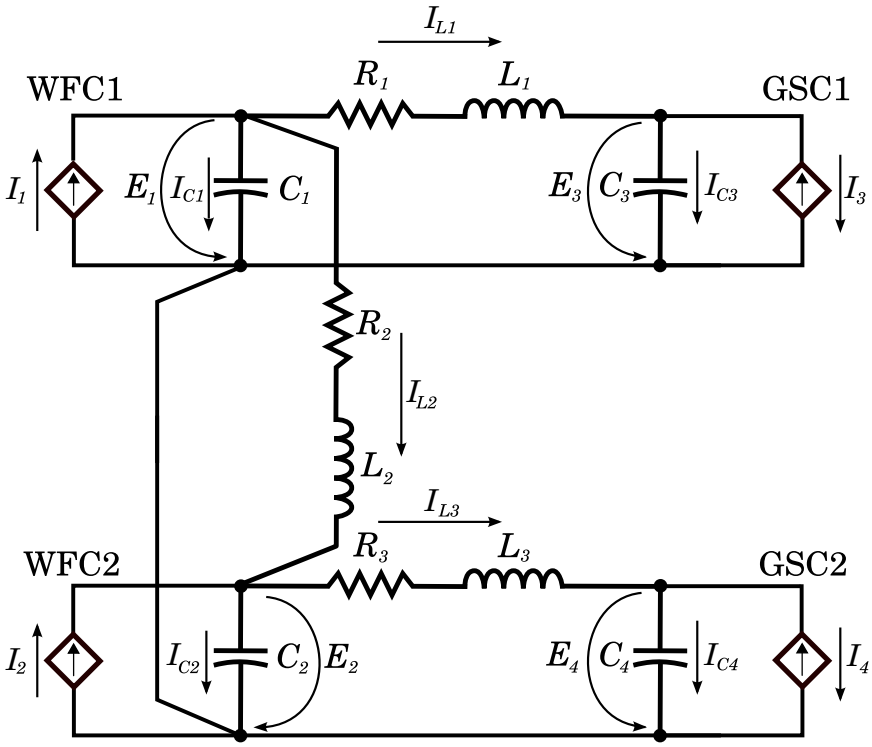

Figure 7.8: Four-terminal grid model used to illustrate the droop constant selection methodology

and the following algebraic equations

$$I_{C_1} = I_1 - I_{L_1} - I_{L_2} \tag{7.31}$$
$$I_{C_2} = I_2 - I_{L_3} + I_{L_2} \tag{7.32}$$
$$I_{C_3} = -I_3 + I_{L_1} \tag{7.33}$$
$$I_{C_4} = -I_4 + I_{L_3} \tag{7.34}$$

There are four equivalent capacitors and three equivalent inductors; therefore, the variables E_1, E_2, E_3, E_4, I_{L_1}, I_{L_2} and I_{L_3} are sufficient to completely define the state of this system

$$x = \begin{bmatrix} E_1 & E_2 & E_3 & E_4 & I_{L_1} & I_{L_2} & I_{L_3} \end{bmatrix}^T \tag{7.35}$$

As the WFCs are injecting all available power into the grid and the GSCs are regulating the DC voltages, the inputs and outputs are

$$w = \begin{bmatrix} I_1 & I_2 \end{bmatrix}^T, \qquad u = \begin{bmatrix} I_3 & I_4 \end{bmatrix}^T \tag{7.36}$$
$$z = \begin{bmatrix} E_1 & E_2 \end{bmatrix}^T, \qquad y = \begin{bmatrix} E_3 & E_4 \end{bmatrix}^T \tag{7.37}$$

The purpose of the droop control applied on the grid side converters of the four-terminal grid in Fig. 7.8 is to maintain the DC voltage stable when the currents coming from the wind farm converters WFC1 and WFC2 change. Therefore, the vector of these currents is the disturbance w and the control input u is the vector of the currents of the GSCs I_3 and I_4. The voltages measured and fed back to the controller are the voltages E_3 and E_4 whereas the voltages E_1 and E_2 are not available for the controller but it is desirable to maintain them close to the rated value. After the previous definitions, substituting the currents in the capacitors in (7.26)–(7.27) by the relations (7.31)–(7.34) and reorganizing the differential equations, the matrices in the

state-space representation (7.4) result

$$\mathbf{A} = \begin{bmatrix} 0 & 0 & 0 & 0 & -\frac{1}{C_1} & -\frac{1}{C_1} & 0 \\ 0 & 0 & 0 & 0 & 0 & \frac{1}{C_2} & -\frac{1}{C_2} \\ 0 & 0 & 0 & 0 & \frac{1}{C_3} & 0 & 0 \\ 0 & 0 & 0 & 0 & 0 & 0 & \frac{1}{C_4} \\ \frac{1}{L_1} & 0 & -\frac{1}{L_1} & 0 & -\frac{R_1}{L_1} & 0 & 0 \\ \frac{1}{L_2} & -\frac{1}{L_2} & 0 & 0 & 0 & -\frac{R_2}{L_2} & 0 \\ 0 & \frac{1}{L_3} & 0 & -\frac{1}{L_3} & 0 & 0 & -\frac{R_3}{L_3} \end{bmatrix} \tag{7.38}$$

$$\mathbf{B_w} = \begin{bmatrix} \frac{1}{C_1} & 0 \\ 0 & \frac{1}{C_2} \\ 0 & 0 \\ 0 & 0 \\ 0 & 0 \\ 0 & 0 \\ 0 & 0 \end{bmatrix}, \quad \mathbf{B_u} = \begin{bmatrix} 0 & 0 \\ 0 & 0 \\ -\frac{1}{C_3} & 0 \\ 0 & -\frac{1}{C_4} \\ 0 & 0 \\ 0 & 0 \\ 0 & 0 \end{bmatrix} \tag{7.39}$$

$$\mathbf{C_z} = \begin{bmatrix} 1 & 0 & 0 & 0 & 0 & 0 & 0 \\ 0 & 1 & 0 & 0 & 0 & 0 & 0 \end{bmatrix} \tag{7.40}$$

$$\mathbf{C_y} = \begin{bmatrix} 0 & 0 & 1 & 0 & 0 & 0 & 0 \\ 0 & 0 & 0 & 1 & 0 & 0 & 0 \end{bmatrix} \tag{7.41}$$

The droop controller in the case of two inputs and two outputs is simply

$$\mathbf{K} = K_g \cdot \begin{bmatrix} 1 & 0 \\ 0 & 1 \end{bmatrix} = K_g \cdot \mathbf{I}_2 \tag{7.42}$$

The constants q_1 and q_2 have been set to 1 because all the lines are approximately of same longitude and it is desired to extract the same amount of power from each terminal.

In Fig. 7.9, the eigenvalues of the closed loop matrix $\mathbf{A}_{\text{cl}}$ for several values of gain K_g can be found. Notice that the real parts of the eigenvalues become more negative for higher values of gain. This stabilizing effect is in accordance with the fact that an increment in the droop constant is similar to incrementing the energy dissipation in the system.

As mentioned in Section 7.3.2, the droop constant is selected in accordance with a performance criterion measured in terms of the 2-norm of the voltage error e, of the voltage not measured z and of the control input u.

The voltage error is given by (7.18), where the particular reference input is $E^* = [145 \text{ kV } 145 \text{ kV}]^T$. In this situation, the transfer function matrix

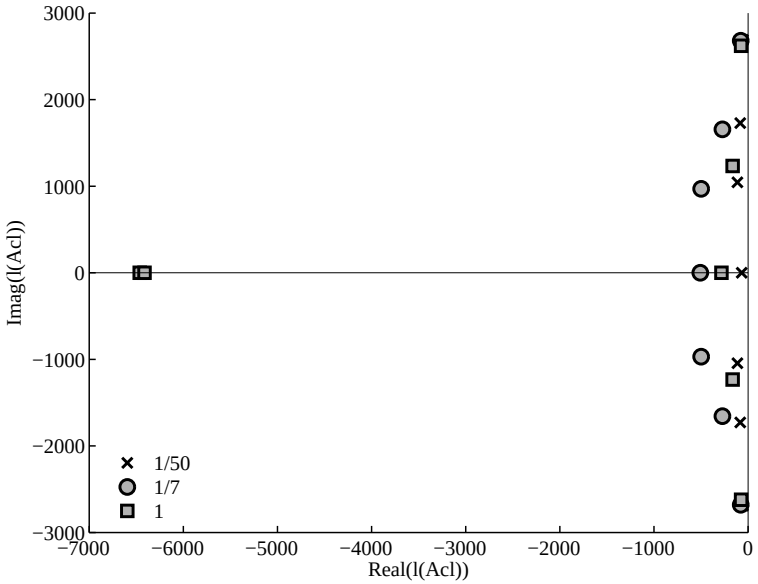

Figure 7.9: Eigenvalues of the closed loop matrix $\mathbf{A}_{\text{cl}}$ for several values of K_g (Case 1)

$\mathbf{S}(s)$ has a transmission zero at $s = 0$ for the particular direction of E^*. For instance, for $K_g = 1$

$$\mathbf{S}(0) = \begin{bmatrix} -0.32 & 0.32 \\ 0.32 & -0.32 \end{bmatrix} \cdot \begin{bmatrix} 145\text{ kV} \\ 145\text{ kV} \end{bmatrix} = \begin{bmatrix} 0 \\ 0 \end{bmatrix} \tag{7.43}$$

this also holds for any other value of K_g. As a consequence, the voltage error reduces to

$$e(s) = \mathbf{S}(s)\mathbf{G}_{\mathbf{yw}}(s)w(s) \tag{7.44}$$

The singular values of $\mathbf{S}(s)\mathbf{G}_{\mathbf{yw}}(s)$ can be seen in Fig. 7.10. It is clear that the larger the K_g, the smaller the error. In particular, at $s = 0$ and for the maximum voltage error of 10% ($e_{\max} = \pm 15$ kV) and the rated current $I^{\text{rtd}} = 667$ A,

$$\bar{\sigma}(\mathbf{S}(0)\mathbf{G}_{\mathbf{yw}}(0)) \leq \frac{\|e(0)\|_2}{\|w(0)\|_2} = \frac{\sqrt{15000^2 + 15000^2}}{\sqrt{667^2 + 667^2}} = 22.5 \tag{7.45}$$

This constraint can be extended to the rest of the frequencies resulting in the shadow area in Fig. 7.10. The constraint on the error is relaxed in

high frequencies since it is impossible to satisfy a uniform limit without violating the bandwidth limitations of the converters. The transfer functions $\mathbf{S}(s)\mathbf{G_{yw}}(s)$, whose singular values are inside the shadow area in Fig. 7.10, satisfy the error constraints. Based on this figure, it can be stated that constants $K_g \geq 1/22.5$ are able to maintain the voltage error at the controlled nodes within the limits.

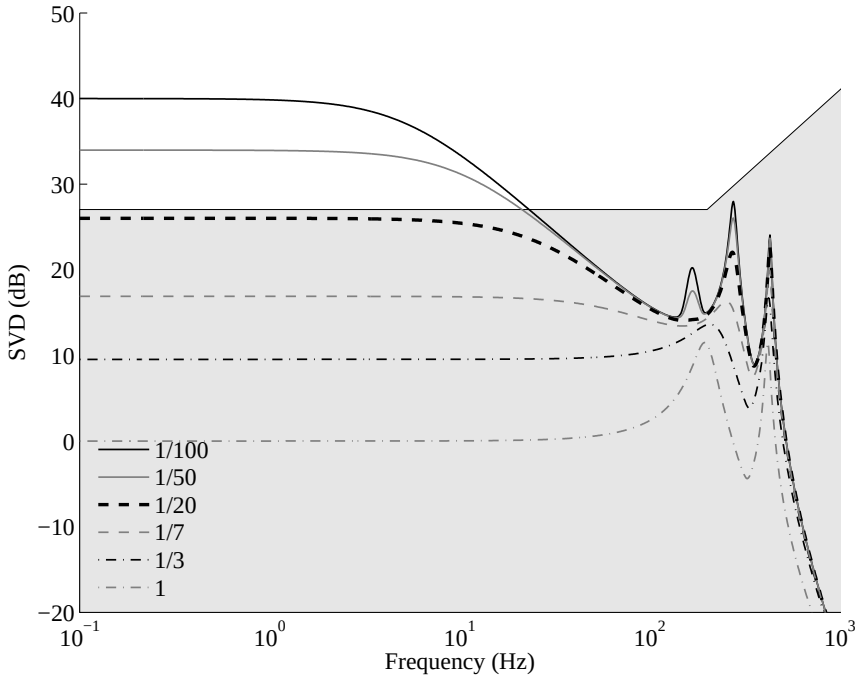

Figure 7.10: The maximum singular values of the function $\mathbf{S}(s)\mathbf{G_{yw}}(s)$ for several values of K_g (Case 1). The singular values inside the shadow area satisfy the error constraint.

The effect of K_g on the output z is given by (7.19). The objective is to maintain the DC voltage in the non directly-controlled terminals close to a rated value. Again, the particular input $E^* = [145 \text{ kV } 145 \text{ kV}]^T$ is considered. For this particular input, the output of $\mathbf{G_{zu}}(s)\mathbf{KS}(s)$ is independent of K_g and results equal to the input, as

$$\mathbf{G_{zu}}(0)\mathbf{KS}(0) \cdot \begin{bmatrix} 145 \text{ kV} \\ 145 \text{ kV} \end{bmatrix} = \begin{bmatrix} 145 \text{ kV} \\ 145 \text{ kV} \end{bmatrix} \tag{7.46}$$

Therefore, it is possible to analyze the deviation from the rated value by

defining $e_z = z - E^*$,

$$e_z(s) = (\mathbf{G_{zw}}(s) + \mathbf{G_{zu}}(s)\mathbf{KS}(s)\mathbf{G_{yw}}(s))w(s) \tag{7.47}$$

Fig. 7.11 shows the singular values of this transfer function. It can be observed that for higher values of K_g the maximum singular values of $\mathbf{G_{zw}}(s)+\mathbf{G_{zu}}(s)\mathbf{KS}(s)\mathbf{G_{yw}}(s)$ become smaller in low frequencies. However, in high frequencies, as Fig. 7.11 shows, an increment of K_g may produce the opposite effect in certain cases. It can be seen that for $K_g \geq 1/20$ the singular values are inside the shadow area, fulfilling the constraints on the variable e_z. In particular, at $s = 0$ and $K_g = 1/22.5$, the voltage in the wind farm nodes result

$$e_z(0) = \begin{bmatrix} 11.54 & 11.41 \\ 11.41 & 11.54 \end{bmatrix} \cdot \begin{bmatrix} 667\,\text{A} \\ 667\,\text{A} \end{bmatrix} = \begin{bmatrix} 15.3\,\text{kV} \\ 15.3\,\text{kV} \end{bmatrix} \tag{7.48}$$

that is, a 10% of error in the voltage.

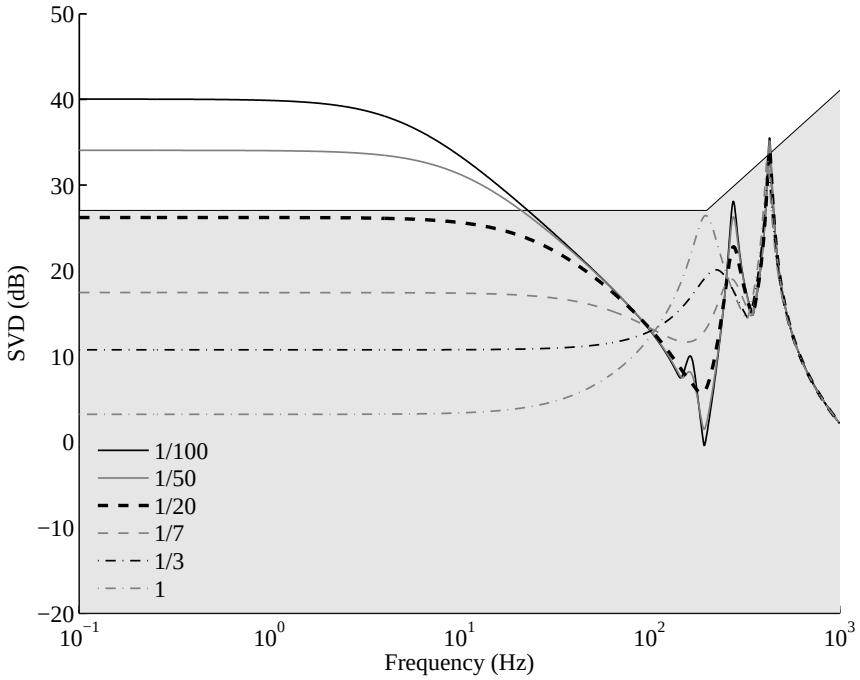

Figure 7.11: The maximum singular values of the function $\mathbf{G_{zw}}(s)+\mathbf{G_{zu}}(s)$ $\mathbf{KS}(s)\mathbf{G_{yw}}(s)$ for several values of K_g (Case 1). The singular values inside the shadow area satisfy the constraint on e_z.

The control input is given by (7.20). Again, as the particular reference input is $E^* = [145 \text{ kV } 145 \text{ kV}]^T$, the control action signal results governed by the transfer function $\mathbf{KS}(s)\mathbf{G_{yw}}(s)$. Fig. 7.12 shows the maximum singular values of $\mathbf{KS}(s)\mathbf{G_{yw}}(s)$ for several values of K_g. The shadow area indicates the singular values that satisfy the performance specifications. Notice that the constraint decreases in high frequencies to consider the limits on the bandwidth of the converters. It can be observed that the low frequency components of the control input are independent of the value of K_g. However, in high frequencies this transfer function presents resonance peaks that for some values of K_g violate the constraints indicated by the shadow area. This constraint imposes an upper limit on the gain K_g. In particular, from Fig. 7.12 it can be concluded that $K_g \leq 1/20$ fulfills the constraint on the control input.

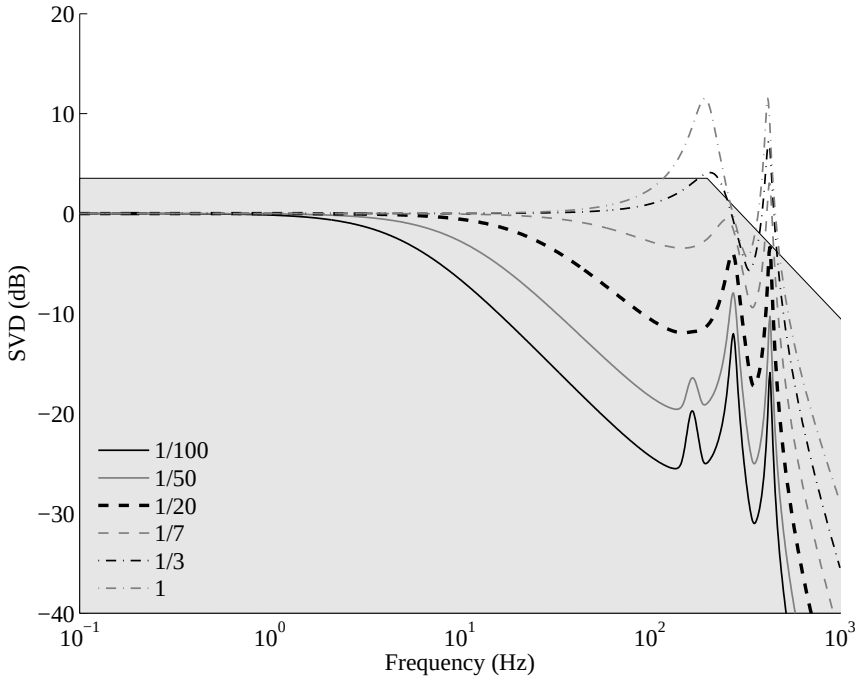

Figure 7.12: The maximum singular values of the function $\mathbf{KS}(s)\mathbf{G_{yw}}(s)$ for several values of K_g (Case 1). The singular values inside the shadow area satisfy the constraint on the control input.

From the previous analysis, it can be concluded that the gain K_g that better suits the performance specifications is 1/20.

In order to evaluate the droop gain previously selected, simulations are carried out in Matlab Simulink®. The analyzed scenario corresponds to two simultaneous and equal changes in the power injected into the DC grid by the WFCs. The power injected by the two converters change from 0 MW to the rated value at 0.05 s and return to 0 MW at 0.20 s. Fig. 7.13a shows the power flow at each converter. The solid lines correspond to the power injected by the WFCs and the dashed lines to the power extracted by the GSCs. It can be observed that the power ongoing from the GSCs is almost coincident due to the selection of the power distribution factors $q_1 = q_2 = 1$. As a consequence, both GSCs extract approximately the same amount of power. The power losses of the DC grid, at rated power transmission, are around 375 kW. The evolution of the terminal voltages can be seen in Fig. 7.13b. The DC voltages remain at 145 kV during the period where the power flow is zero since there is no voltage drop in the grid resistances. Once the power input increases, the DC voltages move towards a new voltage equilibrium. Notice that during non-zero power flow, there are differences between the voltage at the wind farm terminals and the voltage at the grid side terminals due to the power flow direction. Fig. 7.13c shows the currents flowing through each VSC. Both power and current evolutions are similar, except for a scale factor, which indicates that the initial approximation of considering the current proportional to the power has been reasonable. It can also observed that the currents never exceed the converter limits.

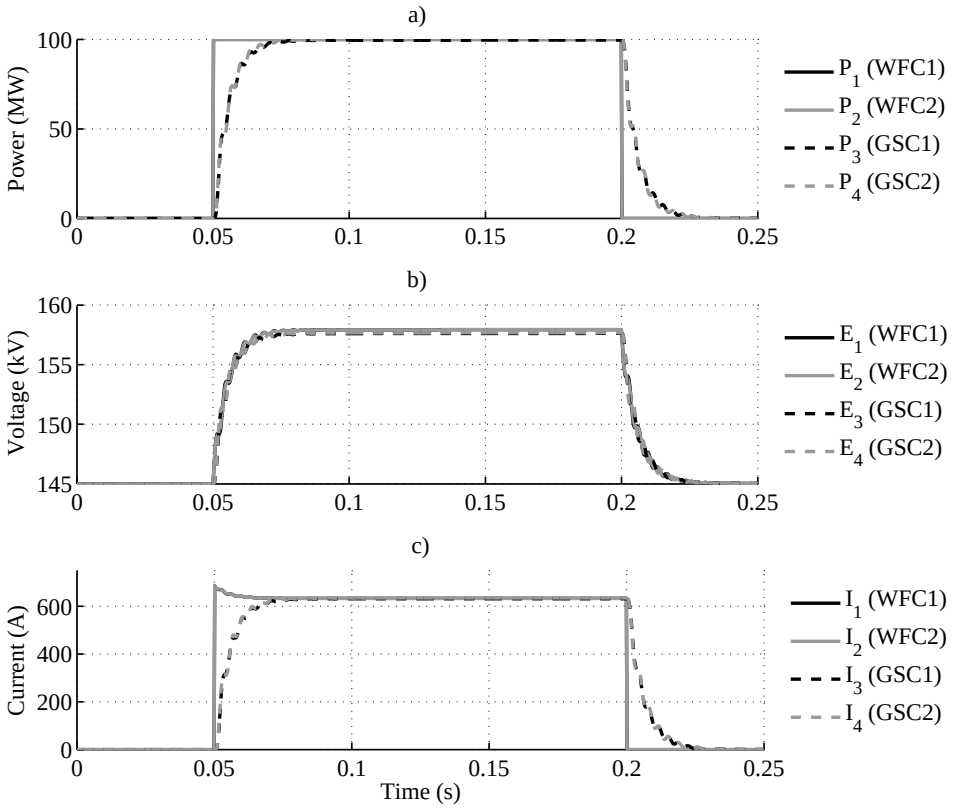

Figure 7.13: Simulations corresponding to a change in the power injected into the grid by the wind farm converters (Case 1)

7.4.2 Case 2: Droop control in the wind farm side

In the second case study, it is assumed that a simultaneous fault in both AC grids forces the GSCs to enter into current limitation mode. In this circumstance, the WFCs are responsible for regulating the DC voltage. Hence, the control inputs are the currents injected by the WFCs and the disturbances are the currents extracted by the GSCs

$$w = \begin{bmatrix} I_3 & I_4 \end{bmatrix}^T, \quad u = \begin{bmatrix} I_1 & I_2 \end{bmatrix}^T \tag{7.49}$$

On the other hand, the measured variables are the wind farm side voltages and the non-directly controlled variables are the grid side voltages

$$z = \begin{bmatrix} E_3 & E_4 \end{bmatrix}^T. \quad y = \begin{bmatrix} E_1 & E_2 \end{bmatrix}^T \tag{7.50}$$

The state space model have the same matrix $\mathbf{A}$ but the input and output matrices are now given by

$$\mathbf{B_w} = \begin{bmatrix} 0 & 0 \\ 0 & 0 \\ -\frac{1}{C_3} & 0 \\ 0 & -\frac{1}{C_4} \\ 0 & 0 \\ 0 & 0 \\ 0 & 0 \end{bmatrix}, \quad \mathbf{B_u} = \begin{bmatrix} \frac{1}{C_1} & 0 \\ 0 & \frac{1}{C_2} \\ 0 & 0 \\ 0 & 0 \\ 0 & 0 \\ 0 & 0 \\ 0 & 0 \end{bmatrix} \tag{7.51}$$

$$\mathbf{C_z} = \begin{bmatrix} 0 & 0 & 1 & 0 & 0 & 0 & 0 \\ 0 & 0 & 0 & 1 & 0 & 0 & 0 \end{bmatrix} \tag{7.52}$$

$$\mathbf{C_y} = \begin{bmatrix} 1 & 0 & 0 & 0 & 0 & 0 & 0 \\ 0 & 1 & 0 & 0 & 0 & 0 & 0 \end{bmatrix} \tag{7.53}$$

The droop controller in the case is

$$\mathbf{K} = K_g \cdot \begin{bmatrix} -1 & 0 \\ 0 & -1 \end{bmatrix} = -K_g \cdot \mathbf{I_2} \tag{7.54}$$

since the droop control is applied in the wind farm side.

Fig. 7.14 shows the eigenvalues of the closed loop matrix $\mathbf{A}_{\text{cl}}$ for several values of gain K_g. Notice that the real parts of the eigenvalues become more negative for higher values of gain.

Also in this scenario, it is considered the case where $E^* = [145 \text{ kV } 145 \text{ kV}]^T$. Therefore, the performance is associated only with the input $w(s)$. In

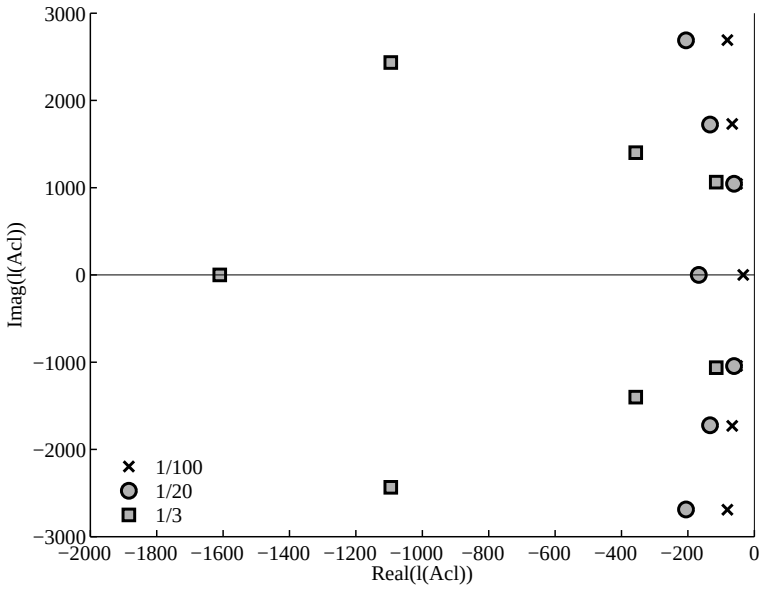

Figure 7.14: Eigenvalues of the closed loop matrix $\mathbf{A}_{\text{cl}}$ for several values of K_g (Case 2)

Figs. 7.15-7.17, it can be seen the maximum singular values of the transfer functions $\mathbf{S}(s)\mathbf{G_{yw}}(s)$, $\mathbf{G_{zw}}(s) + \mathbf{G_{zu}}(s)\mathbf{KS}(s)\mathbf{G_{yw}}(s)$ and $\mathbf{KS}(s)\mathbf{G_{yw}}(s)$ for several values of K_g. The resonance peaks are lighter damped in this case. For this reason, in order to fulfill the low frequencies error, larger values must be accepted at high frequencies. Notice in Fig. 7.17 that the constraint on the control input has been relaxed in high frequency for the same reason. As a consequence, the gain K_g has been set at 1/20.

The system has been also evaluated by simulations. In the scenario considered, both WFCs inject the rated power value while two voltage sags are applied in the AC grid. A three-phase voltage sag of 10% of the nominal AC values is applied to the AC grid connected to the GSC1. At the same time, another voltage sag of 20% is applied to the grid connected to the GSC2. Both sags last 0.2 s. The three-phase voltages at each AC grid are shown in Fig. 7.18, whereas the corresponding three-phase currents can be seen in Fig. 7.19.

Fig. 7.20 presents the evolution of the variables in the DC grid. It can be observed that the AC grid fault causes an increment of the all DC voltages (Fig. 7.20b). These increments are due to the fact that the GSCs operate in current limitation mode to avoid disconnection by over-currents during

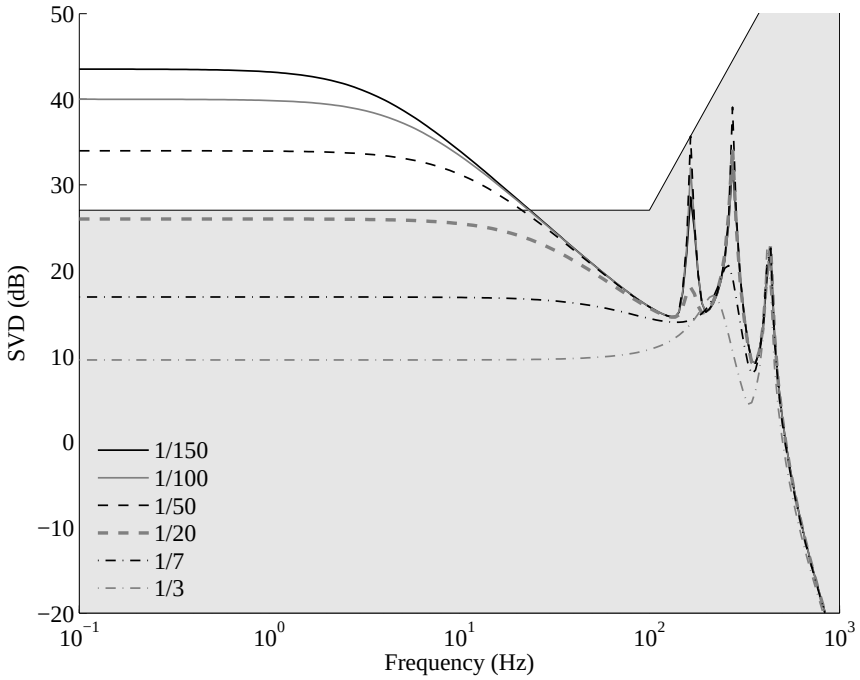

Figure 7.15: The maximum singular values of the function $\mathbf{S}(s)\mathbf{G_{yw}}(s)$ for several values of K_g (Case 2). The singular values inside the shadow area satisfy the error constraint.

the grid fault. When the WFCs voltages exceed 160 kV, the corresponding converters start to apply droop control in the DC grid, reducing the power injected to the grid from 100 MW to 20 MW (Fig. 7.20a). The DC current also decreases during the voltage sag due to the power reduction caused by the droop control in the WFCs (Fig. 7.20c). Notice that the disconnection of the system due to over-voltage was avoided during the fault.

7.5 Conclusions

A design methodology for droop control in multi-terminal HVDC grids has been presented. The methodology includes a systematic procedure to formulate a linear model of multi-terminal grids. Based on this model and a frequency response analysis, a criterion is provided to select the droop gain taking into account the dynamics of the entire multi-terminal HVDC system. The limitation of DC voltage errors and the converter currents de-

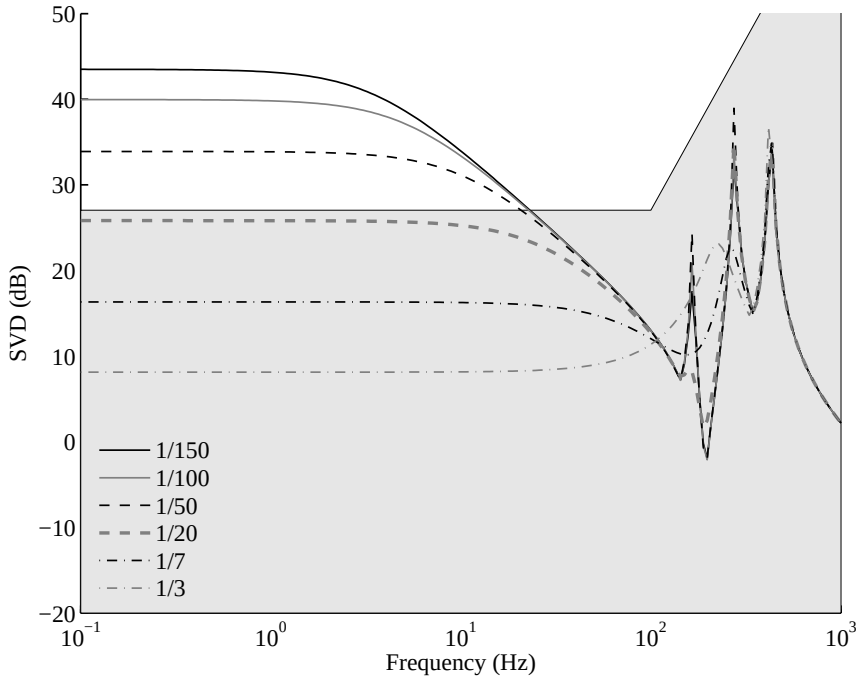

Figure 7.16: The maximum singular values of the function $\mathbf{G_{zw}}(s) + \mathbf{G_{zu}}(s)\,\mathbf{KS}(s)\mathbf{G_{yw}}(s)$ for several values of K_g (Case 2). The singular values inside the shadow area satisfy the constraint on e_z.

fine a range on the droop gains that achieve the best compromise between the specifications. Each local controller can affect the global stability and the DC voltage in other terminals. For these reasons, the droop constant selection must be addressed in the context of multivariable system theory to consider the dynamic behavior of the entire multi-terminal grid, both in normal operation and in fault conditions.

A four-terminal grid example has been used to illustrate the application of the use of this methodology. Nevertheless, the procedure is applicable to any other multi-terminal HVDC grid with more inputs and outputs. The complexity of the model increases with the number of nodes and branches but the computation of the singular values does not involve a serious limitation with the current algorithms. The range of droop gains is obtained only from the maximum singular values; therefore, its computation is independent of the complexity of the particular multi-terminal grid.

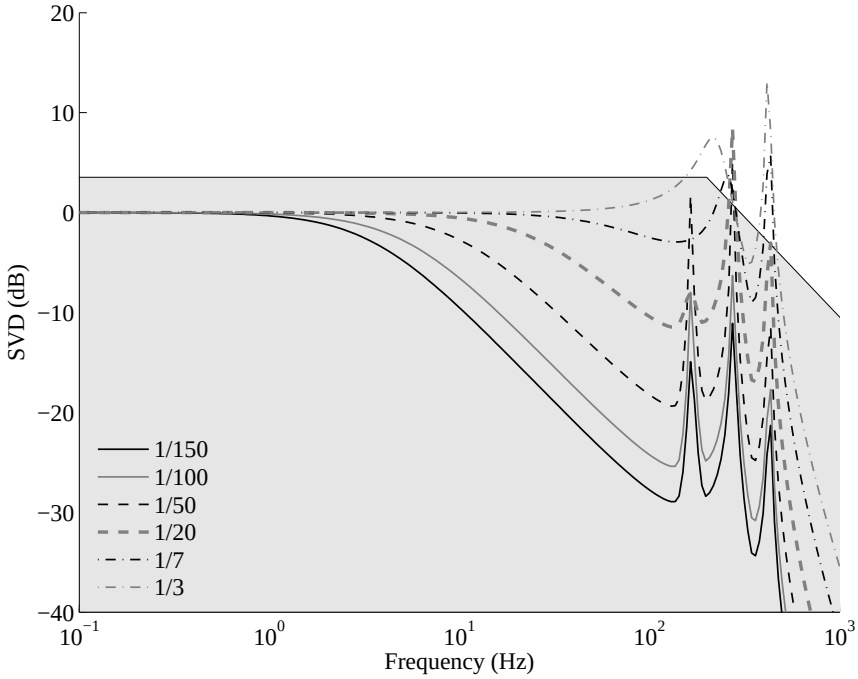

Figure 7.17: The maximum singular values of the function $\mathbf{KS}(s)\mathbf{G_{yw}}(s)$ for several values of K_g (Case 2). The singular values inside the shadow area satisfy the constraint on the control input.

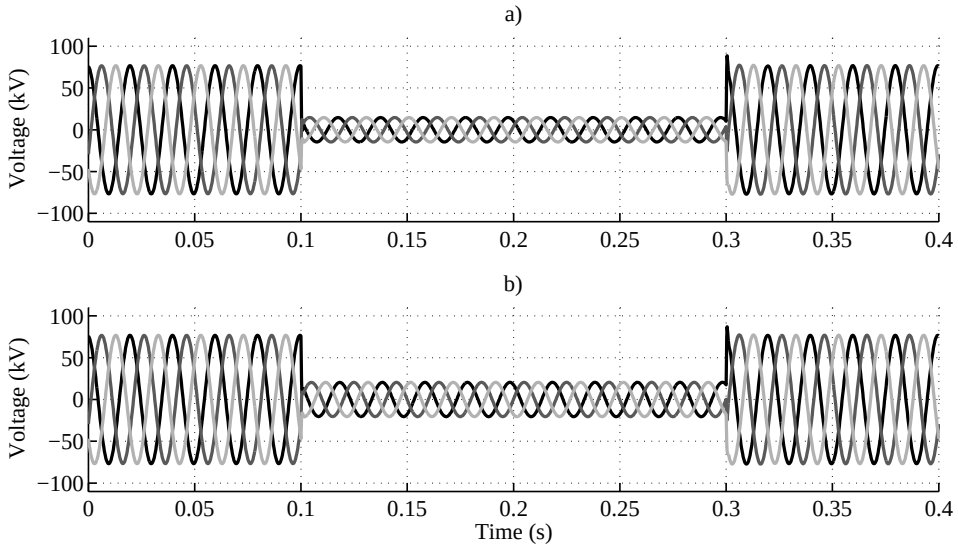

Figure 7.18: Simulations corresponding to a voltage sag in the AC grids (Case 2). a) Three-phase voltages in the grid 1, b) three-phase voltages in the grid 2.

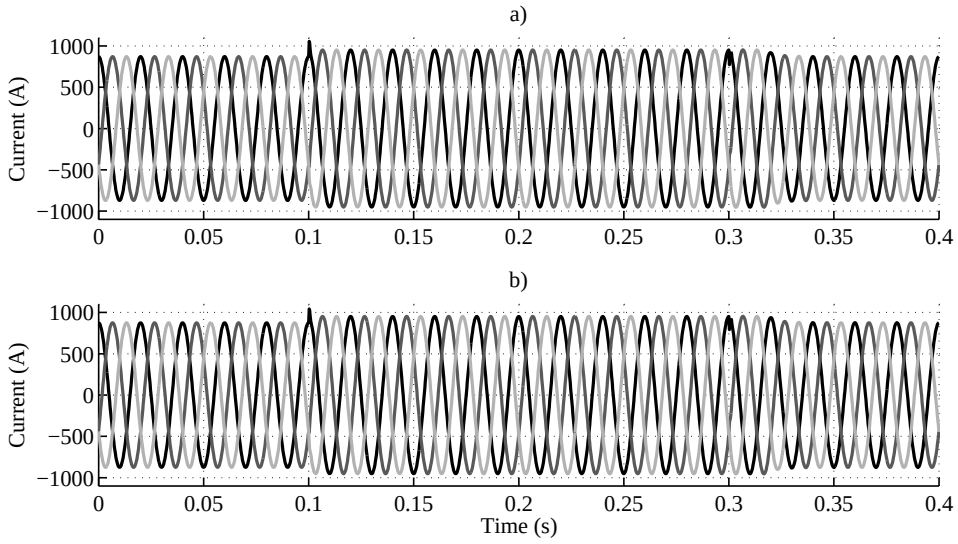

Figure 7.19: Simulations corresponding to a voltage sag in the AC grids (Case 2). a) Three-phase currents in the grid 1, b) three-phase currents in the grid 2.

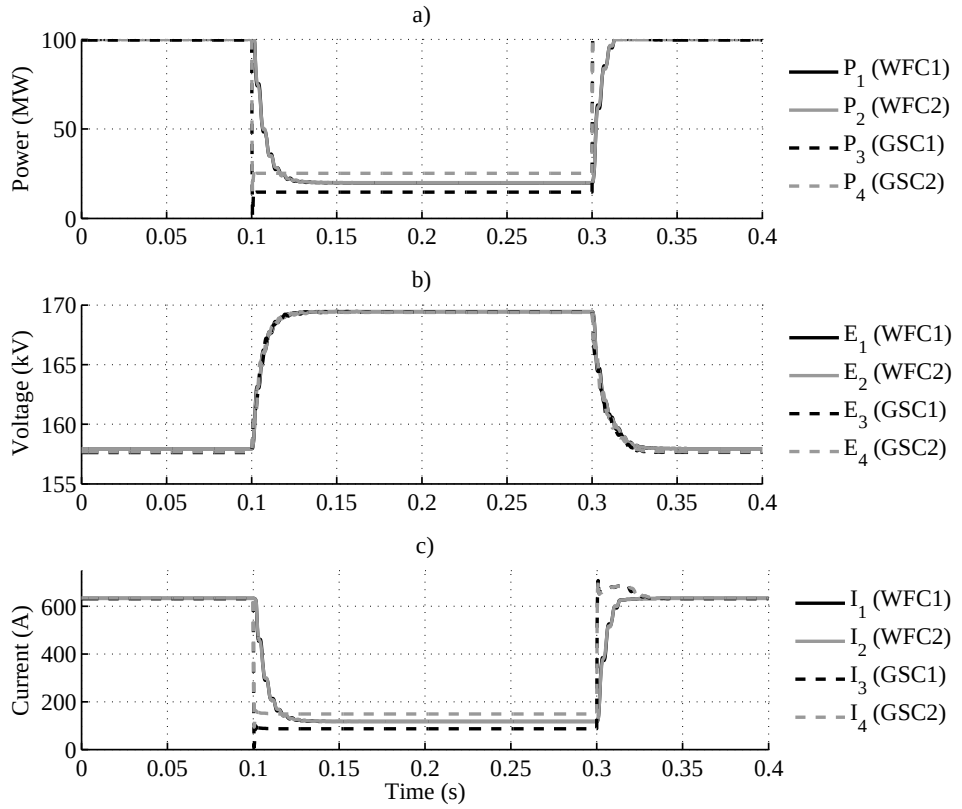

Figure 7.20: Simulations corresponding to a voltage sag in the AC grids (Case 2)

Chapter 8

DC voltage droop control design for multi-terminal HVDC systems considering AC and DC grid dynamics

8.1 Introduction

Different control structures have been proposed to operate multi-terminal High Voltage Direct Current (HVDC) grids. Regarding the primary voltage regulation, the droop control is a widely accepted solution. It allows compensation of fast deviations of the voltage, establishing a power sharing between different converters connected to the DC multi-terminal grid [114]. Different implementations of the droop control, mainly current (see Chapter 7) or power-based, can be found in the literature [115].

Primary droop voltage control design has been widely addressed in different publications. In [112], droop control tuning is performed based on the steady-state characteristics and the resulting power flow sharing [116]. In [117] the droop regulator is designed taking into account the effect of the DC transmission cable over the system dynamics. In [118], a droop selection procedure is detailed to reduce the perturbations imposed by the DC grid over the Alternating Current (AC) grid. In [119], the droop control is designed based on a trade-off between the power losses, the desired power flow and a minimization of voltage deviations. In the previous chapter of this thesis (Chapter 7), the droop constants are selected considering the dynamics of the DC multi-terminal grid and its operational limitations [120].

In this section, a power-based droop control is designed considering the complete HVDC system, including the DC and AC grid dynamics, the converter controllers and a DC voltage oscillation damping loop. This proposal expands the scope of Chapter 7, which addresses the droop control design focusing only on the DC grid dynamics [120]. To do so, a linearized model of the complete multi-terminal HVDC system is developed, gathering the

different system dynamics. Then, the derived linear model is analyzed using multivariable frequency methods to select the most suitable droop controllers to operate the DC grid. The theoretical developments are validated through simulations in a three-terminal grid.

This chapter is organized as follows: the next section describes the droop control operation of multi-terminal Voltage Source Converter (VSC) HVDC grids. Section 8.3 presents the derivation of the linear model of a generic multi-terminal HVDC grid. The control design methodology is described in Section 8.4 and in Section 8.5, the control design strategy is applied to a three-terminal grid. Finally, in Section 8.6 the chapter conclusions are drawn.

8.2 Multi-terminal grid control

A generic VSC-HVDC multi-terminal grid layout is shown in Fig. 7.1. The HVDC grid is built to interconnect the offshore wind power plants and the main land AC grid (or grids) by means of VSC power converters. Wind Farm Converters (WFC) inject the generated power from the wind power plants to the DC grid, whereas Grid Side Converters (GSC) regulate the DC grid voltage employing droop control [25, 114].

The droop control allows the regulation of the DC grid voltage without communications between converters, being implemented at each of the GSCs locally. Also, it allows the establishment of power sharing between converters by acting over the corresponding converter power loop (see Fig. 8.1). Possible power deviations can be compensated through an upper secondary control [121], that could be implemented using communications between the GSCs (Fig. 8.1). In this work, the upper secondary level controller is not included in the analysis as the study is mainly focused on droop-based grid voltage primary control. The power droop control law, implemented in the n different GSCs is

$$P^* = K(E - E^*) \tag{8.1}$$

where E is the voltage measured at the DC terminals of the GSC converter, E^* is the voltage reference for the droop controller, K is the droop constant and P^* is the power reference introduced to the power loop. Based on the power set-point, the power controller (G_P) regulates the power flowing through the converter in order to track the DC grid voltage reference, even assuming a DC voltage error due to the proportional nature of the droop controller. In terms of the AC voltage, it is controlled by means of an AC module voltage regulator (G_U). The outputs of the power and AC voltage

regulators are connected to the inner conventional current loop that applies the corresponding voltages to the AC grid by means of the power converter to track the current references.

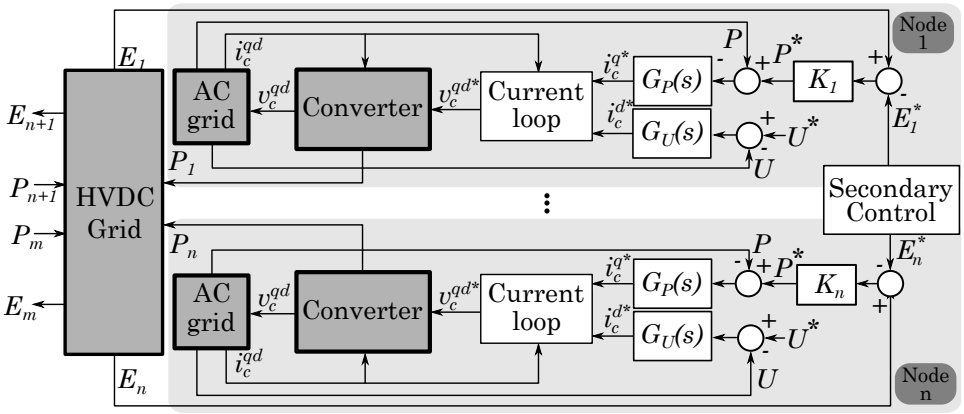

Figure 8.1: Multi-terminal control structure including DC and AC dynamics

Dynamics of the different interconnected systems could affect the droop voltage regulation, such as the DC multi-terminal grid, the AC grid connection points, the AC grid converter filter, the power and voltage controllers or the current inner control. Then, the design of the droop voltage control should be performed considering all the mentioned dynamics in order to ensure a proper control performance. To do so, in this work a complete linear model of the multi-terminal grid is derived. Once the model is obtained, the different controllers, including the droop voltage control, are designed combining classic and modern control techniques.

8.3 System modelling

In this section, the procedure to obtain a linear model of a generic multi-terminal grid (Fig. 7.1) is detailed. The complete model is divided in two parts, the AC system and the DC system. In terms of the AC system, the linearized equations of a GSC connected to an AC grid are described. On the other hand, the linearized DC grid model for a simple DC link is derived and the procedure to expand the model to a larger grid is detailed. The existing link between both parts is the power converter. The converter is modeled based on its average model, employing three voltage sources in the AC side and a dependent current source in the DC side [113]. No losses or Modular Multilevel Converter (MMC) inner dynamics are considered.

8.3.1 AC system

In this section, the model of a VSC-HVDC converter connected to the grid is addressed. The converter grid connection is performed by either an inductance (L) or an inductance and capacitor filter (LC) depending on the application [101, 122], as shown in Fig. 8.2.

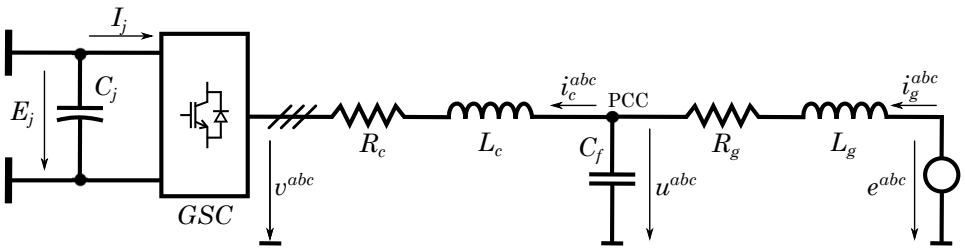

Figure 8.2: Model of the converter connection to the AC grid

In terms of the AC grid connection, it is represented via a simple Thévenin equivalent. The state-space model of the converter grid connection considering the LC filter is

$$\frac{dx_{lc}}{dt} = \mathbf{A_{lc}} x_{lc} + \mathbf{B_{lc}} u_{lc} \tag{8.2}$$

where $\mathbf{A_{lc}}$ and $\mathbf{B_{lc}}$ are

$$\mathbf{A_{lc}} = \begin{bmatrix} -\frac{R_c}{L_c} & -\omega & \frac{1}{L_c} & 0 & 0 & 0 \\ \omega & -\frac{R_c}{L_c} & 0 & \frac{1}{L_c} & 0 & 0 \\ -\frac{1}{C_f} & 0 & 0 & -\omega & \frac{1}{C_f} & 0 \\ 0 & -\frac{1}{C_f} & \omega & 0 & 0 & \frac{1}{C_f} \\ 0 & 0 & -\frac{1}{L_g} & 0 & -\frac{R_g}{L_g} & -\omega \\ 0 & 0 & 0 & -\frac{1}{L_g} & \omega & -\frac{R_g}{L_g} \end{bmatrix} \tag{8.3}$$

$$\mathbf{B_{lc}} = \begin{bmatrix} -\frac{1}{L_c} & 0 & 0 & 0 \\ 0 & -\frac{1}{L_c} & 0 & 0 \\ 0 & 0 & 0 & 0 \\ 0 & 0 & 0 & 0 \\ 0 & 0 & \frac{1}{L_g} & 0 \\ 0 & 0 & 0 & \frac{1}{L_g} \end{bmatrix} \tag{8.4}$$

where L_c is the filter inductance value and R_c its parasitic resistance, ω is the frequency of the grid, C_f is the capacitance of the capacitor filter and L_g

and R_g are the inductance and resistance of the grid Thévenin equivalent. The state and input vectors are

$$x_{lc} = \begin{bmatrix} i_c^q & i_c^d & u^q & u^d & i_g^q & i_g^d \end{bmatrix}^T \tag{8.5}$$

$$u_{lc} = \begin{bmatrix} v^q & v^d & e^q & e^d \end{bmatrix}^T \tag{8.6}$$

where i_c^{qd} are the currents flowing from the Point of Common Coupling (PCC) to the converter, i_g^{qd} are the currents flowing to the grid, e^{qd} are the grid voltages, u^{qd} are the voltages at the PCC and v^{qd} are the voltages applied by the converter in the synchronous reference frame [59]. Applying a linearization to the previous equations, the state-space representation can be expressed as

$$\frac{d\Delta x_{lc}}{dt} = \mathbf{A_{lc}}\Delta x_{lc} + \mathbf{B_{lc}}\Delta u_{lc} \tag{8.7}$$

$$\Delta y_{lc} = \mathbf{C_{lc}}\Delta x_{lc} + \mathbf{D_{lc}}\Delta u_{lc} \tag{8.8}$$

where $\mathbf{A_{lc}}$ and $\mathbf{B_{lc}}$ are the matrices defined in (8.3) and (8.4). Regarding the system output equation, matrices $\mathbf{C_{lc}}$ and $\mathbf{D_{lc}}$ are

$$\mathbf{C_{lc}} = \left[\begin{array}{cccccc} \multicolumn{6}{c}{\mathbf{I_{6x6}}} \\ \hline 0 & 0 & \frac{u_0^q}{U_0} & \frac{u_0^d}{U_0} & 0 & 0 \\ 0 & 0 & \frac{3\,i_{g0}^q}{2} & \frac{3\,i_{g0}^d}{2} & \frac{3\,u_0^q}{2} & \frac{3\,u_0^d}{2} \\ \frac{3\,v_{g0}^q}{2} & \frac{3\,v_{g0}^d}{2} & 0 & 0 & 0 & 0 \end{array}\right] \tag{8.9}$$

$$\mathbf{D_{lc}} = \left[\begin{array}{cccc} \multicolumn{4}{c}{\mathbf{0_{8x4}}} \\ \hline \frac{3\,i_{c0}^q}{2} & \frac{3\,i_{c0}^d}{2} & 0 & 0 \end{array}\right] \tag{8.10}$$

where $\mathbf{I_{6x6}}$ is a 6x6 identity matrix and $\mathbf{0_{8x4}}$ is a zero matrix of 8 rows and 4 columns. The linearized state variables, inputs and outputs are

$$\Delta x_{lc} = \begin{bmatrix} \Delta i_c^q & \Delta i_c^d & \Delta u^q & \Delta u^d & \Delta i_g^q & \Delta i_g^d \end{bmatrix}^T \tag{8.11}$$

$$\Delta u_{lc} = \begin{bmatrix} \Delta v^q & \Delta v^d & \Delta e^q & \Delta e^d \end{bmatrix}^T \tag{8.12}$$

$$\Delta y_{lc} = \begin{bmatrix} \Delta i_c^q & \Delta i_c^d & \Delta u^q & \Delta u^d & \Delta i_g^d & \Delta i_g^d & \Delta U & \Delta P_u & \Delta P \end{bmatrix}^T \tag{8.13}$$

where U is the PCC voltage magnitude, P_u is the power flowing to the AC grid, P is the power flowing through the converter and v_0^{qd}, u_0^{qd}, i_{c0}^{qd}, i_{g0}^{qd} and

U_0 are the system variables at the linearization point. Note also that the Park transformation used for this system is [59]

$$\mathbf{T}(\theta) = \frac{3}{2}\begin{bmatrix} \cos(\theta) & \cos(\theta - \frac{2\pi}{3}) & \cos(\theta + \frac{2\pi}{3}) \\ \sin(\theta) & \sin(\theta - \frac{2\pi}{3}) & \sin(\theta + \frac{2\pi}{3}) \\ \frac{1}{2} & \frac{1}{2} & \frac{1}{2} \end{bmatrix} \tag{8.14}$$

8.3.2 Phase Locked Loop (PLL)

A Phase Locked Loop (PLL) system is required for orienting the converter controllers with the grid angle [63]. The synchronous reference frame is oriented with the d-axis voltage employing a PI regulator. The output of this controller is the estimated frequency of the grid, which is integrated to obtain the angle for the system Park transformations. The PI regulator included in the PLL is

$$K_{pll}(s) = \frac{(k_{p-pll}s + k_{i-pll})}{s} \tag{8.15}$$

where k_{p-pll} and k_{i-pll} are the proportional and integral gains of the regulator, calculated based on the amplitude of the AC voltage and the bandwidth desired for the PLL [63]. The inner dynamics of the PLL system introduce an angle deviation between the real grid angle and the estimated angle, especially during voltage transients. In order to introduce this effect into the converter linear model, the PLL tracking system can be linearized as [122, 123]

$$\Delta e_\theta(s) = -\frac{k_{p-pll}s + k_{i-pll}}{s^2 + u_0^q k_{p-pll}s + u_0^q k_{i-pll}}\Delta u^d(s) \tag{8.16}$$

where e_θ is the angle deviation between the grid angle and the PLL estimated angle, and u_0^q is the voltage of the q axis at the linearization point. In addition, the existing deviation between the grid real and estimated angles must be integrated into the model variables. This effect is included as a rotation of the angle deviation between both angles. Then, two different synchronous reference frames variables are defined: the x^{qd} (x^q and x^d) variables corresponding to the synchronous reference calculated from the grid angle, and the x^{qdc} (x^{qc} and x^{dc}) variables related to the synchronous reference frame calculated from the PLL estimated angle. The transformation $\mathbf{T_c^{qd}}$ relates both references

$$\Delta x^{qdc} = \mathbf{T_c^{qd}}\begin{bmatrix}\Delta x^q & \Delta x^d & \Delta e_\theta\end{bmatrix}^T \tag{8.17}$$

where $\mathbf{T_c^{qd}}$ is

$$\mathbf{T_c^{qd}} = \begin{bmatrix} \cos(e_{\theta_0}) & -\sin(e_{\theta_0}) & -\sin(e_{\theta_0})\ x_0^q - \cos(e_{\theta_0})\ x_0^d \\ \sin(e_{\theta_0}) & \cos(e_{\theta_0}) & \cos(e_{\theta_0})\ x_0^q - \sin(e_{\theta_0})\ x_0^d \end{bmatrix} \tag{8.18}$$

where e_{θ_0} is the angle error deviation value at the linearization point and x_0^d and x_0^q are the x^{qd} components magnitudes at the linearization point. Also, the inverse transformation can be defined as

$$\Delta x^{qd} = \mathbf{T_c^{qd^{-1}}} \begin{bmatrix} \Delta x^{qc} & \Delta x^{dc} & \Delta e_\theta \end{bmatrix}^T \tag{8.19}$$

where $\mathbf{T_c^{qd^{-1}}}$ is

$$\mathbf{T_c^{qd^{-1}}} = \begin{bmatrix} \cos(e_{\theta_0}) & \sin(e_{\theta_0}) & \cos(e_{\theta_0})\ x_0^d - \sin(e_{\theta_0})\ x_0^q \\ -\sin(e_{\theta_0}) & \cos(e_{\theta_0}) & -\cos(e_{\theta_0})\ x_0^q - \sin(e_{\theta_0})\ x_0^d \end{bmatrix} \tag{8.20}$$

8.3.3 Current control

The Current Loop (CL) is based on the conventional vector control strategy [61]. It is based on two different PI regulators G_{CL} besides a decoupling loop, as shown in Fig. 8.3. The current loop is implemented in x^{qdc} variables.

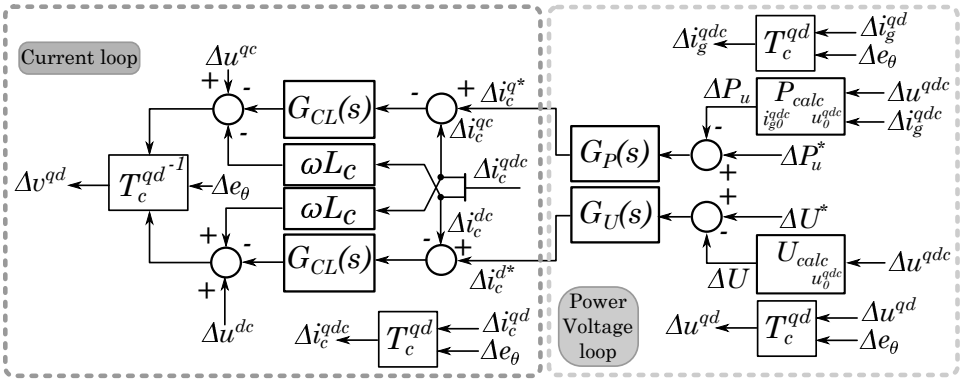

Figure 8.3: Current loop and power and voltage loops linearized control structures

8.3.4 Power and voltage control

The power and voltage controllers are implemented by two different regulators (G_P and G_U), as shown in Fig. 8.3. Typically, both controllers are conventional PI regulators [114]. The power and voltage feedback signals must be linear to be included into the model, then both magnitudes are calculated employing x^{qdc} converter variables

$$\Delta P_u = \frac{3}{2}\left(\Delta i_g^{qc} u_0^q + i_{g0}^q \Delta u^{qc} + \Delta i_g^{dc} u_0^d + i_{g0}^d \Delta u^{dc}\right) \tag{8.21}$$

$$\Delta U = \frac{u_0^q \Delta u^{qc}}{U_0} + \frac{u_0^d \Delta u^{dc}}{U_0} \tag{8.22}$$

where U_0 is $\sqrt{(u_0^q)^2 + (u_0^d)^2}$.

8.3.5 Multi-terminal DC grid system modeling

The approach to model the multi-terminal HVDC link is based on Chapter 7 methodology [120], although in this case the equations are linearized. First, a connection between two DC grid terminals $i - j$ (Fig. 8.4) is used to illustrate how to obtain the linearized grid model of the DC system. The cable is modeled using a π-equivalent model, in which the capacitors at both ends are the result of adding all the capacitors connected in parallel at those points. Next, the differential equations of the generic link are obtained

$$\frac{dE_i}{dt} = \frac{1}{C_i}(I_i - I_{Lij}) = \frac{1}{C_i}(\frac{P_i}{E_i} - I_{Lij}) \tag{8.23}$$

$$\frac{dE_j}{dt} = \frac{1}{C_j}(I_{Lij} - I_j) = \frac{1}{C_j}(I_{Lij} - \frac{P_j}{E_j}) \tag{8.24}$$

$$E_i - E_j = R_{ij} I_{Lij} + L_{ij} \frac{dI_{Lij}}{dt} \tag{8.25}$$

where E_i and E_j are the voltages at the equivalent capacitors, I_i and I_j are the currents flowing through the converters, P_i and P_j are the input/output power flowing through the converters, I_{Lij} is the current flowing through the line, C_i and C_j are the equivalent capacitances at both sides of the DC link and R_{ij} and L_{ij} are the equivalent cable resistance and inductance of the π-equivalent model. Due to the division between variables, the expression of the DC current should be linearized to be included in the model, as shown next for the node i

$$I_i = \frac{P_i}{E_i} \approx \frac{\Delta P_i}{E_{i0}} - \frac{P_{i0}}{E_{i0}^2} \Delta E_i \tag{8.26}$$

where ΔE_i and ΔP_i are linearized variables representing the voltage at the node i and the power flowing through the converter i, respectively. Also, E_{i0} and P_{i0} are the power and the voltage at the linearization point. Finally, combining the previous expressions, the DC link state-space representation can be obtained.

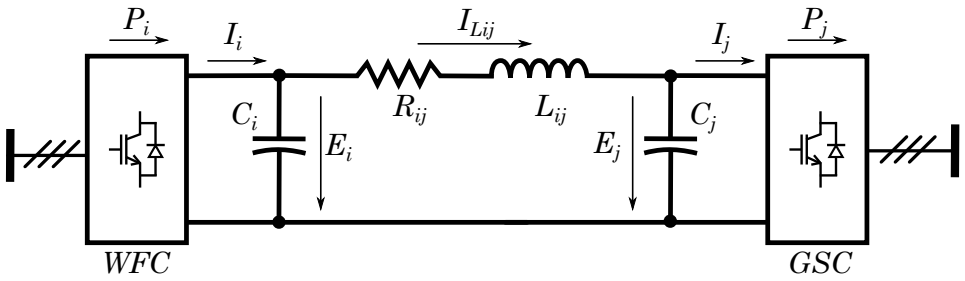

Figure 8.4: DC connection between two nodes of the multi-terminal grid

This model can be extended to a more complex multi-terminal grid, deriving the equivalent circuit of the DC grid and obtaining the system equations as explained above. Then, the linear state-space of DC grid model, obtained based on the grid equations is

$$\begin{aligned} \frac{d\Delta x}{dt} &= \mathbf{A}\Delta x + \mathbf{B_u}\Delta u + \mathbf{B_w}\Delta w, \\ \Delta y &= \mathbf{C_y}\Delta x, \quad \Delta z = \mathbf{C_z}\Delta x, \end{aligned} \tag{8.27}$$

where Δx is the state vector, Δu and Δw are the controlled and non-controlled inputs, Δy and Δz are the controlled and non-controlled outputs, and $\mathbf{A}$, $\mathbf{B_u}$, $\mathbf{B_w}$, $\mathbf{C_y}$ and $\mathbf{C_z}$ are matrices of suitable dimensions. These matrices are obtained after arranging the variables and applying matrix computation laws. Typically, in electrical systems, the inductor currents and the capacitor voltages are selected as state variables. Thus, for a generic multi-terminal grid, the state vector is

$$\Delta x = [\Delta E_1, \cdots, \Delta E_{n+m}, \Delta I_{L_1}, \cdots, \Delta I_{L_r}]^T \tag{8.28}$$

where n is the number of GSCs performing droop control, m the number of wind farms and r the number of branch interconnections (previously defined as $i-j$). The controlled and non-controlled inputs u and w, and the

controlled and non-controlled outputs y and z, can be expressed as

$$\begin{aligned} \Delta u &= [\Delta P_1, \ldots, \Delta P_n]^T, \quad \Delta w = [\Delta P_{n+1}, \ldots, \Delta P_{n+m}]^T \\ \Delta y &= [\Delta E_1, \ldots, \Delta E_n]^T, \quad \Delta z = [\Delta E_{n+1}, \ldots, \Delta E_{n+m}]^T \end{aligned} \tag{8.29}$$

Notice that Δu and Δy are variables related to the GSCs controlling the DC voltage, whereas Δw and Δz are variables related to the WFCs, where the voltage is not controlled. Finally, the presented AC and DC grid side linear models can be combined in order to build a complete model of the multi-terminal grid, as shown in Fig. 8.5. Note that, for simplicity, only the node i AC dynamics are represented in the figure.

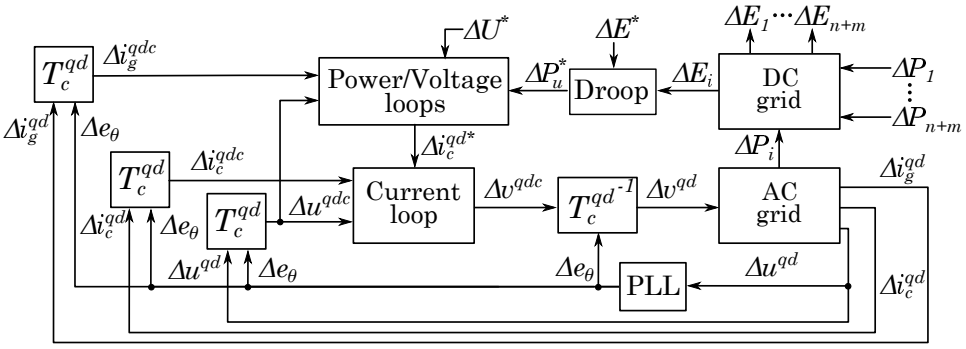

Figure 8.5: Complete linear model of the multi-terminal grid

8.4 Control design methodology

In this section, a theoretical procedure for designing a droop control for multi-terminal grids is addressed. As explained in Section 8.2, the droop control behavior not only depends on the DC or AC grid dynamics, but also on the inner control loops of the converter (Fig. 8.6). Thus, a methodology to design both the inner control loops and the droop voltage control loop is presented.

8.4.1 Current control loop

The inner current control is based on vector control in the synchronous reference frame tuned by Internal Model Control (IMC) technique [61]. Therefore, two PI regulators (G_{CL}) plus a decoupling loop are employed to track the x^{qd} current references in a defined time, following a first order system

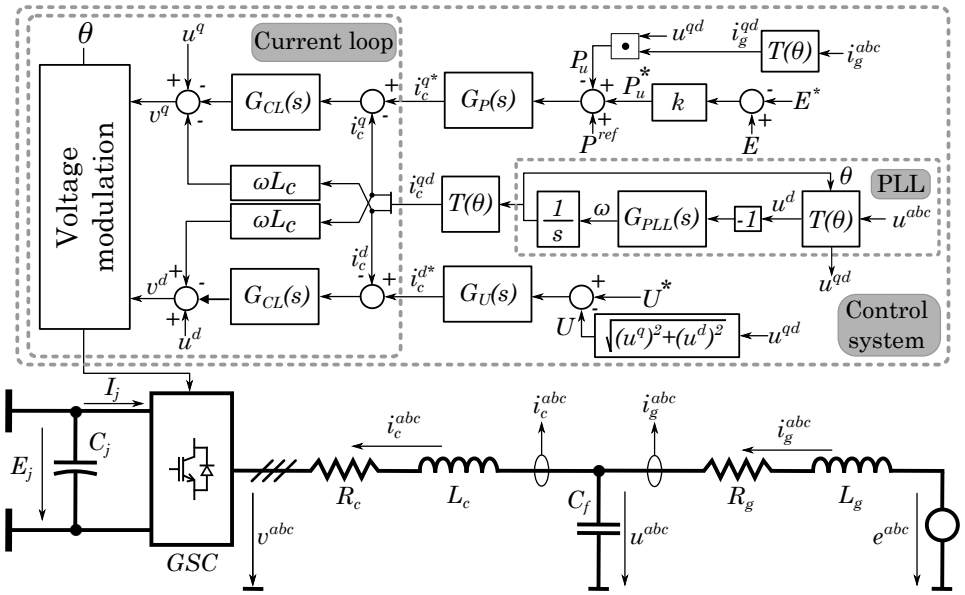

Figure 8.6: Converter control scheme

response with a time constant τ

$$G_{CL}(s) = \frac{k_p s + k_i}{s}, \quad k_p = \frac{L_c}{\tau}, \quad k_i = \frac{R_c}{\tau} \tag{8.30}$$

The control closed loop time constant τ can be calculated based on the desired settling time, which physically represents the time that the system response takes to settle within a range of the final value (usually $\pm 5\%$ or $\pm 2\%$ depending on the criterion). The current loop settling time is typically selected to track current references within a few milliseconds. Saturations are included in the control scheme in order to not exceed the converter's maximum current rating.

8.4.2 Power and voltage loop

As shown in Fig. 8.6, two different controllers, one for tracking power references (G_P) and another to regulate the AC grid voltage (G_U) are introduced as an outer loop of the current vector control. As the power loop is receiving references from the droop voltage loop, fast dynamics could be required to respond to voltage variations in the DC grid. Therefore, the bandwidth for the outer loop controller should be designed to follow relatively fast droop

control outputs without disturbing the inner current control loop. For this reason, the AC side of the system's linear model (Fig. 8.5) is employed to design G_P and G_U, considering the dynamics of the inner current loop. The parameters of both controllers are calculated based on optimization robust control techniques [101, 124]. The optimization inputs are basically the desired settling time for reference tracking for both controllers, expressed as two different objective transfer functions. Then, the optimization algorithm is run to design the PI parameters based on the frequency requirements.

8.4.3 Droop control

The droop design should be carried out considering all the dynamics of the multi-terminal system as these affect the performance of the controller. For this reason, the control analysis should employ the linear model of the multi-terminal grid explained above, which includes the different systems involved in the droop operation. The complete dynamic system of the multi-terminal grid is depicted in Fig. 8.7, where the different control stages of the converter can be identified.

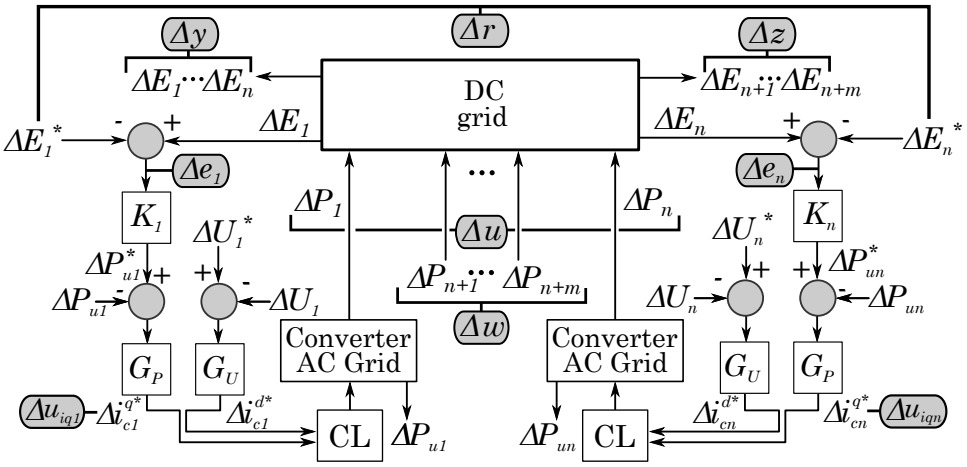

Figure 8.7: HVDC grid control scheme

Fig. 8.7 is redrawn in a conventional feedback structure in Fig. 8.8, showing the control design problem to be addressed. Based on this scheme, different closed loop transfer function matrices can be calculated combining

the converters and both AC and DC grid dynamics

$$\begin{aligned}
&\Delta e(s) = \Delta y(s) - \Delta r(s) = \left[\mathbf{E_w}(s) \quad \mathbf{E_r}(s)\right] \Delta v(s) \\
&\Delta u_{iq}(s) = \left[\mathbf{U_w^{u_{iq}}}(s) \quad \mathbf{U_r^{u_{iq}}}(s)\right] \Delta v(s) \\
&\Delta v(s) = \left[\Delta w(s) \quad \Delta r(s)\right]^T \\
&\Delta r(s) = \left[\Delta E_1^*, \cdots, \Delta E_n^*\right]^T \\
&\Delta u_{iq}(s) = \left[\Delta i_{c1}^{q*}, \cdots, \Delta i_{cn}^{q*}\right]^T
\end{aligned} \tag{8.31}$$

where $\mathbf{E_r}(s)$ and $\mathbf{E_w}(s)$ are the transfer function matrices, relating the droop voltage references r and the power introduced in the HVDC grid by the wind farms w, with the system voltage errors e at the controlled nodes, respectively. Analogously, $\mathbf{U_r^{u_{iq}}}(s)$ and $\mathbf{U_w^{u_{iq}}}(s)$ relate the droop references r and the wind farms incoming power w, with the active current loop references u_{iq}, of the different GSCs.

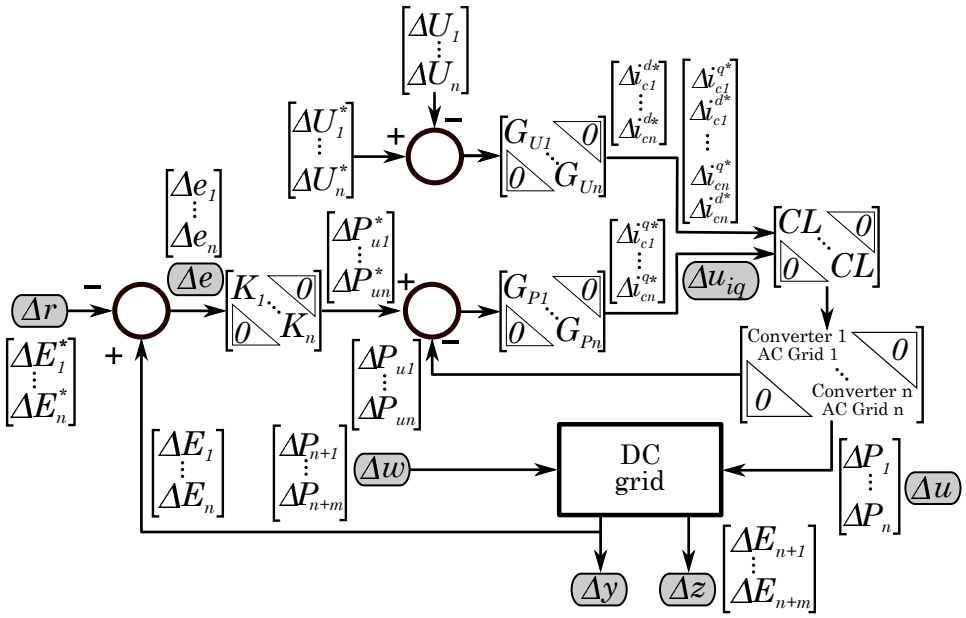

Figure 8.8: HVDC multi-terminal grid control structure

The different droop controller constants can be designed analyzing the frequency response of the multivariable system transfer function matrices, using the singular values representation, further detailed in Chapter 7. Essentially, the specifications for the different droop controllers are: the desired power sharing among the different converters controlling the DC voltage, the maxi-

mum voltage error allowed at the grid terminals and the maximum converter current ratings. These requirements can be transferred as gain boundaries in the multivariable frequency response of the overall system [120], as described in Chapter 7. In order to perform the frequency analysis, the structure of the droop controller is defined as

$$\mathbf{K} = \begin{bmatrix} K_1 & 0 \\ & \ddots \\ 0 & K_n \end{bmatrix} = K_g \begin{bmatrix} q_1 & 0 \\ & \ddots \\ 0 & q_n \end{bmatrix} \tag{8.32}$$

where K_n are the droop constants implemented in each of the GSCs, K_g is a generic scale factor and q_1 to q_n are the weights of the different controllers, which can be calculated based on the power sharing [120]. Thus, in order to dynamically analyze the system, only the parameter K_g needs to be selected, assuming that the q_n constants have already been defined [112]. However, according to [125], scaling the parameter K_g maintaining the different q_n values constant could cause deviation in the desired power sharing between converters. In this work, it is assumed that this deviations can be compensated by the secondary control [121]. Nevertheless, if the power deviation obtained is too large, the droop design solution could be based on performing an analysis of the control dynamics by modifying the q_n parameters as the K_g value is changed, to maintain the defined power sharing.

8.4.4 DC oscillation damping loop

The power and voltage loops are tuned in the range of tens of milliseconds so as not to interact with the lower level current controllers, designed to respond within a few milliseconds. Considering the presented control structure (Fig. 8.6), as the droop controller output is connected to the power loop input, certain fast power transients could cause variations of the DC voltage due to the grid behavior, which could not be properly damped, considering the limited bandwidth of the power loop.

A modification of the presented control scheme (Fig. 8.6) is shown in Fig. 8.9. A compensator between the voltage error and the active current reference is included to damp fast voltage variations of the system, as the current loop has a higher bandwidth compared to the power loop. The suggested compensator is based on a band-pass filter, which does not modify the power sharing in steady state established by the droop control. It should be tuned to act within the frequency range between power regulator and the

current regulator bandwidth. The filter can be designed as

$$G_{bp}(s) = K_{bp} \underbrace{\frac{t_1 s}{t_1 s + 1} \frac{1}{t_2 s + 1}}_{G_f(s)} = K_{bp} G_f(s) \tag{8.33}$$

where K_{bp} is the gain of the band-pass filter and t_1 and t_2 are the time response constants of the high-pass and low-pass filters respectively, compounding the band-pass. If t_1 and t_2 are selected to be the time constants of the power loop and the current loop respectively, the band-pass filter will not interfere in the operation of the mentioned controllers. Also, if different converters include this oscillation damping loop within a multi-terminal grid, different tuning of the filter gains K_{bp} could allow the establishment of an oscillation damping effect sharing between the grid converters, acting similarly to the droop voltage in the defined range of frequencies. Thus, the filter gain could be selected to impose which of the grid converters absorbs a higher percentage of the DC grid voltage oscillations. The multivariable compensator is defined as

$$\mathbf{K_d} = \begin{bmatrix} K_{bp1} G_f(s) & & 0 \\ & \ddots & \\ 0 & & K_{bpn} G_f(s) \end{bmatrix} = K_f \begin{bmatrix} d_1 G_f(s) & & 0 \\ & \ddots & \\ 0 & & d_n G_f(s) \end{bmatrix} \tag{8.34}$$

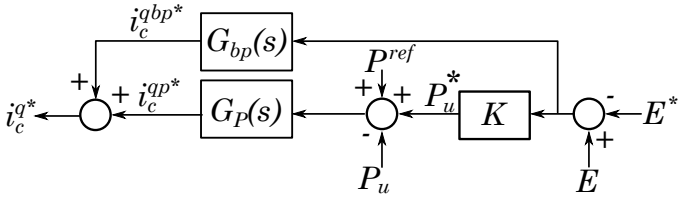

Figure 8.9: Droop and power loop combined with the DC oscillation damping

where K_f is a generic scale factor and d_1 to d_n are the weights of the different compensation loops. Specifically, values from d_1 to d_n can be defined based on the oscillation sharing desired for each GSC, analogously to the droop power sharing parametrization. Thus, selecting the K_f constant, the controller becomes completely defined. To select the mentioned parameter, the singular values of the system transfer function matrices can be analyzed, including the damping loop in the matrix transfer functions calculations.

8.5 Case study

The analyzed HVDC system consists of a three-node multi-terminal VSC-HVDC scheme (Fig 8.10). Two power converters are connected to the AC grid (GSC 1 and GSC 2) and the other is connected to a wind farm (WFC 3). The parameters used for the study are shown in Tables 8.1 and 8.2. The proposed system is analyzed assuming that droop voltage control is carried out by both GSCs, whereas the WFC is supposed to inject all the generated power from the wind power plant to the HVDC grid. It is considered that both GSCs are connected to two different grids under equivalent conditions. The different controllers involved in the system are designed following the methodology described in Section 8.4.

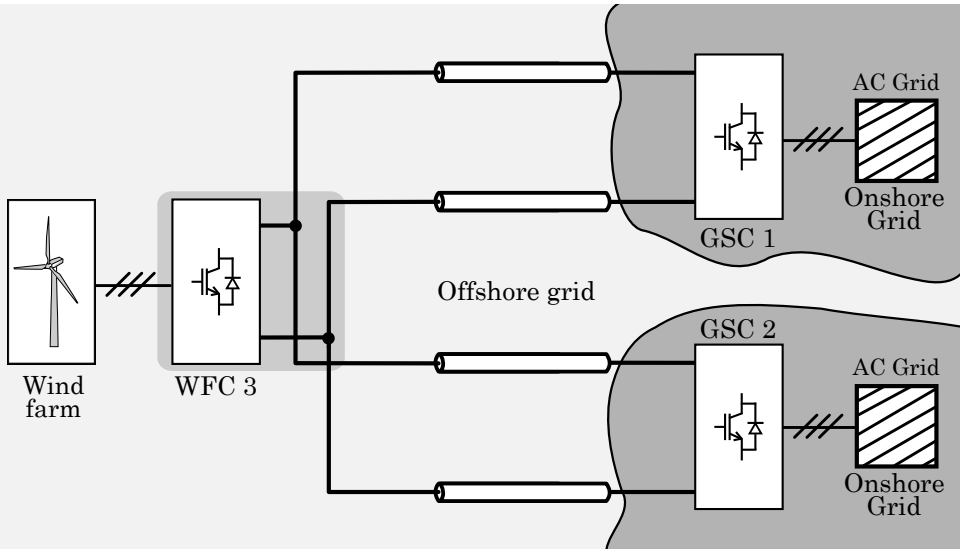

Figure 8.10: Three-terminal VSC-HVDC grid

First, the grid state-space model is obtained. The defined state variables Δx, input signals Δu and Δw, and output signals Δy and Δz are

$$\Delta x = \begin{bmatrix} \Delta E_1 & \Delta E_2 & \Delta E_3 & \Delta I_{L13} & \Delta I_{L23} \end{bmatrix}^T \tag{8.35}$$

$$\Delta u = \begin{bmatrix} \Delta P_1 & \Delta P_2 \end{bmatrix}^T \quad \Delta w = \Delta P_3 \tag{8.36}$$

$$\Delta y = \begin{bmatrix} \Delta E_1 & \Delta E_2 \end{bmatrix}^T \quad \Delta z = \Delta E_3 \tag{8.37}$$

Table 8.1: Parameters of the three-terminal DC grid [114]

DC grid parameters	**Value**	**Units**
Line resistance R	0.0095	Ω/km
Line inductance L	2.112	mH/km
Line capacitance C	0.1906	μF/km
Cable distance 13 d_{13}	100	km
Cable distance 23 d_{23}	150	km
GSC/WFC DC link capacitor C_{dc}	150	μF
GSC rated power P_1, P_2	350	MW
WFC rated power P_3	700	MW
Reference voltage E^*	400	kV

Table 8.2: Parameter of the AC side converters [122]

AC side parameters	**Value**	**Units**
Nominal Power P_1, P_2	350	MW
Nominal Voltage V_{ac}	195	kV
Short Circuit ratio (SCR)	5	-
Grid Thévenin Xn/Rn ratio	10	-
Coupling inductance L_c	0.2	pu
Coupling resistance R_c	0.01	pu
Capacitor filter impedance X_f	5.88	pu

and the linearized state-space matrices are

$$\mathbf{A} = \begin{bmatrix} -\frac{P_{10}}{C_1 E_{10}^2} & 0 & -\frac{1}{C_1} & 0 & 0 \\ 0 & -\frac{P_{20}}{C_2 E_{20}^2} & 0 & 0 & -\frac{1}{C_2} \\ 0 & 0 & +\frac{P_{30}}{C_3 E_{30}^2} & \frac{1}{C_3} & \frac{1}{C_3} \\ \frac{1}{L_{13}} & 0 & -\frac{1}{L_{13}} & -\frac{R_{13}}{L_{13}} & 0 \\ 0 & \frac{1}{L_{23}} & -\frac{1}{L_{23}} & 0 & -\frac{R_{23}}{L_{23}} \end{bmatrix} \tag{8.38}$$

$$\mathbf{B_u} = \begin{bmatrix} \frac{1}{C_1 E_{10}} & 0 \\ 0 & \frac{1}{C_2 E_{20}} \\ \hline \mathbf{0_{3x2}} \end{bmatrix} \mathbf{B_w} = \begin{bmatrix} \mathbf{0_{2x1}} \\ \hline -\frac{1}{C_3 E_{30}} \\ \hline \mathbf{0_{2x1}} \end{bmatrix} \tag{8.39}$$

$$\mathbf{C_y} = \left[\begin{array}{c|c} \mathbf{I_{2x2}} & \mathbf{0_{2x3}} \end{array} \right], \quad \mathbf{C_z} = \left[\begin{array}{c|c|c} \mathbf{0_{1x2}} & 1 & \mathbf{0_{1x2}} \end{array} \right] \tag{8.40}$$

Once the DC grid state-space model is derived, the AC system models for both converters are also obtained. Then, the inner current controller is designed to track references with a settling time of 10 ms [102] based on IMC. It has been observed that the AC grid voltage measured at the capacitors u^{qd} can be significantly affected during a fast active current change, especially for grids with low SCR. As this voltage is employed for the decoupling loop, a low pass filter is applied to the u^{qd} measurement in order to not introduce these fast dynamics into the controller [122]. This low pass filter can be tuned to be around ten times faster than the current loop.

Having defined the current controller, the power and voltage loop PI controllers are designed based on the linear model (Fig. 8.5) applying robust control tuning techniques [101, 124]. The settling time is defined to be approximately 100 ms for both power and voltage regulators [102]. The output of the robust optimization parametric design is shown in Fig. 8.11a, where the closed loop transfer functions of the power and voltage control are depicted, showing an acceptable performance. In addition, a comparison between the complete simulation model and the linear model, derived to design the different controllers, is shown in Fig. 8.11b. This comparison shows that the differences between both models are minimum, thus validating the use of the linear model for control design purposes. Analogously to the current loop, low pass filters are applied to the voltage u^{qd} and current i_g^{qd} measurements employed for calculating the power and voltage feedback signals in order to damp fast transients of the magnitudes. These low pass filters can be also tuned around ten times faster than the current loop.

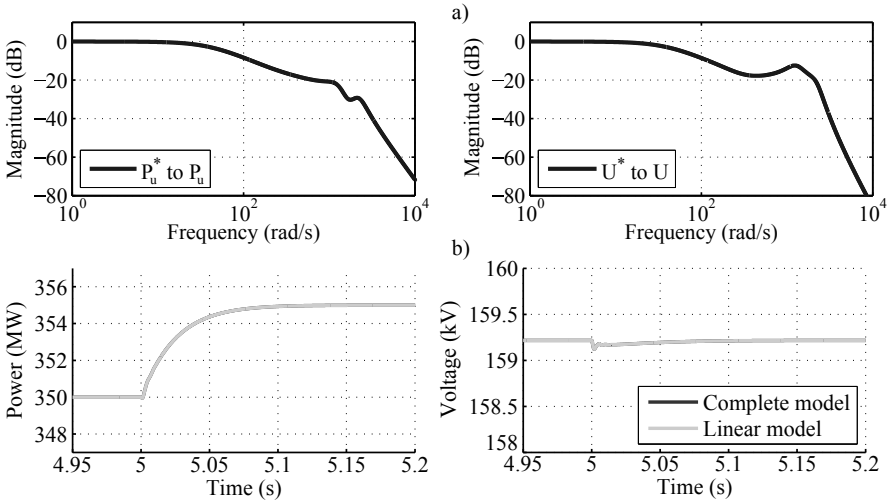

Figure 8.11: Design output of the voltage and power loops of the converter. a) Bode representation of the closed loop transfer functions (P_u^* to P_u and U^* to U). b) Power and voltage response comparison between the complete and linear models for a power step change.

Once the outer power and voltage loops are designed, the multi-terminal droop control is addressed. Assuming that the power generated by the wind power plant, injected to the DC grid by the WFC, must be shared by both GSCs, an initial parametrization is established for the controller. Thus, the multivariable droop controller, considering that GSC 1 and GSC 2 are regulating the voltage, can be defined as

$$\mathbf{K} = \begin{bmatrix} K_1 & 0 \\ 0 & K_2 \end{bmatrix} = K_g \cdot \begin{bmatrix} 1 & 0 \\ 0 & 1 \end{bmatrix} = K_g \cdot \mathbf{I_2} \tag{8.41}$$

where K_1 and K_2 are the droop constants locally implemented at each of the GSCs, expressed in kW/V units. This parametrization could lead to unequal power sharing, depending on the grid impedances and the power flow, something that can be solved by the secondary control. Then, as the exact power sharing is ensured by the upper control layer, this work is focused on the design of the droop control considering the dynamics of the whole multi-terminal grid. Then, based on the linear model of the system, the transfer function matrices $\mathbf{E_w(s)}$, $\mathbf{E_r(s)}$, $\mathbf{U_w^{u_{iq}}}(s)$ and $\mathbf{U_r^{u_{iq}}}(s)$ are obtained following the structure shown in Fig. 8.8. Note that, the reference inputs

E^* do not introduce any voltage error in the system [120], as concluded in Chapter 7. Thus the system analysis will only be focused on $\mathbf{E_w}(s)$ and $\mathbf{U_w^{u_{iq}}}(s)$, which relate wind power input to the voltage errors and the control action, respectively.

Next, the singular values representation of $\mathbf{E_w}(s)$ relating the GSC DC voltage errors and the power coming from the wind farm is depicted in Fig. 8.12a. Assuming a maximum voltage error of a 10% of the nominal value at each terminal and a wind power plant of 700 MW, the singular values representation should not exceed, in steady state, a maximum gain of (see Chapter 7) [120]

$$\bar{\sigma}(\mathbf{E_w}(0)) \leq \frac{||e(0)||_2}{||w(0)||_2} = 20\log_{10}\left(\frac{\sqrt{(e_{mx1}^2 + e_{mx2}^2)}}{P_3}\right) = \\ = 20\log_{10}\left(\frac{\sqrt{(4\cdot 10^5 \cdot 0.1)^2 + (4\cdot 10^5 \cdot 0.1)^2}}{700\cdot 10^6}\right) = -81.85 \text{ dB} \quad (8.42)$$

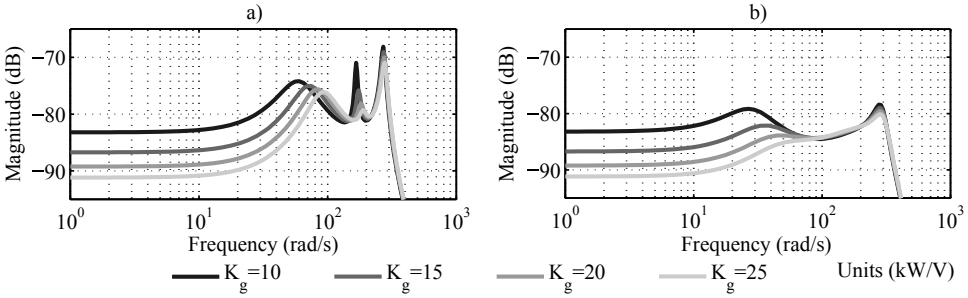

Figure 8.12: Singular values representation of $\mathbf{E_w}(s)$ (DC voltage errors - Wind power input) a) Without oscillation damping, b) With oscillation damping.

According to Fig. 8.12a, all the proposed droop constants K_g are able to maintain the maximum voltage error below 10% of the nominal voltage value, in steady state. However, resonance peaks are observed at relatively low frequencies, which could cause voltage oscillations during wind power flow variations, especially if the wind farm power input excites those frequencies. In order to damp those peaks, the DC oscillation damping loop is implemented in both GSCs defining t_1 and t_2 as the time constants of the current and the power loop respectively. For a first analysis, the same gain is applied to both filters, considering a K_f equal to 1/20 A/V.

Fig. 8.12b shows again the frequency response of $\mathbf{E_w}(s)$, including the designed oscillation damping loop. This graph shows that the gain peaks have been reduced, confirming that the oscillation damping loop is able to improve the droop control performance. Moreover, as the damping effect can be shared between the different GSC converters, Fig. 8.13 is drawn to show how different weights d_1-d_2 affect the overall grid voltage error, as

$$\mathbf{K_d} = \begin{bmatrix} K_{bp1}G_f(s) & 0 \\ 0 & K_{bp2}G_f(s) \end{bmatrix} = \begin{bmatrix} d_1G_f(s) & 0 \\ 0 & d_2G_f(s) \end{bmatrix} \tag{8.43}$$

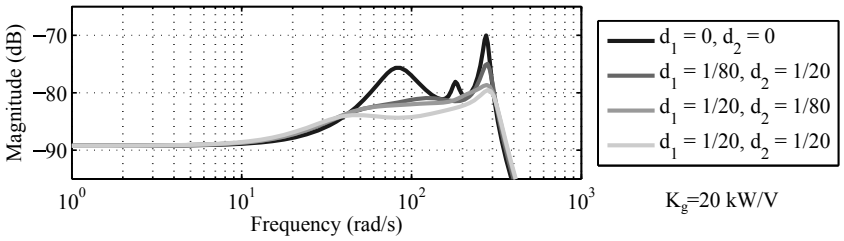

Figure 8.13: Singular values representation of $\mathbf{E_w}(s)$ (DC voltage errors - Wind power input), for different damping loops.

Fig. 8.13 shows that the maximum gains, and consequently the maximum voltage error, are obtained disconnecting the damping loop (d_1 and d_2 equal to 0). On the other hand, the minimum voltage error is achieved when both converters include the same oscillation damping loop. Moreover, two intermediate cases are shown where the damping loop of one of the two GSC converters, has a higher filter gain compared to the other. Both cases show a gain reduction compared to the system without damping loop, revealing that the overall grid error can be compensated acting from different nodes. However, one of the intermediate cases shows lower gain peaks compared to the other. This fact is caused by the difference between the line impedances, which allows one of the GSCs to apply a greater damping effect on the overall grid oscillation damping. This analysis reveals that the damping loop is not only locally affecting the node where it is implemented, but also the overall grid voltage oscillations.

From now on, it is considered that the gain of the damping loop at both GSCs is equal (d_1=d_2=1). Thus, setting the overall gain K_f (see (8.34)), the damping controller is defined. Then, an extended analysis of the singular values of the transfer function $\mathbf{E_w}(s)$, considering several droop constants K_g and including different oscillation damping loops K_f, is shown in Fig. 8.14.

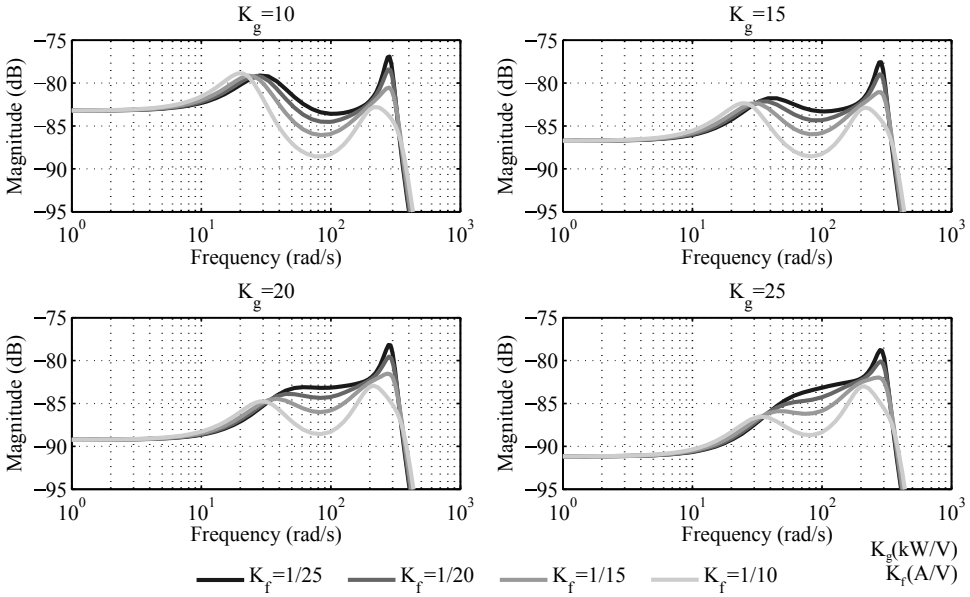

Figure 8.14: Singular values representation of $\mathbf{E_w}(s)$ (DC voltage errors - Wind power input), including damping loop, for different K_g and K_f.

In addition, the singular value representation of the transfer function matrix $\mathbf{U_w^{u_{iq}}}(s)$, relating the control action (represented by the current loop references) and the power coming from the wind farms, is depicted in Fig. 8.15 for several droop constants K_g and different oscillation damping loops K_f.

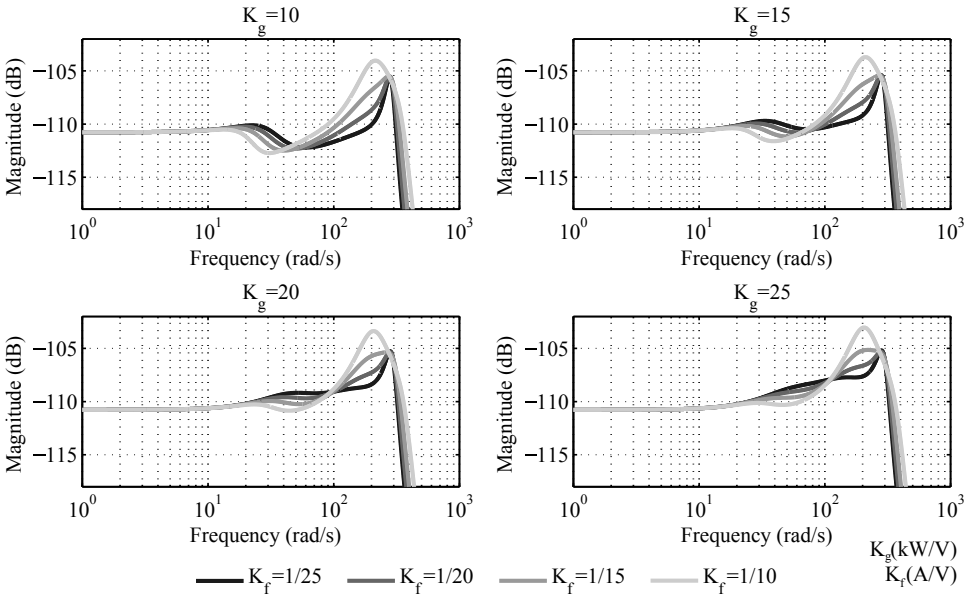

Figure 8.15: Singular values representation of $\mathbf{U_w^{u_{iq}}}(s)$ (Current loop references - Wind power input), including damping loop, for different K_g and K_f.

Figs. 8.14 and 8.15 must be analyzed together in order to decide which are the most favorable constants K_g and K_f for the system. First, analogously to the gain limitation imposed on the frequency response of $\mathbf{E_w(s)}$, another limitation is calculated for the singular values of $\mathbf{U_w^{u_{iq}}}(s)$, considering that the maximum allowed current that could flow through the converter is 110% of the nominal current value. This corresponds to a gain boundary limitation of -109.74 dB.

Before analyzing the singular values, it should be mentioned that the power loop of the WFC is considered to respond with the same bandwidth as the GSC. Then, power disturbances with frequencies larger than approximately 40 rad/s will not be introduced into the system, unless an AC fault occurs in the wind farm. In that case, the WFC could reduce the power injected to the DC grid rapidly to zero.

Fig. 8.14 shows that constants K_g greater than 15 kW/V with K_f also

greater than 1/20 A/V[1] allow the system to be operated maintaining the voltage error under the defined 10%. In addition, as the system wind power disturbances are limited in bandwidth, the error can even be maintained below 5%. To achieve this goal, the GSCs need to inject current to the grid (control action) without exceeding its own limits. Then, the singular values gains of $\mathbf{U_w^{u_{iq}}}(s)$, shown in Fig. 8.15, should be maintained below the calculated boundary. It can be seen that all curves exceed the maximum allowed gain at a certain frequency, which is not desirable from the perspective of converter operation. Specifically, certain combinations of K_g and K_f present gain curves that are crossing the defined boundary below the power loop bandwidth (40 rad/s), which could lead the converter to operate beyond its limits. For this reason, constants K_g higher than 20 kW/V should not be included in the control system. Finally, in order to select the controller constants, among the different possible available combinations, the defined criterion is to minimize the voltage error while keeping the converter operating within its current limits. Based on this criterion, constants K_g of 20 kW/V and K_f of 1/20 A/V are able to operate the system securely, minimizing the error without exceeding the current limitation.

Once the droop control design is concluded, Matlab Simulink® simulations of the three-terminal grid (Fig. 8.10) are carried out to validate the obtained results. Figs. 8.16 and 8.17 show the voltage droop control response (performed by the GSCs) to a nominal power input from the WFC from 0 MW to 700 MW at 2 s. During the simulation, the power reference of both GSCs P_{ref} is maintained at zero to observe how the designed distributed droop controller is able to control the overall DC voltage without communications. The cable model employed is a π-equivalent model with 100 sections. Fig. 8.16 shows that both GSCs meet the power sharing condition because both are extracting approximately the same amount of power, despite the variations introduced by the different cable longitudes. The existing deviation could be compensated by the secondary control. It can also be observed that no voltage error is present when no power is flowing to the grid.

Focusing on the dynamics, during the power transient the voltage is maintained below 10% of the maximum error defined, even below 5%. Also, the currents do not exceed the defined converter limits. Thus, the presented simulations show that the control design is able to operate the system avoiding large variations both in the AC and the DC side variables, keeping the converters operation within their limits.

[1]For lower K_g values 1/15 A/V might be required to avoid exceeding the error limitation.

The same simulation is carried out without including the damping compensation loop in both converters in order to analyze the system behavior. Fig. 8.17 shows that without including this compensation, the oscillations in all system variables increase compared to Fig. 8.16, confirming the effectiveness of the damping loop.

Fig. 8.18 shows a fast power reduction introduced by the WFC caused by an AC fault in the wind farm grid. The power injected from the wind farm is rapidly reduced to zero at 4.5 s. Large oscillations in voltage and current can be seen due to the fast power reduction. This can be explained due to the large gain peaks seen in Figs. 8.14 and 8.15 at high frequencies. Therefore, when these peaks are excited due to the fast power reduction, oscillations at those frequencies appear. Despite these transients, the system reaches the steady state in a few milliseconds without exceeding any limit.

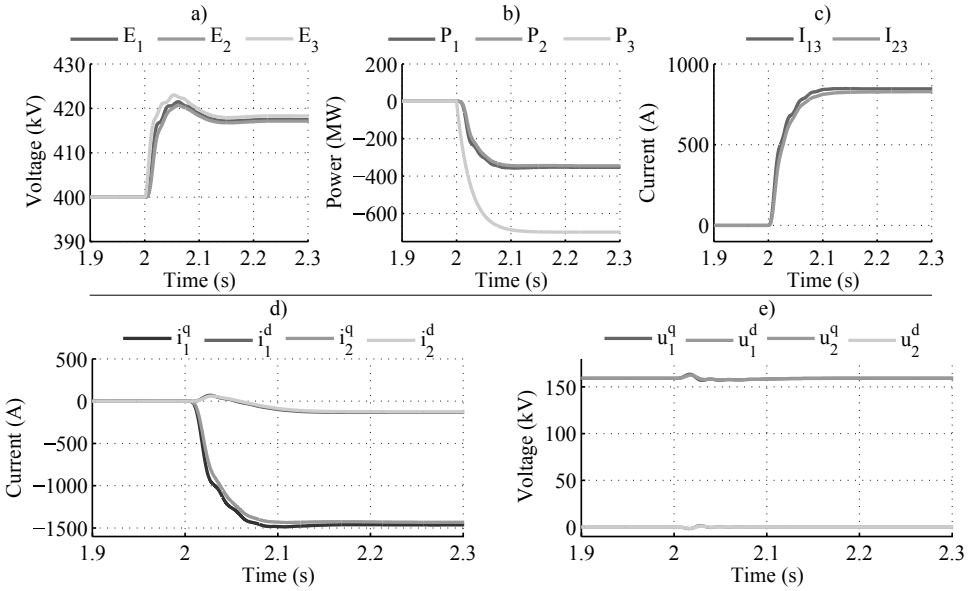

Figure 8.16: Simulation results after applying a WFC reference step power change. a) DC grid voltages. b) Converters power. c) DC lines current. d) Currents in qd frame. e) PCC voltages in qd frame

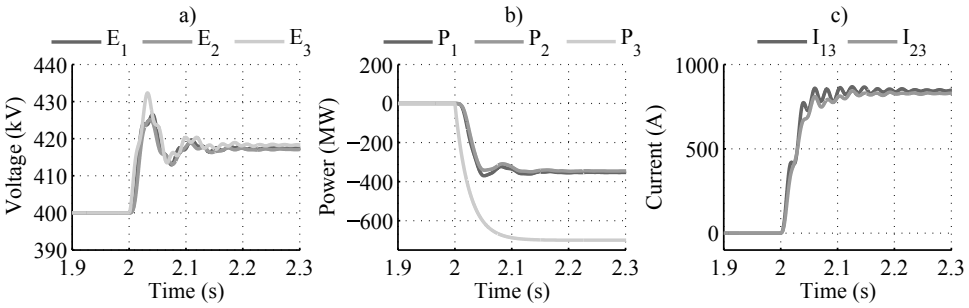

Figure 8.17: Simulation results after applying a WFC reference step power change without including the damping loop. a) DC grid voltages. b) Converters power. c) DC lines current.

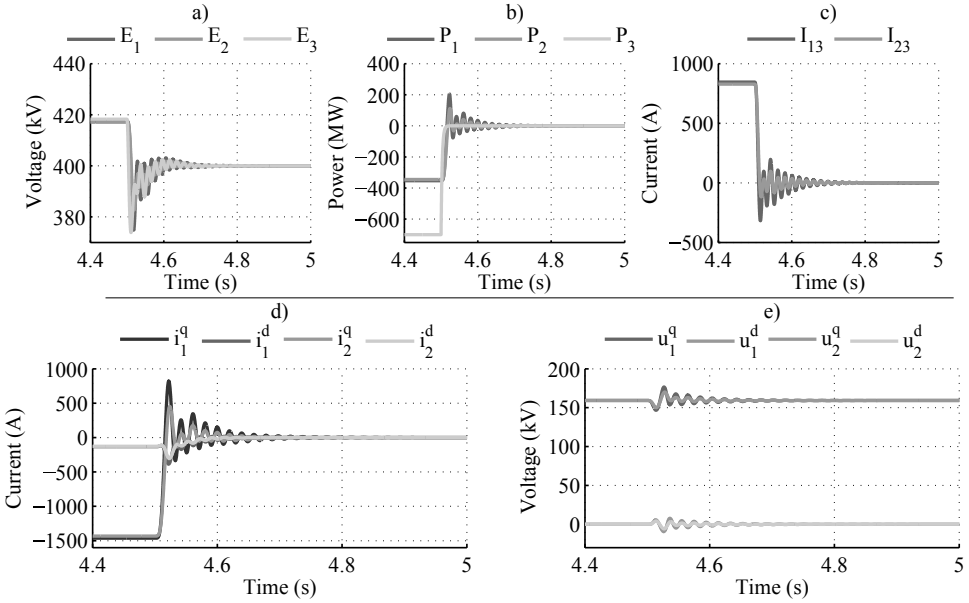

Figure 8.18: Simulation results after a WFC power reduction - DC grid. a) DC grid voltages. b) Converters power. c) DC lines current. d) Currents in qd frame. e) PCC voltages in qd frame.

8.6 Conclusions

A DC voltage droop design methodology considering the different dynamics involving a multi-terminal VSC-HVDC grid is presented. This methodology includes a procedure for obtaining a linearized model of the complete system. Also, a design criterion for the current loop and the power and voltage loops is provided. Once the inner dynamics of the converter are established, a multivariable frequency analysis of the droop control performance can be carried out to determine the proper DC droop voltage gains, in order to accomplish the defined system requirements. In addition, a controller for damping the oscillations introduced by the system frequency resonances is presented. The global control design procedure is validated through dynamic simulations.

Chapter 9

Conclusions

This thesis gathers several studies related with the control of different power converters for offshore wind. This chapter describes the main conclusions and contributions of the work done.

9.1 Contributions

The main findings are detailed structured by chapters:

- In Chapter 3 the decentralized control design of a triple three-phase permanent magnet synchronous generator-based wind turbine is presented. Basically, each three-phase stator of the generator is connected to the wind farm grid through an independent back-to-back converter. The controller is designed to avoid interactions between the different stators, magnetically coupled, even though each stator performs its own independent vector control. The design of the controller is developed based on classic vector control combined with a frequency analysis of the closed loop controller performance. The proposed methodology is first tested on simulations and then validated in a scaled wind turbine generator test rig. The performed tests have shown satisfactory results proving the concept viability. Then, the proposed concept combined with the designed controllers could be an interesting alternative for offshore applications, showing additional capabilities in terms of redundancy and control possibilities.
- In Chapter 4 the control design of a Dual Bridge Series Resonant Converter is addressed. A simple analysis of the classic phase-shift control, reveals that this control strategy may lead to high currents flowing through the HF AC side, even for a reduced active power flow transmission, particularly if the voltage ratio of the DC interconnected systems is far from the nominal value. To solve this problem, an optimized controller based on the three-level modulation is developed,

which is able to minimize the HF AC currents during the converter operation. The concept is validated on simulations, and both strategies are compared, showing that the proposed technique is able to significantly reduce the AC current. Also, a 50 kW DBSRC converter prototype has been developed. Several tests are performed employing the classic control showing a proper behavior. As expected, this operation mode shows large currents flowing through the AC circuit, even transferring a reduced amount of active power, confirming that the optimized control proposed, can be an interesting option to operate this type of converters.

- In Chapter 5 the control of a half-bridge-cell based Modular Multilevel Converter is analyzed in detail. The roles of the current components flowing through the converter are identified to perform a proper power exchange between the AC and the DC grid, while maintaining the converter energy balanced. The design of the current regulators for the grid and additive currents is addressed ensuring a perfect reference tracking for DC and line frequency components. Also, the reference calculation strategy, that allows the calculation of the current references based on the power reference outputs of the energy controllers, is developed considering possible unbalanced AC voltage operation. Then, the design of the energy regulators to balance the converter is addressed covering all the converter degrees of freedom. The different controllers design is carried out using classic control techniques. The control strategy suggested is validated through simulation results.

- In Chapter 6 the operation of half-bridge-cell based Modular Multilevel Converters during specific unbalanced AC grid voltage sags is addressed. Based on Chapter 5 results, it can be observed that the reference calculation strategy developed for the converter inner AC currents (used to balance the energy of the upper and lower converter arms) requires a modification if the positive and the negative sequence AC grid voltages are equal. For this reason, three different techniques are proposed to solve this problem. First, the disconnection of the energy balancing between the upper and lower arms during the voltage sag is proposed, considering that AC voltage sags mainly disturb the energy differences between phase units. Then, two different solutions developed using linear algebra tools for incompatible systems are proposed. The three methodologies are tested for all the possible voltage sags that can cause the problematic grid voltage condition showing

satisfactory results, especially the algebra-based approaches.

- In Chapter 7 a design methodology for droop control in multi-terminal HVDC grids is described. First, the methodology details a systematic procedure to formulate a linear model of generic multi-terminal HVDC grids. Once the model is obtained, a criterion is provided to select the droop gain constants, taking into account the dynamics of the entire multi-terminal HVDC system. The limitation of DC voltage errors and the converter currents define a range on the droop gains that achieve the better compromise between the specifications. Each local controller can affect the global stability and the DC voltage in other terminals. For these reasons, the droop constant selection must be addressed in the context of multivariable system theory to consider the dynamic behavior of the entire multi-terminal grid, both in normal operation and in fault conditions. The procedure is applicable to any other multi-terminal HVDC grid with more inputs and outputs.

- In Chapter 8 the methodology proposed in Chapter 7 is expanded. The droop design methodology is developed considering different dynamics involving a multi-terminal VSC-HVDC grid. The proposed model not only includes the dynamics of the DC grid as in Chapter 7, but also includes the AC grid, the PLL, the current loop and the power and voltage loops dynamics. Also, design criteria for the current loop and the power and voltage loops are provided. Once the linearized model is obtained, including the corresponding converter control loops, a design of the droop controller based on a multivariable frequency analysis can be carried out to determine the proper DC droop voltage gains to meet the defined system requirements. The control structure also considers a controller to damp the oscillations introduced by the system frequency resonances. The global control design procedure is validated through dynamic simulations.

9.2 Future work

Offshore wind technology is one of the most promising renewable energies. It is a relatively new technology and there is still much research to do in many different parts of the offshore wind technology. The work developed on this thesis, related with different power converters of the offshore wind technology, has raised several research lines for future work. Given this, the future research lines are described by chapter:

- Chapter 3
  - Design the current controller considering the reluctance effect for interior permanent magnet machines.
  - Compare the performance between a centralized controller and a decentralized controller.
- Chapter 4
  - Test the three-level operation in the experimental platform, not only for start-up purposes.
  - Include restrictions in the optimization parameters that impose the soft-switching conditions.
  - Test the proposed strategy on a classic Dual Active Bridge converter.
  - Compare the losses between the two-level modulation and the three-level modulation.
- Chapter 5 and 6 (gathered by topic)
  - Perform a similar study for different types of MMCs.
  - Test the control design on an MMC experimental platform.
- Chapter 7 and 8 (gathered by topic)
  - Compare different cable models and their impact on the design.
  - Compare the dynamic performance between different existing droop controllers.

Bibliography

[1] IRENA, "*Renewable energy capacity statistics 2013*," [Online]. Available: http://www.irena.org/Publications. [Accessed: Jan. 13, 2016]. xv, 2, 3

[2] World Energy Council, "*World energy perspective 2013. Cost of energy technologies*," [Online]. Available: http://www.worldenergy.org/publications [Accessed: Jan. 13, 2016]. xv, 2, 4

[3] *The European offshore wind industry - key trends and statistics 2013.* European Wind Energy Association, EWEA, 2013. 5

[4] *Europe's onshore and offshore wind energy potential.* Eur. Environmental Agency, Copenhaguen, 2009. 5, 15

[5] *Wind energy technology roadmap.* Energy Agency, Paris, 2013. 5

[6] S. Faulstich, B. Hahn, and P. J. Tavner, "Wind turbine downtime and its importance for offshore deployment," *Wind Energy*, vol. 14, no. 3, pp. 327–337, 2011. 5, 30

[7] R. Semken, M. Polikarpova, P. Roytta, J. Alexandrova, J. Pyrhonen, J. Nerg, A. Mikkola, and J. Backman, "Direct-drive permanent magnet generators for high-power wind turbines: benefits and limiting factors," *IET Renewable Power Generation*, vol. 6, no. 1, pp. 1–8, Jan. 2012. 5, 29

[8] S. Brisset, D. Vizireanu, and P. Brochet, "Design and optimization of a nine-phase axial-flux PM synchronous generator with concentrated winding for direct-drive wind turbine," *IEEE Trans. Ind. Appl.*, vol. 44, no. 3, pp. 707–715, May 2008. 5, 31, 33

[9] J. Sauter and A. Mirzaian, "Encoderless control of a 6 MW permanent magnet synchronous generator," in *15th Eur. Conf. on Power Electron. and Appl. (EPE)*, Lille, France, Sept. 2013, pp. 1–10. 5, 6, 31, 33

[10] E. Prieto-Araujo, A. Junyent-Ferré, D. Lavèrnia, and O. Gomis-Bellmunt, "Distributed control of a nine-phase permanent magnet generator and scaled platform validation," in *EWEA Annual event 2014*, Barcelona, Spain, Mar. 2014. 5

[11] E. Levi, "Multiphase electric machines for variable-speed applications," *IEEE Trans. Ind. Electron.*, vol. 55, no. 5, pp. 1893–1909, May 2008. 5, 29, 31

[12] S. Lundberg, *Wind farm configuration and energy efficiency studies - Series DC versus AC layouts.* Dept. of Energy and Environment, Electric Power Eng., Chalmers University of Technology, 2006. 6, 57

[13] G. Ortiz, J. Biela, D. Bortis, and J. Kolar, "1 Megawatt, 20 kHz, isolated, bidirectional 12 kV to 1.2 kV DC-DC converter for renewable energy applications," in *2010 Int. Power Electronics Conf. (IPEC)*, Sapporo, Japan, Jun. 2010, pp. 3212–3219. 6, 57

[14] T. Lagier and P. Ladoux, "A comparison of insulated DC-DC converters for HVDC off-shore wind farms," in *5th Int. Conf. on Clean Elect. Power (ICCEP)*, Taormina, Italy, Jun. 2015, pp. 33–39. 6, 57

[15] M. De-Prada-Gil, J. L. Domínguez-García, F. Díaz-González, M. Aragüés-Peñalba, and O. Gomis-Bellmunt, "Feasibility analysis of offshore wind power plants with DC collection grid," *Renewable Energy*, vol. 78, pp. 467–477, 2015. 6, 57

[16] J. Robinson, D. Jovcic, and G. Joos, "Analysis and design of an offshore wind farm using a MV DC grid," *IEEE Trans. Power Del.*, vol. 25, no. 4, pp. 2164–2173, Oct. 2010. 6, 57

[17] R. De Doncker, D. Divan, and M. Kheraluwala, "A three-phase soft-switched high-power-density DC/DC converter for high-power applications," *IEEE Trans. Ind. Appl*, vol. 27, no. 1, pp. 63–73, Jan. 1991. 6, 57

[18] Y. Cheron and C. Goodman, *Soft Commutation.* Springer Netherlands, 1992. 6, 57

[19] T. Ackermann, "Transmission systems for offshore wind farms," *IEEE Power Eng. Rev.*, vol. 22, no. 12, pp. 23–27, Dec. 2002. 6

[20] J. Reeve, "Multiterminal HVDC power systems," *IEEE Trans. Power App. and Syst.*, vol. PAS 99, no. 2, pp. 729–737, 1980. 6

[21] J. Arrillaga, *High Voltage Direct Current Transmission*, 2nd ed. London, U.K.: Institution of Electrical Engineers, 1998. 6

[22] U. Axelsson, A. Holm, C. Liljegren, M. Aberg, K. Eriksson, and O. Tollerz, "The Gotland HVDC light project-experiences from trial and commercial operation," in *Proc. of the 16th Int. Conf. and Exhibition on Contributions Electricity Distribution CIRED*, vol. 1, Amsterdam, Netherlands, Jun. 2001, p. 5. 6

[23] J. Dorn, H. Huang, and D. Retzmann, "A new multilevel voltage-sourced converter topology for HVDC applications," in *Proc. of the CIGRE Session 2008. B4 HVDC and Power Electronics*, 2008. 6

[24] O. Gomis-Bellmunt, J. Liang, J. Ekanayake, R. King, and N. Jenkins, "Topologies of multiterminal HVDC-VSC transmission for large offshore wind farms," *Elect. Power Syst. Res.*, vol. 81, no. 2, pp. 271–281, 2011. 6, 7, 133

[25] O. Gomis-Bellmunt, J. Liang, J. Ekanayake, and N. Jenkins, "Voltage-current characteristics of multiterminal HVDC-VSC for offshore wind farms," *Elect. Power Syst. Res.*, vol. 81, no. 2, pp. 440–450, 2011. 6, 7, 133, 134, 162

[26] M. Barnes and A. Beddard, "Voltage source converter HVDC links - the state of the art and issues going forward," *Energy Procedia*, vol. 24, pp. 108–122, Jan. 2012. 7

[27] A. Lesnicar and R. Marquardt, "An innovative modular multilevel converter topology suitable for a wide power range," in *IEEE Power Tech Conf. Proc.*, vol. 3, Bologna, Italy, Jun. 2003, p. 6. 7, 83, 112

[28] J. Dorn, H. Huang, and D. Retzmann, "A new multilevel voltage-sourced converter topology for HVDC applications," *CIGRE Session. Int. Council on Large Electric Syst.*, Aug. 2008. 7, 83

[29] B. Jacobson, P. Karlsson, G. Asplund, L. Harnefors, and T. Jonsson, "VSC-HVDC transmission with cascaded two-level converters," in *CIGRE B4-110 session*, 2010. 7, 83

[30] M. Merlin, T. Green, P. Mitcheson, D. Trainer, D. Critchley, and R. Crookes, "A new hybrid multi-level voltage-source converter with dc fault blocking capability," in *9th IET Int. Conf. on AC and DC Power Transmission (ACDC)*, London, UK, Oct. 2010, pp. 1–5. 7, 83

[31] J. Liang, O. Gomis-Bellmunt, J. Ekanayake, and N. Jenkins, "Control of multi-terminal VSC-HVDC transmission for offshore wind power," in *13th Eur. Conf. on Power Electron. and Appl. (EPE)*, Barcelona, Spain, Sept. 2009, pp. 1–10. 7, 133

[32] E. Hau, *Wind Turbines: Fundamentals, Technologies, Application, Economics.* Springer, 2005. 15

[33] E. Golding, *The Generation of Electricity by Wind Power.* E. and F. N. Spon Ltd., 1977. 15

[34] J. Slootweg, H. Polinder, and W. L. Kling, *Wind power in power systems*, T. Ackermann, Ed. Wiley, 2005. 15, 20, 22

[35] Global Wind Energy Council, "*Global Wind Statistics 2015*," [Online]. Available: http://www.gwec.net/ [Accessed: Jan. 13, 2016]. 15

[36] H. Li and Z. Chen, "Overview of different wind generator systems and their comparisons," *Renewable Power Generation, IET*, vol. 2, no. 2, pp. 123–138, 2008. 20, 23, 24, 25

[37] H. Helle and F. Blaajberg, *Conceptual survey of Generators and Power Electronics for Wind Turbines.* Risø Nat. Laboratory, 2001. 20, 21

[38] M. Khadraoui and M. Elleuch, "Comparison between OptiSlip and fixed speed wind energy conversion systems," in *5th Int. Multi-Conf. on Syst., Signals and Devices (IEEE SSD)*, Amman, Jordan, 2008, pp. 1–6. 21

[39] R. Pena, J. Clare, and G. Asher, "Doubly fed induction generator using back-to-back PWM converters and its application to variable-speed wind-energy generation," *IEE Proc. Electric Power Appl.*, vol. 143, no. 3, pp. 231–241, 1996. 22

[40] O. Gomis-Bellmunt, A. Junyent-Ferré, A. Sumper, and J. Bergas-Jané, "Ride-through control of a doubly fed induction generator under unbalanced voltage sags," *IEEE Trans. Energy Convers.*, vol. 23, no. 4, pp. 1036–1045, 2008. 22

[41] Z. Zhu and J. Hu, "Electrical machines and power electronic systems for high-power wind energy penetration applications: Part 1 - market penetration, current technology and advanced machine systems," *COMPEL: The Int. Journal for Computation and Mathematics in Elect. and Electron. Eng.*, vol. 32, no. 4, pp. 7–33, 2012. 23, 26, 27

[42] H. Polinder, S. W. de Haan, M. R. Dubois, and J. G. Slootweg, "Basic operation principles and electrical conversion systems of wind turbines," *EPE Journal*, vol. 15, no. 4, pp. 43–50, 2005. 23

[43] F. J. Dubois M., Polinder H., "Comparison of generator topologies for direct-drive wind turbines," *Proc. Nordic Countries Power and Ind. Electron. Conf. (NORPIE)*, pp. 22–26, 2010. 23

[44] H. Polinder, F. Van der Pijl, G.-J. de Vilder, and P. Tavner, "Comparison of direct-drive and geared generator concepts for wind turbines," in *IEEE Int. Conf. on Elect. Machines and Drives*, San Antonio, TX, USA, May 2005, pp. 543–550. 24, 25

[45] A. Grauers, "Design of direct-driven permanent-magnet generators for wind turbines," Ph.D. dissertation, School of Electrical and Computer Engineering, Chalmers University of Technology, 1996. 24

[46] A. EL-Refaie and T. Jahns, "Optimal flux weakening in surface pm machines using fractional-slot concentrated windings," *IEEE Trans. Ind. Appl.*, vol. 41, no. 3, pp. 790–800, 2005. 25

[47] M. Duran, S. Kouro, B. Wu, E. Levi, F. Barrero, and S. Alepuz, "Six-phase PMSG wind energy conversion system based on medium-voltage multilevel converter," in *Proc. of the 14th Eur. Conf. on Power Electron. and Appl. (EPE)*, Aug. 2011, pp. 1–10. 26, 31

[48] R. Bojoi, M. Lazzari, F. Profumo, and A. Tenconi, "Digital field-oriented control for dual three-phase induction motor drives," *IEEE Trans. Ind. Appl.*, vol. 39, no. 3, pp. 752–760, May 2003. 29, 30, 31

[49] L. De Camillis, M. Matuonto, A. Monti, and A. Vignati, "Optimizing current control performance in double winding asynchronous motors in large power inverter drives," *IEEE Trans. Power Electron.*, vol. 16, no. 5, pp. 676–685, Sept. 2001. 29, 30, 34

[50] J. Karttunen, S. Kallio, P. Peltoniemi, P. Silventoinen, and O. Pyrhonen, "Decoupled vector control scheme for dual three-phase permanent magnet synchronous machines," *IEEE Trans. Ind. Electron.*, vol. 61, no. 5, pp. 2185–2196, May 2014. 29, 30

[51] L. Hua, Z. Yunping, and H. Bi, "The vector control strategies for multiphase synchronous motor drive systems," in *IEEE Int. Symp. on Ind. Electron., 2006*, vol. 3, Jul. 2006, pp. 2205–2210. 30

[52] P. Krause, *Analysis of electric machinery*, ser. McGraw-Hill series in Elect. and Comput. Eng. McGraw-Hill, 1986. 31

[53] T. Lipo, "A dq model for six phase induction machines," in *Int. Conf. on Electric Machines*, Helsinki, Finland, Oct. 1980, pp. 860–867. 31

[54] Y. Zhao and T. Lipo, "Space vector PWM control of dual three-phase induction machine using vector space decomposition," *IEEE Trans. Ind. Appl.*, vol. 31, no. 5, pp. 1100–1109, Sep 1995. 31

[55] M. Andriollo, G. Bettanini, G. Martinelli, A. Morini, and A. Tortella, "Analysis of double-star permanent-magnet synchronous generators by a general decoupled d-q model," *IEEE Trans. Ind. Appl.*, vol. 45, no. 4, pp. 1416–1424, Jul. 2009. 31

[56] S. Kallio, M. Andriollo, A. Tortella, and J. Karttunen, "Decoupled d-q model of double-star interior-permanent-magnet synchronous machines," *IEEE Trans. Ind. Electron.*, vol. 60, no. 6, pp. 2486–2494, Jun. 2013. 31, 33

[57] T. Lipo, *Analysis of Synchronous Machines, Second Edition*. Taylor & Francis, 2012. 33

[58] J. Hendershot and T. Miller, *Design of Brushless Permanent Magnet Motors*, ser. McGraw-Hill series in Elect. and Comput. Eng., 2010. 33

[59] C. Ong, *Dynamic Simulation of Electric Machinery: Using MATLAB/SIMULINK*. Prentice Hall PTR, 1998. 34, 165, 166

[60] R. Nelson and P. Krause, "Induction machine analysis for arbitrary displacement between multiple winding sets," *IEEE Trans. Power App. Syst.*, vol. PAS-93, no. 3, pp. 841–848, May 1974. 34

[61] L. Harnefors and H.-P. Nee, "Model-based current control of AC machines using the internal model control method," *IEEE Trans. Ind. Appl.*, vol. 34, no. 1, pp. 133–141, Jan. 1998. 36, 37, 40, 99, 167, 170

[62] S. Skogestad and I. Postlethwaite, *Multivariable feedback control: analysis and design*. Wiley, 1996. 37, 73, 99, 103, 142

[63] S.-K. Chung, "A phase tracking system for three phase utility interface inverters," *IEEE Trans. Power Electron.*, vol. 15, no. 3, pp. 431–438, 2000. 40, 166

[64] X. Li and A. K. Bhat, "Analysis and design of high-frequency isolated dual-bridge series resonant DC/DC converter," vol. 25, no. 4. IEEE, 2010, pp. 850–862. 58, 59

[65] P. Kundur, N. J. Balu, and M. G. Lauby, *Power system stability and control*. McGraw-hill New York, 1994, vol. 7. 58

[66] Y. Du, X. Bian, S. Lukic, B. Jacobson, and A. Huang, "A novel wide voltage range bi-directional series resonant converter with clamped capacitor voltage," in *35th Annu. Conf. of IEEE Ind. Electron. (IECON)*, Porto, Portugal, Nov. 2009, pp. 82–87. 58

[67] L. Corradini, D. Seltzer, D. Bloomquist, R. Zane, D. Maksimovic, and B. Jacobson, "Minimum current operation of bidirectional dual-bridge series resonant DC/DC converters," *IEEE Trans. Power Electron.*, vol. 27, no. 7, pp. 3266–3276, Jul. 2012. 58

[68] R. Steigerwald, "A comparison of half-bridge resonant converter topologies," *IEEE Trans. Power Electron.*, vol. 3, no. 2, pp. 174–182, Apr. 1988. 59

[69] S. Inoue and H. Akagi, "A bi-directional isolated DC/DC converter as a core circuit of the next-generation medium-voltage power conversion system," in *37th IEEE Power Electron. Specialists Conf.*, Jeju, South Korea, Jun. 2006, pp. 1–7. 59

[70] R. Steigerwald, "A comparison of half-bridge resonant converter topologies," *IEEE Trans. Power Electron.*, vol. 3, no. 2, pp. 174–182, Apr. 1988. 59

[71] X. Li and A. Bhat, "Analysis and design of high-frequency isolated dual-bridge series resonant DC/DC converter," *IEEE Trans. Power Electron.*, vol. 25, no. 4, pp. 850–862, Apr. 2010. 67

[72] MathWorks, "*Optimization toolbox. User's Guide 2015*," [Online]. Available: http://uk.mathworks.com. [Accessed: Jan. 13, 2016]. 71

[73] B. Bose, *Power Electronics And Motor Drives: Advances and Trends*. Elsevier Science, 2010. 83

[74] A. Antonopoulos, L. Angquist, and H.-P. Nee, "On dynamics and voltage control of the modular multilevel converter," in *13th Eur. Conf. on Power Electron. and Appl. (EPE)*, Barcelona, Spain, Sept. 2009, pp. 1–10. 84

[75] Q. Tu, Z. Xu, and L. Xu, "Reduced switching-frequency modulation and circulating current suppression for modular multilevel converters," *IEEE Trans. Power Del.*, vol. 26, no. 3, pp. 2009–2017, Jul. 2011. 84, 112

[76] M. Hagiwara, R. Maeda, and H. Akagi, "Control and analysis of the modular multilevel cascade converter based on double-star chopper-cells (MMCC-DSCC)," *IEEE Trans. Power Electron.*, vol. 26, no. 6, pp. 1649–1658, Jun. 2011. 84

[77] L. Harnefors, A. Antonopoulos, S. Norrga, L. Angquist, and H.-P. Nee, "Dynamic analysis of modular multilevel converters," *IEEE Trans. Ind. Electron.*, vol. 60, no. 7, pp. 2526–2537, Jul. 2013. 84, 101

[78] A. Junyent-Ferré, P. Clemow, M. Merlin, and T. Green, "Operation of HVDC modular multilevel converters under DC pole imbalances," in *16th Eur. Conf. on Power Electron. and Appl. (EPE)*, Lappeenranta, Finland, Aug. 2014, pp. 1–10. 84, 114, 116

[79] K. Sharifabadi, R. Teodorescu, H.-P. Nee, L. Harnefors, and S. Norrga, "Modular multilevel converters - MMC: Principles, design, control, modelling and challenges in VSC-HVDC," in *17th Eur. Conf. on Power Electron. and Appl. (EPE)*, Geneva, Switzerland, Sept. 2015. 84

[80] D. Jovcic and A. Jamshidi Far, "Phasor model of modular multilevel converter with circulating current suppression control," *IEEE Trans. Power Del.*, vol. 30, no. 4, pp. 1889–1897, Aug. 2015. 84

[81] M. Guan and Z. Xu, "Modeling and control of a modular multilevel converter-based HVDC system under unbalanced grid conditions," *IEEE Trans. Power Electron.*, vol. 27, no. 12, pp. 4858–4867, Dec. 2012. 84, 111

[82] Q. Tu, Z. Xu, Y. Chang, and L. Guan, "Suppressing DC voltage ripples of MMC-HVDC under unbalanced grid conditions," *IEEE Trans. Power Del.*, vol. 27, no. 3, pp. 1332–1338, Jul. 2012. 84, 111

[83] J.-W. Moon, C.-S. Kim, J.-W. Park, D.-W. Kang, and J.-M. Kim, "Circulating current control in MMC under the unbalanced voltage," *IEEE Trans. Power Del.*, vol. 28, no. 3, pp. 1952–1959, Jul. 2013. 84, 111

[84] M. Vasiladiotis, N. Cherix, D. Siemaszko, and A. Rufer, "Operation of modular multilevel converters under grid asymmetries," in *39th Annu. Conf. of the IEEE Ind. Electron. Soc. (IECON)*, Nov. 2013, pp. 6281–6286. 84, 111

[85] N. Ahmed, L. Angquist, and H.-P. Nee, "Continuous modeling of open-loop control based negative sequence current control of modular multilevel converters for HVDC transmission," in *15th Eur. Conf. on Power Electron. and Appl. (EPE)*, Lille, France, Sept. 2013, pp. 1–10. 84, 111

[86] N. Ahmed, L. Ängquist, S. Norrga, and H. P. Nee, "Efficient modeling of modular multilevel converters in HVDC-grids under fault conditions," in *IEEE Power and Energy Soc. General Meeting*, National Harbor (Washington DC), USA, Jul. 2014, pp. 1–5. 84, 111

[87] S. Li, X. Wang, Z. Yao, T. Li, and Z. Peng, "Circulating current suppressing strategy for MMC-HVDC based on nonideal proportional resonant controllers under unbalanced grid conditions," *IEEE Trans. Power Electron.*, vol. 30, no. 1, pp. 387–397, Jan. 2015. 84, 111

[88] X. Shi, Z. Wang, B. Liu, Y. Liu, L. M. Tolbert, and F. Wang, "Characteristic investigation and control of a modular multilevel converter-based HVDC system under single-line-to-ground fault conditions," *IEEE Trans. on Power Electron.*, vol. 30, no. 1, pp. 408–421, Jan. 2015. 84, 111

[89] J.-J. Jung, S. Cui, S. Kim, and S.-K. Sul, "A cell capacitor energy balancing control of modular multilevel converter considering the unbalanced AC grid conditions," in *Int. Power Electron. Conf. (IPEC)*, Hiroshima, Japan, May 2014, pp. 1268–1275. 84, 111

[90] S. Cui, S. Kim, J.-J. Jung, and S.-K. Sul, "A comprehensive cell capacitor energy control strategy of a modular multilevel converter (MMC) without a stiff dc bus voltage source," in *29th Annu. IEEE Appl. Power Electron. Conf. and Expo. (APEC)*, Fort Worth, TX, USA, Mar. 2014, pp. 602–609. 84, 111

[91] J.-J. Jung, S. Cui, Y. Lee, and S.-K. Sul, "A cell capacitor energy balancing control of MMC-HVDC under the AC grid faults," in *9th Int. Conf. on Power Electron. and ECCE Asia (ICPE-ECCE Asia)*, Seoul, South Korea, Jun. 2015, pp. 1–8. 84, 111

[92] S. Cui, H.-J. Lee, J.-J. Jung, Y. Lee, and S.-K. Sul, "A comprehensive ac side single line to ground fault ride through strategy of a modular multilevel converter for HVDC system," in *Energy Conversion Congr. and Expo. (ECCE)*, Montreal, QC, Canada, Sept. 2015, pp. 5378–5385. 84, 111

[93] S. Fan, K. Zhang, J. Xiong, and Y. Xue, "An improved control system for modular multilevel converters with new modulation strategy and voltage balancing control," *IEEE Trans. Power Electron.*, vol. 30, no. 1, pp. 358–371, Jan. 2015. 84, 111

[94] S. Norrga, L. Angquist, K. Ilves, L. Harnefors, and H.-P. Nee, "Decoupled steady-state model of the modular multilevel converter with half-bridge cells," in *6th IET Int. Conf. on Power Electron. Machines and Drives (PEMD)*, Bristol, UK, Mar. 2012, pp. 1–6. 86

[95] G. Buja and G. Indri, "Improvement of pulse width modulation techniques," *Electrical Engineering (Archiv fur Elektrotechnik)*, vol. 57, no. 5, pp. 281–289, 1975. 87

[96] C. L. Fortescue, "Method of symmetrical co-ordinates applied to the solution of polyphase networks," *Trans. of the Amer. Inst. of Elect. Engineers*, no. 2, pp. 1027–1140, 1918. 88, 120

[97] H. Akagi, Y. Kanazawa, and A. Nabae, "Instantaneous reactive power compensators comprising switching devices without energy storage components," *IEEE Trans. Ind. Appl.*, vol. IA-20, no. 3, pp. 625–630, May 1984. 88, 94

[98] A. Junyent-Ferré, O. Gomis-Bellmunt, T. Green, and D. Soto-Sanchez, "Current control reference calculation issues for the operation of renewable source grid interface VSCs under unbalanced voltage sags," *IEEE Trans. Power Electron.*, vol. 26, no. 12, pp. 3744–3753, Dec. 2011. 94, 95, 111, 113, 114

[99] H. Akagi, E. Watanabe, and M. Aredes, *Instantaneous Power Theory and Applications to Power Conditioning*, ser. IEEE Press Series on Power Eng. Wiley, 2007. 94

[100] L. Shen, M. Barnes, R. Preece, J. Milanovic, K. Bell, and M. Belivanis, "The effect of VSC HVDC control and operating condition on dynamic behavior of integrated AC/DC system," *IEEE Trans. Power Del.*, vol. PP, no. 99, pp. 1–1, 2015. 95

[101] A. Egea-Alvarez, S. Fekriasl, F. Hassan, and O. Gomis-Bellmunt, "Advanced vector control for voltage source converters connected to weak grids," *IEEE Trans. Power Syst.*, vol. 30, no. 6, pp. 3072–3081, Nov. 2015. 95, 164, 172, 178

[102] H. Saad, X. Guillaud, J. Mahseredjian, S. Dennetière, and S. Nguefeu, "MMC capacitor voltage decoupling and balancing controls," *IEEE Trans. Power Del.*, vol. 30, no. 2, pp. 704–712, Apr. 2015. 99, 105, 178

[103] J. Xu, C. Zhao, W. Liu, and C. Guo, "Accelerated model of modular multilevel converters in PSCAD/EMTDC," *IEEE Trans. Power Del.*, vol. 28, no. 1, pp. 129–136, Jan. 2013. 105, 124

[104] A. Beddard, M. Barnes, and R. Preece, "Comparison of detailed modeling techniques for MMC employed on VSC-HVDC schemes," *IEEE Trans. Power Del.*, vol. 30, no. 2, pp. 579–589, Apr. 2015. 105, 124

[105] Q. Tu and Z. Xu, "Impact of sampling frequency on harmonic distortion for modular multilevel converter," *IEEE Trans. Power Del.*, vol. 26, no. 1, pp. 298–306, Jan. 2011. 105, 124

[106] M. Bollen and L. Zhang, "Different methods for classification of three-phase unbalanced voltage dips due to faults," *Elect. Power Syst. Res.*, vol. 66, no. 1, pp. 59–69, 2003. 107, 120

[107] ENTSO-E, "*ENTSO-E network code for requirements for grid connection applicable to all generators*," [Online]. Available: https://www.entsoe.eu [Accessed: Jan. 13, 2016]. 107, 124

[108] *The Grid Code*. National Grid Electricity Transmission PLC, UK, 2015. 107

[109] B. Siciliano, L. Sciavicco, L. Villani, and G. Oriolo, *Robotics: Modelling, Planning and Control*, ser. Advanced Textbooks in Control and Signal Processing. Springer London, 2010. 119

[110] P. Kundur, *Power System Stability and Control*. McGraw-Hill Professional, 1994. 133

[111] J. Machowski, J. Bialek, and J. Bumby, *Power system dynamics and stability*. Wiley, 1997. 133

[112] L. Xu, L. Yao, and M. Bazargan, "DC grid management of a multi-terminal HVDC transmission system for large offshore wind farms,"

in *Proc. of the Int. Conf. Sustain. Power Generation and Supply (SUPERGEN)*, Nanjing, China, 2009, pp. 1–7. 133, 140, 161, 174

[113] G. Zhang, Z. Xu, and Y. Cai, "An equivalent model for simulating VSC based HVDC," in *Proc. of the IEEE/PES Transmission and Distribution Conf. and Exposition*, vol. 1, Atlanta, Georgia, Nov. 2001, pp. 20–24. 137, 163

[114] T. K. Vrana, Y. Yang, D. Jovcic, S. Dennetière, J. Jardini, and H. Saad, "The CIGRE B4 DC grid test system," 2013. xxiii, 161, 162, 168, 177

[115] T. K. Vrana, J. Beerten, R. Belmans, and O. B. Fosso, "A classification of DC node voltage control methods for HVDC grids," *Elect. Power Syst. Res.*, vol. 103, pp. 137–144, 2013. 161

[116] T. M. Haileselassie and K. Uhlen, "Impact of DC line voltage drops on power flow of MTDC using droop control," *IEEE Trans. Power Syst.*, vol. 27, no. 3, pp. 1441–1449, 2012. 161

[117] X. Zhao and K. Li, "Adaptive backstepping droop controller design for multi-terminal high-voltage direct current systems," *IET Generation, Transmission & Distribution*, 2015. 161

[118] R. Eriksson, J. Beerten, M. Ghandhari, and R. Belmans, "Optimizing DC voltage droop settings for AC/DC system interactions," *IEEE Trans. Power Del.*, vol. 29, no. 1, pp. 362–369, Feb. 2014. 161

[119] X. Zhao and K. Li, "Droop setting design for multi-terminal HVDC grids considering voltage deviation impacts," *Elect. Power Syst. Research*, vol. 123, pp. 67–75, 2015. 161

[120] E. Prieto-Araujo, F. Bianchi, A. Junyent-Ferré, and O. Gomis-Bellmunt, "Methodology for droop control dynamic analysis of multiterminal VSC-HVDC grids for offshore wind farms," *IEEE Trans. Power Del.*, vol. 26, no. 4, pp. 2476–2485, Oct. 2011. 161, 168, 174, 180

[121] A. Egea-Alvarez, J. Beerten, D. V. Hertem, and O. Gomis-Bellmunt, "Primary and secondary power control of multiterminal HVDC grids," in *10th IET Int. Conf. on AC and DC Power Transmission (ACDC)*, Birmingham, UK, Feb. 2012. 162, 174

[122] L. Zhang, "Modeling and control of VSC-HVDC links connected to weak ac systems," Ph.D. dissertation, KTH, Electrical Machines and Power Electronics, 2010. xxiii, 164, 166, 177, 178

[123] L. Harnefors, M. Bongiorno, and S. Lundberg, "Input-admittance calculation and shaping for controlled voltage-source converters," *IEEE Trans. Ind. Electron.*, vol. 54, no. 6, pp. 3323–3334, Dec. 2007. 166

[124] P. Apkarian and D. Noll, "Nonsmooth H-infinity synthesis," *IEEE Trans. Autom. Control*, vol. 51, no. 1, pp. 71–86, Jan. 2006. 172, 178

[125] J. Beerten and R. Belmans, "Analysis of power sharing and voltage deviations in droop-controlled DC grids," *IEEE Trans. Power Syst.*, vol. 28, no. 4, pp. 4588–4597, Nov. 2013. 174

[126] T. S. Ustun, C. Ozansoy, and A. Zayegh, "Recent developments in microgrids and example cases around the world-a review," *Renewable and Sustainable Energy Rev.*, vol. 15, no. 8, pp. 4030–4041, 2011. 214

[127] A. Ruiz-Alvarez, A. Colet-Subirachs, F. Alvarez-Cuevas Figuerola, O. Gomis-Bellmunt, and A. Sudria-Andreu, "Operation of a utility connected microgrid using an IEC 61850-based multi-level management system," *IEEE Trans. Smart Grid*, vol. 3, no. 2, pp. 858–865, 2012. 222

[128] V. Salehi, A. Mohamed, A. Mazloomzadeh, and O. Mohammed, "Laboratory-based smart power system, part I: Design and system development," *IEEE Trans. Smart Grid*, vol. 3, no. 3, pp. 1394–1404, 2012. 222

[129] M. Marzband, A. Sumper, J. L. Domínguez-García, and R. Gumara-Ferret, "Experimental validation of a real time energy management system for microgrids in islanded mode using a local day-ahead electricity market and MINLP," *Energy Conversion and Manage.*, vol. 76, no. 0, pp. 314–322, 2013. 222

[130] L. Valverde, F. Rosa, and C. Bordons, "Design, planning and management of a hydrogen-based microgrid," *IEEE Trans. Ind. Informat.*, vol. 9, no. 3, pp. 1398–1404, 2013. 222

[131] M. Sechilariu, B. Wang, and F. Locment, "Building-integrated microgrid: Advanced local energy management for forthcoming smart power grid communication," *Energy and Buildings*, vol. 59, no. 0, pp. 236–243, 2013. 222

[132] B. Belvedere, M. Bianchi, A. Borghetti, C. Nucci, M. Paolone, and A. Peretto, "A microcontroller-based power management system for standalone microgrids with hybrid power supply," *IEEE Trans. Sustain. Energy*, vol. 3, no. 3, pp. 422–431, 2012. 222

[133] X. Huang, Z. Wang, and J. Jiang, "Control and load-dispatching strategies for a microgrid with a DC/AC inverter of fixed frequency," *Int. Journal of Elect. Power & Energy Syst.*, vol. 43, no. 1, pp. 1127–1136, 2012. 222

[134] B. Wu, J. Liu, and F. Zhuo, "The micro-grid fast simulation platform exploitation based on PSCAD," in *26th Annu. IEEE Appl. Power Electron. Conf. and Exposition (APEC)*, Fort Worth, TX, USA, Mar. 2011, pp. 1737–1742. 222

[135] F. Wang, J. Duarte, and M. Hendrix, "Grid-interfacing converter systems with enhanced voltage quality for microgrid application: Concept and implementation," *IEEE Trans. Power Electron.*, vol. 26, no. 12, pp. 3501–3513, 2011. 222

[136] I. Serban and C. Marinescu, "Aggregate load-frequency control of a wind-hydro autonomous microgrid," *Renewable Energy*, vol. 36, no. 12, pp. 3345–3354, 2011. 222

[137] O. Mohammed, M. A. Nayeem, and A. Kaviani, "A laboratory based microgrid and distributed generation infrastructure for studying connectivity issues to operational power systems," in *IEEE Power and Energy Soc. General Meeting*, Minneapolis, Minnesota, USA, Jul. 2010, pp. 1–6. 222

[138] M. Dali, J. Belhadj, and X. Roboam, "Hybrid solar-wind system with battery storage operating in grid-connected and standalone mode: Control and energy management - experimental investigation," *Energy*, vol. 35, no. 6, pp. 2587–2595, 2010. 222

[139] P.-T. Cheng, C.-A. Chen, T.-L. Lee, and S.-Y. Kuo, "A cooperative imbalance compensation method for distributed-generation interface converters," *IEEE Trans. Ind. Appl.*, vol. 45, no. 2, pp. 805–815, 2009. 222

[140] A. Koran, T. LaBella, and J.-S. Lai, "High efficiency photovoltaic source simulator with fast response time for solar power conditioning

systems evaluation," *IEEE Trans. Power Electron.*, vol. 29, no. 3, pp. 1285–1297, 2014. 223

[141] M. de Brito, L. Galotto, L. Sampaio, G. de Azevedo e Melo, and C. Canesin, "Evaluation of the main MPPT techniques for photovoltaic applications," *IEEE Trans. Ind. Electron.*, vol. 60, no. 3, pp. 1156–1167, 2013. 223

[142] C.-C. Chen, H.-C. Chang, C.-C. Kuo, and C.-C. Lin, "Programmable energy source emulator for photovoltaic panels considering partial shadow effect," *Energy*, vol. 54, no. 0, pp. 174 – 183, 2013. 223

[143] C.-H. Chang, E.-C. Chang, and H.-L. Cheng, "A high-efficiency solar array simulator implemented by an LLC resonant DC-DC converter," *IEEE Trans. Power Electron.*, vol. 28, no. 6, pp. 3039–3046, 2013. 223

[144] M. D. Piazza, M. Pucci, and G. Vitale, "Intelligent power conversion system management for photovoltaic generation," *Sustainable Energy Technol. and Assessments*, vol. 2, no. 0, pp. 19–30, 2013. 223

[145] D. D. Lu and Q. N. Nguyen, "A photovoltaic panel emulator using a buck-boost DC/DC converter and a low cost micro-controller," *Solar Energy*, vol. 86, no. 5, pp. 1477–1484, 2012. 223

[146] Y. Kim, W. Lee, M. Pedram, and N. Chang, "Dual-mode power regulator for photovoltaic module emulation," *Applied Energy*, vol. 101, no. 0, pp. 730–739, 2013. 223

[147] A. Vijayakumari, A. Devarajan, and N. Devarajan, "Design and development of a model-based hardware simulator for photovoltaic array," *Int. Journal of Elect. Power & Energy Syst.*, vol. 43, no. 1, pp. 40–46, 2012. 223

[148] R. Kadri, H. Andrei, J.-P. Gaubert, T. Ivanovici, G. Champenois, and P. Andrei, "Modeling of the photovoltaic cell circuit parameters for optimum connection model and real-time emulator with partial shadow conditions," *Energy*, vol. 42, no. 1, pp. 57–67, 2012. 223

[149] R. Kadri, J.-P. Gaubert, and G. Champenois, "An improved maximum power point tracking for photovoltaic grid-connected inverter based on voltage-oriented control," *IEEE Trans. Ind. Electron.*, vol. 58, no. 1, pp. 66–75, 2011. 223

[150] A. Koran, K. Sano, R. young Kim, and J.-S. Lai, "Design of a photovoltaic simulator with a novel reference signal generator and two-stage LC output filter," in *IEEE Energy Conversion Congr. and Expo.*, San Jose, CA, USA, Sept. 2009, pp. 319–326. 223

[151] M. C. D. Piazza and G. Vitale, "Photovoltaic field emulation including dynamic and partial shadow conditions," *Applied Energy*, vol. 87, no. 3, pp. 814–823, 2010. 223

[152] F. Martinez, L. C. Herrero, and S. de Pablo, "Open loop wind turbine emulator," *Renewable Energy*, vol. 63, no. 0, pp. 212–221, 2014. 223

[153] A. Egea-Alvarez, F. Bianchi, A. Junyent-Ferré, G. Gross, and O. Gomis-Bellmunt, "Voltage control of multiterminal VSC-HVDC transmission systems for offshore wind power plants: Design and implementation in a scaled platform," *IEEE Trans. Ind. Electron.*, vol. 60, no. 6, pp. 2381–2391, 2013. 223

[154] C.-H. Lin, "Recurrent modified elman neural network control of PM synchronous generator system using wind turbine emulator of PM synchronous servo motor drive," *Int. Journal of Elect. Power & Energy Syst.*, vol. 52, no. 0, pp. 143–160, 2013. 223

[155] Y. Zou, M. Elbuluk, and Y. Sozer, "Stability analysis of maximum power point tracking (MPPT) method in wind power systems," *IEEE Trans. Ind. Appl.*, vol. 49, no. 3, pp. 1129–1136, 2013. 223

[156] T. H. Nguyen and D.-C. Lee, "Advanced fault ride-through technique for PMSG wind turbine systems using line-side converter as STATCOM," *IEEE Trans. Ind. Electron.*, vol. 60, no. 7, pp. 2842–2850, 2013. 223

[157] A. Abdelkafi, A. Masmoudi, and L. Krichen, "Experimental investigation on the performance of an autonomous wind energy conversion system," *Int. Journal of Elect. Power & Energy Syst.*, vol. 44, no. 1, pp. 581–590, 2013. 223

[158] A. Urtasun, P. Sanchis, I. S. Martín, J. López, and L. Marroyo, "Modeling of small wind turbines based on PMSG with diode bridge for sensorless maximum power tracking," *Renewable Energy*, vol. 55, no. 0, pp. 138–149, 2013. 223

[159] D. Atkinson, G. Pannell, W. Cao, B. Zahawi, T. Abeyasekera, and M. Jovanovic, "A doubly-fed induction generator test facility for grid fault ride-through analysis," *IEEE Instrum. Meas. Mag.*, vol. 15, no. 6, pp. 20–27, 2012. 223

[160] D. Ramirez, S. Martinez, F. Blazquez, and C. Carrero, "Use of STATCOM in wind farms with fixed-speed generators for grid code compliance," *Renewable Energy*, vol. 37, no. 1, pp. 202–212, 2012. 223

[161] A. Masmoudi, L. Krichen, and A. Ouali, "Voltage control of a variable speed wind turbine connected to an isolated load: Experimental study," *Energy Conversion and Manage.*, vol. 59, no. 0, pp. 19–26, 2012. 223

[162] R. Sharma and U. Madawala, "The concept of a smart wind turbine system," *Renewable Energy*, vol. 39, no. 1, pp. 403–410, 2012. 223

[163] D. Ramirez, S. Martinez, C. Carrero, and C. A. Platero, "Improvements in the grid connection of renewable generators with full power converters," *Renewable Energy*, vol. 43, no. 0, pp. 90–100, 2012. 223

[164] I. Serban and C. Marinescu, "A sensorless control method for variable-speed small wind turbines," *Renewable Energy*, vol. 43, no. 0, pp. 256–266, 2012. 223

[165] J. Arribas, C. Veganzones, F. Blazquez, C. Platero, D. Ramirez, S. Martinez, J. Sanchez, and N. Herrero Martinez, "Computer-based simulation and scaled laboratory bench system for the teaching and training of engineers on the control of doubly fed induction wind generators," *IEEE Trans. Power Syst.*, vol. 26, no. 3, pp. 1534–1543, 2011. 223

[166] S. Roy, "Reduction of voltage dynamics in isolated wind-diesel units susceptible to gusting," *IEEE Trans. Sustain. Energy*, vol. 1, no. 2, pp. 84–91, 2010. 223

[167] F. Poitiers, T. Bouaouiche, and M. Machmoum, "Advanced control of a doubly-fed induction generator for wind energy conversion," *Elect. Power Syst. Res.*, vol. 79, no. 7, pp. 1085–1096, 2009. 223

[168] M. E. Mokadem, V. Courtecuisse, C. Saudemont, B. Robyns, and J. Deuse, "Experimental study of variable speed wind generator contribution to primary frequency control," *Renewable Energy*, vol. 34, no. 3, pp. 833–844, 2009. 223

[169] R. Cardenas, R. Peña, P. Wheeler, J. Clare, and G. Asher, "Control of the reactive power supplied by a WECS based on an induction generator fed by a matrix converter," *IEEE Trans. Ind. Electron.*, vol. 56, no. 2, pp. 429–438, 2009. 223

[170] R. Cardenas, R. Peña, J. Clare, G. Asher, and J. Proboste, "MRAS observers for sensorless control of doubly-fed induction generators," *IEEE Trans. Power Electron.*, vol. 23, no. 3, pp. 1075–1084, 2008. 223

[171] H. Camblong, I. M. de Alegria, M. Rodriguez, and G. Abad, "Experimental evaluation of wind turbines maximum power point tracking controllers," *Energy Conversion and Manage.*, vol. 47, no. 18-19, pp. 2846–2858, 2006. 223

[172] F. J. Lin, L. T. Teng, P. H. Shieh, and Y. F. Li, "Intelligent controlled-wind-turbine emulator and induction-generator system using RBFN," *IEE Proc. Electric Power Appl.*, vol. 153, no. 4, pp. 608–618, 2006. 223

[173] H. Li, M. Steurer, K. L. Shi, S. Woodruff, and D. Zhang, "Development of a unified design, test, and research platform for wind energy systems based on hardware-in-the-loop real-time simulation," *IEEE Trans. Ind. Electron.*, vol. 53, no. 4, pp. 1144–1151, 2006. 223

[174] R. Cardenas and R. Peña, "Sensorless vector control of induction machines for variable-speed wind energy applications," *IEEE Trans. Energy Convers.*, vol. 19, no. 1, pp. 196–205, 2004. 223

[175] C. Kana, M. Thamodharan, and A. Wolf, "System management of a wind-energy converter," *IEEE Trans. Power Electron.*, vol. 16, no. 3, pp. 375–381, 2001. 223

[176] P. Battaiotto, R. Mantz, and P. Puleston, "A wind turbine emulator based on a dual DSP processor system," *Control Engineering Practice*, vol. 4, no. 9, pp. 1261–1266, 1996. 223

[177] C. de Beer, P. Barendse, and A. Khan, "Development of an HT PEM fuel cell emulator using a multiphase interleaved DC-DC converter topology," *IEEE Trans. Power Electron.*, vol. 28, no. 3, pp. 1120–1131, 2013. 223

[178] F. Gao, B. Blunier, D. Chrenko, D. Bouquain, and A. Miraoui, "Multirate fuel cell emulation with spatial reduced real-time fuel cell mod-

eling," *IEEE Trans. Ind. Appl.*, vol. 48, no. 4, pp. 1127–1135, 2012. 223

[179] C. Restrepo, C. Ramos-Paja, R. Giral, J. Calvente, and A. Romero, "Fuel cell emulator for oxygen excess ratio estimation on power electronics applications," *Comput. & Elect. Eng.*, vol. 38, no. 4, pp. 926–937, 2012. 223

[180] T. Bjaziv, Z. Ban, and M. Milanovic, "Modeling of current mode controlled boost converter supplied by fuel cell suitable for controller design purposes," *Journal of Power Sources*, vol. 198, no. 0, pp. 203–217, 2012. 223

[181] F. Gao, B. Blunier, M. Simoes, and A. Miraoui, "PEM fuel cell stack modeling for real-time emulation in hardware-in-the-loop applications," *IEEE Trans. Energy Convers.*, vol. 26, no. 1, pp. 184–194, 2011. 223

[182] G. Marsala, M. Pucci, G. Vitale, M. Cirrincione, and A. Miraoui, "A prototype of a fuel cell PEM emulator based on a buck converter," *Applied Energy*, vol. 86, no. 10, pp. 2192–2203, 2009. 223

[183] T. Zhou, B. Francois, M. el Hadi Lebbal, and S. Lecoeuche, "Real-time emulation of a hydrogen-production process for assessment of an active wind-energy conversion system," *IEEE Trans. Ind. Electron.*, vol. 56, no. 3, pp. 737–746, 2009. 223

[184] W. C. Lee and D. Drury, "Development of a hardware-in-the-loop simulation system for testing cell balancing circuits," *IEEE Trans. Power Electron.*, vol. 28, no. 12, pp. 5949–5959, 2013. 223

[185] O. Konig, G. Gregorcic, and S. Jakubek, "Model predictive control of a DC-DC converter for battery emulation," *Control Eng. Practice*, vol. 21, no. 4, pp. 428–440, 2013. 223

[186] O. Konig, C. Hametner, G. Prochart, and S. Jakubek, "Battery emulation for power-hil using local model networks and robust impedance control," *IEEE Trans. Ind. Electron.*, vol. 61, no. 2, pp. 943–955, 2014. 223

[187] H. Dai, X. Zhang, X. Wei, Z. Sun, J. Wang, and F. Hu, "Cell-BMS validation with a hardware-in-the-loop simulation of lithium-ion battery cells for electric vehicles," *Int. Journal of Elect. Power & Energy Syst.*, vol. 52, no. 0, pp. 174–184, 2013. 223

[188] A. D. Bernardinis, S. Butterbach, R. Lallemand, A. Jeunesse, G. Coquery, and P. Aubin, "Double resonant isolated converter for battery charger with fast switching semiconductors used in hybrid electric shunting locomotive," *Elect. Power Syst. Res.*, vol. 92, no. 0, pp. 43–49, 2012. 223

[189] E. Duran, J. Andujar, F. Segura, and A. Barragan, "A high-flexibility DC load for fuel cell and solar arrays power sources based on DC-DC converters," *Applied Energy*, vol. 88, no. 5, pp. 1690–1702, 2011. 223

[190] X. Zhang, C. C. Mi, A. Masrur, and D. Daniszewski, "Wavelet-transform-based power management of hybrid vehicles with multiple on-board energy sources including fuel cell, battery and ultracapacitor," *Journal of Power Sources*, vol. 185, no. 2, pp. 1533–1543, 2008. 223

[191] Y. Rao and M. Chandorkar, "Real-time electrical load emulator using optimal feedback control technique," *IEEE Trans. Ind. Electron.*, vol. 57, no. 4, pp. 1217–1225, 2010. 223

[192] E. Adzic, M. Adzic, V. Katic, D. Marcetic, and N. Celanovic, "Development of high-reliability EV and HEV IM propulsion drive with ultra-low latency HIL environment," *IEEE Trans. Ind. Informat.*, vol. 9, no. 2, pp. 630–639, 2013. 223

[193] E. Prieto-Araujo, P. Olivella-Rosell, M. Cheah-Mañé, R. Villafáfila-Robles, and O. Gomis-Bellmunt, "Renewable energy emulation concepts for microgrids," *Renewable and Sust. Energy Reviews*, vol. 50, pp. 325–345, 2015. 223

Appendix A

Renewable energy emulation concepts

A.1 The emulation concept

An emulator is a device that attempts to mimic the behavior of a real resource. Essentially, it is compounded by two interrelated parts, a software and a hardware layer. On the one hand, the software layer calculates the variables that the real system would show under the same conditions, based on static or dynamic operations. On the other hand, the hardware layer imposes the software calculated variables by means of mechanic, electronic or electrical devices to follow the real system behavior. According to the previous definition, systems of all kinds could be emulated. However, this section is mainly focused on analyzing the emulation structures available for representing energy systems that could be connected to an electrical grid.

In order to clarify the introduced concept, an example of a photovoltaic (PV) emulator operation (Fig. A.1) connected to the grid is explained in detail. In this case, the emulator software layer calculates, based on the real PV installation that is being emulated and the environmental scenario conditions defined for the experiment, the voltage that there would be across the real PV power connection terminals. Once calculated, this voltage is applied by the emulator hardware layer at the emulator power terminals by means, for instance, of a power converter. Therefore, both the real PV installation and the emulator would show the same voltage at its connection terminals, allowing the grid integration converter to perform the same control on them without any difference.

In general, emulation devices present some features that increase the possibilities of the testing system where they are connected, regardless of the resource that is being represented:

- An emulator can represent any possible scenario using the same software and hardware devices. The experiment conditions are imposed by the user.

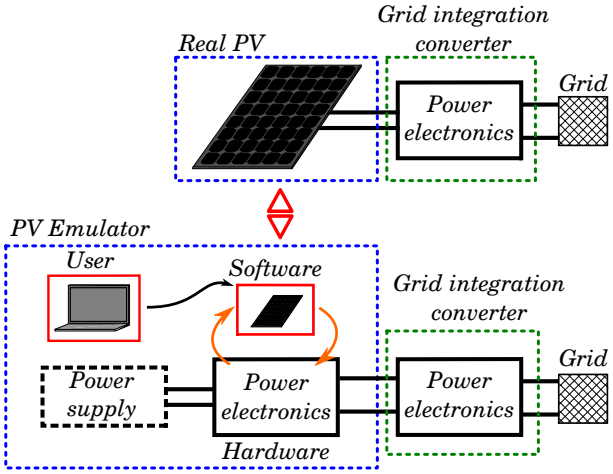

Figure A.1: Photovoltaic emulator concept

- Experiments performed employing emulators avoid damaging real setups. Emulators usually include protections and securities to avoid possible problems while testing.
- Emulation allows changes in the experiment's time scale. For instance, long time evolution of the real system can be concentrated in a short period of time.
- Emulators are usually smaller than the emulated real setups. This feature is interesting for laboratory test benches where the testing space is usually limited.
- Its hardware and associated costs are usually lower in comparison to real systems.
- In certain configurations, an emulator is able to represent different resources or an aggregation of various systems.
- The emulator output power could be scaled to a larger one if it is needed. The hardware can be designed for a desired power level and otherwise, the software layer can scale the results of the emulation.

Typically, emulators are included in experimental setups [126] in a low voltage laboratory testing grid. For the sake of simplicity all the possible emulation levels will be defined within a laboratory environment using a microgrid base structure.

A.2 Emulation levels definition

Based on the emulator literature review developed, it can be stated that emulators can be conceptually classified in different groups, defined in this work as emulation levels. These levels are defined based on the degree of detail used to represent the emulated resource, not on the software and hardware devices used for the emulation. In this section, the established emulation levels are explained using the example microgrid layout depicted in Fig. A.2.

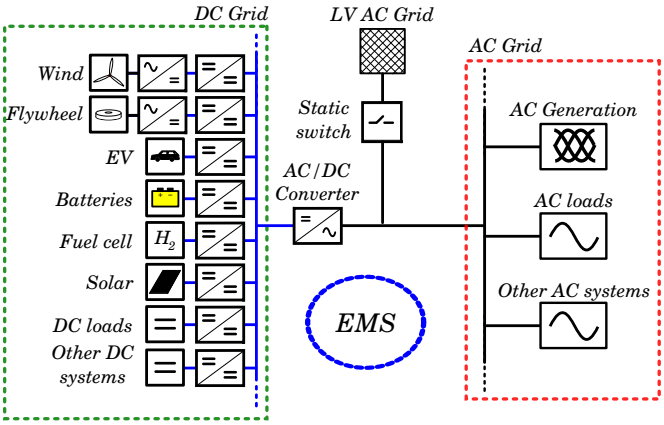

Figure A.2: Microgrid base electrical layout

The example microgrid scheme is divided in two different current nature grids, the Alternating Current (AC) side (black lines) where loads and conventional generation are connected and the Direct Current (DC) side (blue lines) where the renewable generation and storage systems are placed. The connection of the different resources to the DC microgrid part is carried out using DC/DC or AC/DC converters, depending on the system current nature. Also note that the nature of the AC grid is not specified, thus it can be a single-phase, a three-phase or a multi-phase grid.

Once the example layout is introduced, the emulation levels are explained, starting from the most generic to the most specific ones. Essentially, the development of the different levels will be focused on the DC grid side elements of the example microgrid. It should be mentioned that converters drawn with dashed lines are related to emulation, whereas those drawn with solid lines are considered real elements.

A.2.1 Level 1: Global emulation

Fig. A.3 shows the most possible generic emulation of systems, defined as global emulation. This level considers that the generation, storage and load systems connected to a certain grid could be emulated via software (represented by a red square in Fig. A.3) and transformed into an equivalent aggregated active and reactive power consumed or injected to the microgrid by a single hardware layer. The emulator is not representing a single resource, but rather representing the aggregation of a whole system with its different subsystems connected to it.

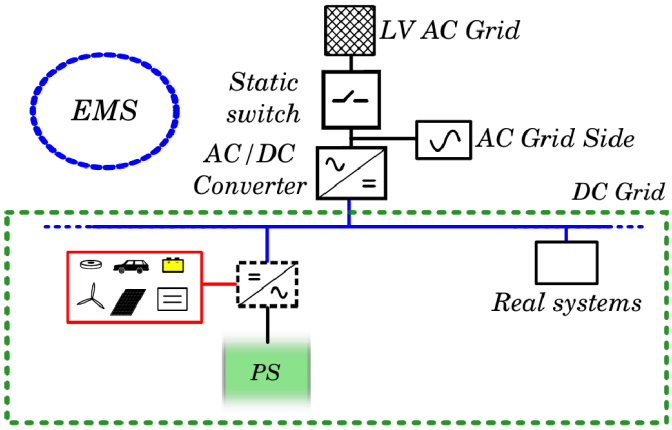

Figure A.3: Level 1 - Global emulation scheme

Therefore, the emulation system exchanges a defined amount of power with the grid based on the total power aggregation computed by the software layer. If so desired, an individual control could be applied to each resource, but it has to be implemented in the software stage of the emulation.

Note that, the green block depicted in Fig. A.3, corresponds to the power supply (PS) of the emulators, needed for the system operation. Thus, if the emulation system consumes energy from the DC grid, this energy must be consumed by the PS system and, on the contrary, if the emulation is injecting power to the grid the PS should deliver it. Therefore, the PS must be bidirectional to accomplish the emulation system requirements. However, if the nature of the emulated system is defined the PS could be designed to be unidirectional. Hereafter, the PS system is depicted using a green box connected to the emulators.

A.2.2 Level 2: Aggregated emulation of generation, storage and loads

This architecture consists of gathering the emulated systems by common flow direction. As shown in Fig. A.4, three different branches can be differentiated. These branches correspond to three emulation groups, generation, storage and loads. The emulator software layer computes the aggregation of different resources by power flow nature, calculating the equivalent power that they are injecting or absorbing from the grid. Then, the hardware layer transforms this calculation in a real power flow. The difference between this emulation level and the previous one is purely conceptual, because the same emulation devices could perform both emulations perfectly. Again, a specific control applied to a single resource has to be computed in the software layer, because everything is calculated in it.

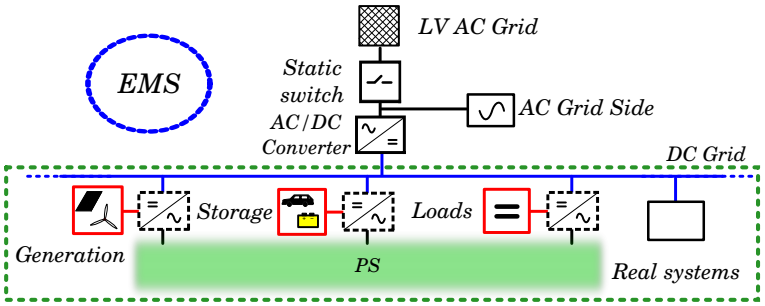

Figure A.4: Level 2 - Aggregated emulation scheme

A.2.3 Level 3: Resource emulation

The conceptual diagram of this emulation is shown in Fig. A.5. Unlike the two previous emulation levels, this architecture dedicates an emulator device to each resource. The emulators employed in this level are power emulators, so they represent the power output that the real resource system would be exchanging with the grid, under the defined conditions. Then, not only is the behavior of the resource being emulated, but also the possible interconnection systems between the resource and the grid. For instance, a solar panel would be emulated together with the converter used for the grid integration of the energy produced. The software layer of the emulator calculates the variables of the system and the power output that the whole real system would be injecting under the same conditions, and the hardware layer will transform the software calculations into real power.

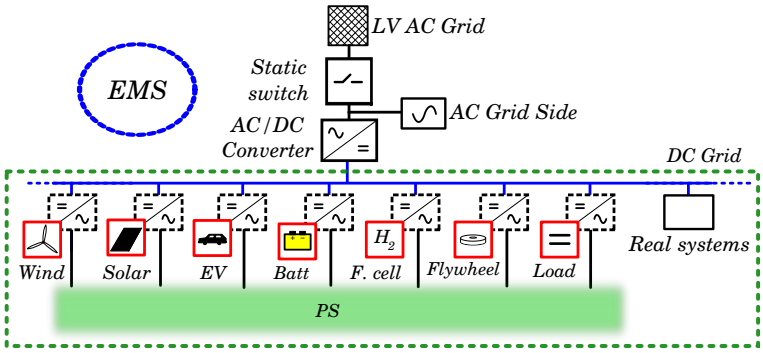

Figure A.5: Level 3 - Resource emulation scheme

The difference between this emulation level and the previous ones is again conceptual, because the same emulator devices could be used for the three different levels. Again, this architecture does not permit carrying out out real control of the emulated resource because the system is based on power emulation. Therefore, if so desired, it should be implemented in the software layer.

A.2.4 Level 4: Specific emulation

This emulation level (Fig. A.6) is focused on the emulation of a resource by representing its electrical variables. The software layer carries out the calculation of the resource variables under the defined scenario conditions and the hardware layer applies these variables to the real system. For instance, the operation of a PV panel could be emulated. Based on a supposed irradiance, the software layer calculates the voltage output that the real system would be applying. Then, the hardware layer regulates the voltage at the output terminals to apply exactly the calculated magnitude. Therefore, if a grid integration converter is connected to the emulator, it will not detect any difference between the emulator and the real system if the first is properly designed. This fact can be observed in Fig. A.6 where real DC/DC converters are performing the integration of the emulators to the real grid in the same way as it would be connecting the real resources to the microgrid.

There is an important difference between the emulation concept described in this level and the previous ones. While in emulation level 3, the emulators act as power sources, in this case, emulators are representing mainly the resource; for instance applying, the same voltage that the real resource would be applying under the same conditions. Therefore, this level allows carrying

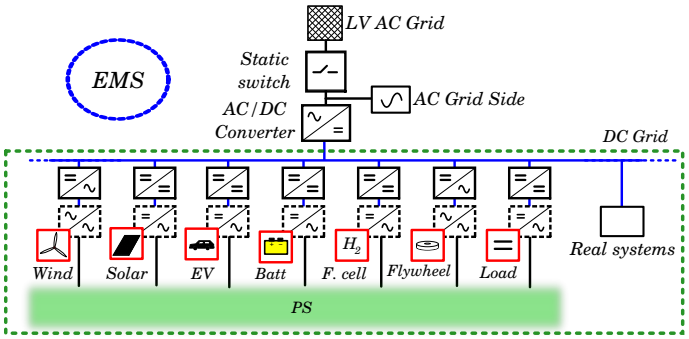

Figure A.6: Level 4 - Specific emulation scheme

out of real control on the emulators as if they were real resources. Moreover, this emulation level permits swapping the emulator with the real emulated resource.

This emulation level defines a boundary on the conceptualization of the emulators. More complex structures can be defined for each resource individually, but further conceptual groups are not easily made. Fig. A.7 shows further emulation possibilities focusing on each of the elements that compound the example microgrid, starting with the emulation presented above in Fig. A.6 (indicated with a number 1), to the real system implementation where the emulator is substituted by a real installation. Next, these structures are described:

- Wind energy emulation
    1. Turbine-generator emulator. The emulator is designed to represent the electrical system gathering the wind turbine and the generator.
    2. Turbine emulation. The wind resource and the turbine are emulated by a motor controlled by a frequency converter. The motor axis is coupled to the real (or scaled) generator. Then, supposing a wind resource and defining the turbine blades, the torque or the speed of the motor could be calculated and regulated by the frequency converter. Then, the real generator could be controlled by a real converter.
    3. Wind emulation. The generator and the turbine are the real ones (or a scaled version). The wind is emulated using a fan, allowing real tests to be carried out with the whole setup.

4. Real wind generation system. The wind emulation system is replaced by the real resource.

- Solar energy emulation
  1. PV cell emulator. The emulator represents the behavior of a PV cell or a combination of them.
  2. Light emulation. The PV emulator is replaced by the real panel (or a scaled version) and it is excited by artificial light.
  3. Real PV installation. The solar emulation system is replaced by the real resource.
- Battery emulation
  1. Battery emulator. The emulator represents the behavior of a battery. It could be designed and configured to represent any type of battery.
  2. Real batteries. The emulator is replaced by a real battery system.
- Electric vehicle emulation
  1. Electric vehicle emulator. The electric vehicle behavior is represented by an emulator. It can be configured as a fast or conventional charging system. It could also include not only the electrical part, but also the communications including different protocols.
  2. Real EV with fast charging capability. The EV emulator is substituted by a car with fast charging capability.
  3. Real EV with conventional battery charger. The EV emulator is substituted by a car with a conventional charging capability.
- Flywheel emulation
  1. Flywheel-generator emulator. The flywheel, together with the generator behavior, is represented by an emulation system.
  2. Flywheel emulator. The flywheel is emulated by a motor and a frequency converter. The real flywheel generator (or a scaled version) is connected to the emulation motor-frequency converter setup that will behave as the rotating mass.
  3. Real flywheel. The emulator is substituted by a real flywheel.
- Fuel cell emulation

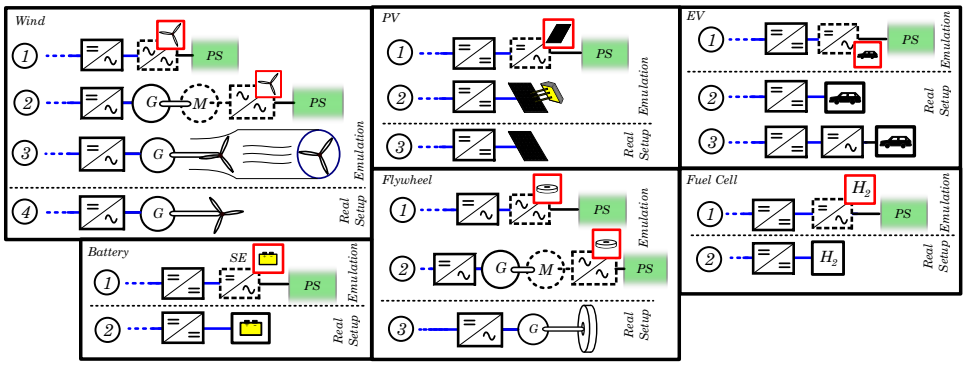

Figure A.7: Level 4 - Specific emulation scheme for each resource

1. Fuel cell emulation. The behavior of a fuel cell is represented by an emulation setup.
2. Real fuel cell. The emulator is replaced by a real fuel cell.

As previously mentioned, it is not possible to define another emulation level including the different emulated resources. Therefore, these emulation proposals are considered inside the frame of the specific emulation.

To conclude, it is interesting to state that researchers always can choose between the different emulation levels proposed. Then, depending on the objectives of the experiment to be performed and the detail of the system variables needed, an emulation level could be selected to accomplish the specifications.

A.2.5 Other considerations

It should be mentioned that the emulation level does not depend on the nature of the grid where the emulator is connected. However, the emulator hardware should be adapted depending on the grid nature to perform a proper emulation. As an example, the connection of the elements to the DC Grid, as shown in Fig. A.2, could be substituted by a connection to an AC grid without modifying the emulation level.

The power supply of the emulators has been shown in all cases represented with a green box for all the emulators. Note that each of the emulators could include its own individual power supply. In addition, the power supply could also be provided in DC current instead of AC as supposed in the different emulation systems.

This document does not include all the systems liable to being emulated. For example, a diesel generator could also be emulated properly. The analysis is focused on renewable resources, as they are the most common emulated systems found in the literature. Nevertheless, if so desired, the emulation level concept can be easily applied to other technologies.

A.3 Emulation literature review

Based on the review presented in this section, the previous emulation level definition has been made. First, this literature analysis is focused on the platform laboratories where emulators are part of the platform structure. Table A.1 shows the results of the literature review, classifying the platforms' emulators according to their corresponding emulation level.

Table A.1: Classification by emulation levels of the laboratory platform emulators found in the literature

Ref.	Wind	PV	Fuel Cell	Battery	EV	Flywheel	Load
[127]	3	-	-	3	-	-	3
[128]	-	4	4	Real	-	-	Real, 3
[129]	3	3	-	3	-	-	3
[130]	3	3	Real	Real	-	-	3
[131]	-	Real	-	Real	-	-	2
[132]	-	4	Real	Real	-	-	Real
[133]	-	-	Real	Real	-	-	3
[134]	3	3	-	-	-	-	Real
[135]	1	1	1	1	-	-	3
[136]	4	-	-	Real	-	-	3
[137]	4	3	3	Real	-	4	Real
[138]	4	4	-	Real	-	-	Real, 3
[139]	2	2	2	-	-	-	Real

In addition to this classification, other emulation test benches have been proposed focused on a single resource. Table A.2 shows the classification of these emulators according to their corresponding emulation level. Note that

as these devices are emulators that are representing a single resource, they can be classified between emulation levels three and four.

Table A.2: Classification by emulation levels of the emulation test benches found in the literature

Emulated resource	**Level 3**	**Level 4**
Solar power	-	[140], [141], [142], [143], [144], [145], [146], [147], [148], [149], [150], [151]
Wind power	-	[152], [153], [154], [155], [156], [157], [158], [159], [160], [161], [162], [163], [164], [165], [166], [167], [168], [169], [170], [171], [172], [173], [174], [175], [176]
Fuel cell	-	[177], [178], [179], [180] ,[181], [182], [183]
Battery	-	[184], [185], [186], [187], [188]
Load	[189], [190]	[191]
Electric vehicle	-	[192]

The information provided in Tables A.1 and A.2 is expanded in [193], where a detailed explanation of the laboratories and the emulators found is further developed. Subsequently, several conclusions are drawn based on this literature review:

- In the majority of laboratories, emulators are combined with real elements, a fact that increases the experimental possibilities of the laboratory, allowing scenarios to be represented that could not be possible without an emulator.
- Laboratories are implemented using an AC grid, a DC grid or a combination of both, with emulators connected at both sides.
- The power levels of the elements included in laboratories, either real resources or emulators, range from 100 W to a few kilowatts.
- One of the main objectives of this type of laboratories is the validation of energy management system strategies.

- The interconnection of several renewable energy sources within the same system is another interesting topic to be analyzed within laboratory platforms.
- The AC side voltage range depends on the country where the laboratory is installed, according to the local typical voltages.
- It can be observed that the most common emulation systems are levels three and four because usually a single emulator is employed to represent a single resource. However, there are examples of emulators representing more than one system, showing that levels one and two are also interesting structures to experiment with.
- Some emulators articles are focused only on the development of the emulation device, whereas in the rest of the reviewed articles, the emulator is used to validate new developments, acting as the real resource.
- Emulators that represent the same resource, employing the same emulation level, have the concept of how the resource is being represented in common. Nevertheless, the software and hardware layers of these emulators could be sufficiently different. For instance, many different PV cell emulators classified into level 4 of emulation are built using various electronic configurations. Of course, depending on the software and hardware employed, the accuracy of the emulation results can vary.
- The hardware layer of the solar emulators reviewed is mainly built based on a DC/DC converter or programmable DC power supply. Different proposals for the structure of the DC/DC converter are shown to improve the transient dynamic response and the efficiency thereof.
- Wind emulators are typically based on a 4-2 emulation level structure, in which the wind resource and the turbine are emulated by a motor controlled by a converter. The current nature and the power rating of the motor included in the emulation structure depends on the experiment.
- Fuel cell and battery emulators hardware layers are based on DC/DC converters or programmable DC power supplies. The different emulators reviewed show a level 4 emulation structure.
- Load emulators are developed based on a DC/DC converter or a three-phase Voltage Source Converter (VSC).

- The electric vehicle emulator found in the literature is based on an Induction Machine (IM) applying a defined torque to the EV motor. The emulation levels included are defined for devices connected to microgrids. In this case, the emulator is developed to analyze the operation of the EV while it is not connected to the grid. Even so, it has been included in the literature review due to the interesting test bench proposal.

- In terms of the emulators software layer, different elements are proposed to control the hardware structures: Digital Signal Processors (DSP), dSPACE® systems, Field Programmable Gate Arrays (FPGA), Peripheral Interface Controllers (PIC®), among other controllers.

- Typically, emulators are custom systems built in the laboratory. However, commercial emulators that represent the behavior of PV panels and fuel cells are available.

The previous points summarize the findings of a selection of the emulation structures present in the literature. Of course, other emulator topologies can be developed, based on the testing requirements.

A.4 Conclusions

In this section, a review of the emulation systems available for different resources is developed. First, based on the literature analysis performed, the emulation concept is defined by differentiating four emulation levels based on the emulation characteristics. Next, features and possibilities of each of these levels are explained through an example microgrid. Then, the literature review results of the laboratory platforms and emulation test benches classified by resource and emulation level are shown.

Finally, it can be concluded that this literature review, along with its classification by emulation levels, could be a useful guide during the design stage of an experiment including emulation systems.

Appendix B

Publications

This section presents the publications related to the specific topics of this thesis the author has contributed to.

Journal papers

Published - Included in the thesis

J1 E. Prieto-Araujo, F.D. Bianchi, A. Junyent-Ferré, O. Gomis-Bellmunt, "Methodology for Droop Control Dynamic Analysis of Multiterminal VSC-HVDC Grids for Offshore Wind Farms," *IEEE Trans. Power Del.*, vol. 26, no. 4, pp. 2476-2485, Oct. 2011.

J2 E. Prieto-Araujo, A. Junyent-Ferré, D. Lavèrnia-Ferrer, O. Gomis-Bellmunt, "Decentralized Control of a Nine-Phase Permanent Magnet Generator for Offshore Wind Turbines," *IEEE Trans. Energy Convers.*, vol. 30, no. 3, pp. 1103-1112, Sept. 2015.

J3 E. Prieto-Araujo, P. Olivella-Rosell, M. Cheah-Mañé, R. Villafáfila-Robles, O. Gomis-Bellmunt, "Renewable energy emulation concepts for microgrids," *Renewable and Sustain. Energy Rev.*, vol. 50, pp. 325-345, Oct. 2015.

J4 E. Prieto-Araujo, A. Egea-Alvarez, S. Fekriasl, O. Gomis-Bellmunt, "DC voltage droop control design for multi-terminal HVDC systems considering AC and DC grid dynamics," *IEEE Trans. Power Del.*, vol. 31, no. 2, pp. 575-585, Apr. 2016.

Published - Not included in the thesis

J5 J.M. Rodriguez-Bernuz, E. Prieto-Araujo, F. Girbau-Llistuella, J.A. Vidal-Clos, A. Sumper, R. Villafáfila-Robles, "Experimental validation

of a single phase Intelligent Power Router", *Sustainable Energy Grids and Networks*, vol. 4, pp. 1-15, Dec. 2015.

J6 J. Sau-Bassols, E. Prieto-Araujo, A. Egea-Alvarez, O. Gomis-Bellmunt, "Modelling and control of an interline Current Flow Controller for meshed HVDC grids," accepted for publication in *IEEE Trans. Power Del.*, Jan. 2016.

Submitted

S-J7 E. Prieto-Araujo, A. Junyent-Ferré, G. Clariana-Colet, O. Gomis-Bellmunt, "Control Design of Modular Multilevel Converters in Normal and AC Fault Conditions for HVDC grids," submitted to *Electric Power Syst. Res.*, Apr. 2016.

S-J8 E. Prieto-Araujo, A. Junyent-Ferré, G. Clariana-Colet, O. Gomis-Bellmunt, "Control of Modular Multilevel Converters under Singular Unbalanced Voltage Conditions with Equal Positive and Negative Sequence Components," submitted to *IEEE Trans. Power Syst.*, Feb. 2016.

Submitted - Not included in the thesis

S-J9 J. Sau-Bassols, E. Prieto-Araujo, O. Gomis-Bellmunt, "Current Source Converter series tapping of a LCC-HVDC transmission system for integration of offshore wind power plants," submitted to *Electric Power Syst. Res.*, Jan. 2016.

Book chapters

Published - Included in the thesis

B1 E. Prieto-Araujo, F.D. Bianchi, "State-space representation of HVDC grids," in *HVDC Grids For Offshore and Supergrid of the Future*, Wiley. ISBN: 978-1-118-85915-5.

B2 E. Prieto-Araujo, O. Gomis-Bellmunt,"Wind turbine technologies," in *HVDC Grids For Offshore and Supergrid of the Future*, Wiley. ISBN: 978-1-118-85915-5.

Published - Not included in the thesis

B3 F.D. Bianchi, E. Prieto-Araujo, "Optimal droop control of multi-terminal VSC-HVDC grids," in *HVDC Grids For Offshore and Supergrid of the Future*, Wiley. ISBN: 978-1-118-85915-5.

Conferences

Published papers - Included in the thesis

C1 E. Prieto-Araujo, F.D. Bianchi, A. Junyent-Ferré, O. Gomis-Bellmunt, "Droop control design of multi-terminal HVDC systems for offshore wind farms," *Seminar for Advanced Control Appl. (SAICA)*, Barcelona, Spain, Nov. 2011.

C2 E. Prieto-Araujo, M. Cheah-Mañé, A. Junyent-Ferré, O. Gomis-Bellmunt, "Development of a laboratory platform for testing new solutions to integrate renewable energy sources in power systems," *15th Eur. Conf. on Power Electron. and Appl. (EPE)*, Lille, France, Sept. 2013.

C3 E. Prieto-Araujo, D. Lavèrnia, A. Junyent-Ferré, O. Gomis-Bellmunt, "Distributed control of a nine-phase permanent magnet generator and scaled platform validation," *Eur. Wind Energy Assoc. (EWEA) Annual Event*, Barcelona, Spain, Mar. 2014.

C4 E. Prieto-Araujo, F.D. Bianchi, A. Junyent-Ferré, O. Gomis-Bellmunt, "Methodology for droop control dynamic analysis of multi-terminal VSC-HVDC grids for offshore wind farms," *IEEE PES General Meeting Conf.*, National Harbor (Washington DC), USA, Jul. 2014.

C5 E. Prieto-Araujo, A. Junyent-Ferré, D. Lavèrnia, O. Gomis-Bellmunt, "Decentralized control design of a nine-phase permanent magnet generator," *Int. Wind Eng. Conf. (IWEC)*, Hannover, Germany, Sept. 2014.

C6 E. Prieto-Araujo, S. Fekriasl, O. Gomis-Bellmunt, "Control and experimental validation of a Dual Active Bridge Series Resonant Converter," *IEEE 6th Int. Symp. on Power Electron. for Distributed Generation Systems (PEDG)*, Aachen, Germany, Jun. 2015.

C7 E. Prieto-Araujo, A. Junyent-Ferré, D. Lavèrnia-Ferrer, O. Gomis-Bellmunt, "Decentralized Control of a Nine-Phase Permanent Magnet

Generator for Offshore Wind Turbines," Accepted in *IEEE PES General Meeting Conf.*, Boston, USA, Jul. 2016.

C8 E. Prieto-Araujo, A. Egea-Alvarez, S. Fekriasl, O. Gomis-Bellmunt, "DC voltage droop control design for multi-terminal HVDC systems considering AC and DC grid dynamics," Accepted in *IEEE PES General Meeting Conf.*, Boston, USA, Jul. 2016.

Published papers - Not included in the thesis

C9 A. Junyent-Ferré, E. Prieto-Araujo, O. Gomis-Bellmunt, F. Bianchi, "Voltage sag ridethrough of PMSG wind turbines using droop control stabilization," *14th Eur. Conf. on Power Electron. and Appl. (EPE)*, Birmingham, UK, Aug. 2011.

C10 A. Junyent-Ferré, M. Cheah-Mañé, E. Prieto-Araujo, O. Gomis-Bellmunt, "Single phase to balanced three phase load converter control," *15th Eur. Conf. on Power Electron. and Appl. (EPE)*, Lille, France, Sept. 2013.

C11 M. Cheah Mañé, E. Prieto-Araujo, R. Villafáfila Robles, A. Sudria-Andreu, O. Gomis Bellmunt, "Microgrids and emulation of distribution energy resources," *I Congreso Iberoamericano sobre microrredes con generación distribuida de renovables*, Soria, Spain, Sept. 2013.

C12 G. Vinyals Canal, J.A. Vidal-Clos, G. Clariana-Colet, E. Prieto-Araujo, R. Villafáfila-Robles, O. Gomis-Bellmunt, O. Sudria-Andreu, "Microrred de laboratorio para la emulación de recursos energéticos distribuidos," *II Congreso Iberoamericano sobre microrredes con generación distribuida de renovables,* Soria, Spain, 2014.

C13 F. Girbau-Llistuella, J.M. Rodriguez-Bernuz, E. Prieto-Araujo, A. Sumper, "Experimental validation of a single phase intelligent power router," in *Innovative Smart Grid Technol. Conf. Eur. (ISGT-Europe)*, Istanbul, Turkey, Oct. 2014.

C14 J. Sau-Bassols, A. Egea-Alvarez, E. Prieto-Araujo, O. Gomis-Bellmunt, "Current Source Converter series tapping of a LCC-HVDC transmission system for integration of offshore wind power plants," *11th IET Int. Conf. on in AC and DC Power Transmission*, Birmingham, UK, Feb. 2015.

C15 S. Akkari, E. Prieto-Araujo, J. Dai, O. Gomis-Bellmunt, X. Guillaud, "Impact of the DC Cable Models on the SVD Analysis of a Multi-Terminal HVDC System," accepted for publication on *19th Power Syst. Computation Conf. (PSCC)*, Genova, Italy, Jun. 2016.

Local conferences

Published papers

C16 E. Prieto-Araujo, J.A. Vidal-Clos, G. Clariana-Colet, R. Villafáfila-Robles, O. Gomis-Bellmunt, "Desarrollo de una Microred de laboratorio para estudios de integración de energías renovables en la red eléctrica," *II Congreso Smart Grids*, Madrid, Spain, Oct. 2014.

C17 P. Olivella-Rosell, G. Vinyals-Canal, E. Prieto-Araujo, J. Bergas-Jané, "Desarrollo de una Microred de laboratorio para estudios de integración de energías renovables en la red eléctrica", *II Congreso Smart Grids*, Madrid, Spain, Oct. 2014.

Patents

P1 O. Gomis-Bellmunt, M. De-Prada-Gil, F. Díaz-González, E. Prieto-Araujo."Harmonics mitigation in multiphase generator conversion systems," Application number: EP13382510.9. Filed in December, 2013.

P2 Inventors: F. Hassan, J. Sau-Bassols, E. Prieto-Araujo, O. Gomis-Bellmunt. "Bridgeless converter for current control in DC grids," Application number: EP14275180. Filed in October, 2014.

P3 Inventors: F. Hassan, J. Sau-Bassols, E. Prieto-Araujo, O. Gomis-Bellmunt. "Distributed current flow control in DC grids," Application number: EP14382445. Filed in November, 2014.

Conferences presentation

P-C1 Presentation of "Control of multi-terminal HVDC systems, droop constants design" in *2nd HVDC Doctoral Colloquium*, Barcelona, Spain, Jul. 2011.

P-C2 Presentation of "Control of a nine-phase wind generator for offshore wind" in *4th HVDC Doctoral Colloquium*, Leuven, Belgium, Jul. 2013.

P-C3 Presentation of "Modular generators for offshore wind turbines" in *VIII International conference on energy innovation: Wind power to the grid*, Barcelona, Spain, Oct. 2013.

P-C4 Presentation of "Multi-terminal HVDC Control" in *HVDC Towards the future Workshop*, Barcelona, Spain, Apr. 2014.

P-C5 Presentation of "Towards the offshore wind power plants" in *Barcelona Global Energy Challenges*, Barcelona, Spain, Jun. 2014.

P-C6 Presentation of "Power converters for energy storage" in *5th HVDC Doctoral Colloquium*, London, UK, Jul. 2014.

P-C7 Presentation of "MMC control under unbalanced grid conditions" in *6th HVDC Doctoral Colloquium*, Roskilde, Denmark, Sept. 2015

Other Contributions

O-J1 E. Prieto-Araujo, A. Sudria-Andreu, R. Villafáfila-Robles, "Energy management in buildings and emulators: a perfect combination" (Gestión de energía en edificios y emuladores: una combinación perfecta), *Automática e Instrumentación*, n. 440, pp. 68-70, May 2012.

O-J2 E. Prieto-Araujo, J.A. Vidal-Clos, G. Clariana-Colet, G. Vinyals-Canal, R. Villafáfila-Robles, O. Gomis-Bellmunt, "Microrredes experimentales basadas en emuladores," *Automática e instrumentación*, n. 470, pp. 67-70, Apr. 2015.

O-J3 M. Aragüés-Peñalba, E. Prieto-Araujo, A. Egea-Alvarez, O. Gomis-Bellmunt. "Superredes, las redes eléctricas del futuro," *Buran (IEEE PES Student Branch Barcelona Review)*, May 2013.

O-J4 X. Pi, O. Miravalles-Soler, A. Chamorro-Coloma, E. Prieto-Araujo, S. Galceran-Arellano. "Sistemas embedded de bajo coste: ¿Uso educativo, de hobby o industrial?," *Automática e instrumentación*, no. 451, pp. 42-50, Jun. 2013.